Theoretical study of isotropic Huygens particles for metasurfaces

Romain Dezert

▶ **To cite this version:**

Romain Dezert. Theoretical study of isotropic Huygens particles for metasurfaces. Physics [physics]. Université de Bordeaux, 2019. English. NNT : 2019BORD0415 . tel-02869591

HAL Id: tel-02869591
https://theses.hal.science/tel-02869591

Submitted on 16 Jun 2020

HAL is a multi-disciplinary open access archive for the deposit and dissemination of scientific research documents, whether they are published or not. The documents may come from teaching and research institutions in France or abroad, or from public or private research centers.

L'archive ouverte pluridisciplinaire **HAL**, est destinée au dépôt et à la diffusion de documents scientifiques de niveau recherche, publiés ou non, émanant des établissements d'enseignement et de recherche français ou étrangers, des laboratoires publics ou privés.

université de BORDEAUX

THÈSE PRÉSENTÉE
POUR OBTENIR LE GRADE DE

DOCTEUR DE L'UNIVERSITÉ DE BORDEAUX

ÉCOLE DOCTORALE DE
SCIENCES PHYSIQUES ET DE L'INGÉNIEUR
spécialité : Lasers, Matière, Nanosciences

Par Romain DEZERT

Theoretical study of isotropic Huygens particles for metasurfaces

Sous la direction de :
Alexandre BARON
Philippe RICHETTI

Soutenue le 17 Décembre 2019

Jury

M. Christophe CRAEYE	Professeur - Université Catholique de Louvain	Rapporteur
M. Antoine MOREAU	Maître de Conférences - Université Clermont Auvergne	Rapporteur
Mme Béatrice DAGENS	Directrice de Recherche - Université Paris-Sud	Examinatrice
Mme Cécile ZAKRI	Professeur - Université de Bordeaux	Présidente
M. Alexandre BARON	Maître de Conférences - Université de Bordeaux	Directeur
M. Philippe BAROIS	Directeur de Recherche - Université de Bordeaux	Co-directeur

Étude théorique de particules de Huygens isotropes pour des applications en métasurfaces

Par Romain DEZERT

Sous la direction de:

Alexandre BARON
Philippe RICHETTI
Philippe BAROIS

Université de Bordeaux
Sciences et technologies
351 cours de la Libération CS 10004
33 405 Talence CEDEX, France

Unité de recherche:

Centre de Recherche Paul Pascal (CRPP)
UMR5031, CNRS & Université de Bordeaux
115 Avenue du Dr Albert Schweitzer, 33600, PESSAC, France

À mon frère et à mes parents
Y en memoria de Ángela

Remerciements

"*It always seems impossible until it's done.*"

Nelson Mandela

Ce manuscrit est le résultat de trois années de travail réalisé au Centre de Recherche Paul Pascal. Je tiens avec les quelques lignes qui suivent à remercier l'ensemble des personnes qui ont contribué, de près ou de loin, à l'aboutissement de ce doctorat.

En premier lieu, je remercie la Directrice du CRPP, Cécile Zakri, de m'avoir accueilli au sein de son laboratoire. Ces travaux ont par ailleurs été rendus possibles grâce au financement du LabEx AMADEus, Cluster of Excellence, dont je remercie toute l'équipe, notamment son Directeur Étienne Duguet.

Je tiens à remercier chaleureusement les membres du jury d'avoir pris sur leur temps pour évaluer mes travaux de thèse. Merci à Antoine Moreau et Christophe Craeye d'avoir accepté la charge de rapporteur de ce manuscrit et à Béatrice Dagens et Cécile Zakri pour leur rôle d'examinatrices.

J'adresse mes sincères remerciements à mes directeurs Alexandre Baron et Philippe Richetti, à qui je dois énormément dans la réussite de ce projet. Merci de m'avoir fait confiance pour cette thèse et de m'avoir guidé et aidé pendant ces trois ans. J'ai énormément appris avec vous sur le plan professionnel. Votre rigueur et votre curiosité scientifique m'auront grandement poussé à étudier mon sujet toujours plus en profondeur. Par ailleurs, si j'ai pris un immense plaisir à travailler avec vous, c'est également de par votre enthousiasme et bonne humeur à tous deux. Je mesure pleinement la chance que j'ai eue et vous suis extrêmement reconnaissant pour la bienveillance dont vous avez fait preuve à mon égard tout au long de cette thèse.

J'aimerais ensuite remercier comme il se doit l'ensemble de l'équipe MaFIC qui m'a accueilli au CRPP. En particulier, je remercie chaleureusement Philippe Barois, d'avoir accepté de prendre part à la codirection de ma thèse, Ashod Aradian, aux côtés de qui j'ai travaillé pour mon projet de fin d'étude, ainsi qu'Olivier Mondain-Monval et Virginie Ponsinet. Merci également à Daniel Torrent, Said El-Jallal et Tong Wu, dont l'expertise m'aura été précieuse, ainsi qu'à Rajam Elancheliyan, Maria Letizia De Marco et Alberto Alvarez Fernandez, avec qui j'ai toujours eu grand plaisir à collaborer et échanger. Je dois dire que cela a été particulièrement agréable de travailler au sein de ce groupe et de prendre part aux réunions hebdomadaires qui en ponctuent la vie. Non seulement lieu d'échange de connaissances et de conseils avisés, ces réunions ont également été l'occasion (ou le prétexte diront certains...) de partager de délicieuses pâtisseries et de bons moments de rigolades. Merci à tous pour votre accueil et pour la bonne ambiance qui règne au sein de l'équipe.

Mes travaux de thèse ont également bénéficié de la collaboration multi-laboratoires du LabEx AMADEus et de l'expertise de chacun des membres de l'équipe "Métamatériaux auto-assemblés". À ce titre, je tiens à remercier Glenna Drisko, Mona Tréguer-Delapierre, Cyril Aymonier, Étienne Duguet, Jacques Leng, Jean-Baptiste Salmon, Kevin Vynck, Philippe Lalanne, Véronique Many, Benoit Cormary, Sara De Cicco et Sanaa Semlali. La pluridisciplinarité qui règne au sein de ce

collectif m'a permis d'acquérir des connaissances s'étendant bien au-delà de ma spécialité et particulièrement intéressantes pour mon ouverture scientifique.

En parallèle à ma thèse, j'ai également eu la chance de contribuer à un travail visant à l'étude des propriétés optiques de réseaux ordonnés de particules obtenues par démouillage de films minces. Merci donc à Paul Jacquet et Iryna Gozhyk de Saint-Gobain Recherche, ainsi qu'à Alexandre, de m'avoir offert l'opportunité de cette collaboration très enrichissante scientifiquement. Merci également à Joseph Lautru, Renaud Podor, Jérémie Teisseire, Jacques Jupille et Rémi Lazzari pour leur contribution à ce travail.

Je tiens également à remercier les différents services du laboratoire. Je pense notamment à Nathalie Touzé à l'accueil, ainsi qu'à Corinne Amengual et Caroline Legrand à la Direction, pour leur gentillesse et leur aide, chaque fois que j'en ai eu besoin. Un grand merci à Jean-Luc Laborde, Sandrine Maillet, Philippe Hortolland et Julien Desenfant du service informatique, qui m'ont fourni une assistance indispensable au bon déroulement de mon travail et de mes simulations numériques (merci Jean-Luc d'avoir dépanné mon PC à plus d'une reprise !). Je souhaite également remercier l'assistante en gestion administrative du LabEx AMADEus, Sylvie Roudier, pour son aide dans l'organisation de mes différentes missions, ainsi que pour sa gentillesse et sa rapidité à traiter chacune de mes demandes.

À titre plus personnel maintenant, je souhaite remercier un certain nombre de personnes ayant animé mes journées (soirées et week-ends aussi !), en commençant par mes co-bureaux. Ils ont été nombreux à se succéder en A123. Tous ont contribué à y créer une atmosphère plaisante et à égayer les journées de travail. Merci notamment à Xuan Wang pour son grand cœur, à Marco Alfonso "chemist of reality" tel qu'il se définissait lui-même, à Armand Roucher (le faiseur de bulles), sans oublier Emmanuel Suraniti (notre monsieur bonhomme officiel) venant compléter le quatuor ! Merci pour tous les moments mémorables que nous avons partagés, à l'instar des traditionnelles sorties au Carpe Diem. Merci également à mes co-bureaux Lachlan Alexander, Junjin Che (le barcelonais made in China), et Anaïs Vales (merci pour le cactus !).

Je voudrais ensuite remercier les doctorants de ma promotion : Raj Kumar Prajapati (mon inséparable acolyte !), Marie-Charlotte Tatry (qui m'aura beaucoup fait voyager dans sa mini cooper), Julien Roman (le hooligan), (Alias Rajou, Maricha et Ju!), Mayte Gómez-Castaño (partie goûter aux charmes de la Catalogne), ainsi qu'Ángela Valentín Pérez, Hanna Anop (HOP!), Maxime Thivolle, Penny Perlepe, Maria Letizia De Marco et Hervé Palis, des personnes exceptionnelles avec qui je suis heureux d'avoir vécu l'aventure de la thèse.

Merci plus généralement à tous ceux que j'ai eu l'occasion de côtoyer au cours de ces trois années: Carlotta Pucci (grazie mille per tutto!), Florian Aubrit (dont la plume n'a d'égal que ses cocktails), Van Son Vo (à la jovialité contagieuse), la ravissante Karen Caicedo, Simone Oldenburg, Rajam Elancheliyan, Emmanuel Picheau, Etienne Lepoivre, Maeva Riegert, Arantza Berenice Zavala Martínez, Valentine de Villedon, Sarah Scheffler, Flavia Mesquita Cabrini, Quentin Flamant, Goce (& Gabbana) Koleski, Emmanuelle Hamon, sans oublier Franco Tardani, Cintia Mateo, Aurélie Vigne, Petra Ivaskovic, Theodor Petkov, Katerina Kampioti, Pierre-Etienne Rouet, Hélène Parant, Artem Kovalenko, Marie Föllmer, Magdalena Murawska, Valentina Musumeci et Marie Haddou. Merci aussi à Joanna Giermanska (et ses plantes vertes !) pour sa gentillesse et sa compagnie les midis. Un très grand merci à Frédéric Louërat pour l'initiation au Hellfest qui restera un souvenir inoubliable et pour les quelques bières partagées de-ci de-là entre deux pogos dans les salles de concert bordelaises. Je tiens à remercier également Ahmed Bentaleb et toute l'équipe de badminton du Trinquet Maïtena.

J'aimerais remercier les musiciens talentueux que sont Bernard Codeso, Alexandre Baron, Thomas et Philippe Barois. Merci pour l'évasion musicale du lundi midi, j'ai pris grand plaisir à jouer avec vous ! (J'écris ces lignes en espérant qu'ils me pardonneront un jour mon départ du groupe au profit de ma carrière solo !). Merci aussi à Nadine et Philippe Barois pour l'organisation du désormais traditionnel apéro-concert chaque été ! Sur scène ou comme spectateur j'en garde de très beaux souvenirs !

Durant ces deux dernières années j'ai également passé beaucoup de temps sur les courts du Tennis Club de Brivazac. J'ai pu y renouer avec ma passion et atteindre l'équilibre dont j'avais besoin entre vie professionnelle et sportive. Le tennis m'aura entre autres permis de décompresser après les longues journées de rédaction. Tout d'abord un grand merci à Juju de la team blade (mon sparring partner préféré et artiste de la balle jaune !). Merci pour ces entrainements magiques et ces rencontres épiques (si on joue un peu c'est 2 et 2 !). Je remercie également Stéphane Reculusa et Christophe Couilleau, des coéquipiers à part (merci pour la coupe et bonne chance pour les prochains titres à décrocher !). Je salue également Sandra Pedemay, Thomas Beneyton, Victor Salvado, Samy Aoued, Jean-Christophe Baret, Éric Grelet, et tous les copains du tennis.

Finalement, j'aimerais remercier de tout cœur Anne qui a su m'épauler et me soutenir pour traverser l'épreuve que constitue la rédaction du mémoire. Merci pour ton soutien indéfectible, ton aide précieuse et pour tout ce que tu m'apportes au quotidien. Je remercie également ma famille, mon frère Lucas et plus particulièrement mes parents. Merci à eux de m'avoir toujours soutenu et de m'avoir mis dans les meilleures conditions pour poursuivre de longues études et arriver au terme de ce doctorat.

Enfin, merci à vous, lecteur, d'avoir pris le temps de vous intéresser à ces quelques lignes. Je vous souhaite également une excellente lecture si vous êtes amenés à vous aventurer plus loin dans ce mémoire qui m'a pris tant de temps à écrire, mais dont je tire finalement une immense satisfaction.

List of Publications

The published results that are included in this thesis are indicated in bold.

R. Dezert, P. Richetti, and A. Baron, "Isotropic Huygens dipoles and multipoles with colloidal particles", *Physical Review B*, vol. 96, no. 18, p. 180201, 2017

V. Many, R. Dezert, E. Duguet, A. Baron, V. Jangid, V. Ponsinet, S. Ravaine, P. Richetti, P. Barois, and M. Tréguer-Delapierre, "High optical magnetism of dodecahedral plasmonic meta-atoms," *Nanophotonics*, vol. 8, no. 4, pp. 549–558, 2019

P. Jacquet, B. Bouteille, R. Dezert, J. Lautru, R. Podor, A. Baron, J. Teisseire, J. Jupille, R. Lazzari, and I. Gozhyk, "Periodic arrays of diamond-shaped silver nanoparticles: From scalable fabrication by template-assisted solid-state dewetting to tunable optical properties", *Advanced Functional Materials*, p. 1901119, 2019

R. Dezert, P. Richetti, and A. Baron, "Complete multipolar description of reflection and transmission across a metasurface for perfect absorption of light", *Opt. Express*, vol. 27, no. 19, pp. 26317-26330, 2019

Contents

Remerciements i

List of Publications v

Contents vii

List of Figures xi

List of Abbreviations xiii

List of Symbols xv

1 Introduction 1
- 1.1 Context . . . 2
  - 1.1.1 An introduction to nanophotonics, metamaterials and metasurfaces . . . 2
  - 1.1.2 From the Huygens-Fresnel principle to Huygens metasurfaces . . . 3
  - 1.1.3 Colloidal nanochemistry and self assembly as promising plateforms for optical metasurfaces . . . 8
- 1.2 Aim and structure of the thesis . . . 9
  - 1.2.1 Motivations . . . 9
  - 1.2.2 Thesis content and outline . . . 10
- 1.3 References . . . 12

2 Theoretical framework and numerical methods 25
- 2.1 Electromagnetic wave propagation . . . 26
  - 2.1.1 Macroscopic Maxwell's equations in matter . . . 26
  - 2.1.2 Helmholtz vector wave equations . . . 27
  - 2.1.3 Monochromatic plane waves . . . 27
  - 2.1.4 Dispersion relation . . . 28
  - 2.1.5 Optical refractive index . . . 28
  - 2.1.6 Wave impedance . . . 28
  - 2.1.7 Poynting vector and energy flux through a surface . . . 29
- 2.2 Light interaction with particles . . . 29
  - 2.2.1 Electromagnetic scattering and multipole expansion . . . 29
    - 2.2.1.a The scattering problem . . . 29
    - 2.2.1.b Poynting theorem, energy conservation and cross-sections . . . 30
  - 2.2.2 Solutions of the Helmholtz equation in spherical coordinates . . . 32
    - 2.2.2.a Solutions to the radial part ψ_r . . . 33
    - 2.2.2.b Solutions to the angular part $\psi_\theta \psi_\varphi$ . . . 34
    - 2.2.2.c General form of the solutions . . . 34
  - 2.2.3 Solving of the scattering problem with the $\mathcal{T}$-Matrix . . . 35
    - 2.2.3.a Transition $\mathcal{T}$-matrix formalism . . . 35
    - 2.2.3.b Boundary conditions . . . 36
  - 2.2.4 Scattering by a single sphere . . . 36

2.2.4.a Mie theory: light scattering from a spherical particle . . . 36
2.2.4.b Absorption, scattering and extinction cross-sections . . . 37
2.2.5 Scattering from multiple spheres . . . 37
2.2.6 Multipole coefficients of the scattered field of arbitrary particles . . . 38
2.2.6.a Projection on the scattered electric field [8, 9] . . . 38
2.2.6.b Link with the currents [14] . . . 39
2.2.6.c Projections with electric current densities [8, 9] . . . 40
2.2.6.d Cross-sections calculation from the multipole coefficients . . . 41
2.2.6.e Link between the cartesian and the spherical multipoles . . . 41
2.3 Finite element method with COMSOL Multiphysics . . . 42
2.3.1 Meshing the simulation domain . . . 43
2.3.2 Scattered field formalism . . . 43
2.3.2.a Perfectly matched layers (PML) . . . 43
2.3.3 Modeling a periodic array of scatterers . . . 44
2.3.3.a Floquet-Bloch periodic boundary conditions . . . 44
2.3.3.b Port excitation and S parameters . . . 45
2.3.4 Multipole decomposition in COMSOL Multiphysics . . . 45
2.4 Concluding remarks . . . 45
2.5 References . . . 46

3 Design of isotropic Huygens sources with colloidal particles 47
3.1 Kerker conditions . . . 48
3.1.1 Far field radiation of multipoles and phase symmetries . . . 48
3.1.2 Generalized Kerker condition . . . 49
3.2 Kerker condition with low index spherical particles [18] . . . 52
3.2.1 Dipolar Huygens sources . . . 52
3.2.2 Broadband Huygens sources . . . 56
3.3 Clusters of particles [18] . . . 59
3.3.1 Homogenization and effective medium theory . . . 60
3.3.1.a Extended Maxwell-Garnett mixing rules . . . 60
3.3.1.b Limitations of the Maxwell-Garnett homogenization . . . 61
3.3.2 Resonant dipolar Huygens sources with clusters . . . 61
3.3.2.a Cluster designs with dielectric and plasmonic inclusions . . . 62
3.3.2.b Limitation of the homogenization approach . . . 64
3.3.3 Broadband multipolar Huygens sources . . . 65
3.3.3.a Comparison with the homogenized sphere . . . 67
3.3.4 Effect of voids, disorder and size polydispersity . . . 68
3.3.5 Conclusions . . . 70
3.4 Unidirectional scattering with multilayered particles . . . 70
3.4.1 Metallo-dielectric core-shells as ideal resonant dipolar Huygens sources . . . 70
3.4.2 All-dielectric core-shells . . . 73
3.5 Concluding remarks . . . 75
3.6 References . . . 76

4 Metasurface Analysis 83
4.1 Interaction of light with a metasurface . . . 84
4.1.1 Surface equivalence principle and generalized boundary conditions . . . 85
4.1.2 Boundary conditions expressed with surface impedances and admittances . . . 86
4.1.3 Transmission line formalism using impedance, scattering and chain matrix . . . 87
4.1.3.a Impedance matrix $[Z]$ . . . 88
4.1.3.b Admittance matrix $[Y]$ . . . 88
4.1.3.c Chain matrix $[ABCD]$ . . . 88
4.1.3.d Scattering matrix $[S]$ . . . 89

4.1.3.e Transmission line of a slab of material . . . 89
4.1.4 Equivalent circuit of metasurfaces . . . 89
4.1.4.a Metasurfaces radiating symmetric distribution of electric field described by $\vec{J}_e$ . . . 90
4.1.4.b Metasurfaces radiating an anti-symmetric distribution of electric field described by $\vec{J}_m$ . . . 90
4.1.4.c Metasurfaces radiating both symmetric and anti-symmetric distributions of electric field . . . 90
4.2 Metasurface analysis in the dipole approximation . . . 91
4.2.1 Effective polarisabilities . . . 91
4.2.2 Induced averaged current densities and surface impedance . . . 92
4.2.3 Metasurface properties expressed with effective polarisabilities . . . 93
4.2.4 Coupled dipole method . . . 93
4.2.4.a Approximate values for the coupling constant . . . 94
4.2.4.b Imaginary part of the coupling constant and energy conservation . . . 95
4.2.5 Lorentzian model . . . 96
4.3 Rigorous analysis of multipolar metasurfaces . . . 97
4.3.1 Link between emitted fields and current sources for periodic arrays . . . 97
4.3.2 Multipole expansion of metasurface properties in spherical coordinates . . . 98
4.3.2.a Transmission and reflection coefficients . . . 99
4.3.2.b Energy balance applied to the metasurface . . . 101
4.3.3 Link with cartesian expansion . . . 103
4.4 Concluding remarks . . . 104
4.5 References . . . 105

5 Multipolar Huygens metasurfaces **109**
5.1 Introduction . . . 110
5.2 Main features of Huygens metasurfaces . . . 110
5.2.1 Understanding of their properties through the dipolar Lorentzian model . . . 110
5.2.1.a Kerker condition with loss-less metasurfaces . . . 110
5.2.1.b From high transmission devices to perfect absorbers: role of losses and critical coupling . . . 112
5.2.2 Generalized conditions on multipoles . . . 115
5.2.2.a Perfect transmission . . . 115
5.2.2.b Perfect absorption . . . 115
5.2.3 Lattice coupling effects on the multipoles . . . 116
5.3 Wavefront shaping with dielectric clusters . . . 118
5.3.1 Phase modulation in the infrared with silicon cluster arrays . . . 118
5.3.1.a Phase modulation by varying the surface density . . . 121
5.3.1.b Phase modulation induced by a variation in the size of the clusters . . . 122
5.3.2 Design of beam shapping devices . . . 124
5.3.2.a Beam deflector . . . 124
5.3.2.b Lens . . . 125
5.3.2.c Comments and perspectives . . . 127
5.3.3 Limitations of transparent Huygens metasurfaces . . . 128
5.4 Perfect Absorbers . . . 130
5.4.1 Absorbers based on dielectric and plasmonic spherical particles . . . 130
5.4.1.a Dielectric particles . . . 130
5.4.1.b Plasmonic particles . . . 133
5.4.2 Total absorption with core-shells . . . 135
5.4.2.a Dipolar core-shells . . . 135
5.4.2.b Tunable absorption peaks in the infrared domain . . . 137
5.4.2.c Broadband absorption with multipolar core-shells . . . 138

5.4.2.d All-dielectric core-shells . . . 140
5.4.3 Cluster based perfect absorbers . . . 143
5.4.3.a Dielectric clusters . . . 143
5.4.3.b Plasmonic clusters . . . 146
5.4.3.c Tunable absorption . . . 147
5.5 Concluding remarks . . . 149
5.6 References . . . 150

6 Conclusions and Outlook **155**

A Appendices **I**
A.1 Spherical functions . . . I
A.2 Field quantities generated from magnetic currents . . . I
A.3 Far field scattering patterns . . . II
A.3.1 Isotropic scaterrers [2, 3] . . . II
A.4 References . . . IV

Résumé **V**

List of Figures

1.1 Electromagnetic spectrum . . . 2
1.2 Examples of metasurface applications for polarization and wavefront control . . . 3
1.3 Huygens Fresnel principle and Huygens metasurfaces . . . 4
1.4 Metasurfaces for beam shaping based on V-antennas and geometric phase . . . 4
1.5 Examples of particles exhibiting Huygens source features . . . 6
1.6 Huygens metasurfaces for high transmission and phase manipulation . . . 6
1.7 Wavefront manipulation with Huygens metasurfaces . . . 7
1.8 Colloidal nano-chemistry and self-assembly on surface . . . 8
1.9 Outline of the thesis . . . 10

2.1 Schematic view of the light scattering problem by an arbitrarily shaped particle . . . 30
2.2 Spherical and cartesian coordinates . . . 32
2.3 Set-up of COMSOL models for simulating isolated scatterers and periodic arrays . . . 44

3.1 Radiation patterns of the first multipoles . . . 49
3.2 Radiation diagrams of multipoles under Kerker condition . . . 50
3.3 First zeros of the Bessel and derivative of the Riccati-Bessel functions . . . 53
3.4 Multipole efficiencies of generalized Huygens sources. . . . 54
3.5 Scattering efficiencies of dipolar Huygens sources . . . 54
3.6 Optimal value of γ for approaching resonant Kerker dipoles with lossy spheres. . . . 55
3.7 Multipole trajectories of lossless dielectric particles . . . 56
3.8 Broadband scattering of TiO_2 and Al_2O_3 dielectric particles . . . 58
3.9 Evolution of γ for *Si* and *Ag* clusters obtained with Maxwell-Garnett homogenization 62
3.10 Dipolar Huygens source features of silicon and silver cluster in the visible domain . 63
3.11 Optical properties of homogenized spheres corresponding to *Si* and *Ag* clusters . . . 65
3.12 Extremely broadband Huygens source features of a silicon cluster . . . 66
3.13 Optical properties of the homogenized sphere equivalent to the broadband *Si* cluster 67
3.14 Effect of voids, disorder, and size polydispersity on the dipolar response of clusters . 68
3.15 Scalable designs of metallo-dielectric core-shell particles . . . 71
3.16 Dipolar Huygens source features of silver and gold core-shell particles . . . 72
3.17 Directional scattering of all-dielectric core-shells . . . 74

4.1 Light-Metasurface interaction and its description with surface currents . . . 84
4.2 Metasurface homogenized by surface current densities and boundary conditions . . . 86
4.3 Representation of a metasurface as a 2 ports network . . . 88
4.4 Equivalent transmission line circuit for metasurfaces of three different kinds . . . 91
4.5 Illustration of the different loss channels available in a dipolar metasurface . . . 96
4.6 Multipole expansion applied to arrays of particles . . . 100
4.7 Decomposition of radiation and absorption cross-sections for an array of sphere . . . 102

5.1 Loss-less metasurface with spectrally separated and overlapped resonances . . . 111
5.2 Impact of material loss on Huygens metasurfaces spectral response . . . 113
5.3 Analysis of the critical coupling conditions . . . 114

5.4 Impact of the lattice coupling on the first multipoles . . . 116
5.5 Transmittance and phase of silicon cluster metasurfaces in the infrared . . . 119
5.6 Transmission and phase modulation induced by varying lattice pitch . . . 121
5.7 Phase modulation for varying clusters size and a constant surface fraction . . . 123
5.8 Phase modulation for varying clusters size and a constant lattice pitch . . . 124
5.9 Design of a beam deflector based on *Si* cluster . . . 125
5.10 Meta-lens with 13 *Si* clusters . . . 126
5.11 Impact of the incidence angle on the transmission of Huygens metasurfaces . . . 129
5.12 Perfect absorption with SiO_2 particles . . . 131
5.13 Angle dependency of the SiO_2 metasurface absorption . . . 132
5.14 Perfect absorption with Al_2O_3 particles . . . 132
5.15 Perfect absorption with *Ag* particles . . . 134
5.16 Perfect absorption with metallo-dielectric core-shells . . . 136
5.17 Angle dependence of the absorption of metallo-dielectric core-shell arrays . . . 137
5.18 Designs of perfect absorbers based on metallo-dielectric core-shell particles . . . 138
5.19 Multipolar origin ot the perfect absorption of metallo-dielectric core-shells arrays . 139
5.20 Perfect absorption with all dielectric core-shells . . . 140
5.21 Angle dependence of the absorption of arrays of all dielectric core-shell spheres . . . 141
5.22 All dielectric core-shells arrays exhibiting two strong absorption peaks . . . 142
5.23 Perfect absorption with *Si* clusters in the visible . . . 144
5.24 Angle dependence of the absorption of a *Si* cluster based metasurface . . . 145
5.25 Perfect absorption with *Ag* clusters . . . 146
5.26 Designs of perfect absorbers with clusters of plasmonic and dielectric particles . . . 147
5.27 Evolution of the absorption spectra of cluster based metasurfaces with f_s . . . 148

List of Abbreviations

CDM	Coupled Dipole Method.
CEMDM	Coupled Electric and Magnetic Dipole Method.
DDA	Discrete Dipole Approximation.
EBCM	Extended Boundary Condition Method.
FDTD	Finite Difference Time Domain.
FEM	Finite Element Method.
GSTC	Generalized Sheet Transition Conditions.
PML	Perfectly Matched Layer.
PMM	Point-Matching Method.
SEM	Scanning Electron Microscopy.
TE	Transverse Electric.
TM	Transverse Magnetic.
VSH	Vector Spherical Harmonics.
VSWF	Vector Spherical Wave Functions.

List of Symbols

$\mathcal{A}$	Geometric area $[m^2]$.
$[ABCD]$	Chain matrix.
α_{eff}	Effective polarisabilities $[m^3]$.
α	Dipolar polarisabilities $[m^3]$.
α^q	Quadrupolar polarisabilities $[m^5]$.
(a_n, b_n)	Lorentz-Mie coefficients.
$(a_{n,m}, b_{n,m})$	Expansion coefficients of the scattered field in spherical coordinates.
$\vec{B}$	Magnetic flux density $[T]$.
β	Interaction constant of a periodic array $[m^3]$.
c	Speed of light in vacuum $\approx 3 \times 10^8$ $[m.s^{-1}]$.
$(c_{n,m}, d_{n,m})$	Expansion coefficients of the internal field in spherical coordinates.
Δ	Laplace operator.
$\delta(x)$	Dirac function.
$\vec{D}$	Displacement field $[C.m^{-2}]$.
$\vec{E}$	Electric field $[V.m^{-1}]$.
$\vec{E}_{inc}$	Incident electric field $[V.m^{-1}]$.
$\vec{E}_{int}$	Internal electric field $[V.m^{-1}]$.
$\vec{E}_{scat}$	Scattered electric field $[V.m^{-1}]$.
$\vec{E}_{tot}$	Total electric field $[V.m^{-1}]$.
$\vec{E}_r$	Reflected electric field $[V.m^{-1}]$.
$\vec{E}_a$	Electric field scattered by an array $[V.m^{-1}]$.
$\vec{E}_t$	Transmitted electric field $[V.m^{-1}]$.
ε	Electric permittivity of a medium $[F.m^{-1}]$.
ε_{eff}	Effective permittivity of a composite medium.
$\hat{\varepsilon}$	Generalized Electric permittivity of a medium $[F.m^{-1}]$.
ε_r	Relative electric permittivity of a medium.
ε_0	Vaccum electric permittivity $\approx 8{,}854 \times 10^{-12}$ $[F.m^{-1}]$.
$\mathcal{E}_n$	Multipole moments radiating an even distribution of electric field.
$\vec{e}_r, \vec{e}_\theta, \vec{e}_\varphi$	Unit vectors of the spherical basis.
$\vec{e}_x, \vec{e}_y, \vec{e}_z$	Unit vectors of the cartesian basis.
f_s	Surface filling fraction of an array of particles.
f_v	Volume filling fraction.
$\overleftrightarrow{G}(\vec{r}, \vec{r}')$	Dyadic Green's function.
$\overleftrightarrow{\mathcal{G}}$	Lattice periodic Green's function.
$G_0(\vec{r}, \vec{r}')$	Scalar Green's function.
$\overleftrightarrow{\mathcal{G}}^0$	Interaction lattice periodic Green's function.
γ	Refractive index contrast.
γ_j	Non-radiative loss rate $[rad.s^{-1}]$.
Γ_j	Radiative loss rate of resonances $[rad.s^{-1}]$.
$h_n^{(1)}$	Spherical Hankel function of the first kind of order n.
$h_n^{(2)}$	Spherical Hankel function of the second kind of order n.

$\vec{H}$	Magnetic field $[A.m^{-1}]$.
$\vec{H}_{inc}$	Incident magnetic field $[A.m^{-1}]$.
$\vec{H}_{int}$	Internal magnetic field $[A.m^{-1}]$.
$\vec{H}_{scat}$	Scattered magnetic field $[A.m^{-1}]$.
$\vec{H}_{tot}$	Total magnetic field $[A.m^{-1}]$.
I_0	Intensity of a wave $[W.m^{-2}]$.
$\overleftrightarrow{I}$	Unit dyad.
$\Im$	Imaginary part operator.
j_n	Spherical Bessel function of order n.
$\vec{J}_c$	Conduction current density $[A.m^{-2}]$.
$\vec{J}$	Current density $[A.m^{-2}]$.
$\vec{J}_e$	Equivalent electric surface current density $[A.m^{-1}]$.
$\vec{J}_m$	Equivalent magnetic surface current density $[V.m^{-1}]$.
$\vec{J}_s$	Source current density $[A.m^{-2}]$.
$\vec{k}$	Wave vector $[m^{-1}]$.
$\vec{\mathcal{L}}$	Angular momentum operator.
L	Lattice pitch $[m]$.
λ_R	Wavelength of the Rayleigh's anomaly cut off [m].
$\vec{m}$	Magnetic dipole moment vector $[T \cdot m^3]$.
$\vec{M}_{n,m}$	Second Hansen solenoidal vector of degree n and order m.
m	Azimuthal angular projection index.
μ	Magnetic permeability of a medium $[H.m^{-1}]$.
μ_{eff}	Effective permeability of a composite medium.
μ_r	Relative magnetic permeability of a medium.
μ_0	Vaccum magnetic permeability $\approx 4\pi 10^{-7}$ $[F.m^{-1}]$.
$\vec{N}_{n,m}$	First Hansen solenoidal vector of degree n and order m.
n	Angular momentum index.
N	Optical refractive index.
N_{eff}	Effective refractive index.
η	Intrinsic wave impedance of a medium [Ω].
η_0	Wave impedance of vacuum $\approx 376,73$[Ω].
$\vec{\nabla}$	Nabla operator.
n_h	Host medium refractive index.
$\mathcal{N}$	Number of particle per unit volume.
θ	Polar angle.
$\mathcal{O}_n$	Multipole moments radiating an odd distribution of electric field.
ω	Pulsation $[rad.s^{-1}]$.
$\vec{p}$	Electric dipole moment vector $[C \cdot m]$.
P_n^m	Associated Legendre polynomial of degree n and order m.
$\vec{\Pi}$	Poynting vector $[W.m^{-2}]$.
$\vec{S}$	Irradiance or time-averaged Poynting vector $[W.m^{-2}]$.
Φ	Phase.
φ	Azimuthal angle.
π_{nm}	Second angle-dependent scalar tesseral function of degree n and order m.
$(p_{n,m}, q_{n,m})$	Expansion coefficients of the incident field in spherical coordinates.
Ψ_n	Riccati-Bessel functions of order n associated to j_n.
Q	Efficiencies or particle size normalized cross-section.
$\overleftrightarrow{Q}_e$	Electric quadrupole moment tensor $[C \cdot m^2]$.
$\overleftrightarrow{Q}_m$	Magnetic quadrupole moment tensor $[T \cdot m^4]$.
$\vec{r}$	Position vector $[m]$.
R	Particle radius $[m]$.

r_p	inclusion radius for a cluster of particles $[m]$.
r_c	Core radius for a core-shell particle $[m]$.
$\Re$	Real part operator.
ρ	Electric free charge density $[C.m^{-3}]$.
$\mathcal{S}$	Unit cell area $[m^2]$.
$[S]$	Scattering matrix.
σ_{abs}	Absorption cross-section $[m^2]$.
σ_{back}	Scattering cross-section in the backward direction $\theta = \pi$ $[m^2]$.
σ_d	Differential scattering cross-section $[m^2]$.
σ_{ext}	Extinction cross-section $[m^2]$.
σ_{for}	Scattering cross-section in the forward direction $\theta = 0$ $[m^2]$.
σ_{scat}	Scattering cross-section $[m^2]$.
$\sigma_{scat,a}$	Scattering cross-section of a unit cell $[m^2]$.
σ_c	Conductivity of a medium $[S.m^{-1}]$.
$\mathcal{T}$	Transition matrix.
τ_{nm}	First angle-dependent scalar tesseral function of degree n and order m.
t	Time $[s]$.
v_p	Phase velocity.
$\vec{V}$	Scattering amplitude vector.
W	Power $[W]$.
x	Size parameter.
$\vec{X}_{n,m}$	Vector spherical harmonics of degree n and order m.
ξ_n	Riccati-Bessel functions of order n associated to $h_n^{(1)}$.
$[Y]$	Admittance matrix.
y_n	Spherical Neumann function of order n.
$Y_{n,m}$	Spherical harmonics of degree n and order m.
Y_m	Magnetic surface admittance $[S]$.
$[Z]$	Impedance matrix.
Z_e	Electric surface impedance $[\Omega]$.
$z_n^{(l)}$	Radial function.
$\cdot$	Scalar product.
$\wedge$	Vector product.

Chapter 1

Introduction

Contents

1.1 Context 2
1.1.1 An introduction to nanophotonics, metamaterials and metasurfaces 2
1.1.2 From the Huygens-Fresnel principle to Huygens metasurfaces 3
1.1.3 Colloidal nanochemistry and self assembly as promising plateforms for optical metasurfaces 8
1.2 Aim and structure of the thesis 9
1.2.1 Motivations 9
1.2.2 Thesis content and outline 10
1.3 References 12

Summary: This introductory chapter briefly discusses the concept of optical Huygens metasurfaces. It provides a context for their emergence and illustrate their strong potential for light manipulation at the sub-wavelength scale. On the other hand, we introduce bottom-up techniques, whose recent developments now enable large scale synthesis and assembly of complex functional building-blocks, being therefore of great interest for the realization of optical metasurface. Based on these considerations, the motivation and outline of this thesis are presented.

1.1 Context

1.1.1 An introduction to nanophotonics, metamaterials and metasurfaces

Nanophotonics is a burgeoning branch of modern research that combines nanotechnology and optics. It can be defined as the science dedicated to the understanding and control of light-matter interactions at the nanoscale. Its wide scope covers nanostructure engineering for the generation, manipulation and detection of light in the infrared, visible and ultraviolet domains of the electromagnetic spectrum (see Fig. 1.1). The manipulation of optical fields at the nanoscale, with properly designed components, is of significant importance for a wide range of fields ranging from communications to health and energy harvesting. It offers therefore a number of promising applications in imaging, sensing, photodetection, lighting and displays, communications (integrated photonic, data storage...), solar energy, computing, opto-electronics, medical targeted treatments, drug delivery, etc. [1–4].

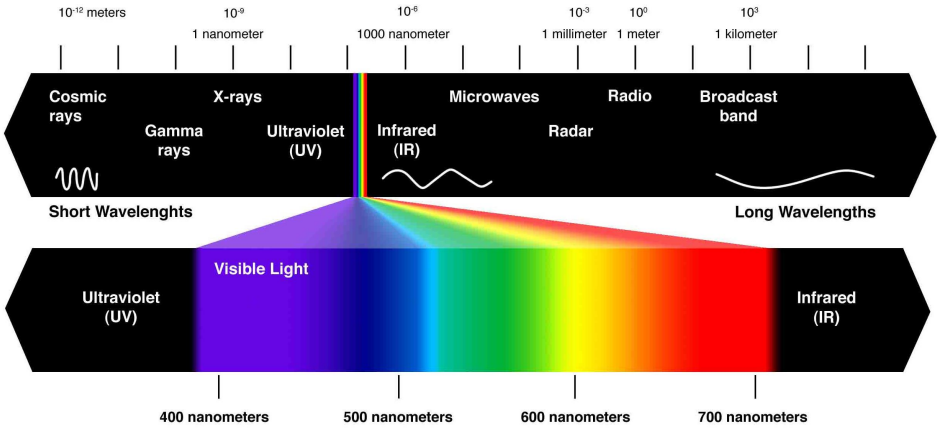

Figure 1.1 – Electromagnetic spectrum. Nanophotonics concerns the generation, manipulation and detection of light for the infrared, visible and ultraviolet domains.

The past 20 years have seen an intense and rapid development of a new branch of nanophotonics dedicated to *metamaterials*. The concept of metamaterials, constructed around the Greek prefix “meta”, meaning “to go beyond”, emerged in the years 2000 [5]. It refers to artificial materials, consisting of periodically arranged sub-wavelength resonators, engineered to exhibit unusual electromagnetic properties that are not naturally encountered. In fact, while natural material properties are mainly defined by their chemical composition, metamaterials inherit their properties from their man-made sub-units, which we may refer to as *meta-atoms*. They have been investigated so as to achieve a number of new physical phenomena such as negative refraction [6, 7], epsilon-near-zero materials [8, 9], giant artificial chirality [10–12], perfect lenses for sub-diffraction-limited imaging [13–15], invisible cloaking and transformation optics [16–19]. Although widely explored at microwave frequencies in the early years, the metamaterial concept was also successfully developed at optical frequencies by downscaling structure sizes [20–22]. Inspite of many elegant realizations, optical metamaterials still face two important issues that limit their use today. Firstly due to their structural complexity that requires 3D fabrication, they are challenging to produce at large scales, often expensive and time-consuming. Moreover, metamaterials usually present high dissipation losses, making it impractical for light to propagate through a bulk portion of the metamaterial.

On the other hand, metasurfaces, the two-dimensional equivalent of metamaterials, for which the above mentioned limitations are relaxed due to their sub-wavelength thickness, has attracted significant research interest over the last decade. As a matter of fact, most initial proposals of metamaterials were actually two-dimensional assemblies of meta-atoms, making it hard to interpret their properties in terms of effective parameters of bulk materials. As a result, the com-

munity gradually shifted towards a surface description of the ensemble properties of the structures, which resulted in considering them as *metasurfaces*. In comparison to bulk metamaterials in which waves propagate through long distances, metasurfaces are ultra-thin interfaces that affect an incident beam of light over a sub-wavelength scale. The basic operation principle relies on the collective scattering behaviour of the sub-units organized into flat subwavelength arrays. An arbitrary manipulation of the amplitude, phase and/or polarization can be achieved by a proper local control of the shape, nature, orientation and organisation of the constituents.

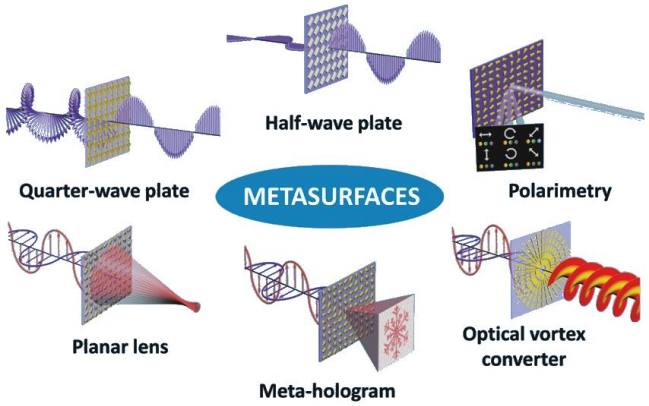

Figure 1.2 – Examples of metasurface applications for polarization and wavefront control. Reproduced from [23]

Due to their exceptional abilities for light manipulation, metasurfaces are expected to be the next generation of optical elements used to control the optical field. In the long term, they could lead to the substitution of bulky conventional optical components or diffractive elements, by compact flat optics. They have been widely explored to realize conventional functionalities of classic components such as lenses [24–36], waveplates [37–40], polarimeters [41–43], beam deflectors [24, 44–48], holograms [49–56], optical vortex converters [46, 57], as illustrated on Fig. 1.2, as well as for applications in light absorption, optical filtering, leaky-wave antennas, nonlinear devices [23], etc. They have also lead to the development of new and innovative functionalities, such as metadevices for the manipulation and measurement of photon quantum states [58, 59], multitasking metadevices [60], etc.

1.1.2 From the Huygens-Fresnel principle to Huygens metasurfaces

The incredible abilities of metasurfaces to manipulate light can be somewhat understood from the Huygens-Fresnel principle. Introduced by Christian Huygens in 1690 in his work entitled *Traité de la Lumière* [61], this principle is a well-known concept in electromagnetism at the foundation of the classic wave theory of light. It states that every point in space that receives an electromagnetic wave becomes the fictitious source of a new spherical wave spreading in the forward direction, explaining thus the gradual propagation of light. These point-sources, illustrated on Fig. 1.3-A, are the so-called Huygens sources and have for a long time remained a purely mathematical commodity used to explain various properties occurring in classical wave physics such as refraction (see Fig. 1.3-B), diffraction, and interference phenomena.

This intuitive picture is useful to qualitatively explain the working principle behind the most common classes of metasurfaces: those dedicated to wavefront engineering. By analogy with the Huygens principle, when illuminated, each resonator on a metasurface can be treated as a new source that scatters light, thus forming a secondary source of wavelets. The new wavefronts, both in transmission and reflection, can be regarded as the combination of all the secondary waves. By introducing spatial variations in the phase retardation of the optical scatterers forming the metasurface, one can create an artificial interface that moulds the optical wavefronts into arbi-

trary shapes. Therefore, such metasurfaces can be seen as the engineered version of the Huygens principle. Any structures of sub-wavelength size that can "catch and release" the electromagnetic field, *i.e* induce a retardation, with a controllable phase shift are good candidates for this type of wave manipulation. An introduction to the numerous approaches existing for engineering phase discontinuities can be found in excellent reviews discussing the recent developments in metasurfaces [23, 56, 62–69]. We will only briefly mention some of the most relevant approaches in the following.

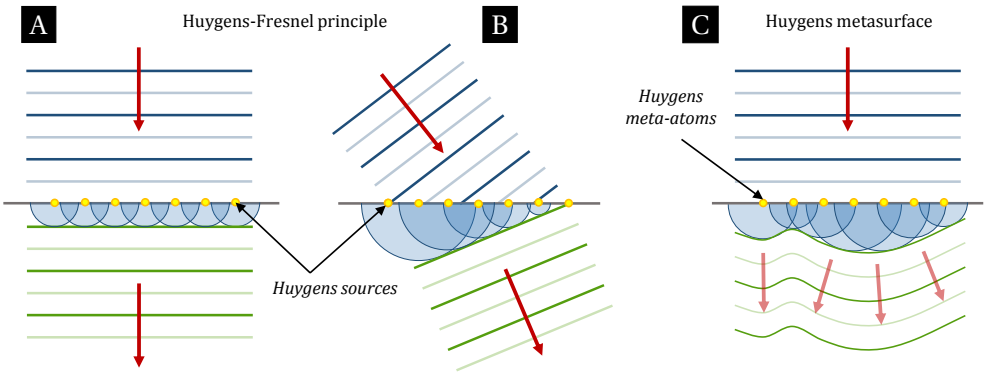

Figure 1.3 – A) Illustration of the Huygens-Fresnel principle showing the gradual propagation of a plane wave through the excitation of secondary waves. B) Huygens-Fresnel principle applied to the refraction phenomenon. C) Illustration of the concept of Huygens' metasurfaces. Assembling in a sub-wavelength array an ensemble of optical resonators exhibiting Huygens source features, it is possible to convert an incident plane wave into an arbitrarily shaped beam.

Most pioneering proposals in wavefront shaping have relied on plasmonic resonances of particles. Indeed, the first proposed nanostructures were V-shaped [39, 70–75] (or similarly C-shaped [76] or Y-shaped [40]) metallic antennas. Such resonators exhibit two orthogonal electric dipole resonances and by changing the opening angle, length and orientation of the particles, an entire variation of the phase from 0 to 2π can be achieved in the infrared domain. This structure has been widely popularized by the work of F. Capasso's group, who also played a significant role in the emergence of the field of optical metasurfaces.

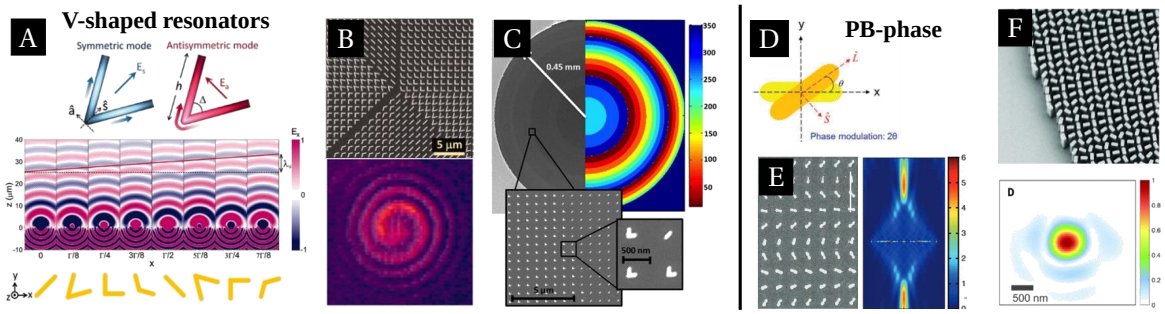

Figure 1.4 – A) Schematic representation of a V-antenna and its supported modes. The bottom panel shows anomalous refraction obtained from a super-cell combining 8 plasmonic V-antennas. Reproduced from [70]. B) V-antennas are arranged so as to generate a phase shift that varies azimuthally from 0 to 2π (top panel), thus producing a helicoidal scattered wavefront (bottom panel). Reproduced from [70]. C) Scanning electron microscopy (SEM) image of a fabricated lens with 3 cm focal distance and the corresponding implemented phase shift profile. Reproduced from [71]. D) Schematic of a Pancharatnam–Berry-phase with nanorods where the phase response is solely determined by the nanorod orientation. Reproduced from [23]. E) SEM image (left panel) of a plasmonic lens made from gold nanorods and intensity distribution (right panel) revealing the focussing of right-circularly polarized incident light. Reproduced from [77]. F) SEM micrograph (top panel) of a fabricated metalens consisting of *TiO2* nanofins on a glass substrate, and measured focal spot intensity profile (bottom panel) of the lens. Reproduced from [29].

Between 2011 and 2012, such meta-atoms have for example been used in the early demonstration of anomalous reflection and refraction enabled by metasurfaces according to the so-called generalized Snell's laws [70, 78] (see Fig. 1.4-A), applied to optical vortex beam generation [75] (see Fig. 1.4-B), as well as the realization of lenses [71] (see Fig. 1.4-C), etc. However, such plasmonic devices present low transmission efficiency in the 10% to 20% range due to the high intrinsic losses of their metallic elements.

Another well-known approach for implementing local phase gradient is to exploit the concept of geometric phase also known as the Pancharatnam-Berry phase [79, 80], developped in the early 2000s by Hasman *et al*. [81, 82]. This concept is based on anisotropic resonators. A simple rotation of an anisotropic scatterers can induce a cross-polarized phase retardation equal to twice the rotation angle (see Fig. 1.4-D). With this approach, it is possible to form metasurfaces consisting of a set of identical resonators with varying orientations so as to produce a desired phase profile. Such a modulation of the phase has been widely used to realize advanced wavefront manipulation of transmitted or reflected waves with both plasmonic [77, 83] (see Fig. 1.4-E) or dielectric resonators [24, 29] (As shown on Fig. 1.4-F). This approach applied to low loss dielectrics makes it possible to design and produce components with high transmission efficiency, typically higher than 85%. Nonetheless, the device must be excited with a circularly or elliptically polarized field and the transmitted light is in a different polarization state compared to the incident beam.

A fundamentally different approach, allowing the realization of polarization-independent metadevices with high efficiencies, has recently emerged with the concept of Huygens metasurfaces. They consist in reflection-less surfaces composed of meta-atoms that do not radiate backward. Analogous to the fictitious sources defined in the Huygens' principle, such meta-atoms are thus widely referred to as Huygens sources in the literature. Indeed Huygens metasurfaces were originally inspired by the surface equivalence theorem [84, 85], a generalization of the Huygens' principle in terms of electric and magnetic surface current densities. They were first proposed by Pfeiffer and Grbic in 2013 [86] and mainly rely on the old idea that a Huygens source behavior can be obtained by a combination of collocated, orthogonal and in phase electric and magnetic dipoles of equal strength [87, 88]. This configuration allows a unidirectional radiation pattern due to destructive interferences between the electromagnetic waves radiated by each dipole in the backward direction as well as constructive interferences in the forward direction. In addition, the excitation of a simple dipole resonance gives a phase shift of π across the resonance. The combination of the two electric and magnetic resonances thus provides sufficient degrees of freedom to achieve a phase excursion over the entire interval between 0 and 2π necessary for full control over the wavefront. Therefore, an array of such pairs of resonant dipoles can be used to create an equivalent sheet of electric and magnetic surface current densities that radiate in the forward direction only, with the possibility to form any arbitrary wavefront pattern and field distribution (see Fig. 1.3-C). The first implementations of this concept were performed at microwave frequencies with metasurfaces consisting in stacks of printed circuit boards containing unit-cells of combined copper wire and loops realizing the electric and magnetic responses. The authors [86] experimentally demonstrated a beam deflector with 86% transmittance. If has been widely investigated at microwave frequencies [89–91], the concept was also scaled down to optical frequencies [92]. The first implementation of optical Huygens metasurfaces were realized with patterned metallic-based unit-cells [93, 94] at telecommunication wavelengths but suffered from limited efficiency due to the ohmic losses.

On the other hand, the recent realization of Huygens optical metasurfaces are essentially based on sub-wavelength polarizable dielectric particles. These Mie resonators, whose scattering pattern can be tailored by their size, shape, or composition, have been widely suggested as optical nano-antennas capable of emitting light in specific direction [95–98] and constitute excellent building blocks to produce Huygens metasurfaces. Indeed, they support both strong electric and magnetic responses in the visible and near infrared range that can overlap in the same spectral range to produce a Huygens source. In particular, zero back-scattering is reached under the condition of balanced multipoles of opposite symmetries, also known as the Kerker condition

in reference to Milton Kerker's pioneering work [99]. Kerker actually realized that spherical particles that have an electric permittivity equal to the magnetic permeability ($\varepsilon = \mu$) have zero back-scattering under plane wave excitation. Zero back-scattering of subwavelength particles have for example been experimentally demonstrated at visible frequencies with *Si* spheres (see Fig. 1.5-A) and *GaAs* cylinders [100, 101]. As illustrated by Fig.1.5, nanoparticles of various shapes and composition such as spheres [102–107], spheroids [108–110], cubes [46, 111–115], cylinders and disks [116–118], core-shell particles [119, 119–124], particles with slits [111, 125] or holes [126], etc have been widely investigated for obtaining unidirectional forward scattering and as potential building blocks for Huygens surfaces.

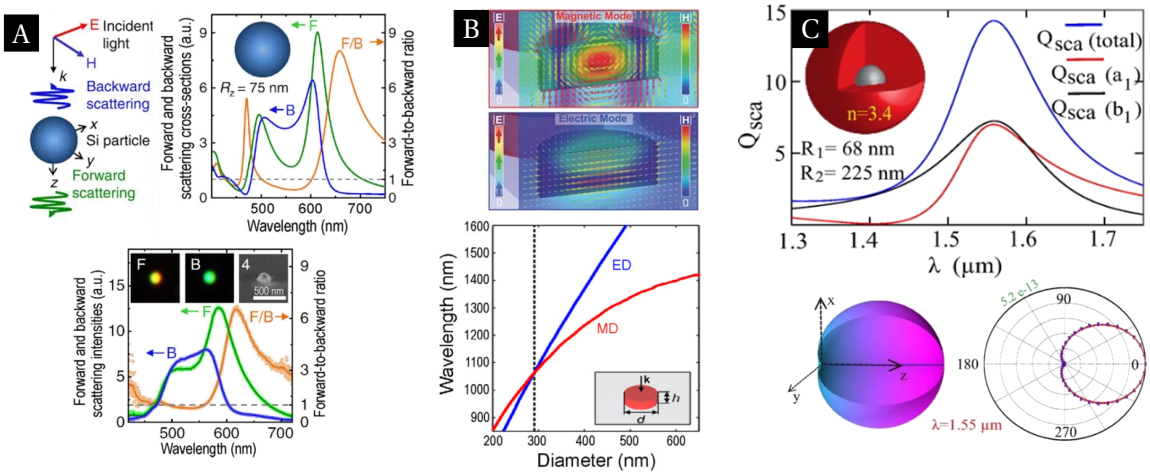

Figure 1.5 – A) Theoretical (top panel) and experimental demonstration (bottom panel) of forward-scattering of light by a single dielectric *Si* nanoparticle of diameter 150nm. Left axes show forward (green) and backward (blue) scattering intensities, and right axes show forward-to-backward ratio (orange curves). Reproduced from [100]. B) Top panel illustrates the electric and magnetic dipole mode profiles of a *Si* nanodisk. The bottom panel shows the position of the electric and magnetic dipole resonance wavelength as a function of the disk diameter. Reproduced from [116, 117]. C) Scattering efficiency (top panel) of a core-shell nanoparticle with a dielectric shell and a silver core. The bottom panel shows the corresponding 3D scattering pattern at the resonance revealing a strong forward scattering. Reproduced from [120].

Huygens metasurfaces made from periodic arrays of dielectric particles have been implemented at optical frequencies using a large variety of planar lithographic fabrication techniques. Resorting to dielectrics with low absorption losses has permit Huygens metasurfaces with high transmissions. Figure 1.6 shows the important contribution made in 2015 by Decker *et al.* [117] who demonstrated a Huygens metasurface with a high transmittance and full phase coverage obtained by spectrally overlapping electric and magnetic resonances of silicon nanodisks in the near-infrared [117] (as shown on Fig. 1.5-B).

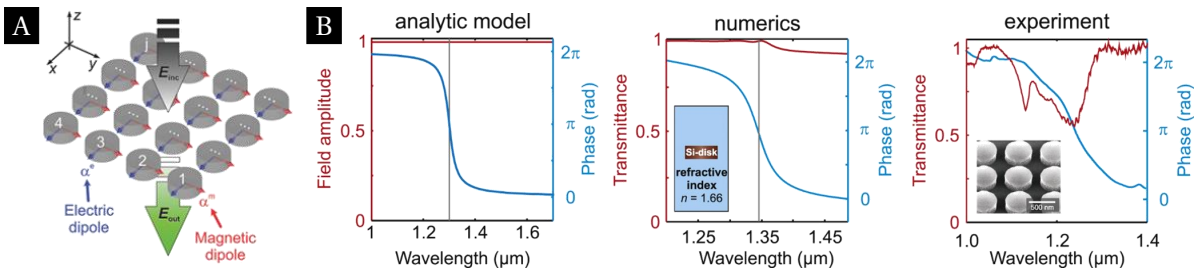

Figure 1.6 – A) Schematic of an array of nanodisks supporting electric and magnetic dipoles resonances. Reproduced from [117]. B) Transmitted field amplitude and phase obtained analytically, numerically and experimentally for an array of silicon nanodisks. Reproduced from [117, 127].

Since this demonstration, high-efficiency lossless all-dielectric Huygens metasurfaces have been demonstrated for a wide range of applications (see Fig. 1.7), such as lenses [128–132], vortex beam generation [46, 57], holographic images [49–51], beam deflectors [45, 46, 48, 133, 134], etc. Metasurfaces consisting of nanopillars of large aspect ratio (close to a unit wavelength thick), also known as high-contrast arrays, are also widely encountered [65] (see Fig. 1.7-C). Similar to the blazed binary optical elements that are at least two decades old [135–137], this structure supports multiple Fabry-Perot resonances. However, their high transmittance can also be analyzed from the unidirectional scattering of their elements that results from the overlapping between several of their odd and even multipoles satisfying the Kerker condition [27, 31, 138]. Hence, they can be seen as highly multipolar Huygens metasurfaces. Although in their most common configuration, Huygens sources consist of dipole resonances, multipolar meta-atoms have received a lot of attention for their ability to drastically extend the range of possibilities for directional scattering with more complex structures and extended spectral ranges of operation [119, 139–142].

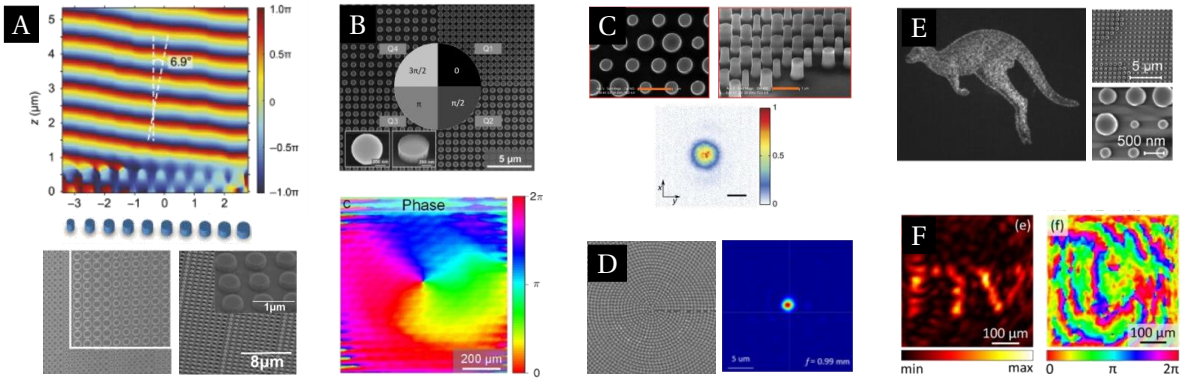

Figure 1.7 – A) Beam deflection with a periodic array consisting in a super-cell of 10 nanodisks of varying diameters. Reproduced from [143]. Examples of fabricated Huygens metasurfaces (bottom panels) for beam-deflection, with super-cells of 8 and 9 *Si* nanodisks for respectively the left and right panels reproduced from [45] and [133]. B) SEM image (top panel) of a fabricated beamshaper consisting in four arrays of silicon nanodisks and corresponding phase profile (bottom panel) of the generated vortex beam. Reproduced from [57]. C) SEM images of silicon posts forming a high-contrast transmitarray micro-lens and corresponding measured 2D intensity profile in the focal plane. Reproduced from [27]. D) SEM images (left panels) of a TiO_2 Huygens meta-lens and measured 2D intensity profile (right panel). Reproduced from [131, 132]. E) Experimental holographic image and SEM pictures of the corresponding Huygens metasurface. F) Experimental hologram image (left panel) obtained with a Huygens metasurface with 40% imaging efficiency, and associated phase reconstruction (right panel) in the sample plane. Reproduced from [50].

Furthermore, Huygens metasurfaces not only benefit from their possible high transmittance but are also advantageous to numerous applications where a surface must reflect as little power as possible. This is for example the case of electromagnetic absorbers that are of prime importance for many applications such as, wave filtering, energy harvesting, sensing, thermal emission control, etc. There are a large variety of metasurfaces developed for perfect absorber applications [144, 145]. However, most designs consist in multilayered structures often backed by a continuous reflecting metal plane, as in the classic Dallenbach [146] and Salisbury configurations [147, 148]. Thus, within that scenario, absorbers are asymmetric, absorbing light from one side only and cannot transmit light outside their absorption band.

Indeed, Huygens metasurfaces bring an important novelty to the field of absorbers since they make it possible to perfectly absorb light with ultimately thin layers made of a monolayer of particles and without the need for a reflecting substrate. The absorption is obtained by organizing lossy Huygens sources, able to dissipate energy, and where the forward scattered wave by the lattice cancels the incident wave by destructive interferences leading to an absence of transmission. This recent idea, that emerged in 2013 with the work of S. Tretyakov *et al.* [149–152], indeed opens the way to symmetric absorbers, that can additionally be fully transparent outside their operating

band.

These considerations make Huygens metasurfaces promising structures of great interest for a wide variety of applications that are not limited to those presented here. Many future developments are expected for Huygens metadevices in the near future.

1.1.3 Colloidal nanochemistry and self assembly as promising plateforms for optical metasurfaces

Nowadays, most metasurfaces are produced by top-down nanofabrication technologies. This provides unequalled spatial resolution for the surface organization of elements of precisely controlled geometry. However, the development of low-cost and large-area fabrication techniques is also needed to avoid relying on currently expensive lithography. A promising avenue is provided by bottom up techniques. The bottom-up fabrication route is based on the combination of colloidal nanochemistry, allowing the synthesis of large numbers of optical meta-atoms (typically $\approx 10^{13}$ per batch in the laboratory), and self-assembly methods for their spontaneous organisation into materials and the production of large-scale 2D structures. It is therefore an excellent alternative for the realization of metasurfaces operating with visible or near infrared light. A large variety of meta-atoms of varying complexity can be synthesized by nanochemistry. Some of them could indeed constitute interesting building blocks for Huygens metasurfaces. As illustrated on Fig. 1.8-A, it is for instance possible to synthesize various dielectric nanoparticles such as *Si*, TiO_2, Cu_2O, etc. As mentioned already, such dielectric particles naturally present strong electric and magnetic Mie resonances that can coexist spectrally, and their ability to scatter light unidirectionally has been demonstrated. Another example is provided by core-shell particles (see Fig. 1.8-E), that have been proposed for the realization of Huygens sources since they can present strong overlapped dipole resonances in the near infrared (As shown on Fig. 1.5-C).

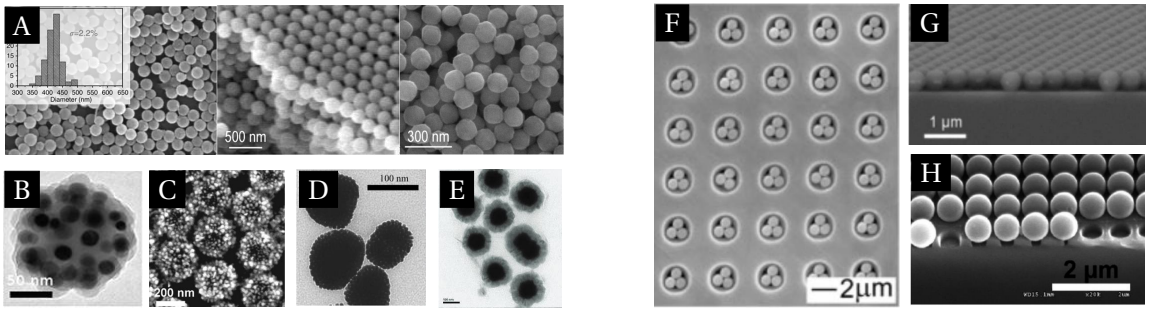

Figure 1.8 – $Si_{0.75}H_{0.25}$ (left panel), TiO_2 (mid panel) and Cu_2O (right panel) colloidal dielectric nanospheres prepared through wet-chemistry methods. Reproduced from [103, 153–155]. B) Electron micrograph of a plasmonic raspberry synthesized by self-assembling silver satellites. Reproduced from [156]. C) SEM image of silver raspberry particles prepared with a polystyrene template. Reproduced from [157]. D) TEM micrographs of plasmonic meta-molecules composed of 10 nm large *Au* nanoparticles with magnetic response at optical frequencies. Reproduced from [158]. E) Core-shell particles made from gold and high-permittivity cuprous oxide (Cu_2O). Reproduced from [159]. F) Periodic array of trigonal planar clusters formed with polystyrene beads in cylindrical holes. Reproduced from [160]. G) Dense single layer prepared by horizontal deposition from a polystyrene particle suspension. Reproduced from [161, 162]. H) Example of a topographic template defining each colloid position in a lattice. Reproduced from [161, 163].

Beyond resorting to Mie magnetic resonances of dielectric materials, magnetic responses, unnatural at optical frequencies but necessary for obtaining dipolar Huygens sources, can be obtained by considering more complex structures that present so-called artificial magnetic responses. They generally consist in a set of metallic nano-objects organized in large clusters that enable the excitation of loops of plasmonic currents which, in turn, generate magnetization oscillating at the frequency of the impinging light. Following the original model of isotropic magnetic nanoclusters

proposed by C. R. Simovski and S. A. Tretyakov [164] and A. Alù and N. Engheta [165, 166], nanoclusters [158, 167, 168] (see Fig. 1.8-D), raspberry-shaped resonators [156, 157, 169–171] (see Figs. 1.8-B,C), dodecapods [172] etc, exhibiting high magnetic responses were indeed successfully synthesized by several authors, including group of researchers from the University of Bordeaux. The search for artificial and isotropic optical magnetism in the visible has stimulated a lot of synthetic efforts, mainly with the original aim of demonstrating double negative index optical bulk metamaterial. The efforts invested for this idea could now benefit the realization of Huygens sources.

Once the meta-atoms have been synthesized, the next challenge is to assemble them into a metasurface while preserving a spatial organisation required for most applications. Several fabrication strategies can be found [161]. Thin films of large area can be produced by Langmuir-Blodgett assembly, dip- and spin-coating or meniscus evaporation for instance (see Fig. 1.8-G). These approaches generally lead to dense surfaces of particles that tend to assume a close-packed geometry. Additional techniques also exist that may be used to harness their arrangement. For example the particle-particle spacing can be modified by varying the length of the coating molecules. Another possibility is instead to employ nanopatterned templates as supports [173–175], so that the nanoparticle arrangement can be guided in a controllable manner. Nanopatterned templates can be realized, by creating a chemical contrast pattern between regions with different affinity to the nanoparticles, by printing processes, or by modifying the surface topography (see Figs. 1.8-F,H). The combined application of patterned substrates and self-assembly for the deposition of nanoparticles is often considered. The self-assembly routes hence appear to be excellent candidates to ensure macroscopic organisation of large numbers of meta-atoms into 2D surfaces. The complexity of the self-assembly procedure can be greatly reduced for isotropic resonators, eliminating the additional alignment problem. If the anisotropic Huygens resonators, such as the disks, have been widely explored and have already demonstrated their full potential, isotropic Huygens sources that would be particularly well suited to these self assembly approaches have received limited attention in the literature.

1.2 Aim and structure of the thesis

1.2.1 Motivations

Since self-assembly processes hold the potential to produce large metasurfaces at potentially low cost, they constitute a highly promising approach to make devices that exploit the exceptional properties of chemically synthesized optical nanoresonators. In recent years, several groups in Bordeaux, from the ICMCB, the CRPP and the LOF, have worked as a consortium in the framework of the AMADEUS LabEx and devoted their research to the bottom-up production of metamaterials based on colloidally synthesized resonators. Many realizations have been made including but not limited to a fully isotropic bulk magnetic metamaterial, hyperbolic metamaterials, adjustable high refractive index metamaterials or topologically dark metamaterials [156, 176–181]. From these successive works on bulk metamaterials, emerged the interest to extend the exploitation of the optical magnetism of colloidal structure and the bottom-up approach to the more recent field of metasurfaces. In particular, the bottom-up feasibility of Huygens metasurfaces was lacking focus in the literature, in strong contrast to the attention paid to the nanodisks and pillars anisotropic structures on which relied the demonstrated lithographically manufactured metasurfaces.

The aim of this PhD work was therefore to evaluate the potential of colloidal particles for the realization of optical Huygens metasurfaces. The underlying goals were to propose theoretical tools and design procedures of Huygens sources, that could lead to functional Huygens metasurfaces realistically feasible by bottom-up techniques.

1.2.2 Thesis content and outline

In this thesis, we study isotropic Huygens sources and their potential applications as metasurfaces, both for wavefront manipulation and for perfect absorption applications. We focus on structures that can typically be obtained by colloidal nano-chemistry. These consist in spherical dielectric and metallic particles, clusters of plasmonic or dielectric inclusions and multilayered particles. The outline is summarized in Fig. 1.9.

The thesis can be divided into two distinct parts. In a first part, we study the scattering properties of meta-atoms considered individually and we present design guidelines to tailor their different multipoles to meet the Kerker condition and achieve resonant or broadband Huygens sources. The second part is devoted to the study of their periodic arrangements as Huygens metasurfaces.

	Chapter 1	Introduction	
Single particles	**Chapter 2**	Theoretical framework and numerical methods	*Theoretical*
	Chapter 3	Design of isotropic Huygens sources with colloidal particles	*Designs*
Metasurfaces	**Chapter 4**	Metasurface Analysis	*Theoretical*
	Chapter 5	Multipolar Huygens metasurfaces	*Designs*
	Chapter 6	Conclusions	

Figure 1.9 – Outline of the thesis

The two main parts each contain two chapters (see Fig. 1.9). The first chapters deal with the theoretical aspects, the implementation of concepts with their associated mathematical and numerical tools that are then exploited in the second chapters in order to propose systems that may be experimentally achieved. The detailed contents of chapters are as follows:

- Chapter 2 aims at presenting the main theoretical concepts involved in the study of the optical properties of nanostructures. Starting from the basics of electromagnetism and wave propagation, we later address the problem of light scattering by particles and its solving with the analytic Mie theory or by means of the $\mathcal{T}$-matrix method. At the same time, this chapter introduces the fundamental tool of multipole expansion, that plays a central role in the understanding and tuning of the scattering responses of particles. Finally, a section is devoted to numerical methods with the commercial finite element software package COMSOL multiphisycs.
- In Chapter 3 we investigate the directional scattering abilities of different isotropic colloidal particles from the theoretical and numerical point of view. In a first part, we introduce the generalized Kerker condition leading to the cancellation of the back-scattering by particles. In a second part, we reveal that both resonant dipolar Huygens sources and extremely broadband forward directed scattering can be obtained considering simple spherical particles of low refractive index. Alternatively, clusters of particles are introduced for the first time as promising Huygens sources. We demonstrate that such composite particles made from homogeneously assembled small inclusions provide a greater flexibility in the design of Huygens sources, combined with better performances compared to simple spheres. Resorting to extended Maxwell-Garnett homogenization theory, we evidence how the control of the effective refractive index by the particle density allows to engineer plasmonic and dielectric clusters as resonant and broadband Huygens sources for the visible domain. Finally, in a last part, we focus on multilayered particles. In particular, we present design guidelines to overlap the electric and magnetic dipole resonances of silver and gold based metallo-dielectric core-shells. All-dielectric core-shells behaving as broadband Huygens sources are also demonstrated.

- Chapter 4 aims at introducing different analytic tools used to analyze or compute the properties of metasurfaces. Firstly, we present the description of metasurfaces in terms of equivalent surface current sources satisfying specific boundary conditions. After introducing the transmission line formalism, these boundary conditions are used to derive the equivalent circuit representations of different kinds of metasurfaces. From there, to get a physical insight into the origin of metasurface features, we model metasurfaces under the dipole approximation. The coupled dipole model, used to semi-analytically compute the coupling term between dipolar particles, is introduced, as well as its simplified version relying on the hypothesis of resonances of a lorentzian spectral form. Finally in a last section, a generalized formalism that links metasurface properties to the multipole coefficients of their constituent meta-atom is presented. This multipole decomposition that evidences the role of symmetric and anti-symmetric multipoles in the absorption and radiation properties of a metasurface will serve as a major tool in chapter 5.
- Chapter 5 is dedicated to the study of Huygens metasurfaces. In a first part, we investigate their properties from a theoretical point of view, based on a simple dipolar lorentzian model. We highlight how a perfect transmission accompanied by a complete coverage of the $[0\,;\,2\pi]$ interval for the phase can be obtained for lossless metasurfaces while a unit absorption can be achieved with resonators under critical coupling. We then generalize the required conditions to achieve these properties to multipolar systems. In a second part we focus on wavefront control applications. We evidence the possibility of achieving a 2π phase shift with quadrupolar resonances of silicon clusters. We apply this result to demonstrate a beam deflector and a focusing lens in the near infrared based on cluster arrays. Finally in a last part, we exploit the generalized absorption conditions written in terms of a balance between multipoles to present various designs of perfect absorbers. Spherical particle, core-shell and cluster arrays, both plasmonic and dielectric, are studied. The specificities of each design allowing for either resonant, dual band or broadband absorption are presented in detail.
- Finally, Chapter 6 summarizes the main results and achievements of this thesis and highlights possible research directions that would be worth exploring in the future.

1.3 References

[1] H. V. Demir and S. V. Gaponenko, *Applied nanophotonics*. Cambridge University Press, 2018. 2

[2] A. McGurn, *Nanophotonics*, vol. 213. Springer, 2018. 2

[3] Nanophotonics Europe Association, "Nanophotonics foresight report," 2011. 2

[4] Nanophotonics Europe Association, "Nanophotonics, a forward look," 2012. 2

[5] D. R. Smith, W. J. Padilla, D. Vier, S. C. Nemat-Nasser, and S. Schultz, "Composite medium with simultaneously negative permeability and permittivity," *Physical review letters*, vol. 84, no. 18, p. 4184, 2000. 2

[6] R. A. Shelby, D. R. Smith, and S. Schultz, "Experimental verification of a negative index of refraction," *science*, vol. 292, no. 5514, pp. 77–79, 2001. 2

[7] D. R. Smith, J. B. Pendry, and M. C. Wiltshire, "Metamaterials and negative refractive index," *Science*, vol. 305, no. 5685, pp. 788–792, 2004. 2

[8] A. Alu, M. G. Silveirinha, A. Salandrino, and N. Engheta, "Epsilon-near-zero metamaterials and electromagnetic sources: Tailoring the radiation phase pattern," *Physical review B*, vol. 75, no. 15, p. 155410, 2007. 2

[9] R. Liu, Q. Cheng, T. Hand, J. J. Mock, T. J. Cui, S. A. Cummer, and D. R. Smith, "Experimental demonstration of electromagnetic tunneling through an epsilon-near-zero metamaterial at microwave frequencies," *Physical review letters*, vol. 100, no. 2, p. 023903, 2008. 2

[10] E. Plum, V. Fedotov, A. Schwanecke, N. Zheludev, and Y. Chen, "Giant optical gyrotropy due to electromagnetic coupling," *Applied Physics Letters*, vol. 90, no. 22, p. 223113, 2007. 2

[11] A. Rogacheva, V. Fedotov, A. Schwanecke, and N. Zheludev, "Giant gyrotropy due to electromagnetic-field coupling in a bilayered chiral structure," *Physical review letters*, vol. 97, no. 17, p. 177401, 2006. 2

[12] C. Helgert, E. Pshenay-Severin, M. Falkner, C. Menzel, C. Rockstuhl, E.-B. Kley, A. Tunnermann, F. Lederer, and T. Pertsch, "Chiral metamaterial composed of three-dimensional plasmonic nanostructures," *Nano letters*, vol. 11, no. 10, pp. 4400–4404, 2011. 2

[13] J. B. Pendry, "Negative refraction makes a perfect lens," *Physical review letters*, vol. 85, no. 18, p. 3966, 2000. 2

[14] Z. Liu, H. Lee, Y. Xiong, C. Sun, and X. Zhang, "Far-field optical hyperlens magnifying sub-diffraction-limited objects," *science*, vol. 315, no. 5819, pp. 1686–1686, 2007. 2

[15] Z. Jacob, L. V. Alekseyev, and E. Narimanov, "Optical hyperlens: far-field imaging beyond the diffraction limit," *Optics express*, vol. 14, no. 18, pp. 8247–8256, 2006. 2

[16] W. Cai, U. K. Chettiar, A. V. Kildishev, V. M. Shalaev, and G. W. Milton, "Nonmagnetic cloak with minimized scattering," *Applied Physics Letters*, vol. 91, no. 11, p. 111105, 2007. 2

[17] D. Schurig, J. Mock, B. Justice, S. A. Cummer, J. B. Pendry, A. Starr, and D. R. Smith, "Metamaterial electromagnetic cloak at microwave frequencies," *Science*, vol. 314, no. 5801, pp. 977–980, 2006. 2

[18] J. B. Pendry, D. Schurig, and D. R. Smith, "Controlling electromagnetic fields," *science*, vol. 312, no. 5781, pp. 1780–1782, 2006. 2

[19] U. Leonhardt, "Optical conformal mapping," *science*, vol. 312, no. 5781, pp. 1777–1780, 2006. 2

[20] C. M. Soukoulis and M. Wegener, "Past achievements and future challenges in the development of three-dimensional photonic metamaterials," *Nature Photonics*, vol. 5, no. 9, p. 523, 2011. 2

[21] V. M. Shalaev, W. Cai, U. K. Chettiar, H.-K. Yuan, A. K. Sarychev, V. P. Drachev, and A. V. Kildishev, "Negative index of refraction in optical metamaterials," *Optics letters*, vol. 30, no. 24, pp. 3356–3358, 2005. 2

[22] G. Dolling, C. Enkrich, M. Wegener, C. M. Soukoulis, and S. Linden, "Simultaneous negative phase and group velocity of light in a metamaterial," *Science*, vol. 312, no. 5775, pp. 892–894, 2006. 2

[23] H.-H. Hsiao, C. H. Chu, and D. P. Tsai, "Fundamentals and applications of metasurfaces," *Small Methods*, vol. 1, no. 4, p. 1600064, 2017. 3, 4

[24] D. Lin, P. Fan, E. Hasman, and M. L. Brongersma, "Dielectric gradient metasurface optical elements," *science*, vol. 345, no. 6194, pp. 298–302, 2014. 3, 5

[25] E. Schonbrun, K. Seo, and K. B. Crozier, "Reconfigurable imaging systems using elliptical nanowires," *Nano letters*, vol. 11, no. 10, pp. 4299–4303, 2011. 3

[26] S. Vo, D. Fattal, W. V. Sorin, Z. Peng, T. Tran, M. Fiorentino, and R. G. Beausoleil, "Subwavelength grating lenses with a twist," *IEEE Photonics Technology Letters*, vol. 26, no. 13, pp. 1375–1378, 2014. 3

[27] A. Arbabi, Y. Horie, A. J. Ball, M. Bagheri, and A. Faraon, "Subwavelength-thick lenses with high numerical apertures and large efficiency based on high-contrast transmitarrays," *Nature communications*, vol. 6, p. 7069, 2015. 3, 7

[28] A. Zhan, S. Colburn, R. Trivedi, T. K. Fryett, C. M. Dodson, and A. Majumdar, "Low-contrast dielectric metasurface optics," *ACS Photonics*, vol. 3, no. 2, pp. 209–214, 2016. 3

[29] M. Khorasaninejad, W. T. Chen, R. C. Devlin, J. Oh, A. Y. Zhu, and F. Capasso, "Metalenses at visible wavelengths: Diffraction-limited focusing and subwavelength resolution imaging," *Science*, vol. 352, no. 6290, pp. 1190–1194, 2016. 3, 4, 5

[30] A. Arbabi, E. Arbabi, S. M. Kamali, Y. Horie, S. Han, and A. Faraon, "Miniature optical planar camera based on a wide-angle metasurface doublet corrected for monochromatic aberrations," *Nature communications*, vol. 7, p. 13682, 2016. 3

[31] E. Arbabi, A. Arbabi, S. M. Kamali, Y. Horie, and A. Faraon, "Multiwavelength polarization-insensitive lenses based on dielectric metasurfaces with meta-molecules," *Optica*, vol. 3, no. 6, pp. 628–633, 2016. 3, 7

[32] W. T. Chen, A. Y. Zhu, M. Khorasaninejad, Z. Shi, V. Sanjeev, and F. Capasso, "Immersion meta-lenses at visible wavelengths for nanoscale imaging," *Nano letters*, vol. 17, no. 5, pp. 3188–3194, 2017. 3

[33] B. Groever, W. T. Chen, and F. Capasso, "Meta-lens doublet in the visible region," *Nano letters*, vol. 17, no. 8, pp. 4902–4907, 2017. 3

[34] M. Khorasaninejad, Z. Shi, A. Y. Zhu, W.-T. Chen, V. Sanjeev, A. Zaidi, and F. Capasso, "Achromatic metalens over 60 nm bandwidth in the visible and metalens with reverse chromatic dispersion," *Nano letters*, vol. 17, no. 3, pp. 1819–1824, 2017. 3

[35] R. Paniagua-Dominguez, Y. F. Yu, E. Khaidarov, S. Choi, V. Leong, R. M. Bakker, X. Liang, Y. H. Fu, V. Valuckas, L. A. Krivitsky, *et al.*, "A metalens with a near-unity numerical aperture," *Nano letters*, vol. 18, no. 3, pp. 2124–2132, 2018. 3

[36] P. Lalanne and P. Chavel, "Metalenses at visible wavelengths: past, present, perspectives," *Laser & Photonics Reviews*, vol. 11, no. 3, p. 1600295, 2017. 3

[37] Y. Zhao and A. Alu, "Tailoring the dispersion of plasmonic nanorods to realize broadband optical meta-waveplates," *Nano letters*, vol. 13, no. 3, pp. 1086–1091, 2013. 3

[38] Y. Zhao and A. Alù, "Manipulating light polarization with ultrathin plasmonic metasurfaces," *Physical Review B*, vol. 84, no. 20, p. 205428, 2011. 3

[39] N. Yu, F. Aieta, P. Genevet, M. A. Kats, Z. Gaburro, and F. Capasso, "A broadband, background-free quarter-wave plate based on plasmonic metasurfaces," *Nano letters*, vol. 12, no. 12, pp. 6328–6333, 2012. 3, 4

[40] M. A. Kats, P. Genevet, G. Aoust, N. Yu, R. Blanchard, F. Aieta, Z. Gaburro, and F. Capasso, "Giant birefringence in optical antenna arrays with widely tailorable optical anisotropy," *Proceedings of the National Academy of Sciences*, vol. 109, no. 31, pp. 12364–12368, 2012. 3, 4

[41] J. B. Mueller, K. Leosson, and F. Capasso, "Ultracompact metasurface in-line polarimeter," *Optica*, vol. 3, no. 1, pp. 42–47, 2016. 3

[42] F. Ding, Y. Chen, and S. I. Bozhevolnyi, "Metasurface-based polarimeters," *Applied Sciences*, vol. 8, no. 4, p. 594, 2018. 3

[43] A. Pors, M. G. Nielsen, and S. I. Bozhevolnyi, "Plasmonic metagratings for simultaneous determination of stokes parameters," *Optica*, vol. 2, no. 8, pp. 716–723, 2015. 3

[44] A. Arbabi, Y. Horie, M. Bagheri, and A. Faraon, "Dielectric metasurfaces for complete control of phase and polarization with subwavelength spatial resolution and high transmission," *Nature nanotechnology*, vol. 10, no. 11, p. 937, 2015. 3

[45] Y. F. Yu, A. Y. Zhu, R. Paniagua-Domínguez, Y. H. Fu, B. Luk'yanchuk, and A. I. Kuznetsov, "High-transmission dielectric metasurface with 2π phase control at visible wavelengths," *Laser & Photonics Reviews*, vol. 9, no. 4, pp. 412–418, 2015. 3, 7

[46] M. I. Shalaev, J. Sun, A. Tsukernik, A. Pandey, K. Nikolskiy, and N. M. Litchinitser, "High-efficiency all-dielectric metasurfaces for ultracompact beam manipulation in transmission mode," *Nano letters*, vol. 15, no. 9, pp. 6261–6266, 2015. 3, 6, 7

[47] D. Sell, J. Yang, S. Doshay, R. Yang, and J. A. Fan, "Large-angle, multifunctional metagratings based on freeform multimode geometries," *Nano letters*, vol. 17, no. 6, pp. 3752–3757, 2017. 3

[48] Z. Zhou, J. Li, R. Su, B. Yao, H. Fang, K. Li, L. Zhou, J. Liu, D. Stellinga, C. P. Reardon, *et al.*, "Efficient silicon metasurfaces for visible light," *ACS Photonics*, vol. 4, no. 3, pp. 544–551, 2017. 3, 7

[49] L. Wang, S. Kruk, H. Tang, T. Li, I. Kravchenko, D. N. Neshev, and Y. S. Kivshar, "Grayscale transparent metasurface holograms," *Optica*, vol. 3, no. 12, pp. 1504–1505, 2016. 3, 7

[50] K. E. Chong, L. Wang, I. Staude, A. R. James, J. Dominguez, S. Liu, G. S. Subramania, M. Decker, D. N. Neshev, I. Brener, *et al.*, "Efficient polarization-insensitive complex wavefront control using Huygens' metasurfaces based on dielectric resonant meta-atoms," *Acs Photonics*, vol. 3, no. 4, pp. 514–519, 2016. 3, 7

[51] W. Zhao, H. Jiang, B. Liu, J. Song, Y. Jiang, C. Tang, and J. Li, "Dielectric Huygens' metasurface for high-efficiency hologram operating in transmission mode," *Scientific reports*, vol. 6, p. 30613, 2016. 3, 7

[52] W. Zhao, B. Liu, H. Jiang, J. Song, Y. Pei, and Y. Jiang, "Full-color hologram using spatial multiplexing of dielectric metasurface," *Optics letters*, vol. 41, no. 1, pp. 147–150, 2016. 3

[53] M. Khorasaninejad, A. Ambrosio, P. Kanhaiya, and F. Capasso, "Broadband and chiral binary dielectric meta-holograms," *Science advances*, vol. 2, no. 5, p. e1501258, 2016. 3

[54] K. Huang, Z. Dong, S. Mei, L. Zhang, Y. Liu, H. Liu, H. Zhu, J. Teng, B. Luk'yanchuk, J. K. Yang, *et al.*, "Silicon multi-meta-holograms for the broadband visible light," *Laser & Photonics Reviews*, vol. 10, no. 3, pp. 500–509, 2016. 3

[55] P. Genevet and F. Capasso, "Holographic optical metasurfaces: a review of current progress," *Reports on Progress in Physics*, vol. 78, no. 2, p. 024401, 2015. 3

[56] Q. Jiang, G. Jin, and L. Cao, "When metasurface meets hologram: principle and advances," *Advances in Optics and Photonics*, vol. 11, no. 3, pp. 518–576, 2019. 3, 4

[57] K. E. Chong, I. Staude, A. James, J. Dominguez, S. Liu, S. Campione, G. S. Subramania, T. S. Luk, M. Decker, D. N. Neshev, *et al.*, "Polarization-independent silicon metadevices for efficient optical wavefront control," *Nano letters*, vol. 15, no. 8, pp. 5369–5374, 2015. 3, 7

[58] K. Wang, J. G. Titchener, S. S. Kruk, L. Xu, H.-P. Chung, M. Parry, I. I. Kravchenko, Y.-H. Chen, A. S. Solntsev, Y. S. Kivshar, *et al.*, "Quantum metasurface for multiphoton interference and state reconstruction," *Science*, vol. 361, no. 6407, pp. 1104–1108, 2018. 3

[59] T. Stav, A. Faerman, E. Maguid, D. Oren, V. Kleiner, E. Hasman, and M. Segev, "Quantum entanglement of the spin and orbital angular momentum of photons using metamaterials," *Science*, vol. 361, no. 6407, pp. 1101–1104, 2018. 3

[60] E. Maguid, I. Yulevich, M. Yannai, V. Kleiner, M. L. Brongersma, and E. Hasman, "Multifunctional interleaved geometric-phase dielectric metasurfaces," *Light: Science & Applications*, vol. 6, no. 8, p. e17027, 2017. 3

[61] C. Huygens, *Traité de la lumière*. Pieter van der Aa, 1690. 3

[62] A. E. Minovich, A. E. Miroshnichenko, A. Y. Bykov, T. V. Murzina, D. N. Neshev, and Y. S. Kivshar, "Functional and nonlinear optical metasurfaces," *Laser & Photonics Reviews*, vol. 9, no. 2, pp. 195–213, 2015. 4

[63] N. Yu and F. Capasso, "Flat optics with designer metasurfaces," *Nature materials*, vol. 13, no. 2, pp. 139–150, 2014. 4

[64] P. Genevet, F. Capasso, F. Aieta, M. Khorasaninejad, and R. Devlin, "Recent advances in planar optics: from plasmonic to dielectric metasurfaces," *Optica*, vol. 4, no. 1, pp. 139–152, 2017. 4

[65] S. M. Kamali, E. Arbabi, A. Arbabi, and A. Faraon, "A review of dielectric optical metasurfaces for wavefront control," *Nanophotonics*, vol. 7, no. 6, pp. 1041–1068, 2018. 4, 7

[66] W. Wan, J. Gao, and X. Yang, "Metasurface holograms for holographic imaging," *Advanced Optical Materials*, vol. 5, no. 21, p. 1700541, 2017. 4

[67] S. B. Glybovski, S. A. Tretyakov, P. A. Belov, Y. S. Kivshar, and C. R. Simovski, "Metasurfaces: From microwaves to visible," *Physics reports*, vol. 634, pp. 1–72, 2016. 4

[68] H.-T. Chen, A. J. Taylor, and N. Yu, "A review of metasurfaces: physics and applications," *Reports on progress in physics*, vol. 79, no. 7, p. 076401, 2016. 4

[69] F. Ding, A. Pors, and S. I. Bozhevolnyi, "Gradient metasurfaces: a review of fundamentals and applications," *Reports on Progress in Physics*, vol. 81, no. 2, p. 026401, 2017. 4

[70] N. Yu, P. Genevet, M. A. Kats, F. Aieta, J.-P. Tetienne, F. Capasso, and Z. Gaburro, "Light propagation with phase discontinuities: generalized laws of reflection and refraction," *science*, vol. 334, no. 6054, pp. 333–337, 2011. 4, 5

[71] F. Aieta, P. Genevet, M. A. Kats, N. Yu, R. Blanchard, Z. Gaburro, and F. Capasso, "Aberration-free ultrathin flat lenses and axicons at telecom wavelengths based on plasmonic metasurfaces," *Nano letters*, vol. 12, no. 9, pp. 4932–4936, 2012. 4, 5

[72] F. Aieta, A. Kabiri, P. Genevet, N. Yu, M. A. Kats, Z. Gaburro, and F. Capasso, "Reflection and refraction of light from metasurfaces with phase discontinuities," *Journal of Nanophotonics*, vol. 6, no. 1, p. 063532, 2012. 4

[73] N. Yu, P. Genevet, F. Aieta, M. A. Kats, R. Blanchard, G. Aoust, J.-P. Tetienne, Z. Gaburro, and F. Capasso, "Flat optics: controlling wavefronts with optical antenna metasurfaces," *IEEE Journal of Selected Topics in Quantum Electronics*, vol. 19, no. 3, pp. 4700423–4700423, 2013. 4

[74] R. Blanchard, G. Aoust, P. Genevet, N. Yu, M. A. Kats, Z. Gaburro, and F. Capasso, "Modeling nanoscale V-shaped antennas for the design of optical phased arrays," *Physical Review B*, vol. 85, no. 15, p. 155457, 2012. 4

[75] P. Genevet, N. Yu, F. Aieta, J. Lin, M. A. Kats, R. Blanchard, M. O. Scully, Z. Gaburro, and F. Capasso, "Ultra-thin plasmonic optical vortex plate based on phase discontinuities," *Applied Physics Letters*, vol. 100, no. 1, p. 013101, 2012. 4, 5

[76] L. Liu, X. Zhang, M. Kenney, X. Su, N. Xu, C. Ouyang, Y. Shi, J. Han, W. Zhang, and S. Zhang, "Broadband metasurfaces with simultaneous control of phase and amplitude," *Advanced materials*, vol. 26, no. 29, pp. 5031–5036, 2014. 4

[77] X. Chen, L. Huang, H. Mühlenbernd, G. Li, B. Bai, Q. Tan, G. Jin, C.-W. Qiu, S. Zhang, and T. Zentgraf, "Dual-polarity plasmonic metalens for visible light," *Nature communications*, vol. 3, p. 1198, 2012. 4, 5

[78] X. Ni, N. K. Emani, A. V. Kildishev, A. Boltasseva, and V. M. Shalaev, "Broadband light bending with plasmonic nanoantennas," *Science*, vol. 335, no. 6067, pp. 427–427, 2012. 5

[79] S. Pancharatnam, "Generalized theory of interference and its applications," in *Proceedings of the Indian Academy of Sciences-Section A*, vol. 44, pp. 398–417, Springer, 1956. 5

[80] M. V. Berry, "Quantal phase factors accompanying adiabatic changes," *Proceedings of the Royal Society of London. A. Mathematical and Physical Sciences*, vol. 392, no. 1802, pp. 45–57, 1984. 5

[81] Z. Bomzon, V. Kleiner, and E. Hasman, "Pancharatnam-Berry phase in space-variant polarization-state manipulations with subwavelength gratings," *Optics letters*, vol. 26, no. 18, pp. 1424–1426, 2001. 5

[82] Z. Bomzon, V. Kleiner, and E. Hasman, "Formation of radially and azimuthally polarized light using space-variant subwavelength metal stripe gratings," *Applied Physics Letters*, vol. 79, no. 11, pp. 1587–1589, 2001. 5

[83] L. Huang, X. Chen, H. Muhlenbernd, G. Li, B. Bai, Q. Tan, G. Jin, T. Zentgraf, and S. Zhang, "Dispersionless phase discontinuities for controlling light propagation," *Nano letters*, vol. 12, no. 11, pp. 5750–5755, 2012. 5

[84] A. E. H. Love, "I. the integration of the equations of propagation of electric waves," *Philosophical Transactions of the Royal Society of London. Series A, Containing Papers of a Mathematical or Physical Character*, vol. 197, no. 287-299, pp. 1–45, 1901. 5

[85] S. Schelkunoff, "Some equivalence theorems of electromagnetics and their application to radiation problems," *The Bell System Technical Journal*, vol. 15, no. 1, pp. 92–112, 1936. 5

[86] C. Pfeiffer and A. Grbic, "Metamaterial Huygens' surfaces: tailoring wave fronts with reflectionless sheets," *Physical review letters*, vol. 110, no. 19, p. 197401, 2013. 5

[87] A. Love, "Some highlights in reflector antenna development," *Radio Science*, vol. 11, no. 8-9, pp. 671–684, 1976. 5

[88] I. Koffman, "Feed polarization for parallel currents in reflectors generated by conic sections," *IEEE Transactions on Antennas and Propagation*, vol. 14, no. 1, pp. 37–40, 1966. 5

[89] J. P. Wong, M. Selvanayagam, and G. V. Eleftheriades, "Design of unit cells and demonstration of methods for synthesizing Huygens metasurfaces," *Photonics and Nanostructures-Fundamentals and Applications*, vol. 12, no. 4, pp. 360–375, 2014. 5

[90] S. L. Jia, X. Wan, X. J. Fu, Y. J. Zhao, and T. J. Cui, "Low-reflection beam refractions by ultrathin Huygens metasurface," *AIP Advances*, vol. 5, no. 6, p. 067102, 2015. 5

[91] A. Epstein and G. V. Eleftheriades, "Huygens' metasurfaces via the equivalence principle: design and applications," *JOSA B*, vol. 33, no. 2, pp. A31–A50, 2016. 5

[92] M. Chen, M. Kim, A. M. Wong, and G. V. Eleftheriades, "Huygens' metasurfaces from microwaves to optics: a review," *Nanophotonics*, vol. 7, no. 6, pp. 1207–1231, 2018. 5

[93] C. Pfeiffer, N. K. Emani, A. M. Shaltout, A. Boltasseva, V. M. Shalaev, and A. Grbic, "Efficient light bending with isotropic metamaterial Huygens' surfaces," *Nano letters*, vol. 14, no. 5, pp. 2491–2497, 2014. 5

[94] F. Monticone, N. M. Estakhri, and A. Alù, "Full control of nanoscale optical transmission with a composite metascreen," *Physical review letters*, vol. 110, no. 20, p. 203903, 2013. 5

[95] A. E. Krasnok, I. S. Maksymov, A. I. Denisyuk, P. A. Belov, A. E. Miroshnichenko, C. R. Simovski, and Y. S. Kivshar, "Optical nanoantennas," *Physics-Uspekhi*, vol. 56, no. 6, p. 539, 2013. 5

[96] A. E. Krasnok, A. E. Miroshnichenko, P. A. Belov, and Y. S. Kivshar, "Huygens optical elements and Yagi-Uda nanoantennas based on dielectric nanoparticles," *JETP letters*, vol. 94, no. 8, pp. 593–598, 2011. 5

[97] A. E. Krasnok, C. R. Simovski, P. A. Belov, and Y. S. Kivshar, "Superdirective dielectric nanoantennas," *Nanoscale*, vol. 6, no. 13, pp. 7354–7361, 2014. 5

[98] B. Rolly, B. Stout, and N. Bonod, "Boosting the directivity of optical antennas with magnetic and electric dipolar resonant particles," *Optics express*, vol. 20, no. 18, pp. 20376–20386, 2012. 5

[99] M. Kerker, D.-S. Wang, and C. Giles, "Electromagnetic scattering by magnetic spheres," *JOSA*, vol. 73, no. 6, pp. 765–767, 1983. 6

[100] Y. H. Fu, A. I. Kuznetsov, A. E. Miroshnichenko, Y. F. Yu, and B. Luk'yanchuk, "Directional visible light scattering by silicon nanoparticles," *Nature communications*, vol. 4, p. 1527, 2013. 6

[101] S. Person, M. Jain, Z. Lapin, J. J. Sáenz, G. Wicks, and L. Novotny, "Demonstration of zero optical backscattering from single nanoparticles," *Nano letters*, vol. 13, no. 4, pp. 1806–1809, 2013. 6

[102] Y. Zhang, M. Nieto-Vesperinas, and J. J. Sáenz, "Dielectric spheres with maximum forward scattering and zero backscattering: a search for their material composition," *Journal of Optics*, vol. 17, no. 10, p. 105612, 2015. 6

[103] S. Zhang, R. Jiang, Y.-M. Xie, Q. Ruan, B. Yang, J. Wang, and H.-Q. Lin, "Colloidal moderate-refractive-index Cu_2O nanospheres as visible-region nanoantennas with electromagnetic resonance and directional light-scattering properties," *Advanced Materials*, vol. 27, no. 45, pp. 7432–7439, 2015. 6, 8

[104] B. García-Cámara, R. A. de La Osa, J. Saiz, F. González, and F. Moreno, "Directionality in scattering by nanoparticles: Kerker's null-scattering conditions revisited," *Optics letters*, vol. 36, no. 5, pp. 728–730, 2011. 6

[105] R. Gomez-Medina, B. Garcia-Camara, I. Suárez-Lacalle, F. González, F. Moreno, M. Nieto-Vesperinas, and J. J. Sáenz, "Electric and magnetic dipolar response of germanium nanospheres: interference effects, scattering anisotropy, and optical forces," *Journal of Nanophotonics*, vol. 5, no. 1, p. 053512, 2011. 6

[106] M. I. Abdelrahman, H. Saleh, I. Fernandez-Corbaton, B. Gralak, J.-M. Geffrin, and C. Rockstuhl, "Experimental demonstration of spectrally broadband Huygens sources using low-index spheres," *APL Photonics*, vol. 4, no. 2, p. 020802, 2019. 6

[107] B. García-Cámara, J. M. Saiz, F. González, and F. Moreno, "Nanoparticles with unconventional scattering properties: Size effects," *Optics Communications*, vol. 283, no. 3, pp. 490–496, 2010. 6

[108] Z. Wang, N. An, F. Shen, H. Zhou, Y. Sun, Z. Jiang, Y. Han, Y. Li, and Z. Guo, "Enhanced forward scattering of ellipsoidal dielectric nanoparticles," *Nanoscale research letters*, vol. 12, no. 1, p. 58, 2017. 6

[109] B. S. Luk'yanchuk, N. V. Voshchinnikov, R. Paniagua-Domínguez, and A. I. Kuznetsov, "Optimum forward light scattering by spherical and spheroidal dielectric nanoparticles with high refractive index," *ACS Photonics*, vol. 2, no. 7, pp. 993–999, 2015. 6

[110] Reena, Y. Kalra, A. Kumar, and R. Sinha, "Tunable unidirectional scattering of ellipsoidal single nanoparticle," *Journal of Applied Physics*, vol. 119, no. 24, p. 243102, 2016. 6

[111] S. Campione, L. I. Basilio, L. K. Warne, and M. B. Sinclair, "Tailoring dielectric resonator geometries for directional scattering and Huygens' metasurfaces," *Optics Express*, vol. 23, no. 3, pp. 2293–2307, 2015. 6

[112] F. Wang, Q.-H. Wei, and H. Htoon, "Generation of steep phase anisotropy with zero-backscattering by arrays of coupled dielectric nano-resonators," *Applied Physics Letters*, vol. 105, no. 12, p. 121112, 2014. 6

[113] Y. Yang, A. E. Miroshnichenko, S. V. Kostinski, M. Odit, P. Kapitanova, M. Qiu, and Y. S. Kivshar, "Multimode directionality in all-dielectric metasurfaces," *Physical Review B*, vol. 95, no. 16, p. 165426, 2017. 6

[114] D. Sikdar, W. Cheng, and M. Premaratne, "Optically resonant magneto-electric cubic nanoantennas for ultra-directional light scattering," *Journal of Applied Physics*, vol. 117, no. 8, p. 083101, 2015. 6

[115] P. Terekhov, H. Shamkhi, E. Gurvitz, K. Baryshnikova, A. Evlyukhin, A. Shalin, and A. Karabchevsky, "Broadband forward scattering from dielectric cubic nanoantenna in lossless media," *Optics express*, vol. 27, no. 8, pp. 10924–10935, 2019. 6

[116] I. Staude, A. E. Miroshnichenko, M. Decker, N. T. Fofang, S. Liu, E. Gonzales, J. Dominguez, T. S. Luk, D. N. Neshev, I. Brener, *et al.*, "Tailoring directional scattering through magnetic and electric resonances in subwavelength silicon nanodisks," *ACS nano*, vol. 7, no. 9, pp. 7824–7832, 2013. 6

[117] M. Decker, I. Staude, M. Falkner, J. Dominguez, D. N. Neshev, I. Brener, T. Pertsch, and Y. S. Kivshar, "High-efficiency dielectric Huygens' surfaces," *Advanced Optical Materials*, vol. 3, no. 6, pp. 813–820, 2015. 6

[118] P. D. Terekhov, K. V. Baryshnikova, A. S. Shalin, A. Karabchevsky, and A. B. Evlyukhin, "Resonant forward scattering of light by high-refractive-index dielectric nanoparticles with toroidal dipole contribution," *Optics Letters*, vol. 42, no. 4, pp. 835–838, 2017. 6

[119] W. Liu, J. Zhang, B. Lei, H. Ma, W. Xie, and H. Hu, "Ultra-directional forward scattering by individual core-shell nanoparticles," *Optics express*, vol. 22, no. 13, pp. 16178–16187, 2014. 6, 7

[120] W. Liu, A. E. Miroshnichenko, D. N. Neshev, and Y. S. Kivshar, "Broadband unidirectional scattering by magneto-electric core–shell nanoparticles," *ACS nano*, vol. 6, no. 6, pp. 5489–5497, 2012. 6

[121] R. Li, X. Zhou, M. Panmai, J. Xiang, H. Liu, M. Ouyang, H. Fan, Q. Dai, and Z. Wei, "Broadband zero backward scattering by all-dielectric core-shell nanoparticles," *Optics express*, vol. 26, no. 22, pp. 28891–28901, 2018. 6

[122] R. R. Naraghi, S. Sukhov, and A. Dogariu, "Directional control of scattering by all-dielectric core-shell spheres," *Optics letters*, vol. 40, no. 4, pp. 585–588, 2015. 6

[123] W. Liu, A. E. Miroshnichenko, R. F. Oulton, D. N. Neshev, O. Hess, and Y. S. Kivshar, "Scattering of core-shell nanowires with the interference of electric and magnetic resonances," *Optics letters*, vol. 38, no. 14, pp. 2621–2624, 2013. 6

[124] W. Liu, B. Lei, J. Shi, and H. Hu, "Unidirectional superscattering by multilayered cavities of effective radial anisotropy," *Scientific reports*, vol. 6, p. 34775, 2016. 6

[125] S. Liu, A. Vaskin, S. Campione, O. Wolf, M. B. Sinclair, J. Reno, G. A. Keeler, I. Staude, and I. Brener, "Huygens' metasurfaces enabled by magnetic dipole resonance tuning in split dielectric nanoresonators," *Nano letters*, vol. 17, no. 7, pp. 4297–4303, 2017. 6

[126] X. M. Zhang, Q. Zhang, S. J. Zeng, Z. Z. Liu, and J.-J. Xiao, "Dual-band unidirectional forward scattering with all-dielectric hollow nanodisk in the visible," *Optics letters*, vol. 43, no. 6, pp. 1275–1278, 2018. 6

[127] M. Decker and I. Staude, "Resonant dielectric nanostructures: a low-loss platform for functional nanophotonics," *Journal of Optics*, vol. 18, no. 10, p. 103001, 2016. 6

[128] J. Cheng, D. Ansari-Oghol-Beig, and H. Mosallaei, "Wave manipulation with designer dielectric metasurfaces," *Optics letters*, vol. 39, no. 21, pp. 6285–6288, 2014. 7

[129] D. A. Czaplewski, D. Lopez, and T. Roy, "Ultra-flat optical device with high transmission efficiency," June 18 2019. US Patent 10,324,314. 7

[130] H. Cai, S. Srinivasan, D. Czaplewski, A. Martinson, T. Loeffler, S. Sankaranarayanan, and D. López, "Ultrathin metasurface for the visible light based on dielectric nanoresonators," in *High Contrast Metastructures VIII*, vol. 10928, p. 109281M, International Society for Optics and Photonics, 2019. 7

[131] D. A. Czaplewski, H. Cai, T. Roy, K. Ogando, L. Stan, and D. López, "Phase control through Huygens' metasurfaces," in *2017 International Conference on Optical MEMS and Nanophotonics (OMN)*, pp. 1–2, IEEE, 2017. 7

[132] H. Cai, D. A. Czaplewski, L. Stan, and D. López, "High-efficiency, low-aspect-ratio planar lens based on Huygens resonators," in *2017 International Conference on Optical MEMS and Nanophotonics (OMN)*, pp. 1–2, IEEE, 2017. 7

[133] A. J. Ollanik, J. A. Smith, M. J. Belue, and M. D. Escarra, "High-efficiency all-dielectric Huygens metasurfaces from the ultraviolet to the infrared," *ACS Photonics*, vol. 5, no. 4, pp. 1351–1358, 2018. 7

[134] N. Vasilantonakis, J. Scheuer, and A. Boag, "Designing high-transmission and wide angle all-dielectric flat metasurfaces at telecom wavelengths," *arXiv preprint arXiv:1711.01430*, 2017. 7

[135] S. Astilean, P. Lalanne, P. Chavel, E. Cambril, and H. Launois, "High-efficiency subwavelength diffractive element patterned in a high-refractive-index material for 633nm," *Optics letters*, vol. 23, no. 7, pp. 552–554, 1998. 7

[136] P. Lalanne, S. Astilean, P. Chavel, E. Cambril, and H. Launois, "Blazed binary subwavelength gratings with efficiencies larger than those of conventional échelette gratings," *Optics letters*, vol. 23, no. 14, pp. 1081–1083, 1998. 7

[137] P. Lalanne, S. Astilean, P. Chavel, E. Cambril, and H. Launois, "Design and fabrication of blazed binary diffractive elements with sampling periods smaller than the structural cutoff," *JOSA A*, vol. 16, no. 5, pp. 1143–1156, 1999. 7

[138] S. M. Kamali, A. Arbabi, E. Arbabi, Y. Horie, and A. Faraon, "Decoupling optical function and geometrical form using conformal flexible dielectric metasurfaces," *Nature communications*, vol. 7, p. 11618, 2016. 7

[139] S. Kruk, B. Hopkins, I. I. Kravchenko, A. Miroshnichenko, D. N. Neshev, and Y. S. Kivshar, "Broadband highly efficient dielectric metadevices for polarization control," *Apl Photonics*, vol. 1, no. 3, p. 030801, 2016. 7

[140] I. M. Hancu, A. G. Curto, M. Castro-López, M. Kuttge, and N. F. van Hulst, "Multipolar interference for directed light emission," *Nano letters*, vol. 14, no. 1, pp. 166–171, 2013. 7

[141] M. I. Abdelrahman, C. Rockstuhl, and I. Fernandez-Corbaton, "Broadband suppression of backscattering at optical frequencies using low permittivity dielectric spheres," *Scientific reports*, vol. 7, no. 1, pp. 1–8, 2017. 7

[142] R. Alaee, R. Filter, D. Lehr, F. Lederer, and C. Rockstuhl, "A generalized Kerker condition for highly directive nanoantennas," *Optics letters*, vol. 40, no. 11, pp. 2645–2648, 2015. 7

[143] A. Özdemir, Z. Hayran, Y. Takashima, and H. Kurt, "Polarization independent high transmission large numerical aperture laser beam focusing and deflection by dielectric Huygens' metasurfaces," *Optics Communications*, vol. 401, pp. 46–53, 2017. 7

[144] C. M. Watts, X. Liu, and W. J. Padilla, "Metamaterial electromagnetic wave absorbers," *Advanced materials*, vol. 24, no. 23, pp. OP98–OP120, 2012. 7

[145] T. Badloe, J. Mun, and J. Rho, "Metasurfaces-based absorption and reflection control: perfect absorbers and reflectors," *Journal of Nanomaterials*, vol. 2017, 2017. 7

[146] W. Dallenbach and W. Kleinsteuber, "Reflection and absorption of decimeter-waves by plane dielectric layers," *Hochfreq. u Elektroak*, vol. 51, pp. 152–156, 1938. 7

[147] W. W. Salisbury, "Absorbent body for electromagnetic waves," June 10 1952. US Patent 2,599,944. 7

[148] R. Alaee, M. Albooyeh, and C. Rockstuhl, "Theory of metasurface based perfect absorbers," *arXiv preprint arXiv:1711.08203*, 2017. 7

[149] Y. Ra'di, V. S. Asadchy, and S. A. Tretyakov, "Total absorption of electromagnetic waves in ultimately thin layers," *IEEE Transactions on Antennas and Propagation*, vol. 61, no. 9, pp. 4606–4614, 2013. 7

[150] V. Asadchy, I. Faniayeu, Y. Ra'Di, I. Semchenko, and S. Khakhomov, "Optimal arrangement of smooth helices in uniaxial 2D-arrays," in *2013 7th International Congress on Advanced Electromagnetic Materials in Microwaves and Optics*, pp. 244–246, IEEE, 2013. 7

[151] Y. Ra'Di, C. Simovski, and S. Tretyakov, "Thin perfect absorbers for electromagnetic waves: theory, design, and realizations," *Physical Review Applied*, vol. 3, no. 3, p. 037001, 2015. 7

[152] R. Alaee, *Optical nanoantennas and their use as perfect absorbers*. PhD thesis, 2015. 7

[153] Z.-J. Yang, R. Jiang, X. Zhuo, Y.-M. Xie, J. Wang, and H.-Q. Lin, "Dielectric nanoresonators for light manipulation," *Physics Reports*, vol. 701, pp. 1–50, 2017. 8

[154] L. Shi, J. T. Harris, R. Fenollosa, I. Rodriguez, X. Lu, B. A. Korgel, and F. Meseguer, "Monodisperse silicon nanocavities and photonic crystals with magnetic response in the optical region," *Nature communications*, vol. 4, p. 1904, 2013. 8

[155] X. Jiang, T. Herricks, and Y. Xia, "Monodispersed spherical colloids of titania: synthesis, characterization, and crystallization," *Advanced Materials*, vol. 15, no. 14, pp. 1205–1209, 2003. 8

[156] S. Gómez-Graña, A. Le Beulze, M. Treguer-Delapierre, S. Mornet, E. Duguet, E. Grana, E. Cloutet, G. Hadziioannou, J. Leng, J.-B. Salmon, *et al.*, "Hierarchical self-assembly of a bulk metamaterial enables isotropic magnetic permeability at optical frequencies," *Materials Horizons*, vol. 3, no. 6, pp. 596–601, 2016. 8, 9

[157] Z. Qian, S. P. Hastings, C. Li, B. Edward, C. K. McGinn, N. Engheta, Z. Fakhraai, and S.-J. Park, "Raspberry-like metamolecules exhibiting strong magnetic resonances," *ACS nano*, vol. 9, no. 2, pp. 1263–1270, 2015. 8, 9

[158] M. R. Bourgeois, A. T. Liu, M. B. Ross, J. M. Berlin, and G. C. Schatz, "Self-assembled plasmonic metamolecules exhibiting tunable magnetic response at optical frequencies," *The Journal of Physical Chemistry C*, vol. 121, no. 29, pp. 15915–15921, 2017. 8, 9

[159] S. Yang, X. Ni, B. Kante, J. Zhu, K. O'Brien, Y. Wang, and X. Zhang, "Experimental demonstration of optical metamaterials with isotropic negative index," in *2016 Conference on Lasers and Electro-Optics (CLEO)*, pp. 1–2, IEEE, 2016. 8

[160] Y. Xia, Y. Yin, Y. Lu, and J. McLellan, "Template-assisted self-assembly of spherical colloids into complex and controllable structures," *Advanced Functional Materials*, vol. 13, no. 12, pp. 907–918, 2003. 8

[161] N. Vogel, M. Retsch, C.-A. Fustin, A. del Campo, and U. Jonas, "Advances in colloidal assembly: the design of structure and hierarchy in two and three dimensions," *Chemical reviews*, vol. 115, no. 13, pp. 6265–6311, 2015. 8, 9

[162] L. Malaquin, T. Kraus, H. Schmid, E. Delamarche, and H. Wolf, "Controlled particle placement through convective and capillary assembly," *Langmuir*, vol. 23, no. 23, pp. 11513–11521, 2007. 8

[163] N. N. Khanh and K. B. Yoon, "Facile organization of colloidal particles into large, perfect one-and two-dimensional arrays by dry manual assembly on patterned substrates," *Journal of the American Chemical Society*, vol. 131, no. 40, pp. 14228–14230, 2009. 8

[164] C. Simovski and S. Tretyakov, "Model of isotropic resonant magnetism in the visible range based on core-shell clusters," *Physical Review B*, vol. 79, no. 4, p. 045111, 2009. 9

[165] A. Alù, A. Salandrino, and N. Engheta, "Negative effective permeability and left-handed materials at optical frequencies," *Optics express*, vol. 14, no. 4, pp. 1557–1567, 2006. 9

[166] A. Alu and N. Engheta, "The quest for magnetic plasmons at optical frequencies," *Optics express*, vol. 17, no. 7, pp. 5723–5730, 2009. 9

[167] J. Dintinger, S. Mühlig, C. Rockstuhl, and T. Scharf, "A bottom-up approach to fabricate optical metamaterials by self-assembled metallic nanoparticles," *Optical Materials Express*, vol. 2, no. 3, pp. 269–278, 2012. 9

[168] S. Mühlig, C. Rockstuhl, V. Yannopapas, T. Bürgi, N. Shalkevich, and F. Lederer, "Optical properties of a fabricated self-assembled bottom-up bulk metamaterial," *Optics express*, vol. 19, no. 10, pp. 9607–9616, 2011. 9

[169] S. Muhlig, A. Cunningham, S. Scheeler, C. Pacholski, T. Burgi, C. Rockstuhl, and F. Lederer, "Self-assembled plasmonic core–shell clusters with an isotropic magnetic dipole response in the visible range," *ACS nano*, vol. 5, no. 8, pp. 6586–6592, 2011. 9

[170] S. N. Sheikholeslami, H. Alaeian, A. L. Koh, and J. A. Dionne, "A metafluid exhibiting strong optical magnetism," *Nano letters*, vol. 13, no. 9, pp. 4137–4141, 2013. 9

[171] V. Ponsinet, P. Barois, S. M. Gali, P. Richetti, J.-B. Salmon, A. Vallecchi, M. Albani, A. Le Beulze, S. Gomez-Grana, E. Duguet, *et al.*, "Resonant isotropic optical magnetism of plasmonic nanoclusters in visible light," *Physical Review B*, vol. 92, no. 22, p. 220414, 2015. 9

[172] V. Many, R. Dézert, E. Duguet, A. Baron, V. Jangid, V. Ponsinet, S. Ravaine, P. Richetti, P. Barois, and M. Tréguer-Delapierre, "High optical magnetism of dodecahedral plasmonic meta-atoms," *Nanophotonics*, vol. 8, no. 4, pp. 549–558, 2019. 9

[173] R. K. Smith, P. A. Lewis, and P. S. Weiss, "Patterning self-assembled monolayers," *Progress in surface science*, vol. 75, no. 1-2, pp. 1–68, 2004. 9

[174] M. Geissler and Y. Xia, "Patterning: Principles and some new developments," *Advanced Materials*, vol. 16, no. 15, pp. 1249–1269, 2004. 9

[175] S. Liu, R. Maoz, and J. Sagiv, "Planned nanostructures of colloidal gold via self-assembly on hierarchically assembled organic bilayer template patterns with in-situ generated terminal amino functionality," *Nano letters*, vol. 4, no. 5, pp. 845–851, 2004. 9

[176] L. Malassis, P. Masse, M. Tréguer-Delapierre, S. Mornet, P. Weisbecker, V. Kravets, A. Grigorenko, and P. Barois, "Bottom-up fabrication and optical characterization of dense films of meta-atoms made of core-shell plasmonic nanoparticles," *Langmuir*, vol. 29, no. 5, pp. 1551–1561, 2013. 9

[177] A. Baron, A. Iazzolino, K. Ehrhardt, J.-B. Salmon, A. Aradian, V. Kravets, A. N. Grigorenko, J. Leng, A. Le Beulze, M. Tréguer-Delapierre, *et al.*, "Bulk optical metamaterials assembled by microfluidic evaporation," *Optical Materials Express*, vol. 3, no. 11, pp. 1792–1797, 2013. 9

[178] L. Malassis, P. Massé, M. Tréguer-Delapierre, S. Mornet, P. Weisbecker, P. Barois, C. R. Simovski, V. G. Kravets, and A. N. Grigorenko, "Topological darkness in self-assembled plasmonic metamaterials," *Advanced Materials*, vol. 26, no. 2, pp. 324–330, 2014. 9

[179] A. Baron, A. Aradian, V. Ponsinet, and P. Barois, "Self-assembled optical metamaterials," *Optics & Laser Technology*, vol. 82, pp. 94–100, 2016. 9

[180] X. Wang, K. Ehrhardt, C. Tallet, M. Warenghem, A. Baron, A. Aradian, M. Kildemo, and V. Ponsinet, "Hyperbolic-by-design self-assembled metamaterial based on block copolymers lamellar phases," *Optics & Laser Technology*, vol. 88, pp. 85–95, 2017. 9

[181] V. Ponsinet, A. Baron, E. Pouget, Y. Okazaki, R. Oda, and P. Barois, "Self-assembled nanostructured metamaterials," *EPL (Europhysics Letters)*, vol. 119, no. 1, p. 14004, 2017. 9

Chapter 2

Theoretical framework and numerical methods

Contents

2.1 Electromagnetic wave propagation . . . 26
2.1.1 Macroscopic Maxwell's equations in matter . . . 26
2.1.2 Helmholtz vector wave equations . . . 27
2.1.3 Monochromatic plane waves . . . 27
2.1.4 Dispersion relation . . . 28
2.1.5 Optical refractive index . . . 28
2.1.6 Wave impedance . . . 28
2.1.7 Poynting vector and energy flux through a surface . . . 29
2.2 Light interaction with particles . . . 29
2.2.1 Electromagnetic scattering and multipole expansion . . . 29
2.2.2 Solutions of the Helmholtz equation in spherical coordinates . . . 32
2.2.3 Solving of the scattering problem with the $\mathcal{T}$-Matrix . . . 35
2.2.4 Scattering by a single sphere . . . 36
2.2.5 Scattering from multiple spheres . . . 37
2.2.6 Multipole coefficients of the scattered field of arbitrary particles . . . 38
2.3 Finite element method with COMSOL Multiphysics . . . 42
2.3.1 Meshing the simulation domain . . . 43
2.3.2 Scattered field formalism . . . 43
2.3.3 Modeling a periodic array of scatterers . . . 44
2.3.4 Multipole decomposition in COMSOL Multiphysics . . . 45
2.4 Concluding remarks . . . 45
2.5 References . . . 46

Summary: The aim of this chapter is to present the main theoretical concepts needed when analyzing and designing optical properties of nanostructures. We start by recalling the basics of electromagnetism and wave propagation. We later address the problem of light scattering by particles and its solving by use of the $\mathcal{T}$-matrix formalism, the analytic Mie theory and numerical simulations. At the same time, this section serves to introduce the fundamental tool of multipole expansion in electromagnetism. Finally in the last part, numerical finite element methods we used in this thesis are presented.

2.1 Electromagnetic wave propagation

2.1.1 Macroscopic Maxwell's equations in matter

All classical electromagnetic phenomena are governed by Maxwell's equations. They consist in a set of four partial differential equations describing the interconnection between fields, sources, and material properties. They are named after the physicist and mathematician James Clerk Maxwell who was the first to formulate these fundamental postulates in the 19^{th} century.

Their macroscopic form in matter read as:

$$\vec{\nabla} \wedge \vec{E}(\vec{r},t) = -\frac{\partial \vec{B}(\vec{r},t)}{\partial t} \qquad (Maxwell - Faraday) \qquad (2.1)$$

$$\vec{\nabla} \cdot \vec{B}(\vec{r},t) = 0 \qquad (Maxwell - Flux) \qquad (2.2)$$

$$\vec{\nabla} \cdot \vec{D}(\vec{r},t) = \rho(\vec{r},t) \qquad (Maxwell - Gauss) \qquad (2.3)$$

$$\vec{\nabla} \wedge \vec{H}(\vec{r},t) = \vec{J}(\vec{r},t) + \frac{\partial \vec{D}(\vec{r},t)}{\partial t} \qquad (Maxwell - Ampere) \qquad (2.4)$$

The first two equations (2.1) and (2.2) are structural equations of the EM field and the last two (2.3) and (2.4) connect these fields to fixed or mobile charges. Here, $\vec{E}(\vec{r},t)$,$\vec{B}(\vec{r},t)$, $\rho(\vec{r},t)$ and $\vec{J}(\vec{r},t)$, are respectively the electric field $[V.m^{-1}]$, the magnetic flux density $[T]$, the electric charge density $[C.m^{-3}]$ and the electric current density $[A.m^{-2}]$. The term $\frac{\partial \vec{D}(\vec{r},t)}{\partial t}$ is often refereed to as the displacement current. In its most general form, $\vec{J}(\vec{r},t)$ is the sum of two contributions: the source current density $\vec{J}_s(\vec{r},t)$ and the induced conduction current density $\vec{J}_c(\vec{r},t)$. The displacement field $\vec{D}(\vec{r},t)$ $[C.m^{-2}]$ and the magnetic field strength $\vec{H}(\vec{r},t)$ $[A.m^{-1}]$ are linked to $\vec{E}$ and $\vec{B}$ through the constitutive equations that describe the behavior of matter under the influence of the fields. On the other hand, the conduction current density $\vec{J}_c(\vec{r},t)$ is related to $\vec{E}$ through the local form of Ohm's law. The form of the constitutive relations depends on the material properties. Assuming an homogeneous, linear, local and isotropic material, the relations take the following scalar forms:

$$\vec{D}(\vec{r},t) = \varepsilon \vec{E}(\vec{r},t) \qquad (2.5)$$

$$\vec{B}(\vec{r},t) = \mu \vec{H}(\vec{r},t) \qquad (2.6)$$

$$\vec{J}_c(\vec{r},t) = \sigma_c \vec{E}(\vec{r},t) \qquad (2.7)$$

$\varepsilon = \varepsilon_r \varepsilon_0$ is the electric permittivity of the medium, with $\varepsilon_0 \approx 8{,}854 \times 10^{-12}$ $F.m^{-1}$ the free space permittivity and ε_r the relative permittivity of the material. $\mu = \mu_r \mu_0$ corresponds to the magnetic permeability where $\mu_0 \approx 4\pi 10^{-7}$ $H.m^{-1}$ is the free space permeability and μ_r the relative permeability of the material. σ_c $[S.m^{-1}]$ corresponds to the conductivity of the material.

When considering a vacuum or a linear material, Maxwell's equations are linear in both the sources and the fields. This important property implies that they can be easily solved in the frequency domain by applying the Fourier superposition principle. The spectrum $\vec{A}(\vec{r},\omega)$ of an arbitrary time-dependent field $\vec{A}(\vec{r},t)$ is given by the Fourier transform:

$$\vec{A}(\vec{r},\omega) = \frac{1}{2\pi} \int_{-\infty}^{+\infty} \vec{A}(\vec{r},t) e^{i\omega t} dt \qquad (2.8)$$

The time-dependent field can in turn be expressed by the inverse transform:

$$\vec{A}(\vec{r},t) = \int_{-\infty}^{+\infty} \vec{A}(\vec{r},\omega) e^{-i\omega t} d\omega \qquad (2.9)$$

Therefore, using the constitutive relations (2.5,2.6,2.7), the Maxwell's equations in the frequency

domain read as:

$$\vec{\nabla} \wedge \vec{E}(\vec{r},\omega) = i\omega\mu(\omega)\vec{H}(\vec{r},\omega) \tag{2.10}$$

$$\vec{\nabla} \cdot \vec{H}(\vec{r},\omega) = 0 \tag{2.11}$$

$$\vec{\nabla} \cdot \vec{E}(\vec{r},\omega) = \frac{\rho(\vec{r},\omega)}{\varepsilon(\omega)} \tag{2.12}$$

$$\vec{\nabla} \wedge \vec{H}(\vec{r},\omega) = \sigma_c(\omega)\vec{E}(\vec{r},\omega) + \vec{J}_s(\vec{r},\omega) - i\omega\varepsilon(\omega)\vec{E}(\vec{r},\omega) \tag{2.13}$$

2.1.2 Helmholtz vector wave equations

In the following, we will consider a source free ($\vec{J}_s = \vec{0}$) and a neutral material at the macroscopic scale with no net charge ($\rho = 0$). Equations (2.13) and (2.12) become:

$$\vec{\nabla} \cdot \vec{E}(\vec{r},\omega) = 0 \tag{2.14}$$

$$\vec{\nabla} \wedge \vec{H}(\vec{r},\omega) = \sigma_c(\omega)\vec{E}(\vec{r},\omega) - i\omega\varepsilon(\omega)\vec{E}(\vec{r},\omega) \tag{2.15}$$

By taking the curl of equations (2.10) and (2.15) and by respectively considering the divergence equations (2.14) and (2.11), we obtain:

$$\Delta\vec{E}(\vec{r},\omega) + \omega^2\mu(\omega)\hat{\varepsilon}(\omega)\vec{E}(\vec{r},\omega) = 0 \tag{2.16}$$

$$\Delta\vec{H}(\vec{r},\omega) + \omega^2\mu(\omega)\hat{\varepsilon}(\omega)\vec{H}(\vec{r},\omega) = 0 \tag{2.17}$$

where Δ is the vector Laplace operator and $\hat{\varepsilon}$, the generalized permittivity including both the conduction and polarization mechanism for respectively free and bound electrons:

$$\hat{\varepsilon}(\omega) = \varepsilon(\omega) + i\frac{\sigma_c(\omega)}{\omega} \tag{2.18}$$

Materials exhibiting a non negligible conductivity σ_c are called conductors (metallic materials for example) while materials with $\sigma \approx 0$ are called insulators or dielectric. To simplify the notations, from this point, $\hat{\varepsilon}$ the generalized permittivity will simply be written as ε. It can be noted that the generalized permittivities of dielectric materials are well described by Lorentz oscillator model giving the motion of bound electrons. On the other hand, for ω below their plasma frequencies, generalized permittivities of common metals (such as Au, Ag, ...) are theoretically well predicted by Drude's model describing the collective movement of the free electrons and they exhibit a negative real part ($\Re(\varepsilon) < 0$). At higher frequencies inter-band transitions become significant and must be taken into account for describing their dielectric constant.

Equations (2.16) and (2.17) are known as the homogeneous Helmholtz wave vector equations. They describe the propagation of electromagnetic waves through a neutral and source free medium.

2.1.3 Monochromatic plane waves

In cartesian coordinates, the eigenmodes of the homogeneous Helmholtz equations (2.16) and (2.17) are plane waves:

$$\vec{E}(\vec{r},\omega) = E_0 e^{i(\vec{k}(\omega)\vec{r}-\omega t)} \tag{2.19}$$

$$\vec{H}(\vec{r},\omega) = H_0 e^{i(\vec{k}(\omega)\vec{r}-\omega t)} \tag{2.20}$$

where we have taken the standard time-dependent convention $e^{-i\omega t}$.

General solutions to an electromagnetic problem using this set of eigenmodes therefore take the following form:

$$\vec{E}(\vec{r},\omega) = \sum_j a_j E_0 e^{i(\vec{k}_j(\omega)\vec{r}-\omega t)} \tag{2.21}$$

where the a_j coefficients and the $\vec{k}_j$ wave vectors are usually determined using appropriate boundary conditions for a given problem.

2.1.4 Dispersion relation

Inserting the plane waves solutions (2.19,2.20) into (2.16,2.17) provides the well known dispersion relation that relates frequency to material properties and wave vector:

$$k^2(\omega) = \omega^2 \mu(\omega)\varepsilon(\omega) = \frac{\omega^2}{c^2}\mu_r(\omega)\varepsilon_r(\omega) \tag{2.22}$$

where the constant $c = \frac{1}{\sqrt{\varepsilon_0 \mu_0}} \approx 3 \times 10^8 m.s^{-1}$ is the speed of light in vacuum. The dispersion relation connects the electromagnetic field variation in space and time.

2.1.5 Optical refractive index

In (2.19), $\Phi = \vec{k}\vec{r} - \omega t$ represents the phase of the wave. By definition, the phase velocity v_p is the $\frac{d\vec{r}}{dt}$ of the equiphase ($d\Phi = 0$) surface. Writing

$$d\Phi = \vec{k} d\vec{r} - \omega dt \tag{2.23}$$

leads to:

$$v_p = \frac{\omega}{k} \tag{2.24}$$

Using the previously established dispersion relation (2.22), the phase velocity reads:

$$v_p = \frac{c}{\sqrt{\varepsilon_r \mu_r}} = \frac{c}{N} \tag{2.25}$$

$\varepsilon_r(\omega)$ and $\mu_r(\omega)$ being function of ω, the phase velocity may vary with frequency: the propagation is dispersive. The quantity $N = \sqrt{\varepsilon_r(\omega)\mu_r(\omega)}$ is the refractive index which describes the ratio between the velocity of light in a vacuum and in a material. Since ε_r and μ_r are complex numbers, the optical index is a complex number:

$$N = n' + in'' \tag{2.26}$$

The real part, n' describes the propagation of a wave while the imaginary part, n'' its attenuation through the medium.

2.1.6 Wave impedance

Inserting the monochromatic plane waves expressions into the four Maxwell's equations (2.10, 2.11, 2.14, 2.15) leads to:

$$i\vec{k} \cdot \vec{E}(\vec{r},\omega) = 0 \tag{2.27}$$

$$i\vec{k} \cdot \vec{H}(\vec{r},\omega) = 0 \tag{2.28}$$

$$i\vec{k} \wedge \vec{E}(\vec{r},\omega) = i\omega\mu(\omega)\vec{H}(\vec{r},\omega) \tag{2.29}$$

$$i\vec{k} \wedge \vec{H}(\vec{r},\omega) = -i\omega\varepsilon(\omega)\vec{E}(\vec{r},\omega) \tag{2.30}$$

These relations illustrate the transverse nature of electromagnetic plane waves. The first two equations imply that both $\vec{E}$ and $\vec{H}$ are perpendicular to $\vec{k}$ while the last two implies the orthogonality of $\vec{E}$ and $\vec{H}$. Therefore $\vec{k}$, $\vec{E}$ and $\vec{H}$ form a right-handed orthogonal triplet.

Furthermore, using (2.29) and (2.30) we can define:

$$\eta = \frac{E(\vec{r},\omega)}{H(\vec{r},\omega)} = \sqrt{\frac{\mu}{\varepsilon}} \tag{2.31}$$

This ratio has units of electrical resistance (Ω) and is called the intrinsic wave impedance of a medium. It relates the electric field to the magnetic field amplitude in a medium. η is a complex value indicating that $\vec{E}$ and $\vec{H}$ are not necessarily in phase. The wave impedance in free space is given by $\eta_0 = \sqrt{\mu_0/\varepsilon_0} \approx 376,73\ \Omega$. Impedance is a concept of prime importance in electronics and electromagnetism when using the transmission line formalism.

2.1.7 Poynting vector and energy flux through a surface

The Poynting vector represents the directional energy flux in both magnitude and orientation. It is defined by:

$$\vec{\Pi}(\vec{r},\omega) = \vec{E}(\vec{r},\omega) \wedge \vec{H}(\vec{r},\omega) \tag{2.32}$$

It has units of $W.m^{-2}$. The net rate at which electromagnetic energy crosses the boundary of a surface Σ of outward normal unit vector $\vec{n}$ is given by:

$$W = \iint_{\Sigma} \vec{\Pi}(\vec{r},\omega) \cdot \vec{n}\, d\Sigma \tag{2.33}$$

Where W is the power crossing Σ expressed in Watts. For high frequencies it is often impractical to follow the instantaneous variation of the Poynting vector. As a result, the average of $\vec{\Pi}$ over many cycles of oscillations is often considered instead. The averaging procedure for monochromatic harmonic plane waves leads to the time-averaged Poynting vector:

$$\vec{S} = \langle \vec{\Pi} \rangle = \frac{1}{2} \Re(\vec{E}(\vec{r},\omega) \wedge \vec{H}^*(\vec{r},\omega)) \tag{2.34}$$

$\vec{S}$ is also known as irradiance or intensity. Using the plane wave properties given in (2.29-2.31) we can write:

$$S = \frac{1}{2\eta} \left| E_0 \right|^2 \tag{2.35}$$

2.2 Light interaction with particles

In the previous part we have studied the propagation of electromagnetic waves in homogeneous media without considering their physical origin. This part is devoted to the study of sources of radiation, and more precisely to the fundamental problem of scattering of light by particles. We will study the emission of radiation by localized distributions of charges and currents based on multipole analysis.

2.2.1 Electromagnetic scattering and multipole expansion

2.2.1.a The scattering problem

In this part, we consider the interaction of a monochromatic plane wave with an arbitrarily shaped three-dimensional object. The scattering problem, illustrated on Fig. 2.1, is the following: an incident electromagnetic wave $(\vec{E}_{inc}, \vec{H}_{inc})$ impinges on a nanostructure called a scatterer. This excitation causes oscillations of charges in the particle (polarization and conduction currents) and results in a distribution of induced electric currents $\vec{J}_s$ in the resonator. These current sources in turn radiate electromagnetic waves with a given radiation pattern which then propagate in the surrounding environment.

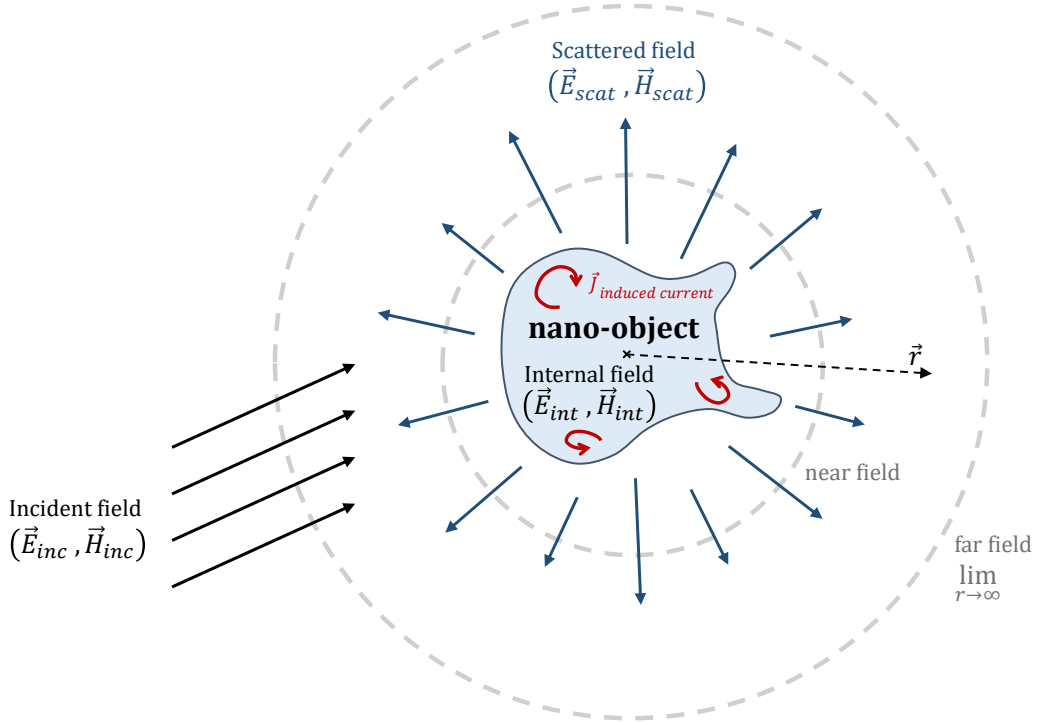

Figure 2.1 – Schematic view of an electromagnetic scattering process by an arbitrarily shaped particle. An incident electric field $\vec{E}_{inc}$ excites an electric current density $\vec{J}$ in the particle resulting in the radiation of a scattered wave $\vec{E}_{scat}$ and an internal field distribution $\vec{E}_{int}$.

We denote by $(\vec{E}_{scat}, \vec{H}_{scat})$ the scattered fields and by $(\vec{E}_{int}, \vec{H}_{int})$ the internal fields distribution. The fields outside the particle denoted by $(\vec{E}_{tot}, \vec{H}_{tot})$ are the superposition of both the incident and the scattered fields:

$$\vec{E}_{tot}(\vec{r},\omega) = \vec{E}_{inc}(\vec{r},\omega) + \vec{E}_{scat}(\vec{r},\omega) \tag{2.36}$$

$$\vec{H}_{tot}(\vec{r},\omega) = \vec{H}_{inc}(\vec{r},\omega) + \vec{H}_{scat}(\vec{r},\omega) \tag{2.37}$$

As $\vec{E}_{scat} = \vec{E}_{tot} - \vec{E}_{inc}$ we see that the scattered field is defined as the difference between the field in the presence of the obstacle and that which would exist in its absence (*i.e.* in an homogeneous medium). In the following , the scatterer is assumed to be a linear and isotropic material. The same holds for the surrounding media which is furthermore considered as lossless.

As illustrated on Fig. 2.1, different regions can be identified around the object: a near field and a far field zone. The far-field, also known as the Fraunhofer region, can be found far from the particle for distances $r \gg 2D^2/\lambda$ where D is the size of the particle. This region is dominated by propagating fields, behaving as spherical waves decaying as $1/r$, and is characterized by an angular radiation pattern that does not change its shape with the distance. In contrast, the near field zone is found in the immediate vicinity of the particle for distance r below a few wavelengths. Non-propagating fields dominate in this region and the distribution of fields is rather complex and vary rapidly with the distance to the source.

2.2.1.b Poynting theorem, energy conservation and cross-sections

The interaction of light with a particle involves two different physical phenomena: scattering and absorption. Absorption, comes from the fact that part of the incident electromagnetic energy is converted into another form, mainly into thermal dissipation, due to the moving charges. The principle of conservation of energy must be satisfied by the system. Energy conservation is given

by the Poynting theorem which takes the following form for the total fields:

$$\oiint_{\Sigma}\left(\vec{E}\wedge\vec{H}\right)\cdot\vec{n}\,d\Sigma=-\iiint_{V}\vec{J}\cdot\vec{E}\,dV-\iiint_{V}\left(\vec{E}\cdot\frac{\partial\vec{D}}{\partial t}+\vec{H}\cdot\frac{\partial\vec{B}}{\partial t}\right)dV \tag{2.38}$$

It can be derived directly from Maxwell's equations (2.1, 2.2, 2.3, 2.4) [1]. This equation states that the energy flowing out through a surface Σ of outward normal $\vec{n}$ surrounding the particle is equal to the work done by all fields on charges in the volume V of the particle plus the changes in the electromagnetic energy within the volume.

Considering a harmonic field, using the temporal average of the Poynting vector and assuming negligible dispersion, the Poynting theorem can be written as:

$$-W_{abs}=\oiint_{\Sigma}\vec{S}_{tot}\cdot\vec{n}\,d\Sigma=-\frac{1}{2}\omega\iiint_{V}\left(\Im(\varepsilon)|\vec{E}_{tot}|^2+\Im(\mu)|\vec{H}_{tot}|^2\right)dV \tag{2.39}$$

where the conduction current is accounted for in the generalized dielectric constant ε. Our $e^{-i\omega t}$ convention implies that $\Im(\varepsilon)>0$ and $\Im(\mu)>0$. We have defined W_{abs} such that by convention, $W_{abs}>0$ indicates that energy is dissipated in the structure. Equation (2.39) indicates that the average flux of the Poynting vector gives the total energy dissipated in the particle due to $\Im(\varepsilon)$ and $\Im(\mu)$.

In addition, energy conservation makes it possible to derive a relationship between absorbed and scattered power. The total Poynting vector can be decomposed as follows:

$$\vec{S}_{tot}=\vec{S}_{inc}+\vec{S}_{scat}+\vec{S}_{ext} \tag{2.40}$$

where:

$$\vec{S}_{tot}=\frac{1}{2}\Re\left(\vec{E}_{tot}\wedge\vec{H}^{*}_{tot}\right) \tag{2.41}$$

$$\vec{S}_{inc}=\frac{1}{2}\Re\left(\vec{E}_{inc}\wedge\vec{H}^{*}_{inc}\right) \tag{2.42}$$

$$\vec{S}_{scat}=\frac{1}{2}\Re\left(\vec{E}_{scat}\wedge\vec{H}^{*}_{scat}\right) \tag{2.43}$$

$$\vec{S}_{ext}=\frac{1}{2}\Re\left(\vec{E}_{inc}\wedge\vec{H}^{*}_{scat}+\vec{E}_{scat}\wedge\vec{H}^{*}_{inc}\right) \tag{2.44}$$

$\vec{S}_{inc}$ is the Poynting vector associated to the incident wave. $\vec{S}_{scat}$ the one associated to the scattered field while the last term $\vec{S}_{ext}$ takes into account interferences between the scattered and incident fields. Equation (2.40) yields a description of the absorbed power as the sum:

$$W_{abs}=W_{inc}-W_{scat}+W_{ext} \tag{2.45}$$

where:

$$W_{abs}=-\oiint_{\Sigma}\vec{S}_{tot}\cdot\vec{n}d\Sigma \tag{2.46}$$

$$W_{inc}=-\oiint_{\Sigma}\vec{S}_{inc}\cdot\vec{n}d\Sigma \tag{2.47}$$

$$W_{scat}=\oiint_{\Sigma}\vec{S}_{scat}\cdot\vec{n}d\Sigma \tag{2.48}$$

$$W_{ext}=-\oiint_{\Sigma}\vec{S}_{ext}\cdot\vec{n}d\Sigma \tag{2.49}$$

$$\tag{2.50}$$

We have followed the definition of [2] to handle positive quantities only. W_{scat} is the scattered power, W_{ext} is called the extinction power and W_{inc} corresponds to the energy flow of the incident wave through the considered surface Σ. W_{inc} vanishes in the case of a lossless surrounding medium as $\vec{S}_{inc}$ is a constant vector independent of r. Equation (2.45) becomes:

$$W_{ext}=W_{scat}+W_{abs} \tag{2.51}$$

W_{ext} represents the total attenuation of energy removed from the incident beam due to both the absorption and scattering mechanisms.

The optical cross-sections σ $[m^2]$ are defined as the powers divided by the intensity of the incident beam I_0:

$$\sigma_{ext} = \frac{W_{ext}}{I_0} \qquad \sigma_{abs} = \frac{W_{abs}}{I_0} \qquad \sigma_{scat} = \frac{W_{scat}}{I_0} \tag{2.52}$$

where $I_0 = \frac{1}{2\eta}|E_0|^2$ as introduced in equation (2.35).

These quantities are independent of the strength of the incident electromagnetic fields, as long as the processes are linear, and can be seen as an equivalent area of interaction between the light and the particle. They characterize the ability of a scatterer to interact with light since they are proportional to the probability of interaction between the incident wave and the considered object. For example, σ_{ext} can be interpreted as the area that would block the incident beam of as much energy as is removed by scattering and absorption. To obtain a quantity being comparable for different particle sizes, it is useful to normalize the cross-sections by the geometric cross-section $\mathcal{A}$ of the considered particle (for a sphere $\mathcal{A} = \pi R^2$ where R is the radius). This defines the dimensionless efficiencies Q :

$$Q_{ext} = \frac{\sigma_{ext}}{\mathcal{A}} \qquad Q_{abs} = \frac{\sigma_{abs}}{\mathcal{A}} \qquad Q_{scat} = \frac{\sigma_{scat}}{\mathcal{A}} \tag{2.53}$$

2.2.2 Solutions of the Helmholtz equation in spherical coordinates

We have introduced the scattering problem, we will now address how it may be treated. Studying the scattering of electromagnetic radiation necessarily involves solving the vector wave equation. While we have seen that monochromatic plane waves form a set of eigenmodes in the cartesian coordinates, scattered waves by individual particles are best described in spherical coordinates. Therefore, in this part, we shall present solutions to the Helmholtz equation in spherical coordinates based on vector spherical harmonics.

The spherical coordinates are defined as in Fig. 2.2 where θ represents the polar angle and φ the azimuthal one.

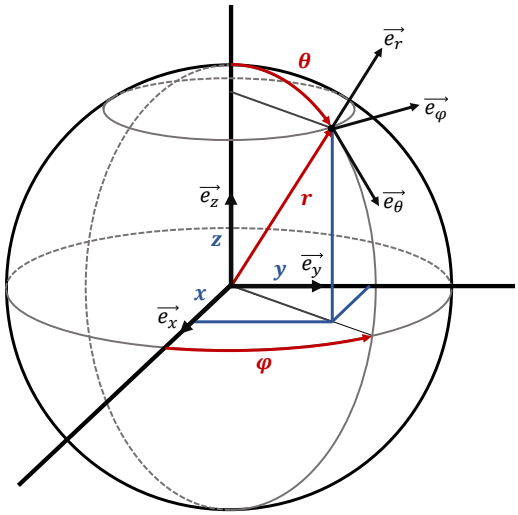

Figure 2.2 – Schematic view of the spherical (r, θ, φ) and cartesian (x, y, z) coordinates.

We seek solutions to the source-free version of Maxwell's equations that satisfy the Helmholtz equation (2.16):

$$\Delta\vec{E}(\vec{r},\omega) + k^2\vec{E}(\vec{r},\omega) = 0 \tag{2.54}$$

The same holds for the magnetic field $\vec{H}$.

Solutions to this equation are given by two linearly independent vector functions $\vec{M}$ and $\vec{N}$ known as the Hansen vectors, defined by:

$$\vec{M}(\vec{r},\omega) = \vec{\nabla} \wedge \left(\vec{r}\psi\right) \tag{2.55}$$

$$\vec{N}(\vec{r},\omega) = \frac{i}{k}\vec{\nabla} \wedge \vec{M}(\vec{r},\omega) \tag{2.56}$$

Using vector identities it can be shown that they satisfy the requirement [1]:

$$\Delta\vec{M}(\vec{r},\omega) + k^2\vec{M}(\vec{r},\omega) = \vec{\nabla} \wedge \left[\vec{r}\left(\Delta\psi(\vec{r},\omega) + k^2\psi(\vec{r},\omega)\right)\right] = 0 \tag{2.57}$$

$$\vec{\nabla} \cdot \vec{M}(\vec{r},\omega) = 0 \tag{2.58}$$

$$\Delta\vec{N}(\vec{r},\omega) + k^2\vec{N}(\vec{r},\omega) = 0 \tag{2.59}$$

$$\vec{\nabla} \cdot \vec{N}(\vec{r},\omega) = 0 \tag{2.60}$$

as long as the scalar function ψ, called the generating function, is a solution to the scalar wave equation:

$$\Delta\psi(\vec{r},\omega) + k^2\psi(\vec{r},\omega) = 0 \tag{2.61}$$

Therefore, exact solutions for the vector fields can be found by solving the scalar wave equation (2.61). In spherical coordinates, equation (2.61) reads:

$$\frac{1}{r^2}\frac{\partial}{\partial r}\left(r^2\frac{\partial\psi}{\partial r}\right) + \frac{1}{r^2\sin\theta}\frac{\partial}{\partial\theta}\left(\sin\theta\frac{\partial\psi}{\partial\theta}\right) + \frac{1}{r^2\sin\theta}\frac{\partial^2\psi}{\partial\varphi^2} + k^2\psi = 0 \tag{2.62}$$

As is well known, it is possible to solve this equation by using separation of variables:

$$\psi(r,\theta,\varphi) = \psi_r(r)\psi_\theta(\theta)\psi_\varphi(\varphi) \tag{2.63}$$

2.2.2.a Solutions to the radial part ψ_r

Solutions to the radial part of (2.62) are given by the spherical Bessel functions of the first and second kinds (also known respectively as the spherical Bessel and Neumann functions), $j_n(kr)$ and $y_n(kr)$.

$$j_n(x) = \sqrt{\frac{\pi}{2x}}J_{n+\frac{1}{2}}(x) \qquad\qquad y_n(x) = \sqrt{\frac{\pi}{2x}}Y_{n+\frac{1}{2}}(x) \tag{2.64}$$

Solutions can also be expressed in terms of spherical Hankel functions of first and second kinds, respectively $h_n^{(1)}(kr)$ and $h_n^{(2)}(kr)$ given by the linear combinations:

$$h_n^{(1)}(x) = j_n(x) + i\,y_n(x) \tag{2.65}$$

$$h_n^{(2)}(x) = j_n(x) - i\,y_n(x) \tag{2.66}$$

While the function $j_n(kr)$, $y_n(kr)$, $h_n^{(1)}(kr)$ and $h_n^{(2)}(kr)$ are all possible mathematical solutions, boundary conditions of the scattering problem determine which functions can be used to express the fields while conserving a physical meaning. For instance, we know that fields outside the particle must decay with increasing distance from the origin and vanish at infinity (Sommerfeld radiation condition). Therefore, only $h_n^{(1)}(kr)$ can be used to express an outgoing wave like a scattered one. On the opposite $h_n^{(2)}(kr)$ would be used to represent an incoming wave converging toward the origin, which is not of interest in this scattering problem. Finally, the spherical Bessel

function $j_n(kr)$ is regular at the origin as it exhibits no singularity at $r = 0$, and is therefore the only one that should be kept for describing the incident wave or the internal field inside the scatterer.

To sum up, radial solution will only take one of the following form:

$$\psi_r^{outgoing}(kr) = h_n^{(1)}(kr) \tag{2.67}$$

$$\psi_r^{regular}(kr) = j_n(kr) \tag{2.68}$$

Only two of the four spherical bessel functions are used in a scattering problem to express the radial dependency of the fields. In the following, we will designate the radial solution by $z_n^{(l)}(kr)$ where $z_n^{(1)}(kr) = j_n(kr)$ and $z_n^{(3)}(kr) = h_n^{(1)}(kr)$ as it is a notation widely used in the literature.

2.2.2.b Solutions to the angular part $\psi_\theta\psi_\varphi$

Solutions to the φ azimuthal angle dependent part of (2.61) are given by harmonic functions of φ:

$$e^{im\varphi} \tag{2.69}$$

where m is an integer taking negative or positive values, known as the azimuthal angular projection index.

On the other hand, solutions that depend on the polar angle θ (see equation (2.61)) are given by the associated Legendre polynomials $P_n^m(\cos\theta)$ of degree n and order m:

$$P_n^m(\cos\theta) = (-1)^m(\sin\theta)^m \frac{d^m P_n(\cos\theta)}{(d\cos\theta)^m} \tag{2.70}$$

where $P_n(\cos\theta)$ are the Legendre polynomials. n is a natural integer corresponding to the angular momentum index, while m is such that $-n < m < n$.

The angular solutions $\psi(\theta)$ and $\psi(\varphi)$ can be combined into a single function known as the spherical harmonics. The normalized spherical harmonics are given by:

$$Y_{n,m}(\theta,\varphi) = \sqrt{\frac{2n+1}{4\pi}\frac{(n-m)!}{(n+m)!}} P_n^m(\cos\theta)e^{im\varphi} \tag{2.71}$$

2.2.2.c General form of the solutions

The solution ψ to the scalar Helmholtz equation finally reads:

$$\psi = \frac{-i}{\sqrt{n(n+1)}} z_n^{(l)}(kr) Y_{n,m}(\theta,\varphi) \tag{2.72}$$

where $1/\sqrt{n(n+1)}$ is a normalization factor inserted for convenience. It is useful at this stage to introduce the radially independent normalized vector spherical harmonics:

$$\vec{X}_{n,m}(\theta,\varphi) = \frac{-i}{\sqrt{n(n+1)}}(\vec{r}\wedge\vec{\nabla})Y_{n,m}(\theta,\varphi) = \frac{1}{\sqrt{n(n+1)}}\vec{\mathcal{L}}\, Y_{n,m}(\theta,\varphi) \tag{2.73}$$

where

$$\vec{\mathcal{L}} = -i\vec{r}\wedge\vec{\nabla} \tag{2.74}$$

is the angular momentum operator.

Using these notations, the Hansen vectors (2.55) and (2.56) solutions of the free space vector Helmholtz equation read:

$$\vec{M}_{n,m}^{(l)}(\vec{r},\omega) = z_n^{(l)}(kr)\vec{X}_{n,m}(\theta,\varphi) \tag{2.75}$$

$$\vec{N}_{n,m}^{(l)}(\vec{r},\omega) = \frac{i}{k}\vec{\nabla}\wedge\left(z_n^{(l)}(kr)\vec{X}_{n,m}(\theta,\varphi)\right) \tag{2.76}$$

They furthermore satisfy the useful relations:

$$\vec{\nabla} \wedge \vec{M}^{(l)}_{n,m}(\vec{r},\omega) = -ik\vec{N}^{(l)}_{n,m}(\vec{r},\omega) \tag{2.77}$$

$$\vec{\nabla} \wedge \vec{N}^{(l)}_{n,m}(\vec{r},\omega) = ik\vec{M}^{(l)}_{n,m}(\vec{r},\omega) \tag{2.78}$$

By combining the two types of spherical vectors, we can write the general solutions to the Helmholtz equations as:

$$\vec{E}(\vec{r},\omega) = E_0 \sum_{n=1}^{\infty} \sum_{m=-n}^{+n} \left(\alpha_{n,m}\vec{N}^{(l)}_{n,m}(\vec{r},\omega) + \beta_{n,m}\vec{M}^{(l)}_{n,m}(\vec{r},\omega) \right) \tag{2.79}$$

$$= E_0 \sum_{n=1}^{\infty} \sum_{m=-n}^{+n} \left(\frac{i}{k}\alpha_{n,m}\vec{\nabla} \wedge \left(z^{(l)}_n(kr)\vec{X}_{n,m}(\theta,\varphi) \right) + \beta_{n,m} z^{(l)}_n(kr)\vec{X}_{n,m}(\theta,\varphi) \right) \tag{2.80}$$

Using the Maxwell-Faraday equation (2.10) and relations (2.77) and (2.78) yields the following magnetic field expression:

$$\vec{H}(\vec{r},\omega) = \frac{E_0}{\eta} \sum_{n=1}^{\infty} \sum_{m=-n}^{+n} \left(\alpha_{n,m} z^{(l)}_n(kr)\vec{X}_{n,m}(\theta,\varphi) - \frac{i}{k}\beta_{n,m}\vec{\nabla} \wedge \left(z^{(l)}_n(kr)\vec{X}_{n,m}(\theta,\varphi) \right) \right) \tag{2.81}$$

Therefore, in the scattering problem, the different fields can be expanded as a sum of terms called multipoles, given by vector spherical harmonics (VSH), and they take the form:

$$\vec{E}_{inc}(\vec{r},\omega) = E_0 \sum_{n=1}^{\infty} \sum_{m=-n}^{+n} \left(p_{n,m}\vec{N}^{(1)}_{n,m}(\vec{r},\omega) + q_{n,m}\vec{M}^{(1)}_{n,m}(\vec{r},\omega) \right) \tag{2.82}$$

$$\vec{E}_{int}(\vec{r},\omega) = E_0 \sum_{n=1}^{\infty} \sum_{m=-n}^{+n} \left(c_{n,m}\vec{N}^{(1)}_{n,m}(\vec{r},\omega) + d_{n,m}\vec{M}^{(1)}_{n,m}(\vec{r},\omega) \right) \tag{2.83}$$

$$\vec{E}_{scat}(\vec{r},\omega) = E_0 \sum_{n=1}^{\infty} \sum_{m=-n}^{+n} \left(a_{n,m}\vec{N}^{(3)}_{n,m}(\vec{r},\omega) + b_{n,m}\vec{M}^{(3)}_{n,m}(\vec{r},\omega) \right) \tag{2.84}$$

It is interesting to notice that the $\vec{N}_{n,m}(\vec{r},\omega)$ vectors are transverse to the radius vector $\vec{r}$. Therefore the $a_{n,m}$, $c_{n,m}$ and $p_{n,m}$ coefficients are often referred to as electric multipole coefficients as they provide the weight of Transverse Electric (TE) multipoles. Conversly, $b_{n,m}$, $d_{n,m}$ and $q_{n,m}$ are called magnetic multipole coefficients as they are associated to Transverse Magnetic (TM) multipoles. Furthermore, a multipole of degree n is a 2^n-pole meaning that $n = 1$ corresponds to dipoles, $n = 2$ to quadrupoles, $n = 3$ to octupoles, and so on.

2.2.3 Solving of the scattering problem with the $\mathcal{T}$-Matrix

2.2.3.a Transition $\mathcal{T}$-matrix formalism

The linearity of Maxwell's equations implies that the relation between the scattered and the incident fields is linear. Since the VSH eigenmodes form an orthogonal set, it is possible to move from the $(p_{n,m}, q_{n,m})$ expansion coefficients of the incident field to the $(a_{n,m}, b_{n,m})$ expansion coefficients of the scattered field, and their relationship may be expressed in a matrix form using the so called $\mathcal{T}$-matrix formalism (transition matrix):

$$\begin{pmatrix} a_{n,m} \\ b_{n,m} \end{pmatrix} = \mathcal{T} \begin{pmatrix} p_{n,m} \\ q_{n,m} \end{pmatrix} \tag{2.85}$$

where $\mathcal{T}$ is an infinite square matrix. The $\mathcal{T}$-matrix entirely describes the interaction of an object with light. The matrix only depends on the material parameters and the geometrical characteristics of the considered particle (refractive index, size, shape, ...) and is completely independent of the incident wave. This means that once the $\mathcal{T}$-matrix of a scatterer has been obtained, its scattering properties can be easily calculated for any given illumination directions or polarization states of the incident field.

The $\mathcal{T}$-matrix is therefore a general concept that allows to solve the scattering problem. It can be obtained by multiple means, the two most common ones being the extended boundary condition method (EBCM) (also known as the null-field method), which requires the computation of specific integrals over the particle surface, and the point-matching method (PMM) which relies on the fulfillment of the boundary conditions at a discrete number of surface points. In any case, obtaining the $\mathcal{T}$-matrix and solving the scattering problem usually requires applying the appropriate boundary conditions at the surface of the scatterer.

2.2.3.b Boundary conditions

The solving of the scattering problem can be carried out by applying the boundary conditions at the surface of the particle given by:

$$\left[\vec{E}_{inc}(\vec{r}_\Sigma,\omega)+\vec{E}_{scat}(\vec{r}_\Sigma,\omega)\right]\wedge\vec{n}=\vec{E}_{int}(\vec{r}_\Sigma,\omega)\wedge\vec{n} \tag{2.86}$$

$$\left[\vec{H}_{inc}(\vec{r}_\Sigma,\omega)+\vec{H}_{scat}(\vec{r}_\Sigma,\omega)\right]\wedge\vec{n}=\vec{H}_{int}(\vec{r}_\Sigma,\omega)\wedge\vec{n} \tag{2.87}$$

These two equations translate the continuity of the tangential fields on the surface of the scatterer and therefore connect the fields of each side of the boundary. $\vec{n}$ is the outward vector normal to the surface Σ of the scatterer described by $\vec{r}_\Sigma$.

The complexity of solving these equations clearly depends on the shape of the particle Σ. For highly symmetrical scatterers such as spheres, analytic solutions can be found and are given by the Lorentz-Mie theory while for other complex geometries, the $\mathcal{T}$-Matrix has to be numerically computed. The next section will be devoted to the presentation of the Lorentz-Mie solutions for spherical particles.

2.2.4 Scattering by a single sphere

2.2.4.a Mie theory: light scattering from a spherical particle

We now consider the simple Mie scattering problem, *i.e.* the scattering of a homogeneous sphere of radius R and refractive index $N=\sqrt{\varepsilon(\omega)\mu(\omega)}$ embedded in a lossless host medium with refractive index $n_h=\sqrt{\varepsilon_h(\omega)\mu_h(\omega)}$. This problem can be analytically solved by applying the boundary conditions (2.86) and (2.87) for $\vec{r}_\Sigma=R\vec{e}_r$ which leads to the following scattering coefficients [2]:

$$a_{n,m}=a_n p_{n,m} \qquad\qquad b_{n,m}=b_n q_{n,m} \tag{2.88}$$

where a_n and b_n are the so-called Mie coefficients [2]:

$$a_n=\frac{\mu_h\gamma^2 j_n(\gamma x)[x j_n(x)]'-\mu j_n(x)[\gamma x j_n(\gamma x)]'}{\mu_h\gamma^2 j_n(\gamma x)[x h_n^{(1)}(x)]'-\mu h_n^{(1)}(x)[\gamma x j_n(\gamma x)]'} \tag{2.89}$$

$$b_n=\frac{\mu j_n(\gamma x)[x j_n(x)]'-\mu_h j_n(x)[\gamma x j_n(\gamma x)]'}{\mu j_n(\gamma x)[x h_n^{(1)}(x)]'-\mu_h h_n^{(1)}(x)[\gamma x j_n(\gamma x)]'} \tag{2.90}$$

and where we have introduced two dimensionless parameters: the size parameter x and the index contrast γ defined by:

$$x=k_h R=\frac{2\pi}{\lambda}n_h R \qquad\qquad \gamma=\frac{k}{k_h}=\frac{N}{n_h} \tag{2.91}$$

Equations (2.88) indicate that for spherical scatterers, the $\mathcal{T}$-matrix is diagonal and its coefficients are simply given by the Mie coefficients:

$$\begin{pmatrix} a_{1,-1} \\ a_{1,0} \\ a_{1,1} \\ \vdots \\ a_{n,m} \\ b_{1,-1} \\ b_{1,0} \\ b_{1,1} \\ \vdots \\ b_{n,m} \end{pmatrix} = \begin{pmatrix} a_1 & & & & & & & & & \\ & a_1 & & & & & & & 0 & \\ & & a_1 & & & & & & & \\ & & & \ddots & & & & & & \\ & & & & a_n & & & & & \\ & & & & & b_1 & & & & \\ & & & & & & b_1 & & & \\ & & & & & & & b_1 & & \\ & & & & & & & & \ddots & \\ & 0 & & & & & & & & b_n \end{pmatrix} \begin{pmatrix} p_{1,-1} \\ p_{1,0} \\ p_{1,1} \\ \vdots \\ p_{n,m} \\ q_{1,-1} \\ q_{1,0} \\ q_{1,1} \\ \vdots \\ q_{n,m} \end{pmatrix} \tag{2.92}$$

2.2.4.b Absorption, scattering and extinction cross-sections

Several physical quantities, such as the cross-sections σ_{scat} , σ_{ext} and σ_{abs} defined in (2.52) can be expressed as a function of the Mie coefficients. The cross-sections are given by [2]:

$$\sigma_{scat} = \frac{2\pi}{k^2} \sum_{n=1}^{\infty} (2n+1) \left(|a_n|^2 + |b_n|^2 \right) \tag{2.93}$$

$$\sigma_{ext} = \frac{2\pi}{k^2} \sum_{n=1}^{\infty} (2n+1) \, \Re\left(a_n + b_n\right) \tag{2.94}$$

$$\sigma_{abs} = \sigma_{ext} - \sigma_{scat} \tag{2.95}$$

2.2.5 Scattering from multiple spheres

Extending the Lorentz-Mie theory, it is possible to analytically calculate the $\mathcal{T}$-matrix for an ensemble of non-overlapping spheres. The procedure has been described in detail in [3–5] and is often refereed to as the generalized multi-particle Mie solution.

When considering clusters of spheres, the particles are no longer isolated and the assumption of an incoming plane wave on each particle can not be used. The electromagnetic field incident on the particle has two contributions: the original incident wave and the field scattered by the other spheres in the ensemble:

$$\vec{E}_{inc}^{(j)} = \vec{E}_0^{(j)} + \sum_{i \neq j} \vec{E}_{i,scat}^{(j)} \tag{2.96}$$

The index $^{(j)}$ in the above equation indicates that the field has to be expressed considering the origin at the center of the sphere j in order to derive an analytic formulation of the boundary condition at the surface of the considered j^{th} sphere. The transformation from one origin to another displaced origin is given by the translational addition theorem for the vector spherical waves functions (VSWF). Applying the boundary conditions on each particles allows one to obtain a self consistent system of equations giving the $a_{n,m}^{(j)}$ and $b_{n,m}^{(j)}$ coefficients of each sphere j.

Once the interactive coefficients $a_{n,m}^{(j)}$ and $b_{n,m}^{(j)}$ are known, the translation addition theorem can be applied again to obtain the $a_{n,m}$ and $b_{n,m}$ coefficients of the ensemble describing the total scattered field from the assembly expanded at a choosen origin (usually taken as the center of mass) of the aggregate:

$$a_{n,m} = \sum_{i=1}^{N_s} \sum_{\nu=1}^{\infty} \sum_{\mu=-\nu}^{\nu} \left(a_{\nu,\mu}^{(i)} A_{nm}^{\nu\mu}((i \to O)) + b_{n,m}^{(i)} B_{nm}^{\nu\mu}((i \to O)) \right) \tag{2.97}$$

$$b_{n,m} = \sum_{i=1}^{N_s} \sum_{\nu=1}^{\infty} \sum_{\mu=-\nu}^{\nu} \left(a_{\nu,\mu}^{(i)} B_{nm}^{\nu\mu}((i \to O)) + b_{n,m}^{(i)} A_{nm}^{\nu\mu}((i \to O)) \right) \tag{2.98}$$

where $A_{nm}^{\nu\mu}$ and $B_{nm}^{\nu\mu}$ denotes translation coefficients of spherical harmonics transforming the expansion coefficients obtained with an origin taken at the i^{th} sphere toward the new origin O defined for the assembly.

In this work, we have used the Fortran $\mathcal{T}$-Matrix code [6] developed by Daniel W. Mackowski available at [7] to calculate the scattering properties of clusters of spherical particles, which will be described in section 3.3.

2.2.6 Multipole coefficients of the scattered field of arbitrary particles

In this section, we will introduce general equations allowing to calculate the dominating multipole moments supported by arbitrary nano-object. This approach requires that the electromagnetic scattering problem has been solved beforehand, *i.e.* that the scattered electric field $\vec{E}_{scat}$ or the current source densities $\vec{J}_s$ in the particle for a given illumination are known. This step is usually performed using numerical methods such as finite difference time domain (FDTD) or finite element method (FEM). The multipole expansion is then used to get physical insight into the excited resonances of a complex meta-atom: the field produced by the particles is analyzed as a superposition of fields created by a set of well-known point multipoles.

There are basically two ways to obtain the multipole moments. We first focus on projections based on the scattered field, and then introduce those based on the current densities. We follow the formalism presented by P. Grahn[8, 9]. In a second step, following the works of R. Alaee [10, 11] we introduce a set of equations allowing to retrieve the multipole moments directly in cartesian coordinates.

2.2.6.a Projection on the scattered electric field [8, 9]

As we have seen in section 2.2.2.c, the scattered electromagnetic fields satisfying the Helmholtz equations can be written in spherical coordinates as a multipole expansion of the form [8]:

$$\vec{E}_s(r,\theta,\varphi) = E_0 \sum_{n=1}^{\infty} \sum_{m=-n}^{n} A_n \left[\frac{1}{k} a_{n,m} \vec{\nabla} \wedge \left(h_n^{(1)}(kr) \vec{X}_{n,m}(\theta,\varphi) \right) + b_{n,m} h_n^{(1)}(kr) \vec{X}_{n,m}(\theta,\varphi) \right] \tag{2.99}$$

$$\vec{H}_s(r,\theta,\varphi) = \frac{E_0}{\eta} \sum_{n=1}^{\infty} \sum_{m=-n}^{n} (-i) A_n \left[a_{n,m} h_n^{(1)}(kr) \vec{X}_{n,m}(\theta,\varphi) + \frac{1}{k} b_{n,m} \vec{\nabla} \wedge \left(h_n^{(1)}(kr) \vec{X}_{n,m}(\theta,\varphi) \right) \right] \tag{2.100}$$

where we have followed the definition of the multipole expansion presented in [8, 9]. Here $A_n = i^n \sqrt{\pi(2n+1)}$ is an arbitrary scaling factor ensuring the expansion to be compatible with the expressions given by Mie theory [2] in the case of a spherical scatterer. This prefactor being arbitrary, it is chosen slightly differently in other references [12].

The spherical vector harmonics form an orthogonal set of functions in the sense that:

$$\int \vec{X}^*_{n',m'}(\theta,\varphi) \cdot \vec{X}_{n,m}(\theta,\varphi) d\Omega = \delta_{n'n} \delta_{m'm} \tag{2.101}$$

$$\int \vec{X}^*_{n',m'}(\theta,\varphi) \cdot (\vec{r} \wedge \vec{X}_{n,m}(\theta,\varphi)) d\Omega = 0 \tag{2.102}$$

Therefore, using the scalar product (2.101) the multipole coefficients can be determined through the projections of the VSH on the scattered fields:

$$a_{n,m} = \frac{\eta}{E_0 (-i) A_n h_n^{(1)}(kr)} \int_0^{2\pi} \int_0^{\pi} \vec{X}^*_{nm}(\theta,\varphi) \cdot \vec{H}_s(\vec{r}) \sin\theta \, d\theta \, d\varphi \tag{2.103}$$

$$b_{n,m} = \frac{1}{E_0 A_n h_n^{(1)}(kr)} \int_0^{2\pi} \int_0^{\pi} \vec{X}^*_{nm}(\theta,\varphi) \cdot \vec{E}_s(\vec{r}) \sin\theta \, d\theta \, d\varphi \tag{2.104}$$

where the integration is performed over any spherical surface fully enclosing the nanostructure. As the spherical vectors have no radial component, those integrals involve only the components: $\vec{E}_{s,\theta}, \vec{E}_{s,\varphi}, \vec{H}_{s,\theta}$ and $\vec{H}_{s,\varphi}$ of the scattered fields. The multipole coefficients can also be obtained from the radial components $\vec{E}_{s,r}$ and $\vec{H}_{s,r}$, via similar projections on $\vec{r}\cdot\vec{E}_s$ and $\vec{r}\cdot\vec{H}_s$ [9, 13]:

$$a_{n,m} = \frac{kr}{E_0 i A_n \sqrt{n(n+1)} h_n^{(1)}(kr)} \int_0^{2\pi}\int_0^{\pi} Y^*_{n,m}(\theta,\varphi)\cdot\vec{E}_{s,r}(\vec{r})\sin\theta\, d\theta\, d\varphi \tag{2.105}$$

$$b_{n,m} = \frac{1}{E_0 A_n \sqrt{n(n+1)} h_n^{(1)}(kr)} \int_0^{2\pi}\int_0^{\pi} Y^*_{n,m}(\theta,\varphi)\cdot\vec{H}_{s,r}(\vec{r})\sin\theta\, d\theta\, d\varphi \tag{2.106}$$

The choice of the projections to be used is completely free. If one only wants to deal with the electric field for example, equations (2.105) and (2.104) can be applied to extract the $a_{n,m}$ and $b_{n,m}$ coefficients.

In this section, we have presented two possible projections to retrieve the multipole moments from the knowledge of the scattered field. These methods are well-suited to study isolated sources in an homogeneous environment. However, if the particles are placed above a substrate or in a lattice composed of a large number of such scatterers, the scattered field from the considered object might be difficult to obtain. Indeed after subtracting the incident wave, the field at any point around the scatterer still contain the field produced by the other particles or the field reflected from the substrate.

An alternative method is to perform a multipole decomposition based on the induced electric currents in the particle, which directly takes into account interactions with other scatterers or with a substrate.

In the following, we will first introduce the link existing between the current sources and the scattered field before presenting in a second step the set of equations allowing to extract the multipole moments directly from the current sources.

2.2.6.b Link with the currents [14]

The origin of the scattered field are the source current densities J_s induced in the volume V of a scatterer. These scattering current source densities are given by:

$$\vec{J}_s(\vec{r}) = -i\omega\varepsilon_0(\varepsilon_{r,part} - \varepsilon_{r,h})\vec{E}_{tot}(\vec{r}) \tag{2.107}$$

The presence of the contrast of permittivities $(\varepsilon_{r,part} - \varepsilon_{r,h})$, where $\varepsilon_{r,h}$ is the relative permittivity of the host medium and $\varepsilon_{r,part}$ the relative permittivity of the particle, is consistent with the fact that in the absence of particle, $\vec{J}_s(\vec{r}) = 0$ and no scattering occurs as the medium is homogeneous.

Source currents and the scattered field are related through Maxwell's equations which read in the presence of sources:

$$\vec{\nabla}\wedge\vec{E}_{scat}(\vec{r},\omega) = i\omega\mu(\omega)\vec{H}_{scat}(\vec{r},\omega) \tag{2.108}$$

$$\vec{\nabla}\cdot\vec{H}_{scat}(\vec{r},\omega) = 0 \tag{2.109}$$

$$\vec{\nabla}\cdot\vec{E}_{scat}(\vec{r},\omega) = \frac{1}{i\omega\varepsilon(\omega)}\vec{\nabla}\cdot\vec{J}_s(\vec{r},\omega) \tag{2.110}$$

$$\vec{\nabla}\wedge\vec{H}_{scat}(\vec{r},\omega) = -i\omega\varepsilon(\omega)\vec{E}_{scat}(\vec{r},\omega) + \vec{J}_s(\vec{r},\omega) \tag{2.111}$$

where we have used the charge continuity equation in (2.12)

$$\frac{\partial\rho}{\partial t} = \vec{\nabla}\cdot\vec{J}_s \tag{2.112}$$

that, for harmonically varying sources, becomes:

$$i\omega\rho(\vec{r},\omega) = \vec{\nabla}\cdot\vec{J}_s(\vec{r},\omega) \tag{2.113}$$

By combining, (2.108) and (2.111), the equations can be written as two inhomogeneous wave equations:

$$\vec{\nabla}\wedge\vec{\nabla}\wedge\vec{E}_{scat}(\vec{r},\omega)-k^2\vec{E}_{scat}(\vec{r},\omega)=i\omega\varepsilon(\omega)\vec{J}_s(\vec{r},\omega) \tag{2.114}$$

$$\vec{\nabla}\wedge\vec{\nabla}\wedge\vec{H}_{scat}(\vec{r},\omega)-k^2\vec{H}_{scat}(\vec{r},\omega)=\vec{\nabla}\wedge\vec{J}_s(\vec{r},\omega) \tag{2.115}$$

They can be solved by means of the green function and the solutions outside of the particle turn out to be:

$$\vec{E}_{scat}(\vec{r},\omega)=i\omega\mu\iiint_{V'}\overleftrightarrow{G}(\vec{r},\vec{r}')\vec{J}_s(\vec{r'},\omega)dV' \tag{2.116}$$

$$\vec{H}_{scat}(\vec{r},\omega)=\iiint_{V'}\left[\vec{\nabla}\wedge\overleftrightarrow{G}(\vec{r},\vec{r}')\right]\vec{J}_s(\vec{r'},\omega)dV' \tag{2.117}$$

where the integrals are performed over the whole volume of the particle. These equations are known as the volume integral equations. $\overleftrightarrow{G}(\vec{r},\vec{r}')$ is the dyadic Green's function, solution to the inhomogeneous Helmholtz equation for a point source:

$$\vec{\nabla}\wedge\vec{\nabla}\wedge\overleftrightarrow{G}(\vec{r},\vec{r}')-k^2\overleftrightarrow{G}(\vec{r},\vec{r}')=\overleftrightarrow{I}\delta(\vec{r}-\vec{r}') \tag{2.118}$$

its expression is calculated from the scalar Green's function $G_0(\vec{r},\vec{r}')$

$$\overleftrightarrow{G}(\vec{r},\vec{r}')=\left[\overleftrightarrow{I}+\frac{1}{k^2}\nabla\nabla\right]G_0(\vec{r},\vec{r}') \tag{2.119}$$

where $\overleftrightarrow{I}$ is the unit dyad and where:

$$G_0(\vec{r},\vec{r}')=\frac{e^{ik|\vec{r}-\vec{r}'|}}{4\pi|\vec{r}-\vec{r}'|} \tag{2.120}$$

denotes a spherical wave that propagates away from the origin.

Therefore, we have seen that (2.116) and (2.117) gives us the electric and magnetic scattered fields due to an arbitrary source current distribution in free space. $\vec{J}_s$ can be viewed as a superposition of point current sources whose contribution to scattering at any point in space are obtain through the field propagator $\overleftrightarrow{G}$.

2.2.6.c Projections with electric current densities [8, 9]

Starting from the inhomogeneous wave equations (2.114) and (2.115) previously introduced, and writing solutions for respectively the components $(\vec{r}\cdot\vec{E}_{scat})$ and $(\vec{r}\cdot\vec{H}_{scat})$, it is possible to derive equations giving the coefficients of the scattered field $a_{n,m}$ and $b_{n,m}$ as a function of the current density $\vec{J}_s$. These equations established in [8, 9] read:

$$a_{n,m}=\frac{k^2\eta}{E_0 i^{n-1}\sqrt{\pi(2n+1)}}O_{nm}\iiint_V e^{-im\varphi}\begin{pmatrix}\left[\Psi_n(kr)+\Psi_n''(kr)\right]P_n^m(\cos\theta)\vec{r}\cdot\vec{J}_s(\vec{r})\\ +\dfrac{\Psi_n'(kr)}{kr}\left[\tau_{nm}(\theta)\vec{e}_\theta\cdot\vec{J}_s(\vec{r})-\pi_{nm}(\theta)\vec{e}_\varphi\cdot\vec{J}_s(\vec{r})\right]\end{pmatrix}dV \tag{2.121}$$

$$b_{n,m}=\frac{k^2\eta}{E_0 i^{n+1}\sqrt{\pi(2n+1)}}O_{nm}\iiint_V e^{-im\varphi}j_n(kr)\left[i\pi_{nm}(\theta)\vec{e}_\theta\cdot\vec{J}_s(\vec{r})+\tau_{nm}(\theta)\vec{e}_\varphi\cdot\vec{J}_s(\vec{r})\right]dV \tag{2.122}$$

Where $\Psi_n(kr)=(kr)j_n(kr)$ are the Riccati-Bessel functions and $\Psi_n'(kr)$,$\Psi_n''(kr)$ their first and second derivative with respect to the argument (kr). In these equations we have:

$$O_{nm}=\frac{1}{\sqrt{n(n+1)}}\sqrt{\frac{2n+1}{4\pi}\frac{(n-m)!}{(n+m)!}}\qquad\tau_{nm}(\theta)=\frac{d}{d\theta}P_n^m(\cos\theta)\qquad\pi_{nm}=\frac{m}{\sin\theta}P_n^m(\cos\theta) \tag{2.123}$$

Projections are performed by integration on the whole volume of the scatterers. Furthermore it is important to emphasize that formulas presented in this part can be applied to retrieve the mulipole coefficients of particles placed in a non-homogeneous environment as for particles in periodic arrays or near a substrate. Actually the influence of the nearby structure is hidden in the total field $\vec{E}_{tot}$, in the expression of the induced current density (2.107). $\vec{E}_{tot}$ contains both the incident plane wave excitation and the fields scattered or reflected from the neighboring structure toward the considered particle.

2.2.6.d Cross-sections calculation from the multipole coefficients

As in Mie theory, the scattering and extinction cross-sections can be obtained from the knowledge of the coefficients $a_{n,m}$ and $b_{n,m}$ computed from the $\mathcal{T}$-matrix or the direct multipole decomposition. Assuming an incident plane wave polarized along $\vec{e}_x$ and propagating along the $\vec{e}_z$ direction, we can write [8]:

$$\sigma_{scat} = \frac{\pi}{k^2} \sum_{n=1}^{\infty} \sum_{m=-n}^{n} (2n+1) \left(\left| a_{n,m} \right|^2 + \left| b_{n,m} \right|^2 \right) \tag{2.124}$$

$$\sigma_{ext} = \frac{\pi}{k^2} \sum_{n=1}^{\infty} \sum_{m=-1,+1} (2n+1) \Re \left(m a_{n,m} + b_{n,m} \right) \tag{2.125}$$

In addition, we can now introduce another quantity of interest: the differential scattering cross-section:

$$\sigma_d(\theta,\varphi) = \frac{dW_{scat}}{d\Omega} = \lim_{r \to +\infty} 4\pi r^2 \frac{\left| \vec{E}_{scat}(\vec{r}) \right|^2}{\left| \vec{E}_{inc} \right|^2} \tag{2.126}$$

where $d\Omega$ is the solid angle in the direction defined by θ and φ: $d\Omega = \sin\theta d\theta d\varphi$. This quantity is indicative of the power scattered in one direction of space.

Forward and backward scattering cross-sections can now be defined by considering the direction $\theta = 0$ and $\theta = \pi$ respectively. They provide the power scattered in these two directions and read [15]:

$$\sigma_{for} = \frac{\pi}{4k^2} \left| \sum_{n=1}^{\infty} \sum_{m=-1,+1} (2n+1) \left[m a_{n,m} + b_{n,m} \right] \right|^2 \tag{2.127}$$

$$\sigma_{back} = \frac{\pi}{4k^2} \left| \sum_{n=1}^{\infty} \sum_{m=-1,+1} (-1)^n (2n+1) [m a_{n,m} - b_{n,m}] \right|^2 \tag{2.128}$$

2.2.6.e Link between the cartesian and the spherical multipoles

The different projections presented thus far make it possible to obtain multipoles expressed in a spherical basis. For some specific problems however, depending on the geometry understudy, it may be more convenient to work in a cartesian basis. Both spherical and cartesian coordinates-based decompositions provide the same physical information. There exist relations for passing from one representation to the other as the multipole coefficients obtained in the spherical coordinates can be related to tensor elements in the cartesian coordinates.

In this manuscript, we use the simple set of projections recently presented in [10] to obtain the different multipole moments directly in the cartesian basis. Multipoles up to quadrupole order

can be calculated by:

$$p_\alpha = -\frac{1}{i\omega}\left[\iiint J_{s,\alpha}\, j_0(kr)\, dV + \frac{k^2}{2}\iiint \frac{j_2(kr)}{(kr)^2}[3(\vec{r}\cdot\vec{J}_s)r_\alpha - r^2 J_{s,\alpha}]\, dV\right] \tag{2.129}$$

$$m_\alpha = \frac{3}{2}\iiint \frac{j_1(kr)}{(kr)}(\vec{r}\wedge\vec{J}_s)_\alpha\, dV \tag{2.130}$$

$$Q^e_{\alpha\beta} = -\frac{3}{i\omega}\left[\begin{array}{l}\iiint \frac{j_1(kr)}{(kr)}\left[3(r_\beta J_{s,\alpha} + r_\alpha J_{s,\beta}) - 2(\vec{r}\cdot\vec{J}_s)\delta_{\alpha\beta}\right] dV \\ +2k^2\iiint \frac{j_3(kr)}{(kr)^3}[5r_\alpha r_\beta(\vec{r}\cdot\vec{J}_s) - (r_\beta J_{s,\alpha} + r_\alpha J_{s,\beta})r^2 - r^2(\vec{r}\cdot\vec{J}_s)\delta_{\alpha\beta}]\, dV\end{array}\right] \tag{2.131}$$

$$Q^m_{\alpha\beta} = 15\iiint \frac{j_2(kr)}{(kr)^2}\left(r_\alpha(\vec{r}\wedge\vec{J}_s)_\beta + r_\beta(\vec{r}\wedge\vec{J}_s)_\alpha\right) dV \tag{2.132}$$

where $\vec{p}$ and $\vec{m}$ are respectively the electric and magnetic dipole vectors and $\overleftrightarrow{Q}_e$ and $\overleftrightarrow{Q}_m$ the electric and magnetic quadrupole tensors. Contrarily to our adopted convention, the $e^{+i\omega t}$ convention was used in reference [10] to derive those projections and the induced electric current density therefore defined by: $\vec{J}_s(\vec{r}) = i\omega\varepsilon_0(\varepsilon_r - \varepsilon_h)\vec{E}_{tot}$. The subscripts α and β indicate the x, y or z component. As in equations (2.121) and (2.122), those expressions can be used for isolated particles as well as for particles in an inhomogeneous environment such as particles in a lattice or above substrates as they only require the knowledge of current distributions in the scatterer.

We want to emphasize here that compared to most works found in the literature, expressions (2.129, 2.130, 2.131, 2.132) were not derived using a classical Taylor expansion approach which assumes a long-wavelength approximation (particles small compared to the wavelength). On the contrary, they were obtained by converting the exact coefficients from the spherical to the cartesian coordinates and therefore constitute an accurate set of expressions valid for any range of wavelengths or particle sizes.

In cartesian coordinates, the scattered far-field is related to the first multipole moments through the expansion [10, 16]:

$$\vec{E}_{scat}(\vec{n}) = \frac{k_0^2}{4\pi\varepsilon_0}\frac{e^{ik_h r}}{r}\left[\vec{n}\wedge(\vec{p}\wedge\vec{n}) + \frac{1}{v_h}(\vec{m}\wedge\vec{n}) - \frac{ik_h}{6}\vec{n}\wedge(\vec{Q}_e\wedge\vec{n}) - \frac{ik_h}{6v_h}(\vec{Q}_m\wedge\vec{n})\right] \tag{2.133}$$

where

$$v_h = \frac{c}{n_h} \qquad\qquad k_h = \frac{2\pi}{\lambda}n_h \tag{2.134}$$

The three components of the vectors $\vec{Q}_e$ and $\vec{Q}_m$ are defined from the tensors by: $Q_\alpha = \sum_\beta Q_{\alpha\beta}\, n_\beta$ with $\vec{n} = \vec{e}_r$ being a unit vector indicating the considered direction of observation.

This section was devoted to the multipolar decomposition of the scattered field produced by an arbitrary particle. We have presented different relevant approaches to retrieve multipole coefficients. Depending on the situation, one can use the knowledge of either the scattered field or the induced electric current distribution in the scatterer to obtain the set of excited multipoles. The coefficients can be arbitrarily expressed in either spherical or cartesian coordinates depending on what the geometry of the problem is. The knowledge of the multipole coefficients provides a powerful tool to analyze optical properties or design nanoresonators.

2.3 Finite element method with COMSOL Multiphysics

Throughout this work we have used the RF module of the commercially available software COMSOL Multiphysics [17] to investigate light propagation through arbitrary 3D geometries. This module comes with different functionalities particularly suited for studying electromagnetic problems at the nanoscale. The software is based on the Finite Element Method (FEM). Therefore the

system understudy is first built in 3D and later discretized in a meshing step into a finite number of sub-domains called "elements". Tetrahedral elements are used as they are more convenient to discretize freely-shaped geometries. Then, appropriate boundary conditions need to be specified at the geometry boundaries. Finally, the software iteratively searches for approximate solutions to Maxwell's equations using the variational weak formulation of the Helmholtz propagation equations. The wave equations are solved for harmonic fields using a frequency domain study. It is important to underline here that COMSOL Multiphysics uses the $e^{+i\omega t}$ convention. Thus, the quantities extracted from COMSOL are later all complex conjugated in order to match the definitions of this manuscript.

A detailed presentation of the FEM methods or the COMSOL Multiphysics software is beyond the scope of this thesis. However, the following subsections are intended to briefly introduce the approaches and the boundary conditions used to set up our models, so that an interested reader would be able to understand how our full wave numerical results were obtained and even reproduce them in any FEM software. Additional informations can be found in the COMSOL Multiphysics user guide [18].

2.3.1 Meshing the simulation domain

The degree of refinement of a mesh is an important parameter in FEM simulation. With too few elements the solutions are poorly converged. On the other hand, if the meshing is too fine, the computational power and time might be higher than actually needed or might even exceed the computer capability. A guideline rule is to find at least five elements per wavelength to properly solve the wave propagation. The mesh has to be set thinner in a high refractive index structure compare to in a low index one, as the wavelength in this material is smaller. In addition, the mesh is in general refined closed to boundaries and corners in order to properly solve the effect occurring at those interfaces. We generally solve between 100 000 and 1 000 000 degrees of freedom depending on the complexity of the studied structure.

2.3.2 Scattered field formalism

The RF module offers the choice between two variables when solving Maxwell's equations: the scattered or the total field formalisms. The scattered field formulation is particularly well suited for problems of an isolated nanostructure in an homogeneous space. In this approach, a user-defined background field (such as a plane wave) corresponding to the excitation is specified. The known background field then becomes a source term and the software solves for the relative electric field only.

As the weight of the calculation increases with the size of the simulation domain it is often impossible to include the far-field regions in the simulation and only the field near the studied structure is in general obtained. However, COMSOL enables to directly retrieve the far field from the solved near field. The near to far field transformation is implemented based on the Stratton-Chu formula where the scattered far-field along a given direction is expressed as an integral of the near-fields over an arbitrary surface enclosing the scatterer [18]:

$$\vec{E}_{scat_{far}}(\vec{e}_r) = \frac{ik}{4\pi}\vec{e}_r \wedge \iint_{S'} \left[\vec{n} \wedge \vec{E}_{scat_{near}}(\vec{r'}) - \eta \vec{e}_r \wedge \left(\vec{n} \wedge \vec{H}_{scat_{near}}(\vec{r'}) \right) \right] e^{ik\vec{e}_{r'}\cdot\vec{e}_r} dS' \tag{2.135}$$

Where $\vec{n}$ is the unit vector normal to the surface S.

This functionality enables us to easily calculate far-field radiation diagrams from particles in homogeneous environments.

2.3.2.a Perfectly matched layers (PML)

To properly simulate light scattering in an unbounded host medium, it is of particular importance to avoid any kind of reflection at the boundary of the computational region. This can be

performed by surrounding the simulation domain with a perfectly matched layer (PML). This additional layer is used to strongly absorb the outgoing waves from the interior of a computational domain without reflection back into the interior. PMLs can be seen as a coordinate transformation of space that virtually stretches out the spatial domain in order to obtain an infinite optical path. In this work we used PMLs to truncate computational regions when studying scattering from isolated particles. An illustration of a set-up for simulating the scattering of a spherical particle can be found on Fig. 2.3-A.

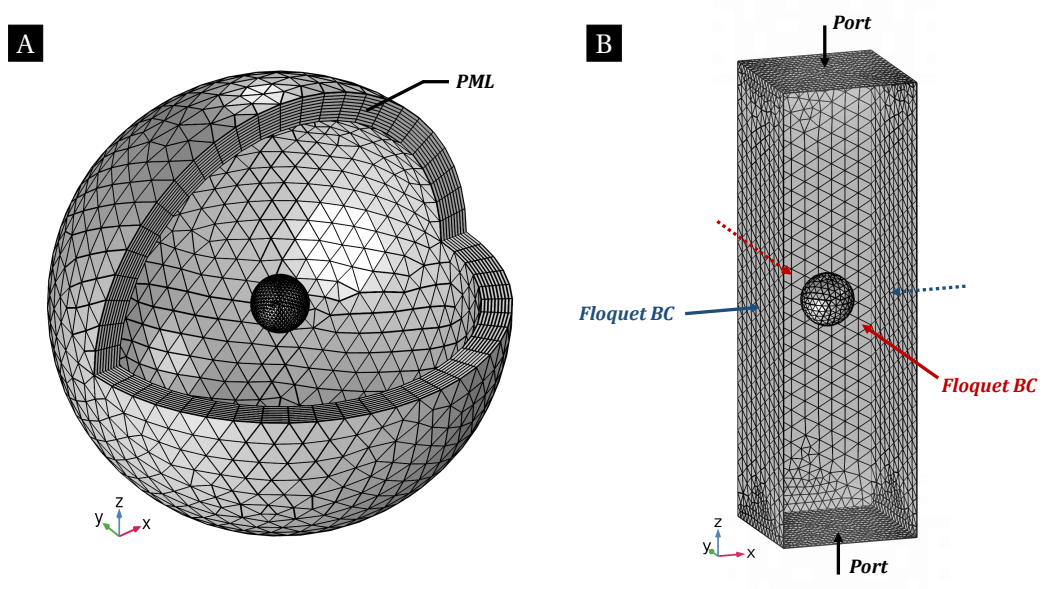

Figure 2.3 – Set-up of COMSOL models for studying A) an isolated scatterer in an infinite homogeneous environment truncated by use of PMLs on the border, B) a periodic array of identical particles. Two Floquet-Bloch periodic conditions reduce the study to a unit cell. Excitation of the structure by a plane wave is performed through one of the two implemented ports.

2.3.3 Modeling a periodic array of scatterers

The scattered field approach combined with PMLs is well-suited for studying the scattering from particles in unbounded media. However, it is not compatible with simulations where periodic boundaries are required such as infinite arrays of scatterers. Dealing with periodic structures, one needs instead to solve for the total field, using periodic Floquet-Bloch boundary conditions on a unit cell and exciting the structure via a port. This configuration is illustrated on Fig. 2.3-B which presents a set-up to simulate an infinite square array of spherical particles. The field scattered by the particle in this case can not be directly accessed in the model but can be later retrieved by subtracting the incident wave to the obtained total field solution.

2.3.3.a Floquet-Bloch periodic boundary conditions

Floquet-Bloch periodic boundary conditions allow to calculate the response of an entire infinite periodic system by simulating only one unit cell. Those conditions enable to copy the solutions at one edge of the simulation domain and to re-inject them at the opposite one while applying a phase correction to the fields. The Floquet-Bloch periodicity corresponds to the relation:

$$\vec{E}(\vec{r}+\vec{L}) = \vec{E}(\vec{r})\,e^{i\vec{k}\cdot\vec{L}} \tag{2.136}$$

where $\vec{L} = L_x\vec{e}_x + L_y\vec{e}_y$ is the lattice vector and where L_x and L_y are the spatial periodicity along x and y.

2.3.3.b Port excitation and S parameters

Using the total field formalism, incident excitations are introduced via ports at a boundary of the domain. The waves then travel from this boundary towards the studied structure. Ports serve as both input and output channels for energy. They are furthermore impedance matched so that no reflection occurs directly at the boundary. When only one port serves as an excitation, a scattering matrix is automatically computed describing the transmission and reflection of electromagnetic waves between the different ports of the domain. The S-parameters of a 2-port network will be introduced more in detail in chapter 4.1.3.d.

In addition, when port excitations are combined with periodic boundary conditions, COMSOL automatically computes the different diffraction orders and assigns a port to each order. Therefore the S-parameters enables one to discriminate between the energy emitted in the specular or diffracted orders.

2.3.4 Multipole decomposition in COMSOL Multiphysics

COMSOL Multiphysics was used to obtain multipole decompositions of particles in both homogeneous space and periodic arrays. A COMSOL model available online [19] served as a basis for the implementation of the decompositions presented in parts 2.2.6.a and 2.2.6.c. For periodic structures, only current based projections were implemented. These require the sole knowledge of the current densities in the particles that takes their origins from both the incident wave and the field produced by the other scatterers of the array. Therefore, the couplings between particles are fully taken into account in the multipole decomposition. For scatterers in homogeneous environments, scattered field based projections were also used to retrieve the multipole coefficients.

2.4 Concluding remarks

In this chapter, we have presented a number of theoretical and numerical tools as well as some important physical quantities, that we use in this thesis to study the light scattering properties of nano-objects. In the next chapter, Mie theory and its extension will indeed be applied to spherical and multilayered particles, and the $\mathcal{T}$-matrix method, to particle assemblies, in order to investigate the directional forward-scattering abilities of these objects.

We have also introduced the key concept of multipole expansion that provides a deep physical understanding of the optical response of a scatterer and constitutes an essential tool for engineering meta-atoms and metasurfaces. The next chapter will in particular reveal how unidirectional scattering originates from the interplay of different multipoles. Furthermore, the implementation of the projections presented in section 2.2.6, in the finite element software COMSOL Multiphysics will enable a retrieval of the excited multipoles of particles within periodic arrays, which will play a prominent role in the study of metasurfaces performed in chapter 4 and 5.

2.5 References

[1] J. D. Jackson, *Classical electrodynamics*. John Wiley & Sons, 2007. 31, 33

[2] C. F. Bohren and D. R. Huffman, *Absorption and scattering of light by small particles*. John Wiley & Sons, 2008. 31, 36, 37, 38

[3] Y.-l. Xu, "Electromagnetic scattering by an aggregate of spheres," *Applied optics*, vol. 34, no. 21, pp. 4573–4588, 1995. 37

[4] D. W. Mackowski, "Analysis of radiative scattering for multiple sphere configurations," *Proceedings of the Royal Society of London. Series A: Mathematical and Physical Sciences*, vol. 433, no. 1889, pp. 599–614, 1991. 37

[5] D. W. Mackowski and M. I. Mishchenko, "Calculation of the T-matrix and the scattering matrix for ensembles of spheres," *JOSA A*, vol. 13, no. 11, pp. 2266–2278, 1996. 37

[6] D. Mackowski and M. Mishchenko, "A multiple sphere T-matrix fortran code for use on parallel computer clusters," *Journal of Quantitative Spectroscopy and Radiative Transfer*, vol. 112, no. 13, pp. 2182–2192, 2011. 38

[7] D. W. Mackowski, "MSTM Version 3.0." http://eng.auburn.edu/users/dmckwski/scatcodes/. 38

[8] P. Grahn, A. Shevchenko, and M. Kaivola, "Electromagnetic multipole theory for optical nanomaterials," *New Journal of Physics*, vol. 14, no. 9, p. 093033, 2012. viii, 38, 40, 41

[9] P. Grahn *et al.*, "Multipole excitations in optical meta-atoms," Master's thesis, 2012. viii, 38, 39, 40

[10] R. Alaee, C. Rockstuhl, and I. Fernandez-Corbaton, "An electromagnetic multipole expansion beyond the long-wavelength approximation," *Optics Communications*, vol. 407, pp. 17–21, 2018. 38, 41, 42

[11] R. Alaee, C. Rockstuhl, and I. Fernandez-Corbaton, "Exact multipolar decompositions with applications in nanophotonics," *Advanced Optical Materials*, vol. 7, no. 1, p. 1800783, 2019. 38

[12] S. Mühlig, C. Menzel, C. Rockstuhl, and F. Lederer, "Multipole analysis of meta-atoms," *Metamaterials*, vol. 5, no. 2-3, pp. 64–73, 2011. 38

[13] S. Nanz, *Toroidal multipole moments in classical electrodynamics: An analysis of their emergence and physical significance*. Springer, 2016. 39

[14] L. Novotny and B. Hecht, *Principles of nano-optics*. Cambridge university press, 2012. viii, 39

[15] D. A. Powell, "Interference between the modes of an all-dielectric meta-atom," *Physical Review Applied*, vol. 7, no. 3, p. 034006, 2017. 41

[16] P. D. Terekhov, K. V. Baryshnikova, Y. A. Artemyev, A. Karabchevsky, A. S. Shalin, and A. B. Evlyukhin, "Multipolar response of nonspherical silicon nanoparticles in the visible and near-infrared spectral ranges," *Physical Review B*, vol. 96, no. 3, p. 035443, 2017. 42

[17] COMSOL, "Comsol multiphysics web page." https://www.comsol.com. 42

[18] COMSOL, "RF Module user's guide, version 5.4," 2018. 43

[19] COMSOL, "Multipole analysis of electromagnetic scattering." https://www.comsol.fr/model/multipole-analysis-of-electromagnetic-scattering-31901, 2018. 45

Chapter 3

Design of isotropic Huygens sources with colloidal particles

Contents

3.1 Kerker conditions . . . 48
3.1.1 Far field radiation of multipoles and phase symmetries . . . 48
3.1.2 Generalized Kerker condition . . . 49
3.2 Kerker condition with low index spherical particles [18] . . . 52
3.2.1 Dipolar Huygens sources . . . 52
3.2.2 Broadband Huygens sources . . . 56
3.3 Clusters of particles [18] . . . 59
3.3.1 Homogenization and effective medium theory . . . 60
3.3.2 Resonant dipolar Huygens sources with clusters . . . 61
3.3.3 Broadband multipolar Huygens sources . . . 65
3.3.4 Effect of voids, disorder and size polydispersity . . . 68
3.3.5 Conclusions . . . 70
3.4 Unidirectional scattering with multilayered particles . . . 70
3.4.1 Metallo-dielectric core-shells as ideal resonant dipolar Huygens sources . . . 70
3.4.2 All-dielectric core-shells . . . 73
3.5 Concluding remarks . . . 75
3.6 References . . . 76

Summary: In this chapter, we investigate the directional scattering abilities of different isotropic colloidal particles from the numerical point of view. In a first part, we illustrate how interferences between multipoles of opposite parity enable the cancellation of the backward scattering by particles. The Kerker condition leading to this Huygens source behaviour is then rigorously introduced. In a second part, we reveal that both resonant dipolar Huygens sources and extremely broadband forward directed scattering can be obtained considering simple spherical particles of low refractive index. As an alternative to such homogeneous spheres, we then demonstrate that composite particles made from homogeneously assembled small inclusions provide a greater flexibility in the design of Huygens sources, combined with better performances. After presenting the extended Maxwell-Garnett homogenization theory, we evidence how the control of the effective refractive index by the particle density allows us to engineer plasmonic and dielectric clusters as resonant and broadband Huygens sources for the visible domain. In a last part, we focus on multilayered particles. In particular, we present design guidelines to overlap the electric and magnetic dipole resonances of silver and gold based metallo-dielectric core-shells. Finally all-dielectric core-shells behaving as broadband Huygens sources are investigated.

3.1 Kerker conditions

3.1.1 Far field radiation of multipoles and phase symmetries

In chapter 2.2.2.c, we saw that the electric field scattered by a localized electromagnetic source distribution can be expressed through the following sum:

$$\vec{E}_s(r,\theta,\varphi) = E_0 \sum_{n=1}^{\infty} \sum_{m=-n}^{n} A_n \left[\frac{1}{k} a_{n,m} \vec{\nabla} \wedge \left(h_n^{(1)}(kr) \vec{X}_{n,m}(\theta,\varphi) \right) + b_{n,m} h_n^{(1)}(kr) \vec{X}_{n,m}(\theta,\varphi) \right] \tag{3.1}$$

Such a multipole expansion constitutes a particularly interesting tool in the understanding and design of radiating systems. It provides insight into the radiation of light by an arbitrary structure. The complex electromagnetic response of an object is thus expressed as a superposition of fields created by a set of simple point multipoles presenting well-known scattering patterns and properties.

In Fig. 3.1, we show schematically the far-field radiation diagram and phase symmetries of the first electric and magnetic multipoles up to the octupoles. The plotted differential scattering cross-sections were calculated in the framework of Mie theory, as detailed in the Appendix A.3, assuming an $\vec{e}_x$ polarized incident plane wave propagating along the $\vec{e}_z$ direction. Each multipole of a particular order exhibits a radiation pattern with a specific geometry. Dipoles present a toroidal radiation, with a zero in intensity along the excitation direction and a maximum isotropic radiation observed in the perpendicular plane. The quadrupoles exhibit a scattering mainly confined in four directions of space, while the octupoles show a scattering pattern with six lobes. Higher order multipoles exhibit a progressively increasing number of lobes, and as a result an angular distribution of the scattered intensity that increases in complexity.

An important feature of electromagnetic multipoles that becomes essential for the study of multipolar interferences and directional scattering, is the phase symmetry of their far-field radiation. It turns out that the radiated fields show different phases in the forward and backward directions with respect to the incident wave. It can be seen on Figs. 3.1-A,B that the electric dipole radiation shows even parity (in electric field) while the magnetic dipole radiation shows odd parity, for which the radiated electric fields in the forward and backward directions are respectively in and out of phase. Regarding the higher order multipoles, both the electric quadrupole and magnetic octupole produce an odd-type pattern, while an even-type response is generated by the magnetic quadrupole and electric octupole terms.

As underlined in [1], the symmetries of the scattered fields originate from the spatial inversion behavior of the spherical harmonics:

$$Y_{n,m}(\pi-\theta,\varphi+\pi) = (-1)^n Y_{n,m}(\theta,\varphi) \tag{3.2}$$

that flip sign or not depending on the order n. In equation (3.1), each vector spherical harmonic $\vec{X}_{n,m}$ and $\vec{\nabla} \wedge \vec{X}_{n,m}$ exhibit respectively the same and opposite parity compare to their associated spherical harmonics $Y_{n,m}$. Therefore multipoles exhibiting radiation of even parity are those associated to the moments $a_{n,m}$ with odd values of n, and $b_{n,m}$ with even values of n. On the contrary, radiation of odd parities happen for multipoles associated to $a_{n,m}$ and $b_{n,m}$ coefficients with respectively even and odd values of n.

In summary, the phase symmetries follow a simple rule: the scattering parities are opposite for multipoles of same nature and adjacent order (for example even parity for the electric dipole and odd parity for the electric quadrupole), and for multipoles of same order but different nature (for example even for the electric octupole and odd for the magnetic octupole). We stress here that we discuss the parities in terms of electric fields, but reversed parities would be true in terms of magnetic fields, as can be seen on Fig. 3.1, due to the electromagnetic duality.

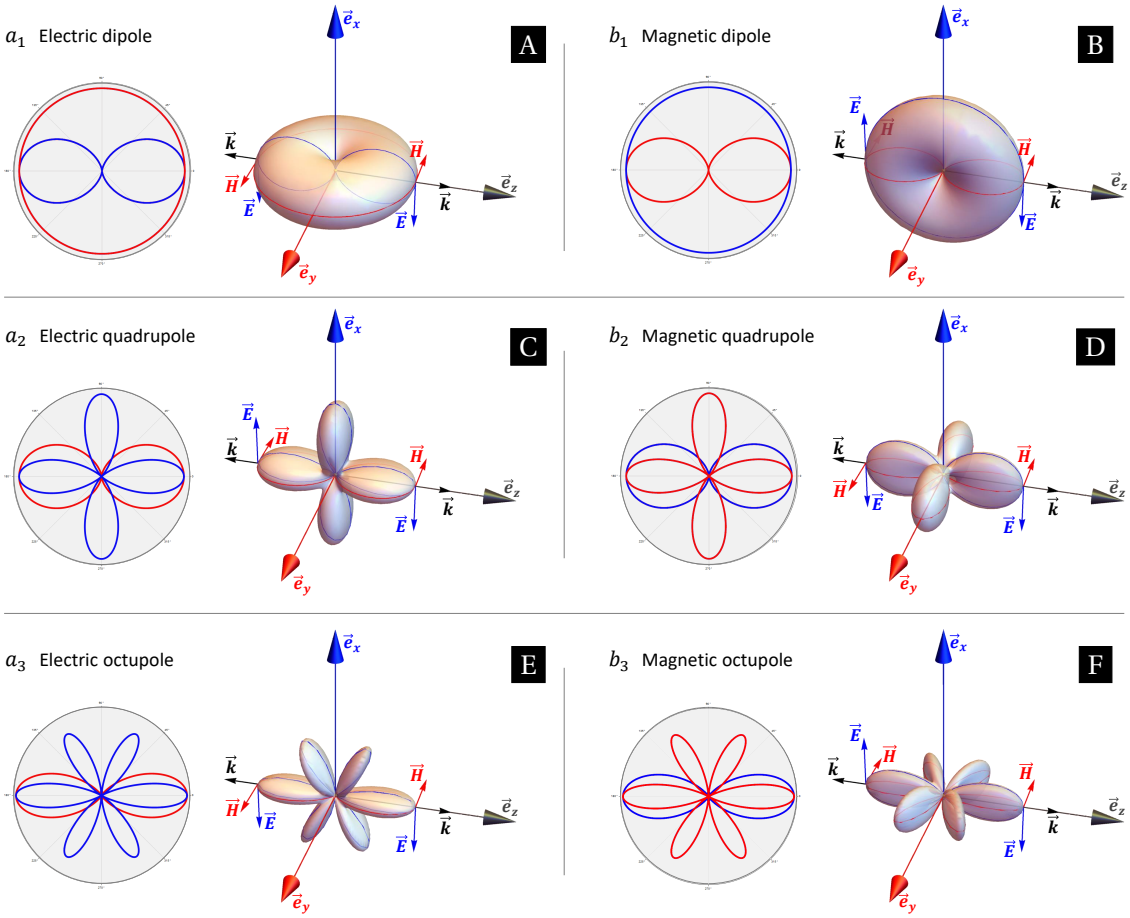

Figure 3.1 – 3D radiation diagrams of the first multipoles under $\vec{e}_x$ polarized incident plane wave. The blue (red) 2D cuts show the radiation pattern in the electric (magnetic) plane. The electromagnetic field orientation is indicated by the blue and red arrows in both the forward ($\theta = 0°$) and backward ($\theta = 180°$) directions.

We emphasize that in the rest of this manuscript, we will use the terms "even multipoles" and "odd multipoles" to refer to the symmetry of their radiation patterns.

3.1.2 Generalized Kerker condition

Interference effects between the fields emitted by different induced multipoles explain the scattering diagram of resonators. When taken individually, each multipole radiates within perfectly identical proportions in the two half spaces located towards the front and the back (all diagrams being symmetrical with respect to the plane $(\vec{e}_x, \vec{e}_y)$ on Fig. 3.1), the combined excitation of multipoles of opposite parity strongly affects the directionality of the radiation and can even lead to unidirectional scattering. From Fig. 3.1, it can be intuitively understood that suppression of radiation in the backward direction can be achieved whenever the combined strength of multipolar modes of a certain parity, matches that of the opposite parity.

To illustrate this, Fig. 3.2-A shows the 3D distribution of the far field scattering intensity obtained by superimposing in phase electric and magnetic dipoles of same magnitude (in terms of total scattered power). This combination of multipoles displays a pronounced asymmetric radiation that takes the shape of a cardioid pattern with the scattering concentrated in the half forward space ($z > 0$). It is maximum for $\theta = 0$ along the direction of the incident wave where the radiated fields interfere constructively, while in the opposite direction, for $\theta = 180°$, since the two dipoles emit fields of opposite sign, the scattering is totally suppressed. This combination of two dipoles

constitutes the simplest implementation of a Huygens source, *i.e.* a punctual source that exhibits forward-scattering as used in the Huygens Fresnel principle.

Based on the same interference process, similar Huygens source features are observed on Figs. 3.2-B,C corresponding to the simultaneous excitation of the two quadrupoles and the two octupoles of same magnitude and phase respectively. The figures reveal in both cases an azimuthally symmetric forward directed scattering pattern. The radiation is totally suppressed in the backward direction $\theta = \pi$. In addition, comparing the different radiation patterns, it can be seen that the angular beam width is significantly narrowed for couples of multipoles of increasing order resulting in an enhanced directionality of the forward scattering [2, 3]. However, for quadrupoles and octupoles (and pairs of higher order modes) significant side scattering lobes are observed on the back half space arising as a trade off for the better forward angular directionality.

It is clear that suppression of backward scattering can be obtained not only for perfectly matched pairs of multipoles of same order, as presented so far, but also for pairs of multipoles of same nature but with different orders, by combining an electric dipole and an electric quadrupole for example, and more generally for even more complex combinations of multipoles of opposite parity.

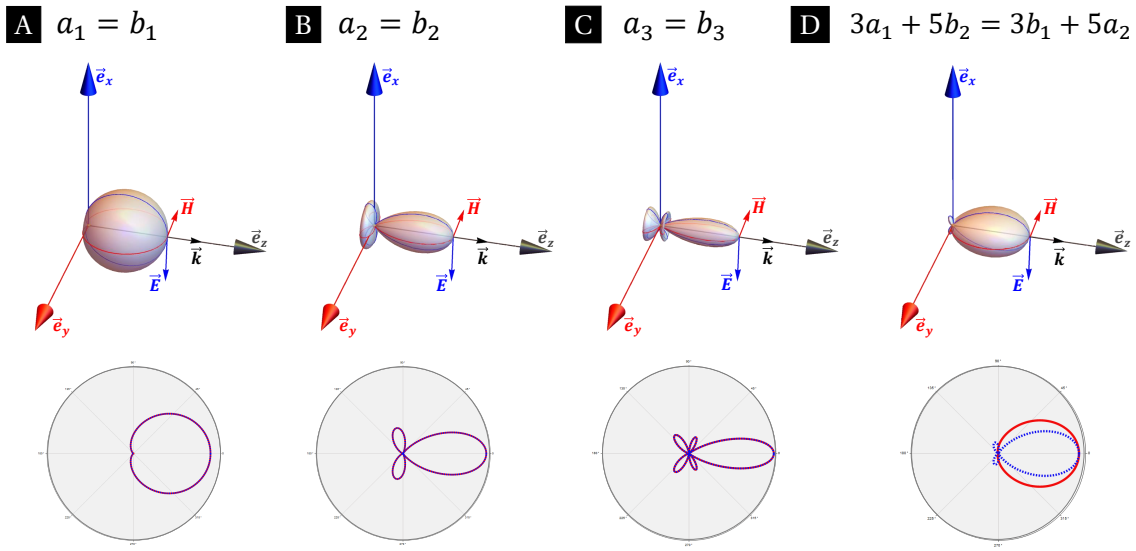

Figure 3.2 – 3D and 2D scattering radiation diagrams under an $\vec{e}_x$ polarized incident plane wave for A) a pair of electric and magnetic dipoles, B) quadrupoles C) octupoles, with same magnitude and phase, and D) for a combination of dipoles and quadrupoles satisfying the Kerker condition $3a1+5b2 = 3b1+5a2$. The blue (red) 2D cuts show the radiation pattern in the electric (magnetic) plane. The electromagnetic field orientation in the forward ($\theta = 0°$) direction is indicated by the blue and red arrows.

In fact, the rigorous condition to obtain zero back-scattering along the $\theta = \pi$ direction, can be derived for any combination of multipoles by simply cancelling σ_{back}, which in the case of an incident plane wave polarized along $\vec{e}_x$ involving only multipoles of degree $m = \pm 1$, and propagating along $\vec{e}_z$, is given by equation (2.128). Cancelling this expression leads to:

$$\sum_{n=1}^{\infty} \sum_{m=-1,+1} (-1)^{n+1}(2n+1)m a_{n,m} = \sum_{n=1}^{\infty} \sum_{m=-1,+1} (-1)^{n+1}(2n+1) b_{n,m} \tag{3.3}$$

This equation (3.3) is known as the generalized first Kerker condition. It is so named in reference to the pioneering work of Kerker *et al.* [4] who first revealed the possible cancellation of the back-scattering by interference between electric and magnetic modes for particles of magnetic permeability $\mu = \varepsilon$. In the rest of this manuscript, we will refer to eq. (3.3) as "the Kerker condition" since the second generalized Kerker condition that cancels the forward-scattering is not considered in this work.

Splitting the even and odd multipoles in eq. (3.3), the Kerker condition takes the following convenient form:

$$\sum_{n=1}^{\infty} \mathcal{O}_n = \sum_{n=1}^{\infty} \mathcal{E}_n \tag{3.4}$$

with

$$\sum_{n=1}^{\infty} \mathcal{E}_n = \sum_{n=1}^{\infty} \sum_{m=-1,+1} m(4n-1)a_{2n-1,m} + \sum_{n=1}^{\infty} \sum_{m=-1,+1} (4n+1)b_{2n,m} \tag{3.5}$$

$$\sum_{n=1}^{\infty} \mathcal{O}_n = \sum_{n=1}^{\infty} \sum_{m=-1,+1} (4n-1)b_{2n-1,m} + \sum_{n=1}^{\infty} \sum_{m=-1,+1} m(4n+1)a_{2n,m} \tag{3.6}$$

being respectively a weighted sum of odd and even multipoles. Expression (3.4) properly translates the required balance between even and odd multipoles for the unidirectional forward scattering to occur.

For scatterers possessing mirror symmetries with respect to the planes of normal $\vec{e}_x$ or $\vec{e}_y$, such as isotropic particles, the coefficients with $m = 1$ and $m = -1$ satisfy [5]:

$$\begin{cases} a_{n,1} = -a_{n,-1} = a_n \\ b_{n,1} = b_{n,-1} = b_n \end{cases} \tag{3.7}$$

In this case, as can be derived in the framework of Mie theory, the Kerker condition is simply:

$$\sum_{n=1}^{\infty} (-1)^{n+1}(2n+1)a_n = \sum_{n=1}^{\infty} (-1)^{n+1}(2n+1)b_n \tag{3.8}$$

which reads, for the first multipoles:

$$3a_1 + 5b_2 + 7a_3 + 9b_4 + ... = 3b_1 + 5a_2 + 7b_3 + 9a_4 + ... \tag{3.9}$$

From equation (3.8) it is obvious that the Kerker condition is met for the particular case presented before when two multipole moments of same order are solely excited and equal, that is for any n:

$$a_n = b_n \tag{3.10}$$

On the other hand, we show on Fig. 3.2-D the scattering diagram obtained for a complex combination of dipoles and quadrupoles satisfying the Kerker condition $3a_1 + 5b_2 = 3b_1 + 5a_2$. Forward directed scattering is indeed observed and a breaking in the azimuthal symmetry of the diagram occurs due to the different amplitudes taken by the multipoles of same order as $a_1 \neq b_1$ and $a_2 \neq b_2$ in this case.

To conclude, the proper understanding and design of the induced multipole moments of a structure is important to tailor its radiation pattern. In this chapter we present how the Kerker condition can be approached for different systems consisting in homogeneous spheres, multilayered spherical particles and clusters of particles. The interesting feature of these systems is that they could be realistically achievable through colloidal synthesis and self-assembly.

Although we focus here on obtaining Huygens source features, the interference effects and phase analysis of multipoles can be extended to a wide range of applications.

It is for instance applicable to other scattering angles [6]. In particular, at $\theta = 0$, a suppression (or rather a minimization) of the forward scattering can be reached under the so-called second Kerker condition [7–10] (that can be derived by canceling σ_{for} given by eq. (2.127)):

$$\sum_{n=1}^{\infty} \sum_{m=-1,+1} (2n+1)\left[m a_{n,m} + b_{n,m}\right] = 0 \tag{3.11}$$

It is also possible to simultaneously cancel the forward and backward scattering as recently revealed [11–14]. Since in this case the radiation is only found in the lateral lobes, this effect is also referred to as “transverse Kerker effect”.

Finally, to give an example other than far field directional radiation possibilities, the engineering of multipole resonances has recently enabled the design of Janus sources [15–17], particles providing side-dependent near field-coupling to wave-guides, which may find applications in photonic circuitry.

Therefore, obtaining Huygens sources constitutes only one of the main aspects of the scattering manipulation permitted by multipole tailoring.

3.2 Kerker condition with low index spherical particles [18]

Recently, dielectric particles of high refractive index have been shown to exhibit strong magnetic resonances in the visible and near infrared range, reaching amplitudes comparable or even stronger than their electric counterparts [19–21]. The Mie magnetic resonances originate from the excitation of circular displacement currents in the particles. Mie type resonances are morphology dependant since they are functions of both the size and shape of the particles. The first excited multipole, as the wavelength is decreased, corresponds to a magnetic dipole and occurs when the wavelength inside the particle becomes comparable to its spatial dimension: $2R \approx \lambda/N$.

Since they can support both electric and magnetic multipoles, dielectric particles are particularly interesting for the realization of Huygens sources. Indeed, directional forward scattering abilities of high index particles have been demonstrated in various works, in the microwave range [22] and visible domain with silicon (Si) spheres [23] and gallium arsenide ($GaAs$) pillars [24] for example. However, in these works, the suppression of the back-scattering was achieved at a single frequency and fulfilled off resonance, generally on the tail of the two dipolar modes, leaving a weak forward scattering. This is due to the fact that resonances of opposite parity are in general spectrally detuned for high index particles.

To overcome this efficiency and bandwidth issue, one should rather seek to obtain perfectly degenerated multipoles of same order, fulfilling the first Kerker condition over a large spectral range including that where the resonances are maximum, leading to a significant forward directed scattering by the particle. The spectral overlap of the multipoles can be reached for instance by tuning the particle geometry which allows for a fine tailoring of the different modes. Geometrical tuning of dielectric particle resonances has been extensively studied in the literature and resonant Huygens sources have been proposed or demonstrated on this principle with disks [25–27], ellipsoids [28, 29], nanobars [30, 31], dimers [32, 33], etc ...

In contrast, in the following, we investigate the possibility of obtaining the resonant Kerker effect with simple dielectric spheres. In particular, we show that low index dielectric particle can exhibit comparable resonant electric and magnetic multipoles of same order approximately meeting the Kerker condition over a broad spectral band. Due to the spherical geometry, the properties obtained are intrinsically polarization independent. Such simple particles could therefore constitute an interesting alternative to the previously mentioned anisotropic Huygens scatterers.

3.2.1 Dipolar Huygens sources

As we have seen in section 2.2.4.a, the Mie scattering coefficients of the electric and magnetic multipoles that describe the behavior of a spherical particle of radius R and refractive index N are given by [34]:

$$a_n(\gamma, x) = \frac{\gamma\Psi_n(\gamma x)\Psi'_n(x) - \mu\Psi_n(x)\Psi'_n(\gamma x)}{\gamma\Psi_n(\gamma x)\xi'_n(x) - \mu\xi_n(x)\Psi'_n(\gamma x)} \tag{3.12}$$

$$b_n(\gamma, x) = \frac{\mu\Psi_n(\gamma x)\Psi'_n(x) - \gamma\Psi_n(x)\Psi'_n(\gamma x)}{\mu\Psi_n(\gamma x)\xi'_n(x) - \gamma\xi_n(x)\Psi'_n(\gamma x)} \tag{3.13}$$

with $\Psi_n(x) = x j_n(x)$ and $\xi_n(x) = x h_n^{(1)}(x)$ being the Riccati-Bessel functions. The Mie coefficients are functions of both the dimensionless size parameter $x = 2\pi n_h R/\lambda$ and the refractive index contrast between the particle and its host medium $\gamma = N/n_h$.

We start by exploring the best performances, in terms of total scattering efficiency, that can be reached by a lossless dielectric sphere under the Kerker condition. We focus on reaching the Kerker condition resonantly with a pair of multipoles of the same order, since this approach suits to dielectric spheres whose pairs of resonances of increasing order are successively excited spectrally. In order to get a Huygens multipole of order n exhibiting zero back-scattering, the condition $a_n = b_n$ must be satisfied. Three particular solutions satisfying this condition can be identified and are detailed in the following:

(i) The first solution corresponds to the case where $\mu = m$. In the situation where in addition $\varepsilon_h = 1$ for the host medium, the solution simply imposes a dual material $\varepsilon = \mu$. This requirement enabling $a_n = b_n$ to be met for every n simultaneously and for any value of x (i.e. on the whole spectrum for a given size of particle) was first underlined by Kerker *et al.* in their pioneer work [4]. It simply implies that the particle impedance is matched to that of the host medium. However, since $\mu = 1$ at optical frequencies for all natural materials, the absence of magnetic materials makes it impossible for this condition to be met with simple spherical particles.

(ii) The second solution is found when $\Psi'_n(\gamma x) = 0$ and leads to $a_n = b_n = \Psi'_n(x)/\xi'_n(x)$. Due to the periodicity of Bessel's functions, $\Psi'_n(x)$ exhibits multiple zeros that we denote as $\Psi'_{n,l}$. The most relevant solution is the one obtained for the highest γx value, *i.e.* for $\gamma x = \Psi'_{n,1}$, the first zero of the first derivative of the Riccati-Bessel function Ψ_n.

(iii) Similarly, $\Psi_n(\gamma x) = 0$ leads to $a_n = b_n = \Psi_n(x)/\xi_n(x)$. Since Ψ_n has the same zeros as the spherical Bessel function j_n, this solution is satisfied whenever $\gamma x = j_{n,l}$, with $j_{n,l}$ the l_{th} root of j_n.

The first zeros of the derivative of the Riccati-Bessel function and the spherical Bessel function, $\Psi'_{n,1}$ and $j_{n,1}$ respectively, are provided by the table on Fig. 3.3 for the first four orders, indicating the value of γx at which the Kerker conditions (ii) and (iii) are met for the pair of multipoles. It can be seen that for increasing γx, condition (ii) occurs before condition (iii).

n	1	2	3	4
$\psi'_{n,1}$	2.744	3.871	4.973	6.062
$j_{n,1}$	4.493	5.763	6.987	8.183

Figure 3.3 – First zeros of $\Psi'_{n,1}$ and $j_{n,1}$ for the first four multipoles

The scattering efficiency $Q_n(x)$ of the n_{th} multipole is given by (see subsection 2.2.6.d):

$$Q_n(x) = \frac{2(2n+1)}{x^2}\left[|a_n|^2 + |b_n|^2\right] \tag{3.14}$$

We denote by $Q_n^{(ii)}$ and $Q_n^{(iii)}$ the scattering efficiencies of the n_{th} multipole under condition (ii) and (iii) respectively. These efficiencies are parametrized by γ as follows:

$$Q_n^{(ii)} = \frac{4\gamma^2(2n+1)}{\Psi'^2_{n,1}}\left|\frac{\Psi'_n\left(\Psi'_{n,1}/\gamma\right)}{\xi'_n\left(\Psi'_{n,1}/\gamma\right)}\right|^2 \tag{3.15}$$

$$Q_n^{(iii)} = \frac{4\gamma^2(2n+1)}{j_{n,1}^2}\left|\frac{\Psi_n\left(j_{n,1}/\gamma\right)}{\xi_n\left(j_{n,1}/\gamma\right)}\right|^2 \tag{3.16}$$

Figure 3.4 shows the evolution of both $Q_n^{(ii)}$ and $Q_n^{(iii)}$ as a function of the contrast index γ, for the first four multipolar orders.

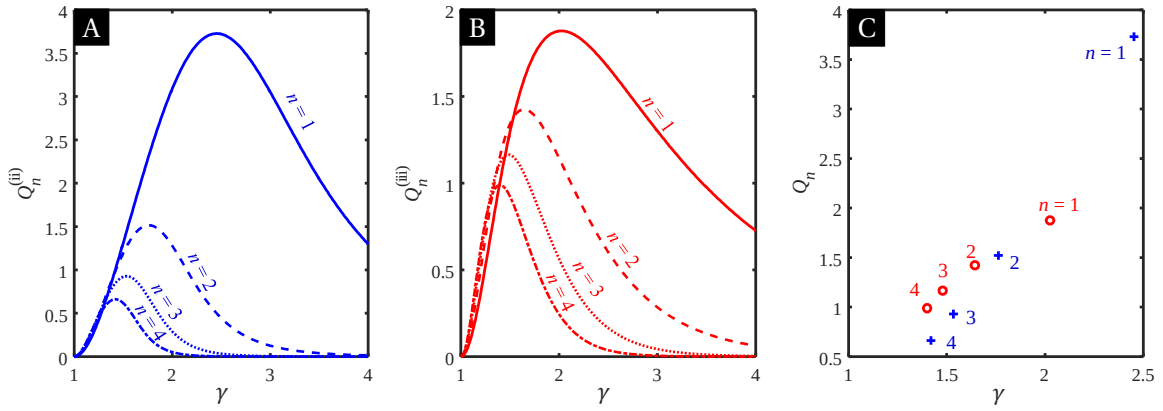

Figure 3.4 – Multipole efficiencies of generalized Huygens sources. A) and B) Graph plotting respectively $Q_n^{(ii)} = f(\gamma)$ and $Q_n^{(iii)} = f(\gamma)$ for $n = 1,...,4$. $Q_n^{(ii)}$ and $Q_n^{(iii)}$ are the scattering efficiency of the n^{th} multipole pair under respectively condition (ii) and (iii). C) Graph marking the (Q,γ) coordinates of the maximum efficiencies $Q_{n,max}^{(ii)}$ and $Q_{n,max}^{(iii)}$. Blue crosses (red rings) show the positions of the maxima of the first four multipoles under condition (ii) (and (iii) respectively).

It can be seen on Figs. 3.4-A,B that for any order n, there exists an optimal efficiency $Q_{n,max}^{(ii)}$ and $Q_{n,max}^{(iii)}$. The maximal efficiency is reached in the dipolar case under condition (ii) (see Fig. 3.4-C). As already noticed in [28, 35] it reaches a value of $Q^* \approx 3.72$, obtained when $\gamma = \gamma^* \approx 2.455$, with the corresponding size parameter $x = x^* = \Psi'_{n,1}/\gamma^* \approx 1.118$. This situation is detailed on panel A of Fig. 3.5, showing how the total scattering efficiency of a sphere evolves as a function of the size normalized wavelength $1/x = \lambda/2\pi R n_h$, when $\gamma \approx 2.455$.

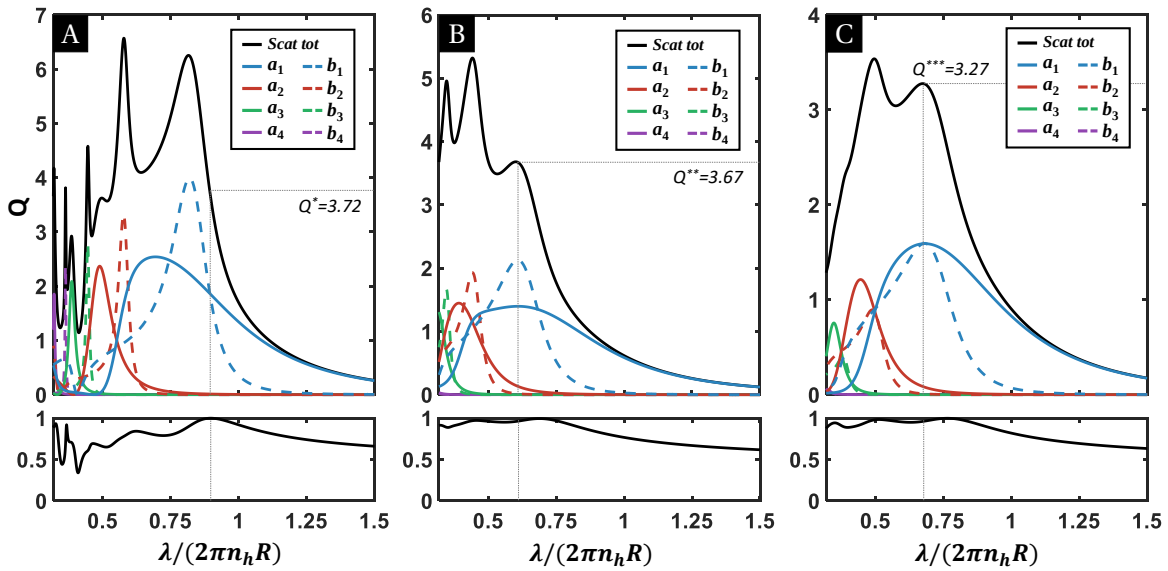

Figure 3.5 – Three cases of scattering efficiency and forward to backward scattering ratio for a dielectric sphere of constant index. On top panels, the black solid curve represents the total scattering efficiency of the sphere as a function of the parameter $1/x$. The solid (dashed) colored lines are the scattering efficiencies of the electric (magnetic) multipoles. The bottom panels indicate the fraction of energy $\sigma_{for}/(\sigma_{for}+\sigma_{back})$ scattered in the forward direction. A),B) Scattering efficiencies of a lossless dielectric sphere for respectively $\gamma = \gamma^* = 2.455$ and $\gamma = \gamma^{**} = 1.87$. C) Scattering efficiencies of a lossy dielectric sphere with $\gamma = \gamma^{***} = 2.1 + 0.095i$.

It should be mentioned that the dimensionless parameter x constitutes a scaling factor that keeps the particle properties unchanged (for a constant index contrast γ). Therefore the plots are fully scalable in wavelength by simply adjusting the particle size R.

The Fig. 3.5-A clearly evidences that for the optimal configuration, the Kerker condition does not occur at the resonance frequency of either dipole. In addition, the fraction of scattered energy emitted in the forward direction $\left(\sigma_{for}/(\sigma_{for}+\sigma_{back})\right)$, plotted on the bottom panel of the figure, peaks at 100% for $1/x^* = 0.894$ but rapidly decreases as $1/x$ deviates from this value. As already mentioned in the introduction of this part, this single operating wavelength is due to the spectral detuning between the two dipoles that prevents their respective moments a_1 and b_1 to take similar phase values except far from both resonance wavelengths, on the tail of the scattering cross-section peak.

Since the Kerker condition can not rigorously be met at the resonance frequencies of the dipoles for an optimal efficiency, we now relax the required condition that $a_1 = b_1$ and we seek the optimal efficiency ensuring $x_{a_1} = x_{b_1}$. x_{a_1} and x_{b_1} are defined as the reduced resonant frequencies corresponding to the position of the maximum of the electric and magnetic dipole scattering efficiencies $Q_{max}(a_1)$ and $Q_{max}(b_1)$. The positions of these maxima do not always correspond to those of the coefficients $|a_1|$ and $|b_1|$, but are close enough so that the two dipoles spectrally coincide with $a_1 \approx b_1$ close to the resonances. The optimal situation is obtained for $\gamma = \gamma^{**} \approx 1.87$. The corresponding scattering efficiencies are shown in Fig. 3.5-B. We see that a maximum efficiency of 3.67 is reached for this pair of dipoles. Not all the scattering occurs in this case in the forward direction mostly due to the mismatch in amplitude $|a_1| \neq |b_1|$ between the electric and magnetic dipoles and to the non-zero contribution of the electric quadrupole, which slightly contributes to the balance between even and odd multipoles. However, a large fraction (> 95%) is still scattered forward at $1/x^{**} \approx 0.61$. In contrast with the previous case, the ratio of forward scattering exhibits a value above 90% on nearly the whole range covered by the dipolar resonances.

Finally, this situation can be even bettered by considering a lossy system. Indeed, since the magnetic dipole mode has a stronger interaction with the particle medium than does the electric dipole mode, losses decrease in higher proportion the scattering amplitude of the magnetic dipole, making it possible for the two dipoles to scatter with the same amplitude.

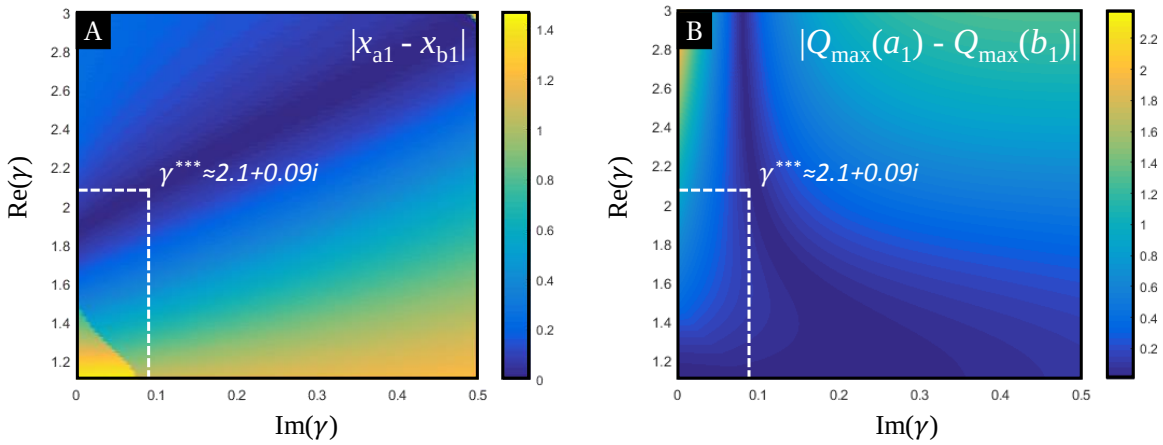

Figure 3.6 – Optimal value of γ in the complex plane for equal amplitudes and frequencies of the electric and magnetic dipole scattering cross-sections. A) The color plot shows the dependence of $|x_{a_1} - x_{b_1}|$, which is the reduced frequency detuning between electric and magnetic dipole resonances. B) color plot $|Q_{max}(a_1) - Q_{max}(b_1)|$, the difference in amplitude of the scattering efficiency at the position of the electric and magnetic dipoles cross-section maxima. The position of γ where both conditions are approximately zero is indicated on the color-map.

On Fig. 3.6 we explore the complex plane with γ, and seek to minimize simultaneously $|x_{a_1} - x_{b_1}|$

which ensures identical frequencies, as well as $\left|Q_{max}(a_1) - Q_{max}(b_1)\right|$, which ensures equal resonance amplitudes. The position γ^{***} that allows both scattering maxima to appear at the same frequency and with equal amplitudes, is indicated by the dashed white lines and is approximately equal to $2.1 + i0.09$.

This situation is further detailled on Fig. 3.5-C showing the evolution of the total scattering efficiency as a function of the size normalized wavelength x. It can be seen that the maximum scattering efficiency reached in this case is $Q^{***} = 3.2$, which is still almost 86% of the value reached when $\gamma = \gamma^*$. In addition, as in the previous case, more than 95% of the scattering occurs in the forward direction at the position of the maximum of the scattering efficiency Q^{***}.

To conclude, the study presented in this part has revealed that pairs of multipoles leading to the optimal efficiency of forward scattering are not resonantly excited for simple dielectric spheres. However, by relaxing the rigorous Kerker condition, resonant Huygens dipoles can be approached with both lossless and lossy particles, for index contrasts approaching respectively 1.9 and $2.1 + 0.1i$. This results in an important fraction of forward scattering obtained at the position of the local maximum of the scattering cross-section of the particles.

3.2.2 Broadband Huygens sources

In the previous part, we have focused on optimizing Huygens dipole scattering. However, for numerous applications, it may be interesting to maximize the forward scattering over a broad range of wavelengths. As we have seen, given a specific size and value of γ, the Kerker condition cannot be fulfilled exactly for all pairs of multipoles at once when $\mu = 1$. However we will show that by relaxing the requirement that the electric multipole be exactly equal to the magnetic one of same order, and just satisfying the condition loosely, *i.e.*, for all n, to obtain $a_n \sim b_n$, a broadband isotropic system may be reached with two by two overlapped multipoles.

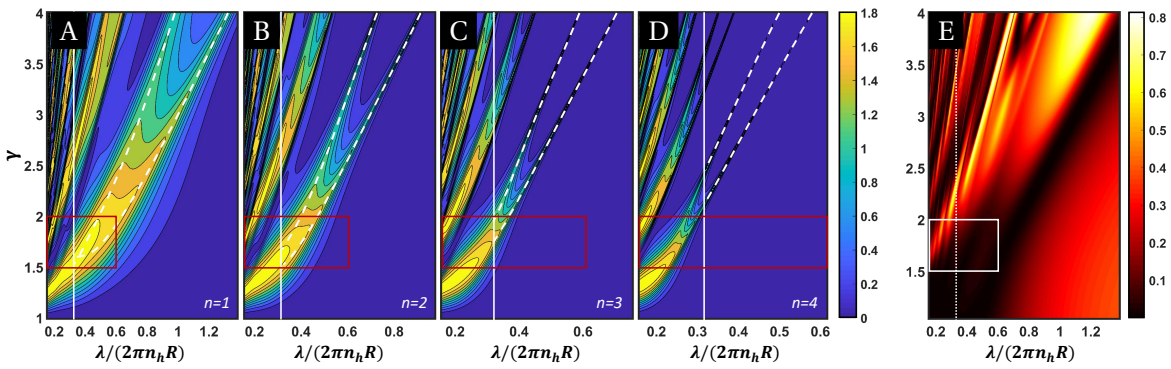

Figure 3.7 – A)-D) Each panel is a contour map of $\left|a_n\right|^2 + \left|b_n\right|^2$ for respectively $n = 1$, $n = 2$, $n = 3$ and $n = 4$, revealing the trajectories taken by the electric and magnetic multipoles in the $(\gamma, 1/x)$ plane. For any n, the white dashed curves giving $\Re(a_n) = 0$ and $\Re(b_n) = 0$, trace the position of the two resonances. The magnetic resonance is the one found at highest values of $1/x$. The vertical white line corresponds to the limit of subwavelength particles $R = \lambda$ for $n_h = 1$ *i.e.* $1/x = 1/\pi \approx 0.32$. E) Fraction of energy scattered in the backward direction $\sigma_{back}/(\sigma_{for} + \sigma_{back})$. The white box (reported in red on the other panels) indicates a region that shows a rather broadband nearly null back-scattering covering the first resonances of the particle. The box is arbitrarily delimited with an index contrast of 2 and 1.5 (for which the resonator is not subwavelength anymore).

On Figs. 3.7-A,B,C and D, we examine the trajectories taken by the scattering resonances of the electric a_n and magnetic b_n coefficients up to order 4 in the (γ,x) plane for lossless spherical particles. It can be seen that, while they remain well separated for large values of index contrast, resonances of same orders all bundle together towards lower values of the reduced wavelength $1/x$ as γ becomes smaller than 2. This is apparent on the figures from both the strong enhancement of the quantity $\left|a_n\right|^2 + \left|b_n\right|^2$ that is observed at low values of γ, as well as from the convergence of the

two dashed white lines corresponding to the trajectories of $\Re(a_n) = 0$ and $\Re(b_n) = 0$. It should be mentioned that for lossless particles, the upper bound of the modulus of the Mie coefficients is 1, achieved at the resonance of the particles for which the real part of the coefficient is canceled and the imaginary part is unitary. Therefore the yellow areas in Fig. 3.7, indicating multipoles having nearly equal maximum amplitudes and satisfying the condition that $|a_n|^2 \sim |b_n|^2 \sim 1$, is a good indicator of spectrally merging resonances.

The visible evolution toward an approximate overlapping of the multipoles of same order results mostly from the drop in the resonance quality factor with the decrease of the index contrast. While resonance peaks are sharp and spectrally well defined for high index particles, with the sum $|a_n|^2 + |b_n|^2$ reaching the approximate value of $|a_n|^2 \sim 1$ and $|b_n|^2 \sim 1$ at their position, the multipoles and in particular the electric ones undergo significant spectral broadening as the index contrast decreases, responsible for their spectral merging.

Moreover for decreasing values of γ, an increasing number of multipoles tend to overlap. In particular, for values close to 1.6, the yellow area appears simultaneously for the first four multipole orders. This indicates that the Kerker condition can be approached multiple times and simultaneously for each couple of multipoles and thus, forward scattering, though not perfect, will occur over a broad range of wavelengths. To evidence this, we show on Fig. 3.7-E the evolution of the fraction of energy scattered in the backward direction $\sigma_{back}/(\sigma_{for} + \sigma_{back})$. Indeed for values close to 2, a very low back-scattering is observed in the spectral band including dipole and quadrupole resonances, in agreement with the observations of Fig. 3.5-B. For lower index contrast close to 1.5, the bandwidth is strongly increased and a null back-scattering now covers the entire range where the four first order resonances are encountered. We reported on Fig. 3.7, by the white and red boxes, the region of interest bounded by an index contrast between 2 and 1.5 where the large band back-scattering cancellation is observed. Importantly, the value of $\gamma = 1.5$ is found as a threshold for obtaining a subwavelength resonator. Below this value all the resonances of the structure occur at wavelengths $\lambda < 2R$ as can be seen on the panels 3.7-A,B,C and D. We restricted our analysis in this work to the range of parameter x where resonators exhibit subwavelength sizes. It appears in this case that, at best, overlapped resonances of only the first three orders can be exploited to achieve the broadband Kerker regime.

Obviously, by further decreasing the refractive index, the overlap between pairs of multipoles can be improved for a larger number of them. Thus, in a study conducted in parallel to our investigation, M. I. Abdelrahman *et al.* revealed the broadband back-scattering suppression of over wavelength-sized spheres made from a low permittivity material with $\gamma \approx 1.3$ [36] and evidenced the approximate duality $a_n \sim b_n$ up to eight multipole orders at its origin. Their work was recently completed by the first experimental demonstration in the microwave range of the broadband Huygens source behaviour of low refractive index spherical particles with both $N = 1.38$ and $N = 1.61$ [37].

In addition, the decrease in the refractive index contrast is necessarily accompanied by a significant reduction of the scattering that vanishes in the limit of $\gamma = 1$, where the particle becomes totally transparent. Thus, for very low index particles a compromise between forward scattering bandwidth and efficiency must be found. For $\gamma = 1.5$ the efficiency reaches a value of 3.5 at the position of the subwavelength resonator limit $1/x = 1/\pi \approx 0.32$. It is a value comparable to that obtained for the dipolar Huygens sources studied in section 3.2.1 Therefore, significant efficiencies remain accessible with low index particles down to $\gamma = 1.5$.

In order to demonstrate the applicability of our findings, we calculated using the Mie theory, the scattering properties of both TiO_2 and Al_2O_3 particles. We used mesured dispersions available in [38] of the refractive index for both these compounds.

The first system investigated is a TiO_2 nano-sphere of radius $R = 150$nm. Due to the relatively high refractive index of titanium dioxide in the visible ($N \approx 2.5$), we considered water $n_h = 1.33$ as the surrounding medium in which the particle is immersed so that $\gamma \approx 1.9$ in this case. The contribution of the multipoles to the scattering efficiency of the particles are revealed on Fig. 3.8-A and the fraction of energy scattered in the forward direction is furthermore indicated in the

bottom panel. In agreement with the results of the study conducted previously, the scattering is significantly radiated in the forward direction in most of the range of wavelengths covered by the overlapped pair of dipoles and quadrupoles.

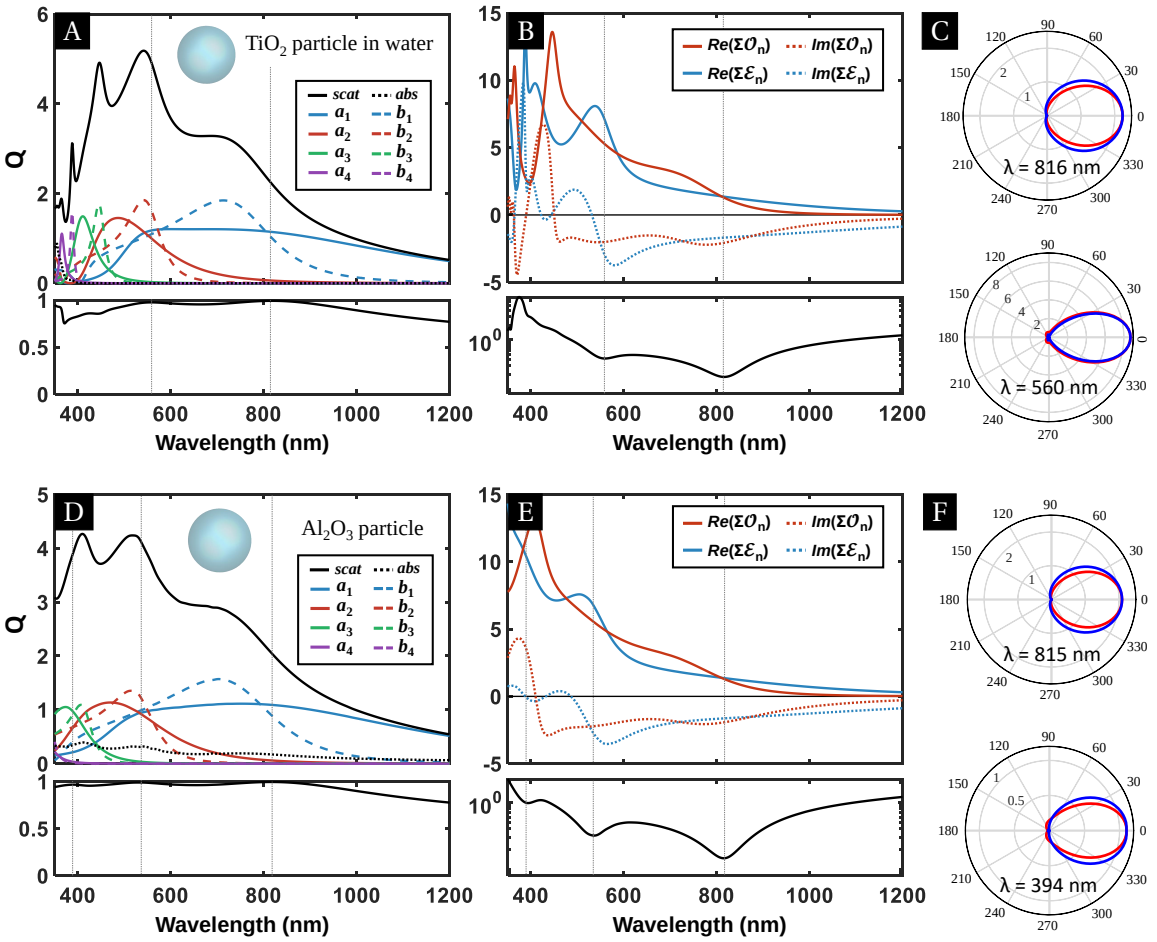

Figure 3.8 – A) Total scattering and absorption efficiencies, (black continuous and doted lines respectively), calculated with the Mie Theory for a TiO_2 nanoparticle of 150nm in radius placed in water ($n_h = 1.33$), for which $\gamma \approx 1.9$. The solid (dashed) colored lines are the scattering efficiencies of the electric (magnetic) multipoles. The bottom panels indicate the fraction of energy $\sigma_{for}/(\sigma_{for}+\sigma_{back})$ scattered in the forward direction. B) Evolution of the real and imaginary parts of the sum of even and odd multipoles $\sum\mathcal{E}_n$ and $\sum\mathcal{O}_n$ of the particle as function of the wavelength. The bottom panel show $\ln\left|(\sum\mathcal{O}_n - \sum\mathcal{E}_n)/Q_{scat}\right|$ for which local minima reveal the wavelengths where the Kerker condition is best met. The position of the minima are evidenced by the vertical dotted lines. C) Scattering radiation diagrams of the particle in both the electric (blue) and magnetic (red) planes. Panels D),E) and F) show respectively the same quantities as A),B) and C) but for an Al_2O_3 particle of radius $R = 200$nm in air, for which $\gamma \approx 1.7$.

The fulfilment of the Kerker condition ($\sum\mathcal{O}_n = \sum\mathcal{E}_n$) on this range is revealed on Fig. 3.8-B. In addition, the quantity $\ln\left|(\sum\mathcal{O}_n - \sum\mathcal{E}_n)/Q_{scat}\right|$ is plotted on the bottom panel revealing the wavelengths at which the difference between the multipoles of opposite parity is minimized. Even and odd multipoles are found to closely coincide both in real and imaginary part over the interval 550nm-850nm. In particular, the Kerker condition is notably well approached at the wavelength of 815nm (at which the real part of the two sums are equal) and 560nm (at which the imaginary part of the two sums are equal), coinciding with the positions where 100% of forward scattering is observed (indicated by the dotted vertical lines on the figure). The Huygens source features of the particle at these two wavelengths is further evidenced by the radiation diagram in the electric (blue) and magnetic (red) planes shown on Fig. 3.8-C. The cardioid pattern, characteristic of a dipolar Huygens source, is found at 816nm while the more directive beam obtained at $\lambda = 560$nm

is in agreement with the excitation of both dipoles and quadrupoles at this wavelength. In addition, it should be noticed that the peak efficiency shows an impressive value of more than 5 at this wavelength.

With the same idea than the one we exploited here, the possibility to reach broadband Huygens source features with particles of moderate index by increasing the refractive index of the surrounding media, has recently been the object of a detailed theoretical study in [39].

Similarly, we investigate on panels D,E and F of Fig. 3.8 the scattering properties of an Al_2O_3 ($N \approx 1.7$) spherical particle of radius R = 200nm surrounded by air ($n_h = 1$). Consistently with the lower value of γ, this particle exhibits an excellent Huygens source behaviour over an even broader bandwidth covering the interval 350nm-1000nm that also includes the range of excitation of the octupolar resonances. In particular the Kerker condition is found to be closely satisfied at three wavelengths of 815nm, 536nm, and 394nm (vertical dotted lines). Although the refractive index of the particle is quite low, the peak efficiency reaches approximately 4 at both 530nm and 400nm due to the simultaneous excitation of numerous multipoles at these wavelengths. It should be mentioned that for this particle, the non negligible losses of Al_2O_3 (see the absorption cross-section on panel D) also benefit to the quality of the overlap since it results in even broader multipole resonances with reduced amplitude differences between electric and magnetic modes.

In conclusion, the study presented here provides a guideline for designing resonant and broadband Huygens sources. We evidenced the possible spectrally large cancellation of the back-scattering, due to overlapped pairs of multipoles, occurring from $\gamma \approx 2$ and with increasing bandwidth as the contrast of index between particles and host medium is reduced. These features have been numerically verified on both TiO_2 and Al_2O_3 particles. Such dielectric particles are particularly interesting since they can be obtained through simple colloidal synthesis and are commercially available. Indeed broadband directional light scattering abilities of colloidal particles in the visible have been reported in different studies [40, 41]. However to our knowledge, reliable experimental proof of the broadband Kerker condition fulfilment for such particles remains to be made. In this regard, the direct measurement of the balance between even and odd excited multipoles, enabled by polarization-resolved static light scattering measurements, could help in the matter [42–44].

On the other hand, our work emphasizes that the refractive index tuning is an interesting alternative to the geometrical tuning to reach the broadband Kerker regime. However, it might be sometimes impossible to find materials exhibiting the appropriate refractive index in a given range of wavelengths and arbitrarily choosing the host medium might not always be an option. In the next section, we will show that by considering clusters of small particles, with densities and sizes that will determine the properties of the aggregate in the end, it is indeed possible to gain flexibility in the design of Huygens sources by controlling at will the effective refractive index of the aggregate.

3.3 Clusters of particles [18]

In the last 15 years, several theoretical and experimental studies have demonstrated that clusters of colloidal nanospheres, sometimes referred to as “meta-molecules”, can exhibit both electric and strong magnetic resonances in the visible domain [45–58]. These studies were largely motivated by the quest for double negative index metamaterials operating at optical frequencies and were triggered by the work of A. Alù *et al.* in 2006 and 2008 [59, 60]. With these papers, the authors proposed the original idea of exploiting the resonant feature of plasmonic nanoparticle organized into two dimensional nano-rings to induce a circulating “displacement” current around this loop of particles. By doing so, a magnetic dipole collective response can coexist with the individual electric resonance supported by each of the nanoparticles composing the cluster. This seminal work on artificial magnetism of tailored assemblies of particles was quickly extended to three-dimensional structures consisting both in nano-shells of particles, termed raspberry-like scatterers, obtained by decorating a dielectric core with plasmonic nanoparticles [48–54], or in

simple homogeneous arrangements of particles into spherical clusters [48, 55–58]. In either cases, the response of the cluster is found to be equivalent to the Mie resonances of dielectrics homogeneous spheres [48, 55, 57]. In fact the composite particle (or layer) is, in an effective way, acting as a homogeneous medium of high permittivity that can therefore be described by homogenization theories well known for bulk materials. However, unlike simple big dielectric spheres, size, nature and volume fraction of the inclusions are parameters that can be exploited to control the optical properties of the aggregates.

Therefore, with this section, we aim to demonstrate the great potential of clusters of particles in obtaining directional scattering effects. We show that a fine tuning of their Mie like resonances is possible, by playing on the previously mentioned levers of control, and that the resonant and broadband Kerker regimes presented in the previous part can be reached with both plasmonic or dielectric inclusions. In particular, the tailoring of their effective refractive index towards low values of γ identified in the previous section is used as a guideline for their design. Therefore, in the following, we start by introducing the homogenization theory, *i.e.* the extended Maxwell-Garnett mixing rules, which constitute a particularly valuable tool for a fast estimation of the cluster properties.

3.3.1 Homogenization and effective medium theory

3.3.1.a Extended Maxwell-Garnett mixing rules

The optical properties of composite particles made from subwavelength inclusions can be described in terms of effective dielectric constants ε_{eff} and μ_{eff} through the widely used Maxwell-Garnett effective medium theory. This model derives from the Clausius–Mossotti relation:

$$\frac{\varepsilon_{eff}-\varepsilon_h}{\varepsilon_{eff}+2\varepsilon_h}=\frac{\mathcal{N}}{3}\alpha_e \tag{3.17}$$

which links the effective permittivity ε_{eff} of a composite material to the mean electric polarizability α_e of its constituents. A similar relation holds between the effective permeability μ_{eff} and the magnetic polarizabilities α_m:

$$\frac{\mu_{eff}-\mu_h}{\mu_{eff}+2\mu_h}=\frac{\mathcal{N}}{3}\alpha_m \tag{3.18}$$

The Clausius-Mossotti relation (3.17) is also known as the Lorentz-Lorenz formula, since it is equivalent to that derived in the Lorentz molecular theory of polarization to compute the macroscopic dielectric permittivity for natural materials, where the constituents are collections of point-like polarizable atoms or molecules in vacuum. In the case we are interested in, the composite medium consists in a collection of polarizable particles of radius R in a background medium of permittivity ε_h and permeability μ_h. In equations (3.17) and (3.18), $\mathcal{N}$ is the number of particles per unit volume, related to the volume fraction of particles through $f_v = (4/3)\pi R^3\mathcal{N}$.

The extended Maxwell-Garnett formulas can be obtained by simply inserting in the Clausius-Mossotti relations, the expressions of the dipolar polarisabilities of particles obtained from the Mie theory:

$$\alpha_e = i\frac{6\pi R^3}{x^3}a_1 \qquad \alpha_m = i\frac{6\pi R^3}{x^3}b_1 \tag{3.19}$$

This approach is also known as the Mie Maxwell-Garnett homogenization procedure and was initially suggested in [61]. In contrast, in the classic Maxwell-Garnett formulas, as originally derived in [62], the particle polarisabilities are calculated within the quasi-static approximation and do not fully account for the size dependencies of the inclusions.

Inserting the expression of the polarisabilities in eqs. (3.17,3.18) yields the following extended Maxwell-Garnett expressions:

$$\varepsilon_{eff}=\varepsilon_h\frac{x^3+3if_va_1}{x^3-\frac{3}{2}if_va_1} \tag{3.20}$$

$$\mu_{eff} = \mu_h \frac{x^3 + 3 i f_v b_1}{x^3 - \frac{3}{2} i f_v b_1} \tag{3.21}$$

that link the composite materials effective properties to the volume fraction, size and Mie coefficients of its constituent particles.

3.3.1.b Limitations of the Maxwell-Garnett homogenization

Since the extended Maxwell-Garnett theory relies on the same approximations as those used to derive the Clausius Mossotti equation, it is obviously restricted in its applicability and can even lead to nonphysical results if not carefully used. Therefore it is important to keep in mind some of its limitations before applying it to different homogenization problems.

First of all, this formalism relies on the dipolar approximation and only relates electric and magnetic dipole moments to the effective material parameters. Therefore it is valid only for small particles (*i.e.* low values of x) and fails for bigger particles if the higher order multipole moments can not be neglected.

Although it accounts for dipolar interactions between nanoparticles, the theory remains accurate for sufficiently diluted media only. At high densities, for closely packed nanoparticles, strong near-field coupling between inclusions may occur, involving higher-order multipole excitations, that are not captured by the theory. Moreover, this restriction might apply more strictly to plasmonic particles compared to dielectric ones since they are known to lead to intense scattered fields and local field enhancements.

In addition, the model hypothesizes a homogeneous distribution of particles over the material and does not account for the local fluctuation of particle density due to spatial disorder or a possible aggregation of the inclusions.

Finally, and importantly, it was underlined by C.F. Bohren [63, 64], that the imaginary part of the effective refractive index obtained from the extended Maxwell-Garnett homogenization cannot be used to accurately evaluate absorption. In fact, for non-absorbing spheres embedded in a non-absorbing medium, the effective refractive index still exhibits an imaginary part that increases with the sphere size and is not related to an increase of the absorption in the system but simply results from an increase of the scattering. Therefore, the imaginary part of the effective refractive index obtained from this theory no longer has the same validity as that of the refractive index of a homogeneous material.

3.3.2 Resonant dipolar Huygens sources with clusters

In what follows, we demonstrate with several examples that clusters constitute a promising solution for obtaining both the resonant dipolar and extremely broadband forward scattering.

The clusters we consider are spherical and composed of identical spherical inclusions of radius r_p arranged quasi-homogeneously. Homogeneous clusters are obtained by minimizing the potential energy of a given number of particles in repulsive interaction constrained inside a spherical capsule [65, 66].

The different designs that we are going to detail, are obtained with the following approach: In a first step, extended Maxwell-Garnett theory is used to select, for a given size of inclusion, a filling fraction that provides an effective refractive index in the range of that enabling the broadband Kerker regimes studied in the previous section 3.2. Then, the full cluster properties are rigorously investigated through $\mathcal{T}$-matrix simulations. At this stage, due to the differences that might exist between the properties predicted for the effective spheres and the one actually observed, slight adjustments on the geometry are likely to be made to optimize the overlap of the multipole resonances.

3.3.2.a Cluster designs with dielectric and plasmonic inclusions

We start by addressing the possibility of obtaining resonant dipolar Huygens sources with dielectric or plasmonic inclusions. Targeting a peak resonance wavelength in the visible, at $\lambda \approx$ 500nm and using extended Maxwell-Garnett theory, we explore the geometrical parameters f_v and r_p, in the case of silicon inclusions in air and silver inclusions in water, with the aim of getting optical scatterers with overlapping electric and magnetic dipole resonances at their efficiency peak.

In particular, the impact of the volume fraction f_v on the effective refractive index is presented in Fig. 3.9 for sizes of inclusion of $r_p = 41$nm for silicon (Fig. 3.9-A) and $r_p = 15$nm for silver particles (Fig. 3.9-B). The optical properties of silver were taken from Palik's compendium [67] and those of silicon from Aspnes and Studna's work [68]. The two color-maps provide the variation of the refractive index contrast $\gamma = \sqrt{\varepsilon_{eff}\mu_{eff}}/n_h$ as a function of the volume fraction f_v of inclusions.

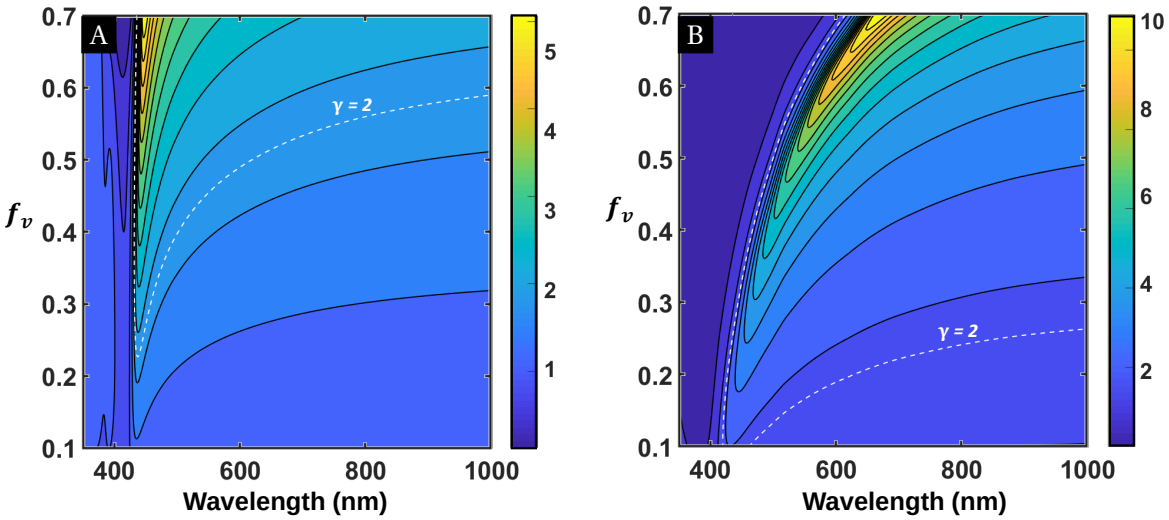

Figure 3.9 – The color-maps show the variations of the refractive index contrast $\gamma = \sqrt{\varepsilon_{eff}\mu_{eff}}/n_h$ as a function of the volume fraction of inclusions that are considered in the clusters. The effective medium properties ε_{eff} and μ_{eff} describing the clusters are calculated with extended Maxwell-Garnett theory for A) *Si* particles of radius 41nm in air ($n_h = 1$) and B) *Ag* particles of radius 15nm in water ($n_h = 1.33$).

It can be observed that very large values of γ are reached in the case of silver particles due to the dipolar plasmonic resonance of the inclusions. The variations are not as large for silicon particles. In this case, at high densities, the effective index is close to that of the particles, *i.e* silicon, while at low densities, it naturally tends towards that of the host environment, $n_h = 1$ here. In addition, the modulations of the effective index is in this case induced by the strong magnetic dipole resonance of the silicon particles at $\lambda = 425$nm.

As was shown in section 3.2.1, the index contrast allowing to obtain two spectrally superimposed dipole resonances is around $\gamma = 2$. This value is indicated by the white dashed line on the figures. It is therefore possible to estimate that densities of particles close to $f_v = 0.4$ are required in the case of *Si* for reaching this value at the targeted wavelength of $\lambda = 500$nm, and close to $f_v = 0.15$ for the silver inclusions. Thus the space of the parameters to be explored is significantly reduced. In addition, the approximate total size required for the clusters to get an operating wavelength of 500nm is known since Mie dipole resonances were found to overlap for $1/x \approx 0.65$ in section 3.2.1. Therefore, knowing f_v and R, the number X of particles to consider in each cluster is also accessible since $f_v = X(r_p/R)^3$.

Following the guideline provided by this homogenization approach, we arrive at 2 clusters presenting a highly satisfying overlap of their two dipolar resonances, which are presented on Fig. 3.10.

The first structure, shown on the inset of Fig. 3.10-A corresponds to a silicon cluster made from inclusions of size $r_p = 41$nm. The cluster consists of 13 particles and presents a outer radius $R = 123$nm with a volume fraction in particles of 47%. The second one displayed in Fig. 3.10-D is a silver cluster consisting of 60 particles with $r_p = 15$nm presenting a total radius $R = 100$nm and a volume fraction of particles of 20%.

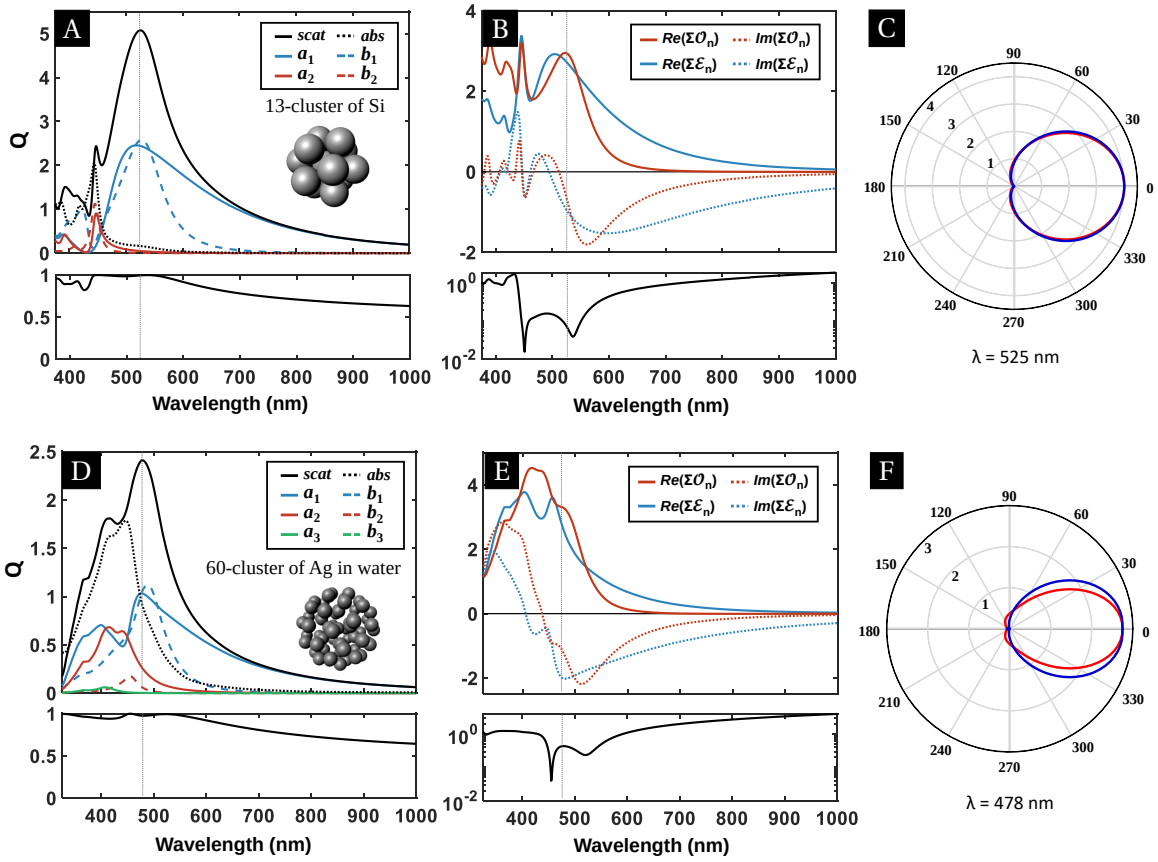

Figure 3.10 – A) Total scattering and absorption efficiencies calculated with the $\mathcal{T}-$Matrix method for a cluster of radius $R = 123$nm made from 13 silicon particles of radius 41nm. The surrounding medium is taken as air. The solid (dashed) colored lines are the scattering efficiencies of the electric (magnetic) multipoles. The bottom panel indicates the fraction of energy $\sigma_{for}/(\sigma_{for}+\sigma_{back})$ scattered in the forward direction. B) Evolution of the real and imaginary parts of $\sum\mathcal{E}_n$ and $\sum\mathcal{O}_n$ as a function of wavelength. The bottom panel shows $\ln\left|(\sum\mathcal{O}_n - \sum\mathcal{E}_n)/Q_{scat}\right|$ for which local minima reveal the positions where the Kerker condition is best met. C) Cuts of scattering radiation diagram of the particle in both the electric (blue) and magnetic (red) planes. Panels D),E) and F) are identical to respectively A),B) and C) but for a silver cluster with $R = 100$nm made from 60 particles of radius 15nm and with the surrounding medium being water.

Figures 3.10-A,D show for both systems the contribution of the different multipoles to the scattering efficiencies, the optical properties being in this case rigorously investigated by mean of the $\mathcal{T}$-matrix solver developed by Mackowski [69]. We see that overlapped dipolar resonances with almost equal amplitudes are reached in both cases near the targeted wavelength, at $\lambda = 525$nm for the dielectric cluster and $\lambda = 478$nm for the plasmonic cluster. As a result, nearly 100% of forward scattering is achieved in the whole interval around the maximum of the dipole resonance between 450nm et 550nm. The fulfilment of the Kerker condition is evidenced in Figs. 3.10-B,E for each system, demonstrating even and odd multipoles very close in real and imaginary part on the whole range where the directional scattering is obtained. In particular, the Kerker condition is found to be particularly well fulfilled in 2 wavelengths, close to 450nm and 550nm, that frame the positions of the resonance peaks. In order to further characterize the strong forward scattering obtained at the wavelengths of the efficiency peaks for each cluster, the radiation diagrams at this wavelength, in both the electric (blue) and magnetic (red) planes are shown on Figs. 3.10-C,F. In each case, a

strongly asymmetric pattern is observed. Figure 3.10-C reveals that, for the dielectric cluster, the radiation pattern obtained in each plane is a cardioid, confirming that the cluster closely behaves as an ideal Huygens dipole at this wavelength. On the contrary, for the plasmonic cluster, the radiation patterns slightly differ from those of an ideal Huygens dipole, with reminiscence of lobes due to the significant quadrupolar contributions at this wavelength, that are visible on Fig. 3.10-D. As a result, the directivity of the forward directed beam is enhanced, most of the scattering occurs in a narrower solid angle.

On the other hand, if the performances in terms of directionality of the scattering are what we want to demonstrate with the cluster, those obtained in terms of efficiency in the case of the dielectric cluster are beyond expectations. On Figs. 3.10-A and D, it can be seen that the scattering peak efficiency reaches 2.5 for the silver cluster and an impressive value of 5 is reached for the silicon cluster. Such a strong value for this cluster is a major result as the scattering efficiency reached by this pure Huygens dipole beats the theoretical maximum scattering efficiency of 3.67 (see subsection 3.2.1) reachable by an ordinary sphere. This extremely large scattering response can be explained by the fact that compared to simple spheres where the permeability μ is equal to 1, the composite particles can exhibit a μ_{eff} larger than one. Thus, the additional modulation of the effective permeability of the material constitutes a clear advantage in resorting to composite particles compared to simple homogeneous spheres. Not only higher efficiencies are made available, as observed here, but the composite particles are also closer to the Kerker condition (i) of impedance matching $\mu_{eff} = \varepsilon_{eff}$, facilitating even more the overlapping of the different multipoles.

Finally before finishing this section, we want to mention that the choice in the size of inclusions is considered in relation to the operating wavelengths and has been made in order to limit the final number of particles in our clusters. This offers the advantage of significantly lightening the simulations performed by $\mathcal{T}$-matrix. It is obvious that to operate at a larger wavelength, with the same size of inclusions as considered here, larger aggregates are required, of potentially several hundreds of particles. Considering aggregates of such large sizes, was not necessary for the proof of principle presented in this part. Of course, such imposing aggregates can also be tuned into Huygens sources following the same design procedure as exposed here. The number of particles is not a constraint in obtaining the resonant Kerker regime.

3.3.2.b Limitation of the homogenization approach

In the previous part, we illustrated with two examples, a versatile procedure to design clusters as resonant dipolar Huygens sources, where the estimation of the effective refractive index of the clusters is used as a guideline. In this section, we want to highlight the strengths and limitations in resorting to this homogenization theory.

For this purpose, we provide on Fig. 3.11, the scattering properties of the effective spheres obtained by homogenizing the clusters studied in the previous section through the extended Maxwell-Garnett theory. The cross-sections and multipolar decomposition are calculated using Mie theory.

Comparing Figs. 3.10 and 3.11, it can be seen that the scattering properties of the clusters are qualitatively well reproduced with the effective spheres, even for that consisting of only 13 particles. The positions of the resonances are properly predicted by the homogenization method, and so are the relative amplitudes between electric and magnetic modes of identical order. This validate our strategy to rely on this homogenization procedure for the design research. Indeed, the overlapping of the dipolar resonances are obtained at almost the same wavelengths, at 528nm and 493nm for the *Si* and *Ag* homogenized spheres respectively. In addition, it is verified that in each case, the effective structure presents a contrast of index extremely close to the targeted optimal value of $\gamma^{***} = 2.1 + 0.095i$ determined previously. For the silicon cluster, the effective refractive index is $N_{eff} = 2.174 + i0.127$ at $\lambda = 525$nm while for the silver cluster, it is $N_{eff} = 2.7 + 0.33i$ at $\lambda = 478$nm which gives $\gamma = 2.03 + 0.33i$ at this wavelength.

We can however notice limitations in the homogenization model which dramatically overestimates the absorption cross-section of the silicon cluster and fails to accurately predict the am-

plitude of the scattering cross-sections, which are underestimated in each case. In particular, the large response of the silicon cluster beating the theoretical maximum scattering efficiency of natural spheres is not reproduced by the homogenized particle that exhibit a maximal efficiency of 3.31.

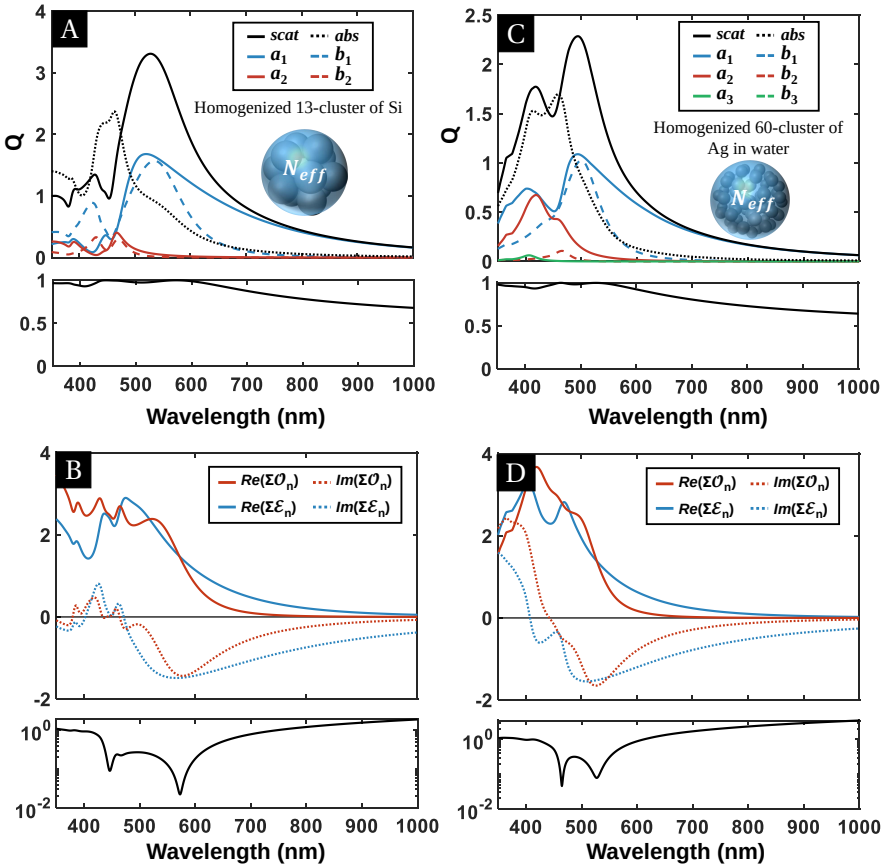

Figure 3.11 – A) Total scattering and absorption efficiencies calculated with the Mie theory for a homogenized cluster of radius $R = 123$nm made from 13 silicon particles of radius $r_p = 41$nm. The surrounding medium is taken as air. The solid (dashed) colored lines are the scattering efficiencies of the electric (magnetic) multipoles. The bottom panel indicates the fraction of energy $\sigma_{for}/(\sigma_{for} + \sigma_{back})$ scattered in the forward direction. B) Evolution of the real and imaginary parts of $\sum\mathcal{E}_n$ and $\sum\mathcal{O}_n$ as a function of wavelength. The bottom panel shows $\ln\left|(\sum\mathcal{O}_n - \sum\mathcal{E}_n)/Q_{scat}\right|$ for which local minima reveal the positions where the Kerker condition is best met. The couple of panels {C),D)} are the same as {A),B)} but for an homogenized silver cluster with $R = 100$nm made from 60 particles of radius 15nm where the surrounding medium is water.

These differences explain the need to resort to rigorous $\mathcal{T}$-matrix simulations for the fine tuning of the cluster properties in the last stage of the design procedure. In addition it indicates that Maxwell-Garnett theory fails to provide reliable effective properties ε_{eff} and μ_{eff} for the clusters. As a consequence, this renders impossible any attempt to optimize the forward-scattering efficiency of clusters by fulfilling the condition of impedance matching $\varepsilon_{eff} = \mu_{eff}$ corresponding to Kerker condition (i).

3.3.3 Broadband multipolar Huygens sources

With the same approach as that used in the previous section, we present here a cluster design that behaves as an extremely broadband Huygens multipole, demonstrating therefore that such structures are also suitable to obtain the extremely extended Kerker regime revealed in section 3.2.2.

The studied cluster, for which the scattering properties are analyzed in Fig. 3.12, has a radius of 300nm and consists in 80 silicon particles of radius r_p = 50nm, with water as a host medium. The volume fraction is $f_v = 0.37\%$.

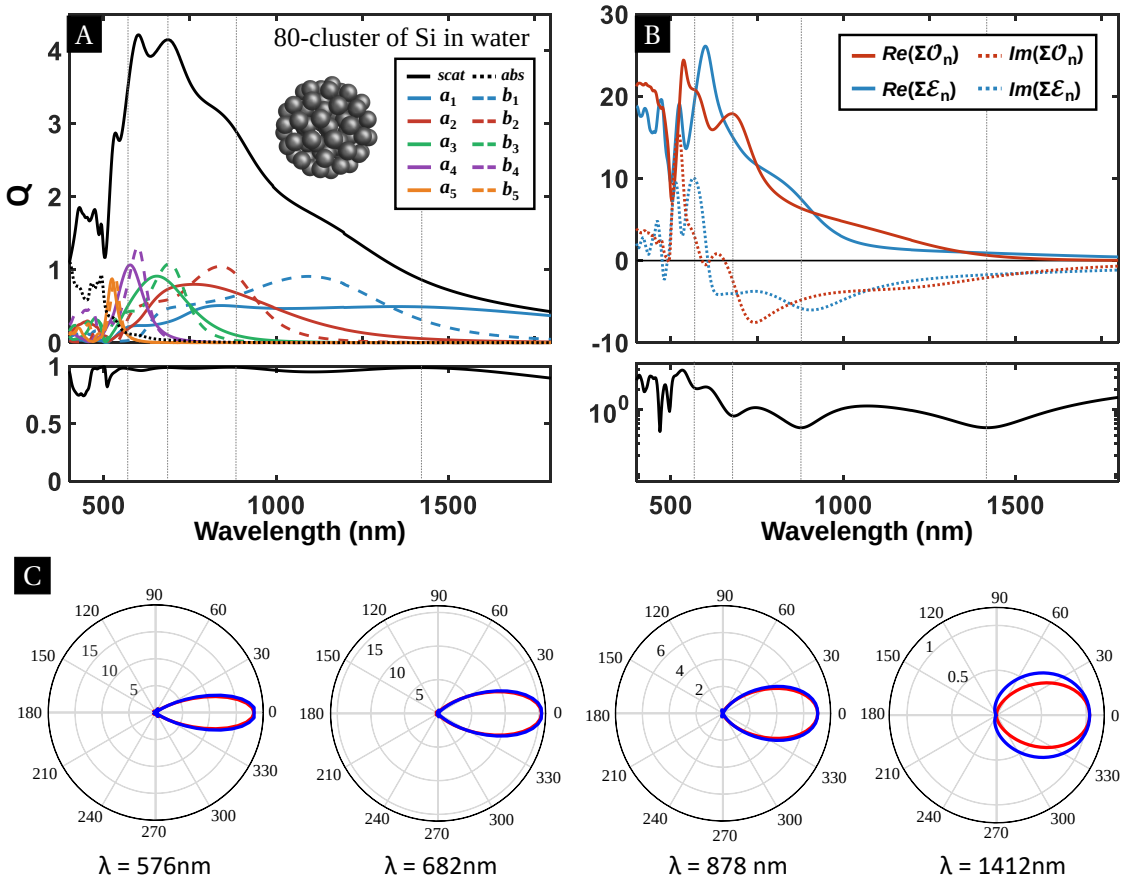

Figure 3.12 – A) Total scattering and absorption efficiencies calculated with the $\mathcal{T}$-Matrix method for a cluster of radius R = 300nm made of 80 silicon particles of radius 50nm. The surrounding medium is water (n_h = 1.33). The solid (dashed) colored lines are the scattering efficiencies of the electric (magnetic) multipoles. The bottom panel indicates the fraction of energy scattered in the forward direction. B) Evolution of the real and imaginary parts of the weighted sums of even and odd multipoles $\sum \mathcal{E}_n$ and $\sum \mathcal{O}_n$ as a function of wavelength. The bottom panel shows $\ln\left|(\sum \mathcal{O}_n - \sum \mathcal{E}_n)/Q_{scat}\right|$ revealing the positions where the Kerker condition is best met. C) Scattering radiation diagrams of the cluster in both the electric (blue) and magnetic (red) planes for four different wavelengths.

Compared to the silicon clusters studied previously (Figs. 3.10-A,B,C), the size of the inclusions as well as the radius of the structure were increased in order to obtain resonances at higher wavelengths in the near-infrared and visible domains. Moreover, the density of the cluster is lower while the host medium refractive index is increased, both in order to obtain a lower index contrast γ favourable for a broadband Kerker regime. The effective refractive index of the cluster is $N_{eff} = 2.123 + 0.1i$ at 682nm and takes values slightly inferior at larger wavelengths. Therefore the index contrast satisfies $1.4 < \gamma < 1.6$, for most of the studied spectrum.

Figure 3.12-A indeed reveals the extremely broadband Huygens source feature of this cluster spanning over an impressive 1000nm range, achieved from 500nm to 1500nm, for which the fraction of energy scattered forward reaches almost 100%. As can be seen, This large bandwidth is the result of the excellent overlap two by two of the dipoles, quadrupoles, octupoles and hexadecapoles successively excited over the spectral range. The resulting rough broad overlapping between the symmetric and anti-symmetric multipoles can clearly be seen on Fig. 3.12-B. In particular the Kerker condition is optimally fulfilled at four wavelengths of 1412nm, 878nm, 682nm and

576nm minimizing the distance between the sum of multipoles of opposite parity in the complex plane. The radiation diagrams at these particular wavelengths are shown on Fig. 3.12-C. Strongly forward directed scattering is observed in each case and the diagrams also reveal the clear improvement in the angular directivity of the radiation as higher order multipoles are involved in the scattering.

In addition, due to the coexistence of numerous multipoles between 600nm and 700nm, the scattering efficiency reaches a value of 4 in the visible.

3.3.3.a Comparison with the homogenized sphere

For comparison, the scattering properties of this cluster homogenized as an effective sphere with the Maxwell-Garnett theory are detailed on Fig. 3.13. The large forward scattering resulting from the successive overlap of the electric and magnetic multipoles of the first four orders is also obtained with the homogenization approach. The broadband Kerker regime is found on the same interval from 500nm to 1500nm. However, the same comments as those made previously on section 3.3.2.b apply. The effective absorption cross-section is almost null between 500nm and 1000nm for the cluster on Fig. 3.12-A and is significantly high in the case of the effective particle on Fig. 3.13-A. In addition, an important underestimation is made on the resonance amplitudes. Nevertheless, since the relative positions and relative amplitudes of the different multipoles are quite well predicted, our design strategy is effective in this case too.

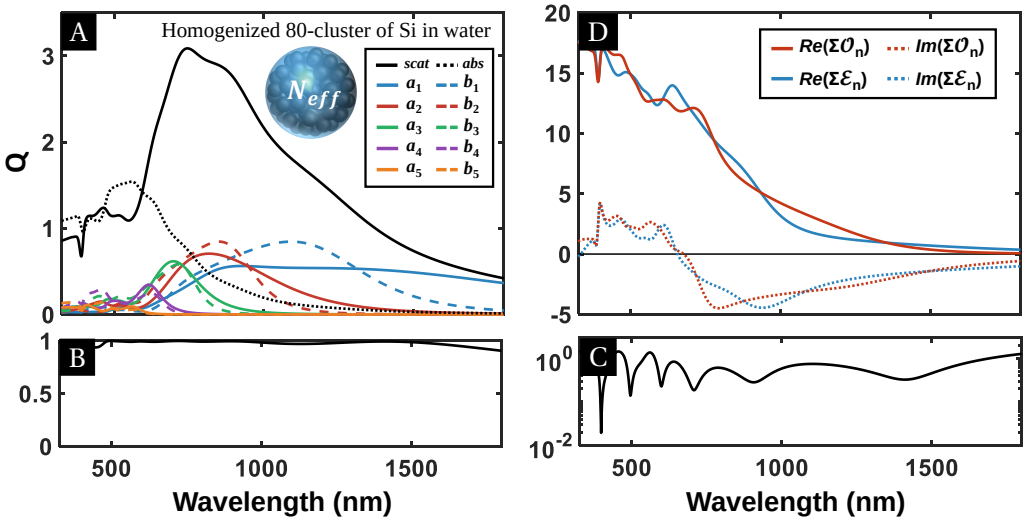

Figure 3.13 – A) Total scattering and absorption efficiencies calculated with the Mie theory for a homogenized silicon cluster with $R = 300$nm made from 80 particles of radius 50nm where the surrounding medium is water. The solid (dashed) colored lines are the scattering efficiencies of the electric (magnetic) multipoles. The bottom panel indicates the fraction of energy $\sigma_{for}/(\sigma_{for}+\sigma_{back})$ scattered in the forward direction. B) Evolution of the real and imaginary parts of $\sum\mathcal{E}_n$ and $\sum\mathcal{O}_n$ as a function of wavelength. The bottom panel shows $\ln\left|(\sum\mathcal{O}_n - \sum\mathcal{E}_n)/Q_{scat}\right|$ for which local minima reveal the positions where the Kerker condition is best met.

So far, we have demonstrated the potential and some clear advantages of using clusters to obtain isotropic Huygens sources with controllable bandwidth. We have used ideal structures, *i.e.* spherical and very homogeneous clusters, formed of perfectly mono-disperse and spatially ordered inclusions. However even state-of-the-art nano-chemistry techniques can not produce such ideal structures, real systems made by colloidal self assembly will inherently present irregularities. Therefore it is necessary to explore the sustainability of the properties of clusters with possible geometric imperfections. In that respect, the following section is dedicated to a brief study of the impact of different irregularities on the cluster resonances.

3.3.4 Effect of voids, disorder and size polydispersity

Since reaching the Huygens regime relies on the quality of the overlap between the electric and magnetic resonances of the structure, it is relevant to wonder what is its robustness with structural imperfections that would be experimentally encountered. Therefore in this section, the effects on the resonances of different types of structural deviations from an ideal cluster geometry are explored. We limit ourselves to the study of the first two excited resonances, *i.e.* the two dipolar resonances.

We start by considering an ideal cluster that will be used as the reference. The chosen cluster is an *Ag* cluster with a radius of $R = 100$nm composed of 60 particles of radius $r_p = 15$nm dispersed homogeneously in air with a filling fraction $f_v = 0.20$. The optical constant of silver is taken from P.B. Johnson and R.W. Christy's work [70]. Metallic clusters are chosen for this study since plasmonic particles are known to be more sensitive to coupling with neighbors. This choice is thus well suited to explore the effects of local variations in the environment of the inclusions especially the robustness of the magnetic dipole resonance, known to result from collective behaviour of particles [59].

As can be seen on Fig. 3.14-A, an excellent overlap of the two dipole resonances is reached at a wavelength of 390nm resulting in full forward scattering near the resonances.

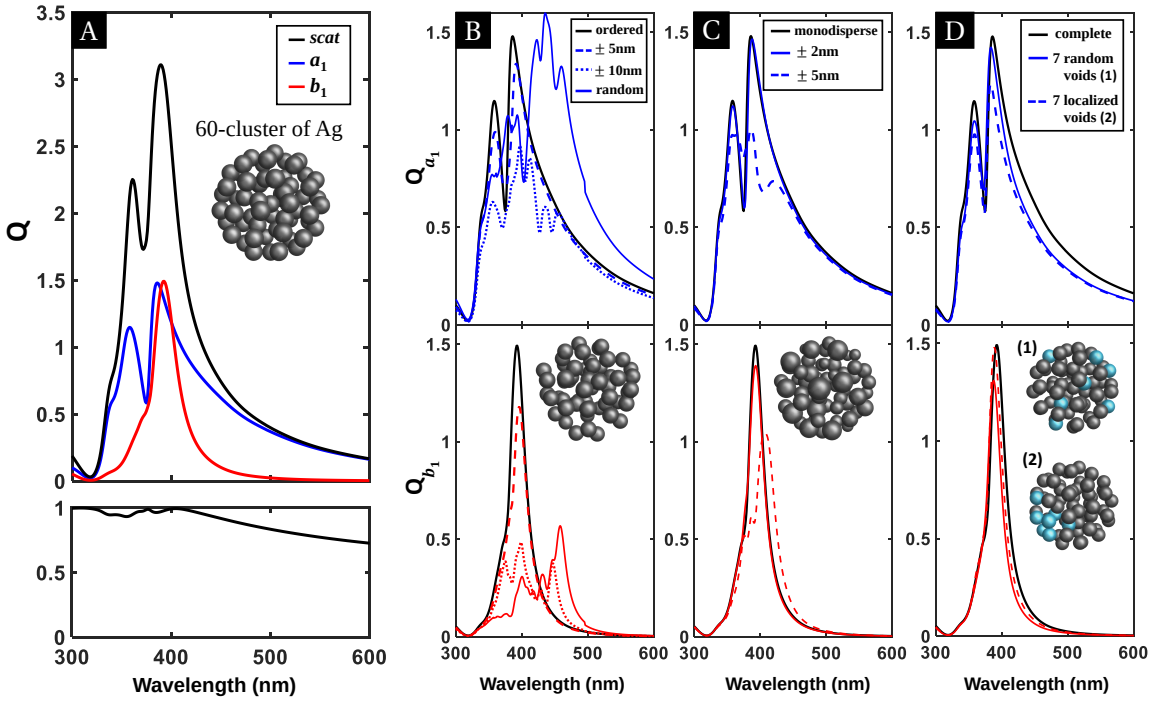

Figure 3.14 – A) Total scattering and absorption efficiencies calculated with the $\mathcal{T}$−Matrix method for a cluster of radius R=100nm made of 60 silver particles of radius r_p =15nm in air. The blue (red) line is the scattering efficiency of the electric (magnetic) dipole. The bottom panel indicates the fraction of energy scattered in the forward direction. B) Evolution of the electric and magnetic dipole scattering efficiencies when the initial positions of particles are randomly moved by a maximum amplitude of 5nm, 10nm and for a completely randomly determined cluster shown in the inset. C) Evolution when the size of particles is randomly increased or decreased by a maximum value of 2nm and 5nm. This later case is shown on the inset. D) Evolution when 7 particles are randomly or locally removed as shown on the 2 insets.

We start by studying the effect of positional inhomogeneity of particles on the electric and magnetic dipole responses. Three cases are studied and presented in Fig. 3.14-B. First of all, a uniform random noise is induced on the initial positions of each particles allowing a displacement with maximum amplitude of ±5nm in all directions of space simultaneously. To appreciate the magnitude of the induced disorder, it should be noted that, for the homogeneous cluster, the aver-

age inter-particle distance between adjacent spheres is 12.8nm. This distance between neighbors is obtained with the pair correlation function (also known as radial distribution function). Thus, the maximum amplitude of ±5nm already introduces an important disorder since in an extreme case, particles could be brought in close contact, although this event has a rather low probability of occurring. Then, the positional disorder is increased allowing a displacement of a maximum amplitude of ±10nm, leading to strongly disordered clusters. Finally, in the last case, the position of the inclusions in a sphere of radius R are generated totally randomly, the only constraint being the non-intersection of the particles. This later extreme case is shown on the inset of Fig. 3.14-B. As we can see, both electric and magnetic resonances are strongly impacted. The study reveals the existence of a threshold in the acceptable disorder since for the two situations of strong disorder, the collective magnetic response of the aggregate almost vanishes. On the contrary, for small displacements of the positions, both dipolar responses are rather well preserved. On the other hand, the electric response is sustained for the totally random cluster, but is on average red-shifted, broadened and exhibits various peaks that result from the strong coupling and hybridization between the plasmonic response of the particles brought close to one another.

In a second study, we explore with two examples, presented on Fig. 3.14-C, the effect of polydispersity in the particle size, while keeping the initial homogeneous distribution. Starting from the monodisperse cluster of Fig. 3.14-A, the size of each particle is randomly increased or decreased with a maximum amplitude of ±2nm at first, and then ±5nm, this later case leading to the cluster presented on the inset of the figure. As expected, the effect of low polydispersity is almost unnoticed for both types of resonances. The impact is all the more pronounced as polydispersity increases, resulting mostly in a decrease in the amplitude of the resonances. Interestingly, the two resonances are impacted in relatively similar proportions, which indicates that an overlapping of the two dipoles is still achievable in this case.

Finally, on Fig. 3.14-D, we investigate defect impacts by creating voids in the cluster. In a first situation displayed on the inset (1) of the figure, seven particles are randomly removed from the homogeneous cluster of Fig. 3.14-A. Then, as represented on the inset (2), seven particles are removed in a same region to create a bigger local defect on the cluster. As can be seen, in both cases, the particles removed (blue) belong to the external and internal layers of the cluster. Surprisingly, both the electric response and the collective magnetic response of the aggregate are highly resistant to the presence of both types of voids, which only weakly affect their amplitude.

To conclude this part, it is clear that the study conducted here is far from comprehensive and severely lacks statistical investigations, both concerning the repeatability of the simulations and the averaging on the orientation of the clusters in regard to the incident wave, which would provide information on the anisotropy resulting from the defects. Such a complete and detailled investigation, that would of course constitute an interesting extension to this work, is beyond the scope of this thesis. Our aim here was rather to present some preliminary information that might serve as guidelines for establishing a set of requirements for fabrication. It should be mentioned that a detailed study on these irregularity effects exists in the literature [71], but has been carried out on nano-clusters consisting in a central dielectric core surrounded by several silver satellites. This structure might nevertheless share certain similarities with the clusters we consider regarding the physical origin of the electric and magnetic resonances.

Although we performed limited simulations, we believe the results presented here are still representative of a general trend. In particular, it is highly likely that the most impacting parameter is the positional disorder of the particles that can compromise the existence of a strong magnetic response. Experimentally, a low index coating on the plasmonic inclusions might prevent high degrees of disorder by ensuring a minimal inter-particle distance during the self-assembly process. We did not investigate dielectric clusters. However, similar trends can be expected in that case and such clusters might even present a lower dependency to the disorder due to the weaker coupling existing between dielectric particles compared to plasmonic ones.

3.3.5 Conclusions

We demonstrated in this section the benefits of using composite particles to obtain isotropic Huygens sources with high scattering efficiencies. First of all, the cluster system is rich as it is scalable and its optical properties can be tuned by varying the nature, amount, size, and volume fraction of inclusions. This structure thus allows great flexibility to obtain the directional scattering properties at desired wavelengths with a given material. In some cases clusters offers much higher performances than simple particles in terms of scattering efficiencies. In addition, we provided through this work guidelines for their designs which consist mostly in exploiting the homogenization techniques to target specific values of contrast of index that were revealed in section 3.2.

In view of the significant progress made in the field of colloidal self-assembly in recent years, [47, 53, 57, 72–78], we expect the Huygens behaviour of self-assembled clusters will be experimentally verified in the near future. Several recent examples have indeed shown the possibility to self-assemble plasmonic nanoparticles in clusters of submicrometric sizes. In addition, the simultaneous excitation of electric and magnetic resonances of these structures has already been evidenced [53, 57]. However, making it possible to overlap these two modes currently requires an important increase in the magnetic response of the objects synthesized thus far. Nonetheless, considering the progress of the ongoing work in our team on an emulsion-based fabrication route of clusters, we are confident that exceptionally strong magnetic responses of clusters will be demonstrated soon, paving the way for the development of cluster-based Huygens sources.

3.4 Unidirectional scattering with multilayered particles

Multilayered particles constitute an other alternative for realizing fully 3D isotropic Huygens sources. The superposition of layers of different nature and controlled size indeed provides enough degree of freedom to adjust with a certain flexibility even and odd multipoles for reaching the Kerker regimes [2, 79, 80]. In the following, we investigate the use of both metallo-dielectric core-shell and all-dielectric multilayered particles to achieve Huygens sources exhibiting overlapped multipoles.

3.4.1 Metallo-dielectric core-shells as ideal resonant dipolar Huygens sources

We consider in this part, metallo-dielectric core-shells consisting in a plasmonic core (gold or silver) and a dielectric shell. Such objects are known to exhibit strong dipole resonances in the infrared. Since the magnetic response arises from the magnetic Mie resonance of the dielectric shell, while the electric one is due to the localized plasmon resonance of the metallic core, electric and magnetic dipoles can be engineered in such structures to overlap at the same resonant wavelength by properly tuning the relative thickness of the two layers. Using this principle, such particles were originally proposed in [79, 80] to achieve the resonant suppression of the backward scattering. This approach extends of course to two-dimensional systems and to the overlapping of dipole resonances of coated cylinders, which was revealed in [81]. Although these results are several years old and the directional scattering properties of such core-shells have been studied in several publications since then [2, 7], only few theoretical design proposals of such resonant Huygens sources can be found in the literature. To address this situation, we present in the following the results of an extensive study exploring the different geometric parameters of the core-shell, that provides the conditions under which resonant dipolar Huygens sources can be obtained. In particular, this will reveal the large scalability and great performances enabled by such scaterrers.

The study we conducted concerns both core-shells with a silver core, where the optical constants are taken from E.D. Palik handbook [67], and gold core, with material data taken from P. B. Johnson and R. W. Christy's work [70]. To clarify the notation, the core-shells consist in a core of radius r_c and present a total outer radius denoted R. The refractive index N of the dielectric shell is constant and lossless.

In order to get dipolar Huygens sources with maximum efficiencies, we explore the space of parameters composed by (R, r_c, N) with the goal of obtaining core-shells with electric and magnetic dipolar resonances at the same wavelength. In particular, the criterion we seek to satisfy is $\Re(a_1(\lambda^*)) = \Re(b_1(\lambda^*)) = 0$, *i.e.* that the first zeros of the real part of the two Mie dipole coefficients, indicating the position of each resonances, strictly coincide at a wavelength that we denote λ^*. The multipolar coefficients are calculated from Mie theory generalized to multilayered particles [34, 82, 83] using the Matlab code *Matscat*, developed by J. Schäfer, freely available online [84, 85].

The results of this study are presented in the form of a chart in Fig. 3.15-A and B for respectively the *Ag* and *Au* core-shells. The figure shows for different plasmonic core radii r_c (y-axis), the total size R (x-axis) required for the core-shell, thus indirectly the thickness of the dielectric layer, to achieve the superposition of resonances at a wavelength λ^* indicated by the color scale. In addition three distinct values of N are explored for the dielectric shell: $N = 3.5$, $N = 3.0$ and $N = 2.5$. Each point on the chart thus corresponds to an optimized dipolar Huygens source design.

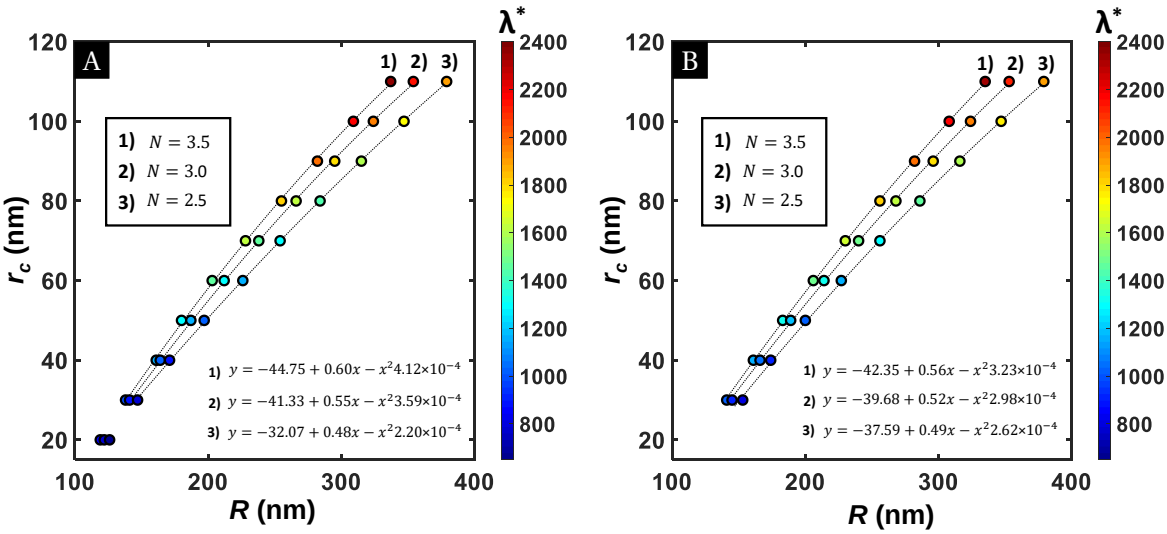

Figure 3.15 – A) Chart presenting combinations of geometric parameters for silver core-shells allowing the two dipole resonances of the particle to be excited at the same spectral position. The resonance wavelength λ^* of each design is indicated by the color scale. The dependence of r_c (y-axis) with R (x-axis) is fitted through a polynomial function of order 2 (whose equation is written on the figure) for the three different values of the shell refractive index N investigated. B) provides the same information as panel A but for core-shells with gold cores.

Quite logically, the overlapping resonances are obtained at wavelengths that are larger as the structure sizes and the dielectric index are high. The outstanding scalability of the system is highlighted since it is possible to obtain Huygens sources over the entire near infrared range between 800nm and 2400nm for the range of size studied. On the other hand, for a given shell index, the increase (decrease) in the size of the core, that essentially affects the electric plasmon resonance, is necessarily followed by an increase (decrease) in the dielectric layer thickness to maintain the overlapping. In particular, for each value of N, the relationship between the geometric parameters is indicated on the figures: the dependence of r_c with R is fitted through a polynomial function of order 2 for which the equation is given in each case. Finally, by comparing Figs. 3.15-A and B, we notice the high similarity between the designs obtained with gold and silver. Obtaining the resonant Kerker condition is therefore weakly dependent on the choice of the plasmonic core.

In order to reveal the quality of the overlap achieved in each case and to evidence the directional scattering abilities of the different designs of Fig. 3.15, we detail in the following the scattering properties of two core-shells located at extreme positions on the chart. The first one, presented on Figs. 3.16-A,B,C, consist in a silver core and a dielectric shell with $N = 3.5$. Its geometric parameters $R = 337$nm and $r_c = 110$nm are among the largest investigated. The second one presented on

Figs. 3.16-D,E,F is made of a gold core with a dielectric shell of index $N = 2.5$ and for which small geometric parameters are considered: $R = 174$nm, $r_c = 40$nm.

Both Figs. 3.16-A and D, allow to realize the excellent spectral superposition of the dipoles obtained at $\lambda = 2339$nm and $\lambda = 921$nm for respectively the silver and gold core-shell. Not only the resonances do occur at the same spectral positions but they present in addition very similar amplitudes. It should be mentioned that this agreement in amplitude was observed for every core-shell presented on the chart of Fig. 3.15, at the exception of the silver core-shell with $r_c = 20$nm for which the small size of the core no longer allows to obtain a plasmonic resonance of sufficient amplitude. Due to the fine tuning and balance of the two dipoles, the Kerker condition is optimally fulfilled at the resonance of the particles, as visible on Figs. 3.16-B,E, and a broadband forward scattering is observed in the large range of wavelengths where the amplitude difference between the electric and magnetic dipoles remains acceptable. Moreover, the resonances of higher orders are excited far away spectrally. Therefore the core-shells investigated constitute all a purely dipolar system and the radiation pattern obtained at the position of the maximum of efficiency, shown on Figs. 3.16-C,F are that of an ideal dipolar Huygens source.

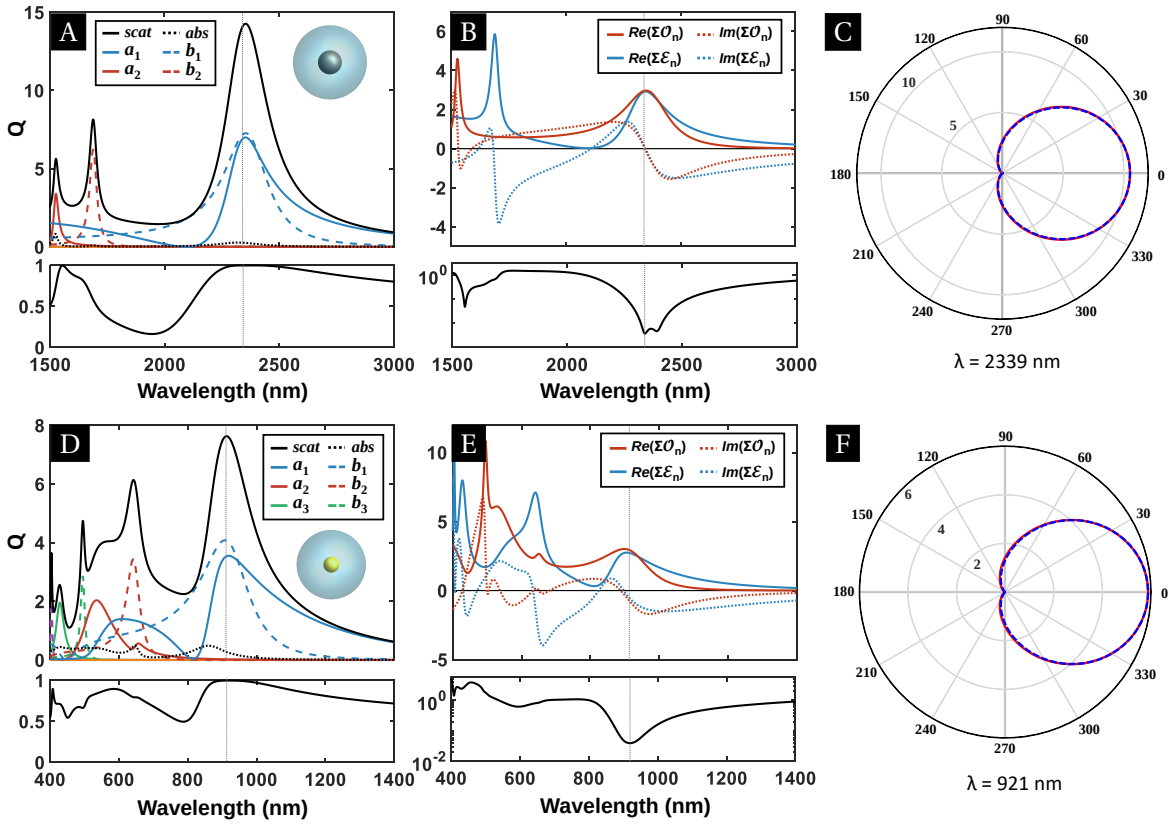

Figure 3.16 – A) Total scattering and absorption efficiencies calculated with the extended Mie theory for a core-shell of radius $R = 337$nm consisting in a dielectric shell of refractive index $N = 3.5$ and a silver core of radius $r_c = 110$nm. The solid (dashed) colored lines are the scattering efficiencies of the electric (magnetic) multipoles. The bottom panel indicates the fraction of energy $\sigma_{for}/(\sigma_{for} + \sigma_{back})$ scattered in the forward direction. B) Evolution of the real and imaginary parts of $\sum \mathcal{E}_n$ and $\sum \mathcal{O}_n$ as a function of wavelength. The bottom panel shows $\ln\left|(\sum \mathcal{O}_n - \sum \mathcal{E}_n)/Q_{scat}\right|$ for which local minima reveal the positions where the Kerker condition is best met. C) Scattering radiation diagrams of the particle in both the electric (blue) and magnetic (red) planes. Panels D),E) and F) are identical to respectively A),B) and C) but for a core-shell of radius $R = 174$nm consisting in a dielectric shell of refractive index $N = 2.5$ and a gold core of radius $r_c = 40$nm.

To conclude, metallo-dielectric core-shells are an extremely promising meta-atoms to obtain the resonant Huygens dipole sources. They present the advantage of exhibiting extremely high ef-

ficiencies in the infrared domain that rival that of the anisotropic structure obtained by top-down approaches. This is due to the fact that, unlike the spheres and clusters previously investigated, the overlapping of the resonances is not reached at the expense of a high refractive index. The object sustains both a strong plasmonic resonance and a strong Mie magnetic resonance originating from the high index layer.

Since they behave as ideal dipole systems, with great efficiencies, and due to their large scalability, these isotropic objects are by far the most promising one that could be obtained through the self-assembly platform. Nevertheless, everthough they have been extensively studied theoretically and numerically, such Huygens sources have not been experimentally realized yet, to our knowledge, due to the fact that their synthesis is challenging. Indeed, it requires the ability to synthesize plasmonic particles of quite large size and to coat them with a dielectric layer of high refractive index and thickness ranging from 2 to 4 times the size of the core. Nonetheless, with the increasing efforts put in the synthesis of core-shell particles [86], fabrication processes enabling to obtain the proposed designs should soon reach maturity. Various works have indeed revealed the possibility to coat plasmonic nanospheres with dielectric layers of variable thicknesses [87–90]. Therefore, the core-shells we studied numerically are plausible and we believe the extensive chart we provide could both stimulate and guide the community toward fabricating them.

In addition, we have focused here on obtaining dipolar Huygens sources, however, by exploiting generalized Kerker condition, the back scattering cancellation can be obtained with higher order resonances of core-shells as well [2, 7]. Moreover, we have restricted ourselves to two layers, which offers already sufficient freedom to tune the electric and magnetic modes and make sure they overlap. Nevertheless, employing core-shells with more layers is possible, the additional layers providing even more control parameters for obtaining the Kerker condition [91, 92].

3.4.2 All-dielectric core-shells

Alternatively, in recent years, all-dielectric core-shells were also proposed to achieve directional scattering effects [93–95]. Although the physics of these objects is close to that of simple dielectric particles, we will show with two examples, different advantages provided by the addition of layers. Compared to the exhaustive study conducted on the metallo-dielectric core-shells, the examples presented in this section are the result of an empirical research.

We first consider a dielectric core-shell (shown on the inset of Fig. 3.17) consisting of 2 layers. The core presents a refractive index $N = 4$ and a size $r_c = 60$nm, while the index of the shell is $N = 1.75$. The total radius of the object is $R = 175$nm. Figure 3.17-A presents the scattering efficiency of the particles and its multipolar decomposition. As can be seen, an excellent overlap of the two dipoles is obtained at $\lambda = 650$nm with dipoles reaching almost the same amplitude at this wavelength. The Kerker condition is closely fulfilled on the range of the dipole overlap between 500nm and 700nm, with forward-scattering ratio reaching 1 on this range. The scattering diagram plotted on Fig. 3.17-C in particular reveals the forward directed scattering pattern obtained at 650nm, corresponding to the position of the peak efficiency. The efficiency of 4 obtained at this wavelength with the core-shell, is higher than that obtained with the optimized simple lossless dielectric particle (see subsection 3.2.1). This is due to the fact that, while high index spheres with $N \gg 2$ cannot be considered to reach the resonant superposition of the multipoles, the insertion of an intermediate layer by coating a central sphere smooths the index contrast between the outside and the high index core. This gives an average high refractive index for the layered particle and an overall good impedance matching with the outside matrix, enabling in turn the duality $a_n = b_n$ to be reached for the electric and magnetic multipoles.

Therefore, we evidence that multilayered particles can clearly outperform simple spheres in terms of efficiency. With our second example, we reveal even more strikingly that the improvement of the overlapping between multipoles is made possible by the addition of layers.

The particle we consider this time has 3 layers. The core of radius $r_c = 55$nm is made of a dielectric of index $N = 3.5$. The intermediate layer is 85nm thick and presents a refractive index of

$N = 2$, while the outer layer is 60nm thick and its index is $N = 1.5$. The extraordinarily good superposition both in position and amplitude of the multipoles of same order is shown in Fig. 3.17-D. As a consequence, the particle exhibits a flat 100% forward-scattering over the entire visible domain, ranging from 350nm to 750nm, while the efficiency oscillates around a value close to 3. The rigorous fulfillment of the Kerker condition over this broad range of wavelengths is clearly shown on Fig. 3.17-E. This broadband behavior results from the wide index gradient induced by the three dielectric layers of decreasing index with r, that makes the core-shell well impedance matched. In addition, the scattering pattern observed at the maximum of the quadrupolar resonances is shown on Fig. 3.17-F.

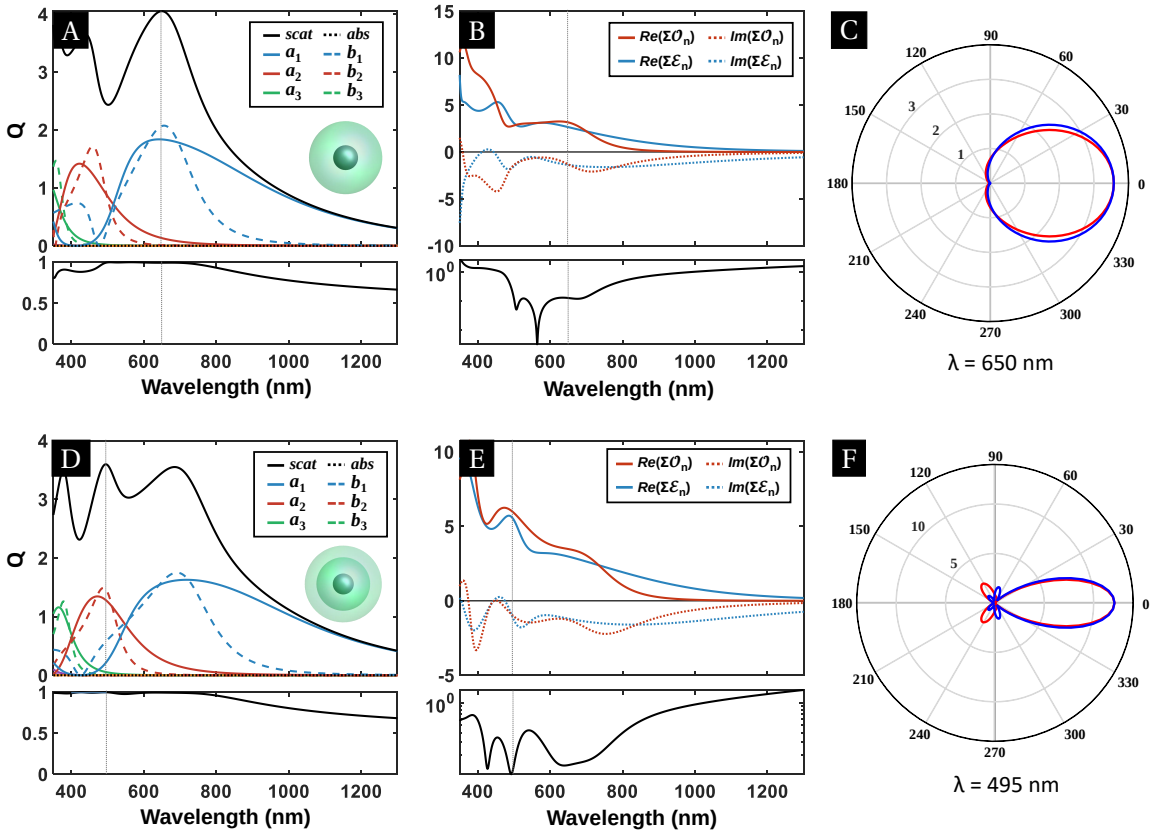

Figure 3.17 – A) Scattering efficiencies calculated with the extended Mie theory for an all dielectric lossless core-shell of radius $R = 175$nm consisting in a dielectric shell of refractive index $N = 1.75$ and a core of index $N = 4$ and radius $r_c = 60$. The solid (dashed) colored lines are the scattering efficiencies of the electric (magnetic) multipoles. The bottom panel indicates the fraction of energy $\sigma_{for}/(\sigma_{for} + \sigma_{back})$ scattered in the forward direction. B) Evolution of the real and imaginary parts of $\sum \mathcal{E}_n$ and $\sum \mathcal{O}_n$ as a function of wavelength. The bottom panel shows $\ln\left|(\sum \mathcal{O}_n - \sum \mathcal{E}_n)/Q_{scat}\right|$ for which local minima reveal the positions where the Kerker condition is best met. C) Scattering radiation diagrams of the particle in both the electric (blue) and magnetic (red) planes. Panels D),E) and F) are identical to respectively A),B) and C) but for a core-shell of radius $R = 200$nm consisting in 3 layers. the outer (intermediate) layer is 60nm (85nm) thick, and present a refractive index $N = 1.5$ ($N = 2$), while the core has $r_c = 55$nm and $N = 3.5$

Therefore, considering multilayered all dielectric particles is also a promising approach to obtain both the resonant and extremely broadband Huygens source features. While the multipolar content of these particles resembles that obtained with clusters, the physical origin of the broadband directional scattering observed in this case is slightly different. The introduction of layers of decreasing index from center to exterior ensure a good impedance adaptation to the core of the Mie resonator, that has a high refractive index which provides an overall high scattering efficiency. We have seen that by adding an increasing number of layers of controlled refractive index and thickness, the index contrast can be smoothed and made more gradual. The structure can there-

fore be tuned so that $a_n = b_n$ is reached with a large number of couples of multipoles of identical order. Also we did not investigate this case, we expect that a gradual change of index from center to exterior, for example with a linear profile, would provide similar results. In addition, a logical extension to this work would be to explore the limits of such an all dielectric multilayered particle and to look for their optimized performances.

3.5 Concluding remarks

In this chapter, we explored the possibility of fulfilling the Kerker condition for zero backscattering with several types of isotropic scatterers. The main findings and original contributions of our work are listed below:

- First of all, the study has revealed the potential of low index particles in realizing Huygens sources. The results contrast with the traditional approach in the literature where high index materials such as *Si*, TiO_2 are used in most metasurface demonstrations. Moreover, this finding is of interest to the nanochemistry community, since colloidal synthesis of high index particles is rather challenging (amorphous, porosity, oxidation, etc...) while particles of moderate or low index are simpler to fabricate.
- In contrast to the usual approach consisting in tuning the aspect ratio of anisotropic particles of high refractive index, we present an alternative, consisting in the engineering of the index contrast. In particular, we have determined the value of $\gamma = 2.1 + 0.1i$ as a reference for obtaining satisfying dipolar Huygens source. In addition, for lower index contrasts down to 1.5, we have highlighted the possibility of obtaining broadband Huygens sources which, to our knowledge, had not been revealed until then. The index contrast tuning has two possible levers: the control over the host medium (that we have exploited in the case of the TiO_2 particles immersed in water in section 3.2.2) or control over the index of the particle. The latter case can be achieved by resorting to composite particles.
- As a result, we have presented as a new idea, clusters of small inclusions for the realization of resonant and broadband Huygens sources. We have shown the potential of these objects and in particular that of the *Si* clusters whose performance in terms of scattering efficiencies exceeds that of single natural spheres. In addition, we presented a design procedure based on homogenization theory that, in spite of its current limitations, is a versatile and effective approach that may be applied to both dielectric and plasmonic inclusions.

Having revealed the potential of several building blocks as Huygens sources, the following chapters are dedicated to metasurfaces. In particular the next chapter will introduce theoretical tools for their study.

3.6 References

[1] S. Kruk, B. Hopkins, I. I. Kravchenko, A. Miroshnichenko, D. N. Neshev, and Y. S. Kivshar, "Broadband highly efficient dielectric metadevices for polarization control," *Apl Photonics*, vol. 1, no. 3, p. 030801, 2016. 48

[2] W. Liu, J. Zhang, B. Lei, H. Ma, W. Xie, and H. Hu, "Ultra-directional forward scattering by individual core-shell nanoparticles," *Optics express*, vol. 22, no. 13, pp. 16178–16187, 2014. 50, 70, 73

[3] W. Liu, "Ultra-directional super-scattering of homogeneous spherical particles with radial anisotropy," *Optics express*, vol. 23, no. 11, pp. 14734–14743, 2015. 50

[4] M. Kerker, D.-S. Wang, and C. Giles, "Electromagnetic scattering by magnetic spheres," *JOSA*, vol. 73, no. 6, pp. 765–767, 1983. 50, 53

[5] P. Grahn, A. Shevchenko, and M. Kaivola, "Electromagnetic multipole theory for optical nanomaterials," *New Journal of Physics*, vol. 14, no. 9, p. 093033, 2012. 51

[6] B. García-Cámara, J. M. Saiz, F. González, and F. Moreno, "Nanoparticles with unconventional scattering properties: Size effects," *Optics Communications*, vol. 283, no. 3, pp. 490–496, 2010. 51

[7] Y. Li, M. Wan, W. Wu, Z. Chen, P. Zhan, and Z. Wang, "Broadband zero-backward and near-zero-forward scattering by metallo-dielectric core-shell nanoparticles," *Scientific reports*, vol. 5, p. 12491, 2015. 51, 70, 73

[8] B. García-Cámara, R. A. de La Osa, J. Saiz, F. González, and F. Moreno, "Directionality in scattering by nanoparticles: Kerker's null-scattering conditions revisited," *Optics letters*, vol. 36, no. 5, pp. 728–730, 2011. 51

[9] J. Y. Lee, A. E. Miroshnichenko, and R.-K. Lee, "Reexamination of Kerker's conditions by means of the phase diagram," *Physical Review A*, vol. 96, no. 4, p. 043846, 2017. 51

[10] A. Alù and N. Engheta, "How does zero forward-scattering in magnetodielectric nanoparticles comply with the optical theorem?," *Journal of Nanophotonics*, vol. 4, no. 1, p. 041590, 2010. 51

[11] J. Y. Lee, A. E. Miroshnichenko, and R.-K. Lee, "Simultaneously nearly zero forward and nearly zero backward scattering objects," *Optics express*, vol. 26, no. 23, pp. 30393–30399, 2018. 51

[12] Y. Ni, L. Gao, A. Miroshnichenko, and C. Qiu, "Controlling light scattering and polarization by spherical particles with radial anisotropy," *Optics express*, vol. 21, no. 7, pp. 8091–8100, 2013. 51

[13] H. K. Shamkhi, K. V. Baryshnikova, A. Sayanskiy, P. Kapitanova, P. D. Terekhov, P. Belov, A. Karabchevsky, A. B. Evlyukhin, Y. Kivshar, and A. S. Shalin, "Transverse scattering and generalized Kerker effects in all-dielectric Mie-resonant metaoptics," *Physical review letters*, vol. 122, no. 19, p. 193905, 2019. 51

[14] H. K. Shamkhi, A. Sayanskiy, A. C. Valero, A. S. Kupriianov, P. Kapitanova, Y. S. Kivshar, A. S. Shalin, and V. R. Tuz, "Transparency and perfect absorption of all-dielectric resonant metasurfaces governed by the transverse Kerker effect," *Physical Review Materials*, vol. 3, no. 8, p. 085201, 2019. 51

[15] M. F. Picardi, A. V. Zayats, and F. J. Rodriguez-Fortuno, "Janus and Huygens dipoles, near-field directionality beyond spin-momentum locking," *Physical review letters*, vol. 120, no. 11, p. 117402, 2018. 52

[16] T. Wu, A. Baron, P. Lalanne, and K. Vynck, "Intrinsic multipolar contents of nanoresonators for tailored scattering," *arXiv preprint arXiv:1907.04598*, 2019. 52

[17] J. E. Vazquez-Lozano, A. Martinez, and F. J. Rodriguez-Fortuno, "Near-field directionality beyond the dipole approximation: Electric quadrupole and higher-order multipole angular spectra," *Phys. Rev. Applied*, vol. 12, p. 024065, 2019. 52

[18] R. Dezert, P. Richetti, and A. Baron, "Isotropic Huygens dipoles and multipoles with colloidal particles," *Physical Review B*, vol. 96, no. 18, p. 180201, 2017. viii, 47, 52, 59

[19] A. B. Evlyukhin, S. M. Novikov, U. Zywietz, R. L. Eriksen, C. Reinhardt, S. I. Bozhevolnyi, and B. N. Chichkov, "Demonstration of magnetic dipole resonances of dielectric nanospheres in the visible region," *Nano letters*, vol. 12, no. 7, pp. 3749–3755, 2012. 52

[20] A. I. Kuznetsov, A. E. Miroshnichenko, Y. H. Fu, J. Zhang, and B. Luk'Yanchuk, "Magnetic light," *Scientific reports*, vol. 2, p. 492, 2012. 52

[21] A. Garcia-Etxarri, R. Gómez-Medina, L. S. Froufe-Perez, C. Lopez, L. Chantada, F. Scheffold, J. Aizpurua, M. Nieto-Vesperinas, and J. J. Sáenz, "Strong magnetic response of submicron silicon particles in the infrared," *Optics express*, vol. 19, no. 6, pp. 4815–4826, 2011. 52

[22] J.-M. Geffrin, B. García-Cámara, R. Gómez-Medina, P. Albella, L. Froufe-Pérez, C. Eyraud, A. Litman, R. Vaillon, F. González, M. Nieto-Vesperinas, *et al.*, "Magnetic and electric coherence in forward-and back-scattered electromagnetic waves by a single dielectric subwavelength sphere," *Nature communications*, vol. 3, p. 1171, 2012. 52

[23] Y. H. Fu, A. I. Kuznetsov, A. E. Miroshnichenko, Y. F. Yu, and B. Luk'yanchuk, "Directional visible light scattering by silicon nanoparticles," *Nature communications*, vol. 4, p. 1527, 2013. 52

[24] S. Person, M. Jain, Z. Lapin, J. J. Sáenz, G. Wicks, and L. Novotny, "Demonstration of zero optical backscattering from single nanoparticles," *Nano letters*, vol. 13, no. 4, pp. 1806–1809, 2013. 52

[25] I. Staude, A. E. Miroshnichenko, M. Decker, N. T. Fofang, S. Liu, E. Gonzales, J. Dominguez, T. S. Luk, D. N. Neshev, I. Brener, *et al.*, "Tailoring directional scattering through magnetic and electric resonances in subwavelength silicon nanodisks," *ACS nano*, vol. 7, no. 9, pp. 7824–7832, 2013. 52

[26] A. B. Evlyukhin, C. Reinhardt, and B. N. Chichkov, "Multipole light scattering by nonspherical nanoparticles in the discrete dipole approximation," *Physical Review B*, vol. 84, no. 23, p. 235429, 2011. 52

[27] P. D. Terekhov, K. V. Baryshnikova, A. S. Shalin, A. Karabchevsky, and A. B. Evlyukhin, "Resonant forward scattering of light by high-refractive-index dielectric nanoparticles with toroidal dipole contribution," *Optics Letters*, vol. 42, no. 4, pp. 835–838, 2017. 52

[28] B. S. Luk'yanchuk, N. V. Voshchinnikov, R. Paniagua-Domínguez, and A. I. Kuznetsov, "Optimum forward light scattering by spherical and spheroidal dielectric nanoparticles with high refractive index," *ACS Photonics*, vol. 2, no. 7, pp. 993–999, 2015. 52, 54

[29] Z. Wang, N. An, F. Shen, H. Zhou, Y. Sun, Z. Jiang, Y. Han, Y. Li, and Z. Guo, "Enhanced forward scattering of ellipsoidal dielectric nanoparticles," *Nanoscale research letters*, vol. 12, no. 1, p. 58, 2017. 52

[30] Y. Yang, A. E. Miroshnichenko, S. V. Kostinski, M. Odit, P. Kapitanova, M. Qiu, and Y. S. Kivshar, "Multimode directionality in all-dielectric metasurfaces," *Physical Review B*, vol. 95, no. 16, p. 165426, 2017. 52

[31] H.-S. Ee, J.-H. Kang, M. L. Brongersma, and M.-K. Seo, "Shape-dependent light scattering properties of subwavelength silicon nanoblocks," *Nano letters*, vol. 15, no. 3, pp. 1759–1765, 2015. 52

[32] S. Campione, L. I. Basilio, L. K. Warne, and M. B. Sinclair, "Tailoring dielectric resonator geometries for directional scattering and Huygens' metasurfaces," *Optics Express*, vol. 23, no. 3, pp. 2293–2307, 2015. 52

[33] Y. Wang, X. Zeng, E. Yang, Y. Lu, D. Zhang, and P. Wang, "Tailoring magnetic and electric resonances with dielectric nanocubes for broadband and high-efficiency unidirectional scattering," *Chinese Optics Letters*, vol. 14, no. 1, p. 011601, 2016. 52

[34] C. F. Bohren and D. R. Huffman, *Absorption and scattering of light by small particles*. John Wiley & Sons, 2008. 52, 71

[35] Y. Zhang, M. Nieto-Vesperinas, and J. J. Sáenz, "Dielectric spheres with maximum forward scattering and zero backscattering: a search for their material composition," *Journal of Optics*, vol. 17, no. 10, p. 105612, 2015. 54

[36] M. I. Abdelrahman, C. Rockstuhl, and I. Fernandez-Corbaton, "Broadband suppression of backscattering at optical frequencies using low permittivity dielectric spheres," *Scientific reports*, vol. 7, no. 1, p. 14762, 2017. 57

[37] M. I. Abdelrahman, H. Saleh, I. Fernandez-Corbaton, B. Gralak, J.-M. Geffrin, and C. Rockstuhl, "Experimental demonstration of spectrally broadband Huygens sources using low-index spheres," *APL Photonics*, vol. 4, no. 2, p. 020802, 2019. 57

[38] "Refractive index database." https://refractiveindex.info. 57

[39] P. Terekhov, H. Shamkhi, E. Gurvitz, K. Baryshnikova, A. Evlyukhin, A. Shalin, and A. Karabchevsky, "Broadband forward scattering from dielectric cubic nanoantenna in lossless media," *Optics express*, vol. 27, no. 8, pp. 10924–10935, 2019. 59

[40] Y. Cho, J.-H. Huh, K. J. Park, K. Kim, J. Lee, and S. Lee, "Using highly uniform and smooth selenium colloids as low-loss magnetodielectric building blocks of optical metafluids," *Optics express*, vol. 25, no. 12, pp. 13822–13833, 2017. 59

[41] S. Zhang, R. Jiang, Y.-M. Xie, Q. Ruan, B. Yang, J. Wang, and H.-Q. Lin, "Colloidal moderate-refractive-index Cu_2O nanospheres as visible-region nanoantennas with electromagnetic resonance and directional light-scattering properties," *Advanced Materials*, vol. 27, no. 45, pp. 7432–7439, 2015. 59

[42] N. L. Sharma, "Nondipole optical scattering from liquids and nanoparticles," *Physical review letters*, vol. 98, no. 21, p. 217402, 2007. 59

[43] V. Ponsinet, P. Barois, S. M. Gali, P. Richetti, J.-B. Salmon, A. Vallecchi, M. Albani, A. Le Beulze, S. Gomez-Grana, E. Duguet, *et al.*, "Resonant isotropic optical magnetism of plasmonic nanoclusters in visible light," *Physical Review B*, vol. 92, no. 22, p. 220414, 2015. 59

[44] V. Many, R. Dézert, E. Duguet, A. Baron, V. Jangid, V. Ponsinet, S. Ravaine, P. Richetti, P. Barois, and M. Tréguer-Delapierre, "High optical magnetism of dodecahedral plasmonic meta-atoms," *Nanophotonics*, vol. 8, no. 4, pp. 549–558, 2019. 59

[45] F. Monticone and A. Alù, "The quest for optical magnetism: from split-ring resonators to plasmonic nanoparticles and nanoclusters," *Journal of Materials Chemistry C*, vol. 2, no. 43, pp. 9059–9072, 2014. 59

[46] F. Shafiei, F. Monticone, K. Q. Le, X.-X. Liu, T. Hartsfield, A. Alù, and X. Li, "A subwavelength plasmonic metamolecule exhibiting magnetic-based optical fano resonance," *Nature nanotechnology*, vol. 8, no. 2, p. 95, 2013. 59

[47] C. Rockstuhl and T. Scharf, *Amorphous Nanophotonics*. Springer Science & Business Media, 2013. 59, 70

[48] C. Simovski and S. Tretyakov, "Model of isotropic resonant magnetism in the visible range based on core-shell clusters," *Physical Review B*, vol. 79, no. 4, p. 045111, 2009. 59, 60

[49] A. Vallecchi, M. Albani, and F. Capolino, "Collective electric and magnetic plasmonic resonances in spherical nanoclusters," *Optics Express*, vol. 19, no. 3, pp. 2754–2772, 2011. 59

[50] S. Mühlig, A. Cunningham, S. Scheeler, C. Pacholski, T. Burgi, C. Rockstuhl, and F. Lederer, "Self-assembled plasmonic core–shell clusters with an isotropic magnetic dipole response in the visible range," *ACS nano*, vol. 5, no. 8, pp. 6586–6592, 2011. 59

[51] M. Fruhnert, S. Mühlig, F. Lederer, and C. Rockstuhl, "Towards negative index self-assembled metamaterials," *Physical Review B*, vol. 89, no. 7, p. 075408, 2014. 59

[52] Z. Qian, S. P. Hastings, C. Li, B. Edward, C. K. McGinn, N. Engheta, Z. Fakhraai, and S.-J. Park, "Raspberry-like metamolecules exhibiting strong magnetic resonances," *ACS nano*, vol. 9, no. 2, pp. 1263–1270, 2015. 59

[53] M. R. Bourgeois, A. T. Liu, M. B. Ross, J. M. Berlin, and G. C. Schatz, "Self-assembled plasmonic metamolecules exhibiting tunable magnetic response at optical frequencies," *The Journal of Physical Chemistry C*, vol. 121, no. 29, pp. 15915–15921, 2017. 59, 70

[54] C. Li, S. Lee, Z. Qian, C. Woods, S.-J. Park, and Z. Fakhraai, "Controlling magnetic dipole resonance in raspberry-like metamolecules," *The Journal of Physical Chemistry C*, vol. 122, no. 12, pp. 6808–6817, 2018. 59

[55] C. Rockstuhl, F. Lederer, C. Etrich, T. Pertsch, and T. Scharf, "Design of an artificial three-dimensional composite metamaterial with magnetic resonances in the visible range of the electromagnetic spectrum," *Physical review letters*, vol. 99, no. 1, p. 017401, 2007. 59, 60

[56] A. Alù and N. Engheta, "The quest for magnetic plasmons at optical frequencies," *Optics express*, vol. 17, no. 7, pp. 5723–5730, 2009. 59, 60

[57] J. Dintinger, S. Mühlig, C. Rockstuhl, and T. Scharf, "A bottom-up approach to fabricate optical metamaterials by self-assembled metallic nanoparticles," *Optical Materials Express*, vol. 2, no. 3, pp. 269–278, 2012. 59, 60, 70

[58] S. Mühlig, C. Rockstuhl, V. Yannopapas, T. Bürgi, N. Shalkevich, and F. Lederer, "Optical properties of a fabricated self-assembled bottom-up bulk metamaterial," *Optics express*, vol. 19, no. 10, pp. 9607–9616, 2011. 59, 60

[59] A. Alù, A. Salandrino, and N. Engheta, "Negative effective permeability and left-handed materials at optical frequencies," *Optics express*, vol. 14, no. 4, pp. 1557–1567, 2006. 59, 68

[60] A. Alù and N. Engheta, "Dynamical theory of artificial optical magnetism produced by rings of plasmonic nanoparticles," *Physical Review B*, vol. 78, no. 8, p. 085112, 2008. 59

[61] W. T. Doyle, "Optical properties of a suspension of metal spheres," *Physical review B*, vol. 39, no. 14, p. 9852, 1989. 60

[62] J. M. Garnett, "Xii. colours in metal glasses and in metallic films," *Philosophical Transactions of the Royal Society of London. Series A, Containing Papers of a Mathematical or Physical Character*, vol. 203, no. 359-371, pp. 385–420, 1904. 60

[63] C. F. Bohren, "Applicability of effective-medium theories to problems of scattering and absorption by nonhomogeneous atmospheric particles," *Journal of the atmospheric sciences*, vol. 43, no. 5, pp. 468–475, 1986. 61

[64] R. Ruppin, "Evaluation of extended Maxwell-Garnett theories," *Optics communications*, vol. 182, no. 4-6, pp. 273–279, 2000. 61

[65] B. Clare and D. Kepert, "The closest packing of equal circles on a sphere," *Proceedings of the Royal Society of London. A. Mathematical and Physical Sciences*, vol. 405, no. 1829, pp. 329–344, 1986. 61

[66] D. Kottwitz, "The densest packing of equal circles on a sphere," *Acta Crystallographica Section A: Foundations of Crystallography*, vol. 47, no. 3, pp. 158–165, 1991. 61

[67] E. D. Palik, *Handbook of optical constants of solids*, vol. 3. Academic press, 1998. 62, 70

[68] D. E. Aspnes and A. Studna, "Dielectric functions and optical parameters of *Si*, *Ge*, *GaP*, *GaAs*, *GaSb*, *InP*, *InAs*, and *InSb* from 1.5 to 6.0 eV," *Physical review B*, vol. 27, no. 2, p. 985, 1983. 62

[69] D. W. Mackowski, "Multiple sphere T-Matrix (MSTM) code." `http://www.eng.auburn.edu/~dmckwski/scatcodes/`. 63

[70] P. B. Johnson and R.-W. Christy, "Optical constants of the noble metals," *Physical review B*, vol. 6, no. 12, p. 4370, 1972. 68, 70

[71] A. Vallecchi, M. Albani, and F. Capolino, "Effect of irregularities of nanosatellites position and size on collective electric and magnetic plasmonic resonances in spherical nanoclusters," *Optics express*, vol. 21, no. 6, pp. 7667–7685, 2013. 69

[72] A. S. Urban, X. Shen, Y. Wang, N. Large, H. Wang, M. W. Knight, P. Nordlander, H. Chen, and N. J. Halas, "Three-dimensional plasmonic nanoclusters," *Nano letters*, vol. 13, no. 9, pp. 4399–4403, 2013. 70

[73] J. K. Stolarczyk, A. Deak, and D. F. Brougham, "Nanoparticle clusters: assembly and control over internal order, current capabilities, and future potential," *Advanced materials*, vol. 28, no. 27, pp. 5400–5424, 2016. 70

[74] J. Lacava, P. Born, and T. Kraus, "Nanoparticle clusters with Lennard-Jones geometries," *Nano letters*, vol. 12, no. 6, pp. 3279–3282, 2012. 70

[75] A. Sánchez-Iglesias, M. Grzelczak, T. Altantzis, B. Goris, J. Perez-Juste, S. Bals, G. Van Tendeloo, S. H. Donaldson Jr, B. F. Chmelka, J. N. Israelachvili, *et al.*, "Hydrophobic interactions modulate self-assembly of nanoparticles," *ACS nano*, vol. 6, no. 12, pp. 11059–11065, 2012. 70

[76] V. A. Turek, Y. Francescato, P. Cadinu, C. R. Crick, L. Elliott, Y. Chen, V. Urland, A. P. Ivanov, L. Velleman, M. Hong, *et al.*, "Self-assembled spherical supercluster metamaterials from nanoscale building blocks," *Acs Photonics*, vol. 3, no. 1, pp. 35–42, 2015. 70

[77] L. Wang and J. Wang, "Self-assembly of colloids based on microfluidics," *Nanoscale*, vol. 11, no. 36, pp. 16708–16722, 2019. 70

[78] J. Schmitt, S. Hajiw, A. Lecchi, J. Degrouard, A. Salonen, M. Impéror-Clerc, and B. Pansu, "Formation of superlattices of gold nanoparticles using Ostwald ripening in emulsions: transition from fcc to bcc structure," *The Journal of Physical Chemistry B*, vol. 120, no. 25, pp. 5759–5766, 2016. 70

[79] R. Paniagua-Domínguez, F. López-Tejeira, R. Marqués, and J. A. Sánchez-Gil, "Metallo-dielectric core–shell nanospheres as building blocks for optical three-dimensional isotropic negative-index metamaterials," *New Journal of Physics*, vol. 13, no. 12, p. 123017, 2011. 70

[80] W. Liu, A. E. Miroshnichenko, D. N. Neshev, and Y. S. Kivshar, "Broadband unidirectional scattering by magneto-electric core–shell nanoparticles," *ACS nano*, vol. 6, no. 6, pp. 5489–5497, 2012. 70

[81] W. Liu, A. E. Miroshnichenko, R. F. Oulton, D. N. Neshev, O. Hess, and Y. S. Kivshar, "Scattering of core-shell nanowires with the interference of electric and magnetic resonances," *Optics letters*, vol. 38, no. 14, pp. 2621–2624, 2013. 70

[82] A. L. Aden and M. Kerker, "Scattering of electromagnetic waves from two concentric spheres," *Journal of Applied Physics*, vol. 22, no. 10, pp. 1242–1246, 1951. 71

[83] L. Kai and P. Massoli, "Scattering of electromagnetic-plane waves by radially inhomogeneous spheres: a finely stratified sphere model," *Applied optics*, vol. 33, no. 3, pp. 501–511, 1994. 71

[84] J.-P. Schäfer, *Implementierung und Anwendung analytischer und numerischer Verfahren zur Lösung der Maxwellgleichungen für die Untersuchung der Lichtausbreitung in biologischem Gewebe*. PhD thesis, Verlag nicht ermittelbar, 2011. 71

[85] J. Schäfer, "Matscat, MATLAB package solving the scattering of electromagnetic radiation by stratified spheres or cylinders." https://www.mathworks.com/matlabcentral/fileexchange/36831-matscat. 71

[86] R. Ghosh Chaudhuri and S. Paria, "Core/shell nanoparticles: classes, properties, synthesis mechanisms, characterization, and applications," *Chemical reviews*, vol. 112, no. 4, pp. 2373–2433, 2011. 73

[87] K. Aslan, M. Wu, J. R. Lakowicz, and C. D. Geddes, "Fluorescent core-shell $Ag@SiO_2$ nanocomposites for metal-enhanced fluorescence and single nanoparticle sensing platforms," *Journal of the American Chemical Society*, vol. 129, no. 6, pp. 1524–1525, 2007. 73

[88] J. Yang, F. Zhang, Y. Chen, S. Qian, P. Hu, W. Li, Y. Deng, Y. Fang, L. Han, M. Luqman, *et al.*, "Core-shell $Ag@SiO_2@mSiO_2$ mesoporous nanocarriers for metal-enhanced fluorescence," *Chemical Communications*, vol. 47, no. 42, pp. 11618–11620, 2011. 73

[89] R. T. Tom, A. S. Nair, N. Singh, M. Aslam, C. Nagendra, R. Philip, K. Vijayamohanan, and T. Pradeep, "Freely dispersible $Au@TiO_2$, $Au@ZrO_2$, $Ag@TiO_2$, and $Ag@ZrO_2$ core-shell nanoparticles: one-step synthesis, characterization, spectroscopy, and optical limiting properties," *Langmuir*, vol. 19, no. 8, pp. 3439–3445, 2003. 73

[90] N. Cathcart, N. Murshid, P. Campbell, and V. Kitaev, "Selective plasmonic sensing and highly ordered metallodielectrics via encapsulation of plasmonic metal nanoparticles with metal oxides," *ACS Applied Nano Materials*, vol. 1, no. 11, pp. 6514–6524, 2018. 73

[91] Y. Li, L. Shao, F. Zhong, P. Ding, B. Chu, F. Luo, K. Xu, F. Zeng, and Y. Du, "Light control based on unidirectional scattering in metal–dielectric core–shell nanoparticles," *Optics Communications*, vol. 426, pp. 483–489, 2018. 73

[92] W. Liu, B. Lei, J. Shi, and H. Hu, "Unidirectional superscattering by multilayered cavities of effective radial anisotropy," *Scientific reports*, vol. 6, p. 34775, 2016. 73

[93] Y. Tsuchimoto, T.-a. Yano, T. Hayashi, and M. Hara, "Fano resonant all-dielectric core/shell nanoparticles with ultrahigh scattering directionality in the visible region," *Optics express*, vol. 24, no. 13, pp. 14451–14462, 2016. 73

[94] R. Li, X. Zhou, M. Panmai, J. Xiang, H. Liu, M. Ouyang, H. Fan, Q. Dai, and Z. Wei, "Broadband zero backward scattering by all-dielectric core-shell nanoparticles," *Optics express*, vol. 26, no. 22, pp. 28891–28901, 2018. 73

[95] R. R. Naraghi, S. Sukhov, and A. Dogariu, "Directional control of scattering by all-dielectric core-shell spheres," *Optics letters*, vol. 40, no. 4, pp. 585–588, 2015. 73

Chapter 4

Metasurface Analysis

Contents

4.1 Interaction of light with a metasurface 84
4.1.1 Surface equivalence principle and generalized boundary conditions 85
4.1.2 Boundary conditions expressed with surface impedances and admittances 86
4.1.3 Transmission line formalism using impedance, scattering and chain matrix 87
4.1.4 Equivalent circuit of metasurfaces 89
4.2 Metasurface analysis in the dipole approximation 91
4.2.1 Effective polarisabilities 91
4.2.2 Induced averaged current densities and surface impedance 92
4.2.3 Metasurface properties expressed with effective polarisabilities 93
4.2.4 Coupled dipole method 93
4.2.5 Lorentzian model 96
4.3 Rigorous analysis of multipolar metasurfaces 97
4.3.1 Link between emitted fields and current sources for periodic arrays 97
4.3.2 Multipole expansion of metasurface properties in spherical coordinates . . 98
4.3.3 Link with cartesian expansion 103
4.4 Concluding remarks 104
4.5 References 105

Summary: This chapter aims to introduce different analytic tools used to analyze or compute the properties of metasurfaces. Firstly, we will see that periodic arrays can be described in terms of equivalent surface current sources satisfying specific boundary conditions. After introducing the transmission line formalism, these boundary conditions will be used to derive the equivalent circuit representations of different kind of metasurfaces. From there, we will seek to get a physical insight into the origin of metasurfaces features. A first section will address this issue assuming metasurfaces under the dipole approximation. The coupled dipole model, used to semi-analytically compute the coupling term existing between dipolar particles, will be introduced, as well as its simplified version relying on the hypothesis of particles exhibiting resonances of a lorentzian spectral form. Finally in the last section, a generalized formalism that links metasurface properties to the multipole coefficients of their constituent meta-atom will be presented. This multipole decomposition evidences the role of symmetric and anti-symmetric multipoles in the absorption and radiation properties of a metasurface.

4.1 Interaction of light with a metasurface

Metasurfaces (MSs) are two-dimensional arrays of resonant subwavelength scatterers, called meta-atoms, organized with a subwavelength separation. These ultra thin nanostructured layers are used and designed to modify different aspects of an incoming radiation. Size, shape, material and spatial arrangement of its constituent elements can be properly chosen to locally control the amplitude, phase, polarization or spectrum of the incoming excitation both in reflection or transmission.

The principle of interaction between light and a metasurface is illustrated in Fig. 4.1-A. Along this chapter, we shall consider an incident plane wave $\vec{E}_{inc}$ propagating along $\vec{e}_z$ under normal incidence on a periodic array of identical particles placed in an homogeneous space.

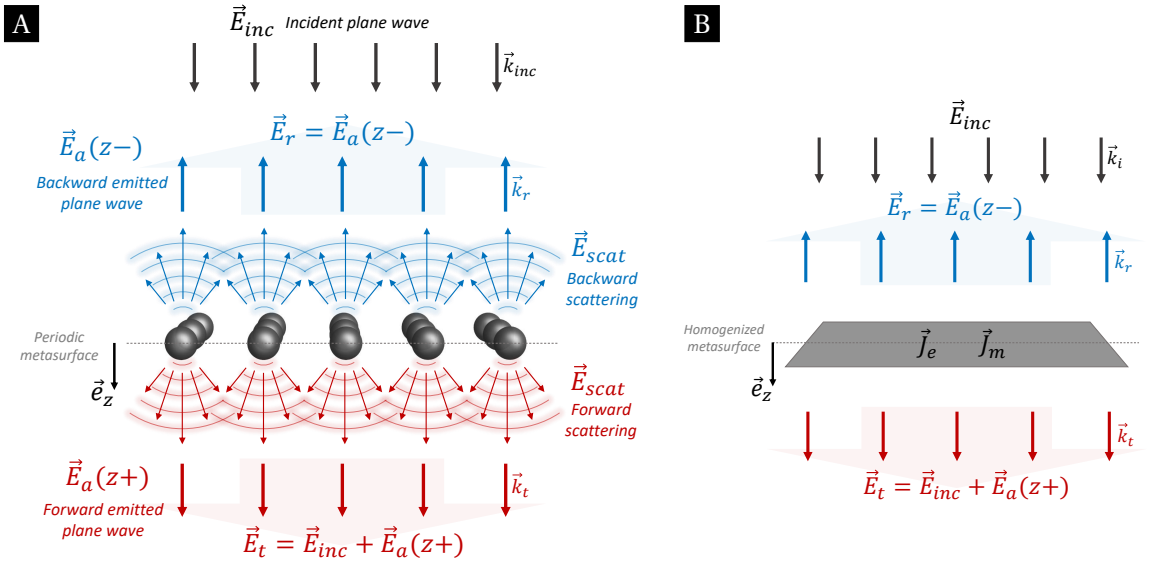

Figure 4.1 – A) Interaction between light and a metasurface. An incident plane wave $\vec{E}_{inc}$ propagating along $\vec{e}_z$ impinges the metasurface at normal incidence. Each meta-atom scatters a field $\vec{E}_{scat}$. The field emitted by the array is $\vec{E}_a$. The reflected $\vec{E}_r$ and transmitted $\vec{E}_t$ waves are defined on each side of the array. B) The metasurface can equivalently be seen as a thin sheet with induced electric and magnetic surface current densities $\vec{J}_e$ and $\vec{J}_m$ at the origin of the emitted waves.

Each meta-atom of the array is optically excited and re-radiates a field $\vec{E}_{scat}$. Compared to the case of isolated nanostructures, the excitation of a scatterer in the array is due to the presence of both the incident wave and the radiation produced by the neighboring particles impinging on the considered element. Thus, it exists an interaction coupling between the particles. The response of the array to the incident wave is the result of interferences between the waves scattered by each of its constituent particles:

$$\vec{E}_a = \sum_{j=1}^{N_b} \vec{E}_{scat,j} \tag{4.1}$$

where $\vec{E}_a$ is the net field produced by the array and N_b is the number of particles. In the case of a periodic arrangement of identical meta-atoms, this response simply consists of two plane waves $\vec{E}_a(z+)$ and $\vec{E}_a(z-)$ emitted on both sides of the metasurface (*i.e.* respectively along $+\vec{e}_z$ for $z > 0$ and $-\vec{e}_z$ for $z < 0$). In the forward direction, the wave scattered by the array interferes with the incident one to produce the transmitted wave $\vec{E}_t$:

$$\vec{E}_t = \vec{E}_{inc} + \vec{E}_a(z+) \tag{4.2}$$

while in the backward direction the reflected wave is directly given by the emitted wave:

$$\vec{E}_r = \vec{E}_a(z-) \tag{4.3}$$

Finally, the total field is given by the superposition of the incident and scattered field:

$$\vec{E}_{tot} = \vec{E}_{inc} + \vec{E}_a \tag{4.4}$$

Therefore in the forward direction, for positive z, the total field simply reads:

$$\vec{E}_{tot}(z+) = \vec{E}_t \tag{4.5}$$

while in the backward direction, for negative z, it reads:

$$\vec{E}_{tot}(z-) = \vec{E}_{inc} + \vec{E}_r \tag{4.6}$$

With this part, we have clarified the notations adopted to refer to the different fields involved when describing the interaction of light with a metasurface. The notations presented here for the electric fields also stand for the magnetic fields.

This chapter aims at introducing different analytic tools used to analyze or compute the properties of metasurfaces. First of all, we will present in the following part how metasurfaces can be described in terms of equivalent surface currents from the equivalence principle, or in terms of surface impedance and admittance as used in the transmission line formalism. Section 4.2 is then devoted to the study of metasurfaces assuming a dipolar behavior of its resonators. The coupled dipole model, used to semi-analytically compute the coupling term between dipolar particles, will be introduced, as well as its simplified version relying on the hypothesis of resonances having lorentzian shapes. Finally, in section 4.3 we will show that the link between the fields scattered by the meta-atoms and the emitted plane waves (illustrated by equation 4.1) enables for a general description of metasurface properties in terms of the multipolar coefficients (up to any degree) of the particles in the array.

4.1.1 Surface equivalence principle and generalized boundary conditions

The surface equivalence principle is a powerful tool in electromagnetism. It was first developed by Love [1] and later generalized by Schelkunoff [2] and it states that fictitious electric and magnetic surface currents can be introduced on a surface to produce arbitrary independent field distributions in the two regions of space separated by this surface. The introduced electric and magnetic currents satisfy the generalized boundary conditions expressing the discontinuity of the tangential fields across the surface:

$$\vec{n} \wedge (\vec{H}_2 - \vec{H}_1) = \vec{J}_e \tag{4.7}$$

$$\vec{n} \wedge (\vec{E}_2 - \vec{E}_1) = -\vec{J}_m \tag{4.8}$$

where $\vec{n}$ is a unit vector normal to the surface and where the subscript $_1$ or $_2$ indicates fields on the two different sides of the boundary. In particular, 2 designates the region of space in the direction given by the normal $\vec{n}$.

Using the equivalence principle, the real metasurface acting as a 2D discontinuity can be homogenized and substituted by an equivalent infinitely thin sheet with excited surface currents $\vec{J}_e$ and $\vec{J}_m$ that rigorously produce the same field as the true array. This idea is illustrated by the two schematic equivalent descriptions of the problem presented on Figs. 4.1-A for the particle grid and on Fig. 4.1-B for the homogenized ultra-thin layer. In this case the two current densities $\vec{J}_e$ and $\vec{J}_m$ are all that are required to model the interaction between light and the metasurface. Of course this description is only valid in the far field domain. Furthermore, it is important to note that the reverse approach is usually that followed when designing metasurfaces: given a desired field distribution for an application, one may later engineer the meta-atoms to locally reproduce the required electric and magnetic surface currents derived by the boundary conditions.

We now consider the infinitesimally thin sheet with fictitious surface currents used as an homogenization of the metasurface (Fig. 4.1-B). We use the notations presented on Fig. 4.2, and denote by the subscript 1 the fields in the back half space with negative z and by 2 the field in the front half space with positive z.

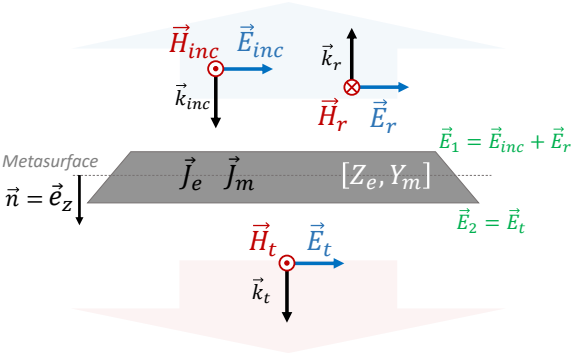

Figure 4.2 – Schematic view of an infinitesimally thin sheet with fictitious surface current $\vec{J}_e$ and $\vec{J}_m$. The boundary conditions relate those currents to the discontinuity of the tangential field $(\vec{E}_1, \vec{H}_1)$ and $(\vec{E}_2, \vec{H}_2)$ on both sides of the surface which can be expressed in terms of incident $(\vec{E}_{inc}, \vec{H}_{inc})$, reflected $(\vec{E}_r, \vec{H}_r)$ and transmitted $(\vec{E}_t, \vec{H}_t)$ fields.

Applying the boundary conditions (4.7,4.8) to the metasurface and using $\vec{E}_2 = \vec{E}_t$ and $\vec{E}_1 = \vec{E}_{inc} + \vec{E}_r$, the transmitted and reflected field can be expressed. They read:

$$\vec{E}_t = \vec{E}_{inc} - \frac{1}{2}(\eta \vec{J}_e - \vec{n} \wedge \vec{J}_m) \qquad \vec{H}_t = \vec{H}_{inc} - \frac{1}{2}\left(-\vec{n} \wedge \vec{J}_e + \frac{\vec{J}_m}{\eta}\right) \tag{4.9}$$

$$\vec{E}_r = -\frac{1}{2}(\eta \vec{J}_e + \vec{n} \wedge \vec{J}_m) \qquad \vec{H}_r = -\frac{1}{2}\left(\vec{n} \wedge \vec{J}_e + \frac{\vec{J}_m}{\eta}\right) \tag{4.10}$$

The fields emitted in the forward and backward directions are simply given by:

$$\vec{E}_a(z+) = -\frac{1}{2}(\eta \vec{J}_e - \vec{n} \wedge \vec{J}_m) \tag{4.11}$$

$$\vec{E}_a(z-) = -\frac{1}{2}(\eta \vec{J}_e + \vec{n} \wedge \vec{J}_m) \tag{4.12}$$

These two last relations contain an important physical result: The electric and magnetic surface currents produce different (odd and even) types of symmetry for the radiated fields. The electric surface current $\vec{J}_e$ radiates an even distribution of electric field $-\frac{1}{2}(\eta \vec{J}_e)$ while the magnetic surface current $\vec{J}_m$ radiates an odd distribution given by $\pm\frac{1}{2}(\vec{n} \wedge \vec{J}_m)$ with opposite signs in each half space delimited by the metasurface. Therefore, equations (4.11) and (4.12) are general relations expressing the decomposition of the field emitted by a metasurface in terms of even and odd contributions given by equivalent electric and magnetic surface current densities.

4.1.2 Boundary conditions expressed with surface impedances and admittances

The surface equivalence principle is formulated in terms of surface currents at a boundary. However for designing metasurfaces, it may be appropriate to express the problem as an impedance boundary condition.

The surface currents taking place on the considered thin boundary can be related to the averaged tangential local field experienced by the metasurface through an electric surface impedance Z_e and a magnetic surface admittance Y_m defined by:

$$\vec{E}_{av} = Z_e \vec{J}_e \tag{4.13}$$

$$\vec{H}_{av} = Y_m \vec{J}_m \tag{4.14}$$

where $\vec{H}_{av}$ and $\vec{E}_{av}$ are the averaged values of the tangential fields taken from both sides of the array:

$$\vec{E}_{av} = \frac{\vec{E}_1 + \vec{E}_2}{2} = \frac{\vec{E}_{inc} + \vec{E}_r + \vec{E}_t}{2} \tag{4.15}$$

$$\vec{H}_{av} = \frac{\vec{H}_1 + \vec{H}_2}{2} = \frac{\vec{H}_{inc} + \vec{H}_r + \vec{H}_t}{2} \tag{4.16}$$

These averaged quantities are introduced as approximate values of the fields at the position $z = 0$ of the surface in the case of a sufficiently low refractive index contrast between the front and back media (here the front and back media are the same as the metasurface is supposed to be placed in an homogeneous environment). For simplicity, we assume that the metasurface is isotropic so that the sheet impedance and admittance reduce to a scalar, however they are tensorial quantities in the general case of anisotropic surfaces.

Combining the definitions (4.13,4.14) with the generalized boundary conditions (4.7,4.8), leads to two relations known as the generalized sheet transition conditions (GSTCs) [3–5] expressed in terms of surface impedance and admittance:

$$\frac{1}{2}\left(\vec{E}_1 + \vec{E}_2\right) = Z_e\left[\vec{n} \wedge (\vec{H}_2 - \vec{H}_1)\right] \tag{4.17}$$

$$\frac{1}{2}\left(\vec{H}_1 + \vec{H}_2\right) = -Y_m\left[\vec{n} \wedge (\vec{E}_2 - \vec{E}_1)\right] \tag{4.18}$$

These expressions link the tangential fields on both sides of the surface discontinuity. In addition, from equations (4.9) and (4.10), the average fields can be written as:

$$\vec{E}_{av} = \vec{E}_{inc} - \frac{1}{2}\eta\vec{J}_e \qquad \vec{H}_{av} = \vec{H}_{inc} - \frac{1}{2}\frac{\vec{J}_m}{\eta} \tag{4.19}$$

allowing to express the surface impedance and admittance as:

$$Z_e = \frac{\left|\vec{E}_{inc}\right|}{\left|\vec{J}_e\right|} - \frac{\eta}{2} \qquad Y_m = \frac{\left|\vec{H}_{inc}\right|}{\left|\vec{J}_m\right|} - \frac{1}{2\eta} \tag{4.20}$$

or equivalently the current densities as:

$$\vec{J}_e = \frac{\vec{E}_{inc}}{Z_e + \eta/2} \qquad \vec{J}_m = \frac{\vec{H}_{inc}}{Y_m + 1/2\eta} \tag{4.21}$$

These last relations underline the link existing between the two descriptions with currents or impedances: for a given incident field, by properly adjusting the surface impedance/admittance Z_e and Y_m when designing the metasurface, the required surface currents will be induced and generate the targeted fields.

4.1.3 Transmission line formalism using impedance, scattering and chain matrix

The transmission line model was introduced in 1885 by Oliver Heaviside to describe current and voltage waves propagation in cables. This formalism is widely used for guided communication systems and especially in microwave engineering. The waves equations giving the dependence of harmonic voltage V and current I on a guided structure are known as the telegrapher's equations, which can be written as:

$$\frac{d^2V}{dz^2} + k^2V = 0 \tag{4.22}$$

$$\frac{d^2I}{dz^2} + k^2I = 0 \tag{4.23}$$

where k is the propagation constant and z the spatial position along the line.

Due to the similarity between the telegrapher's equations and the wave equations for unguided electromagnetic plane waves, the transmission line model can be used in optics for solving propagation problems. Simple circuit analysis thus makes it possible to address the multiple reflections and transmissions occurring in cascaded material slabs and cascaded 2D interfaces. With this analogy, it is possible to model metasurfaces as an equivalent electric circuit taking the form of a 2-port network. As illustrated on Fig. 4.3-B electric and magnetic field intensities $\vec{E}_1$,$\vec{E}_2$,$\vec{H}_1$ and $\vec{H}_2$ of the plane waves respectively replace the voltages and currents V_1,V_2,I_1 and I_2 of the conventional 2-port networks presented in Fig. 4.3-A.

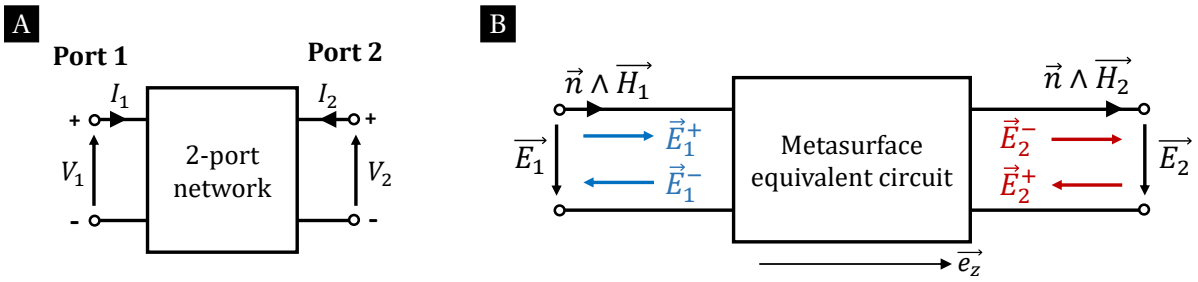

Figure 4.3 – A) Representation of the usual convention for a 2-port network. B) Description of a metasurface through a 2-port network. $\vec{E}_1^-$,$\vec{E}_2^-$ designate the outward fields on the ports and $\vec{E}_1^+$,$\vec{E}_2^+$ the inward fields.

The following subsections aim at introducing different matrix representations used to characterize a 2-port network. We will use the sign conventions for the fields presented in Fig. 4.3-B where $\vec{n} \wedge \vec{H}_1$ is defined as incoming in the network while $\vec{n} \wedge \vec{H}_2$ is outgoing. In additions, for later convenience, like in [6], the electric fields are represented with opposite directions compared to the usual convention adopted for the tension V of a network.

4.1.3.a Impedance matrix $[Z]$

The metasurface can be characterized by an impedance matrix relating the electric fields to the magnetic ones as:

$$\begin{pmatrix} -\vec{E}_1 \\ -\vec{E}_2 \end{pmatrix} = \begin{pmatrix} Z_{11} & Z_{12} \\ Z_{21} & Z_{22} \end{pmatrix} \begin{pmatrix} \vec{n} \wedge \vec{H}_1 \\ -\vec{n} \wedge \vec{H}_2 \end{pmatrix} \tag{4.24}$$

4.1.3.b Admittance matrix $[Y]$

Similarly, the magnetic fields can be obtained from the knowledge of the electric ones using an admittance matrix:

$$\begin{pmatrix} \vec{n} \wedge \vec{H}_1 \\ -\vec{n} \wedge \vec{H}_2 \end{pmatrix} = \begin{pmatrix} Y_{11} & Y_{12} \\ Y_{21} & Y_{22} \end{pmatrix} \begin{pmatrix} -\vec{E}_1 \\ -\vec{E}_2 \end{pmatrix} \tag{4.25}$$

The $[Z]$ and $[Y]$ matrix are inverse of each other:

$$[Y] = [Z]^{-1} \tag{4.26}$$

4.1.3.c Chain matrix $[ABCD]$

The previously defined impedance and admittance matrix relate electric fields to magnetic fields on both sides of the network. It is now convenient to introduce a 2×2 matrix connecting the fields at one side of the metasurface to the fields at the other side. This matrix is known as the $[ABCD]$ chain matrix (or transmission matrix):

$$\begin{pmatrix} -\vec{E}_1 \\ \vec{n} \wedge \vec{H}_1 \end{pmatrix} = \begin{pmatrix} A & B \\ C & D \end{pmatrix} \begin{pmatrix} -\vec{E}_2 \\ \vec{n} \wedge \vec{H}_2 \end{pmatrix} \tag{4.27}$$

The $[ABCD]$ matrix allows cascade connections between multiple 2-port networks. The total transmission matrix is then easily found by multiplying the $[ABCD]$ matrices of the individual networks. This formalism can for example be used to determine optical properties of a complex system consisting of combinations of uncoupled metasurfaces, multi-layers and substrates.

4.1.3.d Scattering matrix $[S]$

The previous matrices are defined for the total fields at the two ports of the metasurface. However those total fields can be decomposed in terms of inward and outward waves flowing respectively from and toward the considered port:

$$\vec{E}_j = \vec{E}_j^+ + \vec{E}_j^- \tag{4.28}$$

$$\vec{H}_j = \vec{H}_j^+ + \vec{H}_j^- \tag{4.29}$$

where the subscript $j \in \{1,2\}$ designates one of the two ports and the superscripts $+$ and $-$ indicate respectively inward and outward waves, as illustrated on Fig. 4.3-B. The scattering matrix $[S]$ relates the incoming waves to the outgoing ones:

$$\begin{pmatrix} \vec{E}_1^- \\ \vec{E}_2^- \end{pmatrix} = \begin{pmatrix} S_{11} & S_{12} \\ S_{21} & S_{22} \end{pmatrix} \begin{pmatrix} \vec{E}_1^+ \\ \vec{E}_2^+ \end{pmatrix} \tag{4.30}$$

Futhermore, the reflection coefficient r of the metasurface can be obtained by the $S_{11} = \vec{E}_1^- / \vec{E}_1^+$ scattering parameters giving the reflection at port 1 when no incident waves are considered on port 2. Similarly the transmission coefficient t is directly given by the $S_{21} = \vec{E}_2^- / \vec{E}_1^+$ parameter giving the reflected wave at port 2 for incident waves on port 1 only. For reciprocal metasurfaces, the $[S]$ matrix is symmetric *i.e.* $S_{12} = S_{21}$. For a symmetric metasurface, the reflection coefficients are furthermore equal ($S_{11} = S_{22}$) and the scattering matrix takes the following form:

$$[S] = \begin{pmatrix} r & t \\ t & r \end{pmatrix} \tag{4.31}$$

$[Z]$, $[Y]$, $[S]$ and $[ABCD]$ are equivalent matrix representations of the metasurface and conversion tables between their components can be found for example in [7].

4.1.3.e Transmission line of a slab of material

In the coming section 4.1.4, transmission line equivalent circuits of different types of metasurfaces will be introduced. To solve complex problem of propagation we find it relevant to also present the matrix representation of a continuous material.

Propagation on a distance Δz in a lossless homogeneous material of index N and impedance η produces a phase shift that can be expressed through the following $[ABCD]$ chain matrix:

$$\begin{pmatrix} -\vec{E}_1 \\ \vec{n} \wedge \vec{H}_1 \end{pmatrix} = \begin{pmatrix} \cos\left(\frac{2\pi}{\lambda} N\Delta z\right) & i\eta \sin\left(\frac{2\pi}{\lambda} N\Delta z\right) \\ \frac{i}{\eta} \sin\left(\frac{2\pi}{\lambda} N\Delta z\right) & \cos\left(\frac{2\pi}{\lambda} N\Delta z\right) \end{pmatrix} \begin{pmatrix} -\vec{E}_2 \\ \vec{n} \wedge \vec{H}_2 \end{pmatrix} \tag{4.32}$$

This chain matrix can then be cascaded with the matrices of metasurfaces to solve complex propagation wave problems through multiple layers and metasurfaces.

4.1.4 Equivalent circuit of metasurfaces

This subsection aims at introducing the equivalent circuit of three different kinds of metasurfaces and to relate them to the surface impedance Z_e and admittance Y_m characterizing the layer.

4.1.4.a Metasurfaces radiating symmetric distribution of electric field described by $\vec{J}_e$

We first consider the case of metasurfaces described by electric current densities $\vec{J}_e$ only with $\vec{J}_m = 0$. As we have seen in 4.1.1 such metasurfaces radiate exclusively an even electric field distribution. The boundary conditions (4.8,4.17) satisfied by the tangential fields across the surface read:

$$\vec{n} \wedge \vec{E}_1 = \vec{n} \wedge \vec{E}_2 \tag{4.33}$$

$$\frac{1}{2}\left(\vec{E}_1 + \vec{E}_2\right) = Z_e\left(\vec{n} \wedge (\vec{H}_2 - \vec{H}_1)\right) \tag{4.34}$$

These relations indicate that a discontinuity is induced on the magnetic field only while the tangential electric field remains continuous at the crossing of the surface. This kind of metasurfaces can be described through a shunt impedance with value Z_e as illustrated on Fig. 4.4-A. By applying Kirchhoff's laws, the boundary conditions can be easily retrieved from the equivalent circuit. Furthermore, equations (4.33,4.34) can be written in matrix form leading to the following $[Z]$-matrix of the metasurface:

$$\begin{pmatrix} -\vec{E}_1 \\ -\vec{E}_2 \end{pmatrix} = \begin{bmatrix} Z_e & Z_e \\ Z_e & Z_e \end{bmatrix} \begin{pmatrix} \vec{n} \wedge \vec{H}_1 \\ -\vec{n} \wedge \vec{H}_2 \end{pmatrix} \tag{4.35}$$

with the corresponding chain $[ABCD]$-matrix:

$$\begin{pmatrix} -\vec{E}_1 \\ \vec{n} \wedge \vec{H}_1 \end{pmatrix} = \begin{bmatrix} 1 & 0 \\ \dfrac{1}{Z_e} & 1 \end{bmatrix} \begin{pmatrix} -\vec{E}_2 \\ \vec{n} \wedge \vec{H}_2 \end{pmatrix} \tag{4.36}$$

4.1.4.b Metasurfaces radiating an anti-symmetric distribution of electric field described by $\vec{J}_m$

Equivalently, for metasurfaces described by magnetic current densities $\vec{J}_m$ only (with $\vec{J}_e = 0$) radiating an anti-symmetric electric field distribution, the boundary conditions (4.7,4.18) read:

$$\vec{n} \wedge \vec{H}_1 = \vec{n} \wedge \vec{H}_2 \tag{4.37}$$

$$\frac{1}{2}\left(\vec{H}_1 + \vec{H}_2\right) = -Y_m\left[\vec{n} \wedge (\vec{E}_2 - \vec{E}_1)\right] \tag{4.38}$$

Therefore the surface induces a discontinuity on the tangential electric field only, while the tangential magnetic field remains continuous. The equivalent circuit model capturing the GSTCs in this case is illustrated on Fig. 4.4-B and consists in a series impedance of value $1/Y_m$. From the boundary conditions (4.37,4.38) the $[Y]$-matrix of the metasurface can be obtained:

$$\begin{pmatrix} \vec{n} \wedge \vec{H}_1 \\ -\vec{n} \wedge \vec{H}_2 \end{pmatrix} = \begin{bmatrix} Y_m & -Y_m \\ -Y_m & Y_m \end{bmatrix} \begin{pmatrix} -\vec{E}_1 \\ -\vec{E}_2 \end{pmatrix} \tag{4.39}$$

The chain matrix reads:

$$\begin{pmatrix} -\vec{E}_1 \\ \vec{n} \wedge \vec{H}_1 \end{pmatrix} = \begin{bmatrix} 1 & \dfrac{1}{Y_m} \\ 0 & 1 \end{bmatrix} \begin{pmatrix} -\vec{E}_2 \\ \vec{n} \wedge \vec{H}_2 \end{pmatrix} \tag{4.40}$$

4.1.4.c Metasurfaces radiating both symmetric and anti-symmetric distributions of electric field

In the most general case, a metasurface can be described with both electric and magnetic surface current densities inducing a discontinuity in both $\vec{E}$ and $\vec{H}$. The GSTCs (4.17,4.18) satisfied

by the sheet can be rewritten to derive the following chain $[ABCD]$-matrix of the metasurface [8]:

$$\begin{pmatrix} -\vec{E}_1 \\ \vec{n}\wedge\vec{H}_1 \end{pmatrix} = \begin{bmatrix} \frac{4Z_eY_m+1}{4Z_eY_m-1} & \frac{4Z_e}{4Z_eY_m-1} \\ \frac{4Y_m}{4Z_eY_m-1} & \frac{4Z_eY_m+1}{4Z_eY_m-1} \end{bmatrix} \begin{pmatrix} -\vec{E}_2 \\ \vec{n}\wedge\vec{H}_2 \end{pmatrix} \tag{4.41}$$

As presented in [5], the metasurface can be in this case modeled by an equivalent transmission line circuit consisting of a crossed network of series and shunt impedances with respective values $1/(2Y_m)$ and $2Z_e$ as illustrated in Fig. 4.4-C. This representation clearly illustrates the cross dependencies taking place for the fields due to the entanglement of the two kind of currents excited on the sheet.

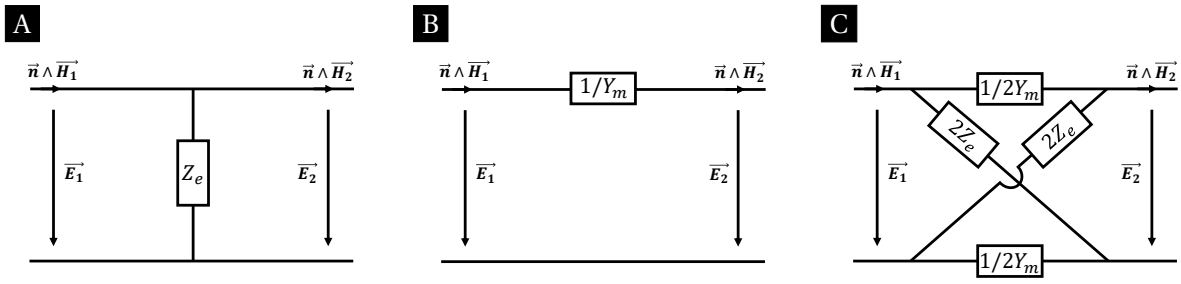

Figure 4.4 – Equivalent transmission line circuit of A) a metasurface radiating symmetric distributions of electric fields described by a density current $\vec{J}_e$. The equivalent circuit consists of a shunt impedance Z_e. B) a metasurface radiating odd distribution of electric field described by a magnetic current density $\vec{J}_m$. The equivalent circuit consists of a series admittance Y_m. C) a metasurface radiating simultaneously symmetric and anti-symmetric distributions of electric field described by both $\vec{J}_e$ and $\vec{J}_m$. The equivalent circuit consists of crossed shunt impedances $2Z_e$ and series admittances $2Y_m$.

It is important to underline that the chain matrix or equivalent circuit presented for this general case can not be reproduced by simply cascading two metasurfaces, one supporting solely electric current densities and the other one magnetic current densities. Therefore, the simultaneous excitation of symmetric and anti-symmetric modes in a single metasurface makes it possible for a richer physical behaviour.

4.2 Metasurface analysis in the dipole approximation

So far, we have presented the problem of interaction of light with a metasurface, as well as its description by the appropriate boundary conditions and via the transmission line formalism. In this section, we address its solving assuming metasurfaces in the dipole approximation, where each meta-atom behaves as an electric or (and) magnetic polarizable punctual dipole. This description is usually valid in the limit of very small resonators compared to the incident wavelength.

Therefore, from this point, the considered metasurface consists in an infinite array of optically small particles with excited electric or (and) magnetic dipoles. We will present the link existing between metasurfaces properties and those of their individual dipolar constituents.

4.2.1 Effective polarisabilities

By definition, polarisabilities link the dipole moments of a particle to the local fields experienced by the particle.

$$\vec{p} = \alpha_e\varepsilon_0\vec{E}_{loc} \qquad \vec{m} = \alpha_m\mu_0\vec{H}_{loc} \tag{4.42}$$

where α_e and α_m are respectively the electric and magnetic polarisabilities of the scatterer. Using these definitions both polarisabilities are expressed in $[m^3]$. The electric dipole $\vec{p}$ is expressed in

$[C \cdot m]$ while the magnetic dipole $\vec{m}$, since μ_0 is included in its definition, is expressed in $[T \cdot m^3]$. In the case of an isolated scatterer, as the local fields correspond to the incident ones:

$$\alpha_e = \frac{|\vec{p}|}{\varepsilon_0 |\vec{E}_{inc}|} \qquad \alpha_m = \frac{|\vec{m}|}{\mu_0 |\vec{H}_{inc}|} \tag{4.43}$$

However, considering now an infinite 2D array of particles, the local field at the position of the particle is the sum of both the incident field and an interaction one $\vec{E}_{inter}$ produced by the rest of scatterers in the array:

$$\vec{E}_{loc} = \vec{E}_{inc} + \vec{E}_{inter} \tag{4.44}$$

where

$$\vec{E}_{inter} = \sum_{j=1}^{\infty} \vec{E}_{scat,j} \tag{4.45}$$

Similar relations hold for the magnetic fields. It can be shown that for periodic infinite grids of identical dipoles, the interaction fields are simply proportional to the excited dipoles [6, 9]:

$$\vec{E}_{inter} = \frac{\beta}{\varepsilon_0}\vec{p} \qquad \vec{H}_{inter} = \frac{\beta}{\mu_0}\vec{m} \tag{4.46}$$

The proportionality coefficient β is known as the interaction constant and its value is given by a lattice sum of Green's functions (see subsection 4.2.4). We say "constant" to underline the fact that it is independent from the properties of the particles and only depends on the lattice pitch.

The incident wave being the known quantity in the problem, we are interested in connecting the dipole moments induced in the particles to the incident excitation. By inserting (4.42) and (4.46) in (4.44), the dipoles can be related to the incident fields through:

$$\vec{p} = \varepsilon_0 \alpha^e_{eff} \vec{E}_{inc} \qquad \vec{m} = \mu_0 \alpha^m_{eff} \vec{H}_{inc} \tag{4.47}$$

where α^e_{eff} and α^m_{eff} are known as the effective polarisabilities of the particles in the array and are given by:

$$\alpha^e_{eff} = \frac{1}{(\alpha_e)^{-1} - \beta} \qquad \alpha^m_{eff} = \frac{1}{(\alpha_m)^{-1} - \beta} \tag{4.48}$$

Equations (4.47,4.48) reveals that two parameters can impact the response of an array of particles to an incident wave. The first one is the polarisability α, an intrinsic characteristic of the meta-atom while the second one is the coupling term β depending only on the surface organization. Both parameters can therefore be engineered to tune the response of a metasurface. In the following we will show how the properties of a metasurface can be expressed in terms of these induced effective dipole polarisabilities.

4.2.2 Induced averaged current densities and surface impedance

The averaged surface current densities of the homogenized array are directly related to the dipole moments induced per unit-cell area. By definition they read:

$$\vec{J}_e = \frac{1}{\mathcal{S}}\frac{\partial \vec{p}}{\partial t} = \frac{-i\omega\vec{p}}{\mathcal{S}} = \frac{-i\omega\varepsilon_0\alpha^e_{eff}}{\mathcal{S}}\vec{E}_{inc} \tag{4.49}$$

$$\vec{J}_m = \frac{1}{\mathcal{S}}\frac{\partial \vec{m}}{\partial t} = \frac{-i\omega\vec{m}}{\mathcal{S}} = \frac{-i\omega\mu_0\alpha^m_{eff}}{\mathcal{S}}\vec{H}_{inc} \tag{4.50}$$

where $\mathcal{S}$ is the area of the unit-cell.

Using equations (4.20) enables to express the surface impedance and admittance of the dipolar screen in terms of unit-cell effective polarisabilities:

$$Z_e = \frac{i\mathcal{S}}{\omega\varepsilon_0\alpha^e_{eff}} - \frac{\eta}{2} \qquad Y_m = \frac{i\mathcal{S}}{\omega\mu_0\alpha^m_{eff}} - \frac{1}{2\eta} \tag{4.51}$$

4.2.3 Metasurface properties expressed with effective polarisabilities

By using the current densities introduced in the previous subsection, in (4.10) and (4.9), the expressions of the transmission $t = E_t/E_{inc}$ and reflection $r = E_r/E_{inc}$ coefficients of the metasurface can be derived:

$$r = \frac{ik}{2\mathcal{S}}\left(\alpha^e_{eff} - \alpha^m_{eff}\right) \tag{4.52}$$

$$t = 1 + \frac{ik}{2\mathcal{S}}\left(\alpha^e_{eff} + \alpha^m_{eff}\right) \tag{4.53}$$

Therefore, metasurfaces properties can be simply expressed in terms of effective dipole polarisabilities. The following section is devoted to the analytic calculation of these effective polarisabilities.

4.2.4 Coupled dipole method

The coupled-dipole method (CDM), also known as the discrete dipole approximation (DDA) has been developed to study the scattering of light by complex particles of arbitrary shape, where the scatterers are discretized over a spatial grid and represented as a collection of punctual electric dipoles [10]. This method has been generalized by G. Mulholland *et al.* [11] to take into account interactions in grid comprising both electric and magnetic dipoles and is known as the coupled electric and magnetic dipole method (CEMDM). This extension also provides an appropriate theoretical framework for addressing metasurface problems [9, 12, 13].

The starting point in deriving the coupled dipole equations for metasurfaces is the volume integral equations introduced in 2.2.6.b and generalized in order to take into account both electric and magnetic current sources. The volume integral equations for magnetic sources are presented in Annexes A.2. The fields produced by distributions of electric $\vec{J}_{s,e}$ and magnetic $\vec{J}_{s,m}$ current sources read:

$$\vec{E}_{scat}(\vec{r},\omega) = i\omega\mu \iiint_{V'} \overleftrightarrow{G}(\vec{r},\vec{r}')\vec{J}_{s,e}(\vec{r'},\omega)dr'^3 - \iiint_{V'} \left[\vec{\nabla} \wedge \overleftrightarrow{G}(\vec{r},\vec{r}')\right] \vec{J}_{s,m}(\vec{r'},\omega)dr'^3 \tag{4.54}$$

$$\vec{H}_{scat}(\vec{r},\omega) = i\omega\varepsilon \iiint_{V'} \overleftrightarrow{G}(\vec{r},\vec{r}')\vec{J}_{s,m}(\vec{r'},\omega)dr'^3 + \iiint_{V'} \left[\vec{\nabla} \wedge \overleftrightarrow{G}(\vec{r},\vec{r}')\right] \vec{J}_{s,e}(\vec{r'},\omega)dr'^3 \tag{4.55}$$

Under the dipolar approximation, the currents for each particle can be discretized as:

$$\vec{J}_{s,e} = -i\omega\vec{p}\delta(\vec{r} - \vec{R}_{lq}) \qquad \vec{J}_{s,m} = -i\omega\vec{m}\delta(\vec{r} - \vec{R}_{lq}) \tag{4.56}$$

where the position of each point source is given by the vector $\vec{R}_{lq} = lL_x\vec{e}_x + qL_y\vec{e}_y$ with L_x and L_y the lattice pitches along the $\vec{e}_x$ and $\vec{e}_y$ directions and with $(l,q) \in \mathbb{Z}^2$. Using these notations, the fields produced by the array of particles in any point of space are given by:

$$\vec{E}_a(\vec{r},\omega) = \omega^2\mu \sum_{l,q=-\infty}^{+\infty} \overleftrightarrow{G}(\vec{r},\vec{R}_{lq})\vec{p} + i\omega \sum_{l,q=-\infty}^{+\infty} \left[\vec{\nabla} \wedge \overleftrightarrow{G}(\vec{r},\vec{R}_{lq})\right] \vec{m} \tag{4.57}$$

$$\vec{H}_a(\vec{r},\omega) = \omega^2\varepsilon \sum_{l,q=-\infty}^{+\infty} \overleftrightarrow{G}(\vec{r},\vec{R}_{lq})\vec{m} - i\omega \sum_{l,q=-\infty}^{+\infty} \left[\vec{\nabla} \wedge \overleftrightarrow{G}(\vec{r},\vec{R}_{lq})\right] \vec{p} \tag{4.58}$$

Furthermore, we recall the relations giving the dipole moments:

$$\vec{p} = \varepsilon_0\alpha_e\vec{E}_{loc} = \varepsilon_0\alpha_e\left[\vec{E}_{inc} + \vec{E}_{inter}\right] \tag{4.59}$$

$$\vec{m} = \mu_0\alpha_m\vec{H}_{loc} = \mu_0\alpha_m\left[\vec{H}_{inc} + \vec{H}_{inter}\right] \tag{4.60}$$

Using expressions (4.57,4.58) enables to express the interaction fields at the position $\vec{R}$ of a particle ($\vec{E}_{inter}(\vec{R}) = \vec{E}_a(\vec{R})$) and to derive a set of self-consistent equations to solve for obtaining the dipole moments $\vec{p}$ and $\vec{m}$:

$$\vec{p} = \varepsilon_0 \alpha_e \left[\vec{E}_{inc}(\vec{R}) + \omega^2 \mu \sum_{l,q=-\infty}^{+\infty} \overleftrightarrow{G}(\vec{R}, \vec{R}_{lq}) \vec{p} + i\omega \sum_{l,q=-\infty}^{+\infty} \left[\vec{\nabla} \wedge \overleftrightarrow{G}(\vec{R}, \vec{R}_{lq}) \right] \vec{m} \right] \tag{4.61}$$

$$\vec{m} = \mu_0 \alpha_m \left[\vec{H}_{inc}(\vec{R}) + \omega^2 \varepsilon \sum_{l,q=-\infty}^{+\infty} \overleftrightarrow{G}(\vec{R}, \vec{R}_{lq}) \vec{m} - i\omega \sum_{l,q=-\infty}^{+\infty} \left[\vec{\nabla} \wedge \overleftrightarrow{G}(\vec{R}, \vec{R}_{lq}) \right] \vec{p} \right] \tag{4.62}$$

As every particle have the same dipole moment, the system of equations can be solved considering the particle located at the origin ($\vec{R} = 0$). Evlyukhin *et al.* have shown in [9] that for an infinite array, due to the periodicity in x and y, the sum given by $\sum_{l,q=-\infty}^{+\infty} \vec{\nabla} \wedge \overleftrightarrow{G}(0, \vec{R}_{lq})$ is null while the tensor $\overleftrightarrow{\mathcal{G}^0} = \sum_{l,q=-\infty}^{+\infty} \overleftrightarrow{G}(0, \vec{R}_{lq})$ is diagonal. This indicates that the coupling between the electric and magnetic dipoles in (4.61,4.62) disappears and that both dipoles can be determined separately. The solutions for an $\vec{e}_x$ polarized incident plane wave are finally given by [9]:

$$\vec{p} = \alpha^e_{eff} \varepsilon_0 \vec{E}_{inc} \tag{4.63}$$

$$\vec{m} = \alpha^m_{eff} \mu_0 \vec{H}_{inc} \tag{4.64}$$

with

$$\alpha^e_{eff} = \frac{1}{{\alpha_e}^{-1} - k^2 \mathcal{G}^0_{xx}} \tag{4.65}$$

$$\alpha^m_{eff} = \frac{1}{{\alpha_m}^{-1} - k^2 \mathcal{G}^0_{yy}} \tag{4.66}$$

where $\mathcal{G}^0_{xx}$ and $\mathcal{G}^0_{yy}$ are the x and y components of the interaction lattice periodic Green's function $\overleftrightarrow{\mathcal{G}^0}$.

This analytic model therefore enables calculating the interaction constant β (introduced in the previous section) between the dipoles. The interaction constants for $\vec{p}$ and $\vec{m}$ are given by different components of the periodic Green's function $\overleftrightarrow{\mathcal{G}^0}$ that depends on the array period along the x and y directions. Therefore, one can differently affect the electric or magnetic response of the array by specifically tuning the x or y metasurface periodicities. Only in the case of a square array the electric and magnetic responses of the metasurface are similarly affected by the pitch choice and the interaction constant read:

$$\beta = k^2 \mathcal{G}^0_{xx} = k^2 \mathcal{G}^0_{yy} \tag{4.67}$$

It is interesting to note that this analytic approach for obtaining the coupling term between dipoles can be generalized to include higher order resonances. Thus, in [14–18] coupled dipole-quadrupole equations are introduced to investigate the collective interactions between electric and magnetic dipoles as well as electric quadrupole resonances in arrays of particles. However, obtaining and calculating the coupling terms for higher order resonances presents much more complexity than in the dipolar case.

4.2.4.a Approximate values for the coupling constant

We have seen that the electromagnetic problem can be formally solved by computing the interaction constant given by a sum of Green's functions running on all the particles of the array. For infinite arrays, this sum must be numerically calculated on a large enough number of particles to ensure a good convergence of β. On the other hand, approximate analytic expressions of β

can be used to get a first insight in the metasurface properties without resorting to the numerical calculation of $\overleftrightarrow{\mathcal{G}}^0$. The interaction constant may approximates as:

$$\beta = \frac{1}{4\mathcal{S}L_0}\left[1 - ikL_0\right]e^{-ikL_0} \tag{4.68}$$

where:

$$L_0 = \frac{L}{1.438} \tag{4.69}$$

is an effective interparticle distance obtained from the quasi-static approximation of the interaction field. L is the lattice pitch of the square array. These expressions are established in [6] for dense enough arrays given by the condition $kL \leq 1.5$. The upper limit for kL is in fact approximately between 1.5 and 2. Furthermore, for compact latices with $L << \lambda$ the following truncated Taylor expansion can be used: $e^{-ikL_0} \sim 1 - ikL_0$, leading to:

$$\beta \approx \frac{1}{4\mathcal{S}L_0}\left[1 - ikL_0\right]^2 \tag{4.70}$$

Therefore at order zero, β is a pure constant solely determined by the lattice pitch L:

$$\beta \sim \frac{1}{4\mathcal{S}L_0} \tag{4.71}$$

4.2.4.b Imaginary part of the coupling constant and energy conservation

For a periodic array, the imaginary part of the interaction constant can be determined analytically using energy conservation [6, 19, 20]. If one considers an array of lossless small particles represented by electric dipoles $\vec{p}$, the absorbed power P_{abs} in the structure is null. Therefore the radiated power (given by $P_{rad} = \eta|\vec{J}_e|^2/4$) is simply equal to the extinction one, *i.e.* the overall power extracted from the impinging plane wave by the array ($P_{ext} = \Re(\vec{J}_e^*\vec{E}_{inc})/2$). Equalizing these two terms for $\vec{J}_e = -i\omega\varepsilon_0\alpha^e_{eff}\vec{E}_{inc}/\mathcal{S}$ leads to:

$$\Im(\beta - {\alpha_e}^{-1}) = \frac{k}{2\mathcal{S}} \tag{4.72}$$

For lossless particles, $\Im({\alpha_e}^{-1})$ is known and corresponds to the scattering losses $k^3/(6\pi)$ of an isolated particle. Therefore the interaction constant reads:

$$\beta = \Re(\beta) - i\left(\frac{k^3}{6\pi} - \frac{k}{2\mathcal{S}}\right) \tag{4.73}$$

and

$$\Im(\beta) = -\frac{k^3}{6\pi} + \frac{k}{2\mathcal{S}} \tag{4.74}$$

The first term $-k^3/(6\pi)$ is related to the radiation losses of a single particle indicating that in an ordered array the scattering losses are removed, while the second term of the expression, $k/2\mathcal{S}$ is related to the emission of coherent plane waves by the averaged electric surface currents. Since the interaction constant does not depend on the particle properties, equation (4.74) remains valid when considering lossy particles. For simplicity, this relation has been introduced here considering electric dipoles only, but it holds in the general case where magnetic dipoles are added.

It is interesting to note that in the case of disordered (amorphous) arrays of particles, the imaginary part of the interaction constant is reduced to [21]:

$$\Im(\beta) = +\frac{k}{2\mathcal{S}} \tag{4.75}$$

The term that compensates the particles scattering losses is absent indicating that in this case, the particles scatter individually. The net response of the array is then a collective plane wave with individual scatterings.

4.2.5 Lorentzian model

In order to understand metasurface properties from a fundamental point of view, it is interesting to consider idealized dipole resonances whose spectral dependencies are modeled by lorentzians. The dispersion of the polarisabilities are then parametrized as follow [21, 22]:

$$\alpha_j = \frac{\alpha_0^j}{\omega_{0,j}^2 - \omega^2 - i\omega\gamma_j - i\frac{k^3}{6\pi}\alpha_0^j} \tag{4.76}$$

where $\omega_{0,j}$ is the resonance frequency, γ_j is a term corresponding to the dissipation (ohmic) losses, $i\frac{k^3}{6\pi}\alpha_0^j$ corresponds to the scattering losses of the dipole and α_0^j is the oscillator amplitude that gives the strength of the resonance. The subscript $_j$ is used to indicate either the electric ($j = e$) or magnetic ($j = m$) dipole resonance. By using equation (4.48) and the expression of the interaction constant given by (4.73), the effective polarisabilities in a periodic array can be written as:

$$\alpha_{eff}^j = \frac{\alpha_0^j}{\omega_{0,i}'^2 - \omega^2 - i\omega\left(\gamma_j + \frac{k}{2\mathcal{S}c}\alpha_0^j\right)} \tag{4.77}$$

where ${\omega'_{0,i}}^2 = {\omega_0}^2 - Re(\beta)\alpha_0^j$ is the modified resonance frequency. We note that the term in $\frac{k^3}{6\pi}$ has disappeared from the equation giving the effective polarisabilities as it has canceled with the term contained in the imaginary part of the interaction constant. This is consistent with the fact that there is no individual scattering in an ordered array of dipoles. The only radiative losses correspond to the emission of the coherent plane wave given by the term in $\frac{k}{2\mathcal{S}}$. Finally, using (4.52,4.53) the reflection and transmission coefficients read:

$$r = \frac{i\omega\Gamma_e}{\omega_e'^2 - \omega^2 - i\omega\left(\Gamma_e + \gamma_e\right)} - \frac{i\omega\Gamma_m}{\omega_m'^2 - \omega^2 - i\omega\left(\Gamma_m + \gamma_m\right)} \tag{4.78}$$

$$t = 1 + \frac{i\omega\Gamma_e}{\omega_e'^2 - \omega^2 - i\omega\left(\Gamma_e + \gamma_e\right)} + \frac{i\omega\Gamma_m}{\omega_m'^2 - \omega^2 - i\omega\left(\Gamma_m + \gamma_m\right)} \tag{4.79}$$

with $\Gamma_j = \dfrac{\alpha_0^j}{2\mathcal{S}c}$. Therefore, from a physical point of view, equations (4.78,4.79) link the reflection and transmission coefficients to the four different available energetic damping channels. Those channels are illustrated on Fig. 4.5 where an incident plane wave can couple to the electric or magnetic dipole resonances of the particles in the metasurface.

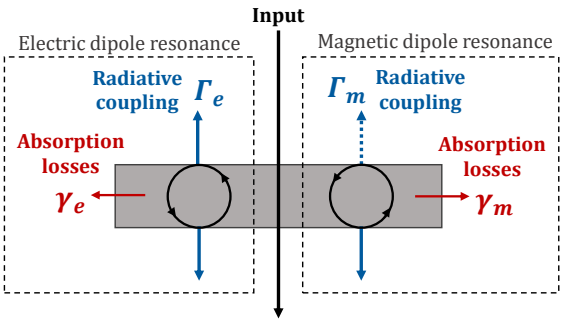

Figure 4.5 – Illustration of the different loss channels available in a dipolar ordered metasurface. An incident plane wave can couple to both the electric or magnetic resonance of the dipolar array. For each resonance, the available channels are the radiative losses Γ through plane wave re-radiation and the internal dissipation of energy given by γ. The dotted blue line illustrates that the magnetic resonance radiates an anti-symmetric distribution of electric field.

For each resonance two different damping channels are available: i) a radiative one, given by Γ_j, consisting in re-radiation of power leaking energy out of the resonator via out-going plane

wave emissions in the upper and lower half-space, and ii) a non-radiative one corresponding to internal dissipation of energy in the structure given by γ_j.

In chapter 5 we will resort to this simple Lorentzian model to understand under which circumstances perfect transmission and absorption can be reached.

4.3 Rigorous analysis of multipolar metasurfaces

In the previous section we have seen how it is possible to express metasurface properties in terms of effective polarizabilities of its constituting meta-atoms. This description, widely used in the literature, nevertheless has limited domain of applications since it can only apply to resonators in the dipole approximation. Therefore this dipole-based description is not relevant in the general case of meta-atoms supporting higher order multipole resonances.

In this section, we generalize the previously introduced formalism to take full account of contributions from higher multipolar orders. This generalized formalism enables to rigorously link metasurface properties to the spherical multipole coefficients characterizing the radiation pattern of the particles in the array.

The approach is as follows: the field emitted by the array is first connected to that scattered by a single unit-cell. Performing a spherical multipole expansion of the field scattered by one element, it is thus possible to obtain the corresponding multipole expansion of the forward and backward emitted waves from the array, and consequently that of the transmission and reflection coefficients. The contribution of the symmetric and anti-symmetric multipoles to both absorption and scattering can then be accessed. In practice, this multipole expansion applies to the array and can be performed numerically from the knowledge of the current densities induced in one meta-atom by using the projection presented in 2.2.6.c.

4.3.1 Link between emitted fields and current sources for periodic arrays

The starting point in obtaining multipole expansions of metasurface responses is to derive the relationship between the forward and backward emitted field from the array to that scattered from a single unit-cell. The establishment of this relation has been presented in [23] (supplemental material). To help in understanding the physical origin of this relation, we reproduce here the main steps of its derivation. Their approach is similar to that of Evlyukhin *et al.* [9] for expressing the coupled dipole equation, but generalized in terms of any induced currents in the particles rather than just punctual dipole moments.

We begin by considering the current distribution $\vec{J}_s$ induced in a single particle of an infinite array. The field scattered by this unit-cell can be found from the volume integral equation (2.116). Considering far field scattering, the expression of the dyadic Green's function simplifies and the scattered electric far field reads:

$$\vec{E}_{scat}(\vec{r}) \approx i\omega\mu_0 \iiint_{V'} \frac{e^{ikR}}{4\pi R} \vec{J}_s(\vec{r'}) dr'^3 \tag{4.80}$$

where $R = \left|\vec{r} - \vec{r}'\right|$. From this expression, the electric field in the forward ($\vec{e}_z$) or backward ($-\vec{e}_z$) direction can be derived. Using the approximation that $R \approx |z|$ the scattered field from the individual unit-cell reads:

$$\vec{E}_{scat}(\pm\vec{e}_z) \approx i\omega\mu_0 \frac{e^{ik|z|}}{4\pi|z|} \iiint_{V'} \vec{J}_s(\vec{r'}) e^{ik(|z\vec{e}_z - \vec{r}'| - |z|)} dr'^3 \tag{4.81}$$

The field produced by the array at a position $\vec{r}$ of space is obtained by summing the field scattered by every particle of the array:

$$\vec{E}_a(\vec{r}) = \sum_{l,q=-\infty}^{+\infty} i\omega\mu_0 \iiint_{V'} \overleftrightarrow{G}(\vec{r}, \vec{r}' + L(l\vec{e}_x + q\vec{e}_y)) \vec{J}_s(\vec{r}' + L(l\vec{e}_x + q\vec{e}_y)) dr'^3 \tag{4.82}$$

$$= i\omega\mu_0 \iiint_{V'} \overleftrightarrow{\mathcal{G}}(\vec{r}, \vec{r}') \vec{J}_s(\vec{r}') dr'^3 \tag{4.83}$$

where $\overleftrightarrow{\mathcal{G}}(\vec{r},\vec{r}') = \sum_{l,q=-\infty}^{+\infty} \overleftrightarrow{G}(\vec{r},\vec{r}'+L(l\vec{e}_x+q\vec{e}_y))$ is the lattice periodic Green's function. For subwavelength lattice spacing L and far field scattering, its expression is given by:

$$\overleftrightarrow{\mathcal{G}}(\vec{r},\vec{r}') \approx \frac{ie^{ikR}}{2k\mathcal{S}} \tag{4.84}$$

The lattice period of the metasurface has to be smaller than the considered wavelength to ensure that no diffracted plane waves are generated. Using this expression, the field corresponding to the specular mode emitted by the array in the far field domain, in the forward and backward directions, reads:

$$\vec{E}_a(\pm\vec{e}_z) = i\omega\mu_0 \frac{ie^{ik|z|}}{2k\mathcal{S}} \iiint_{V'} \vec{J}_s(\vec{r}')e^{ik(|z\vec{e}_z-\vec{r}'|-|z|)}dr'^3 \tag{4.85}$$

Substituting the expression of the scattered field (4.81) in this equation, the field emitted by the grid can be expressed in terms of the field scattered by an individual unit-cell:

$$\vec{E}_a(\pm\vec{e}_z) = \frac{2\pi i|z|}{k\mathcal{S}}\vec{E}_{scat}(\pm\vec{e}_z) \tag{4.86}$$

In the following section the multipole expansion of the field $\vec{E}_{scat}(\pm\vec{e}_z)$ scattered by a single element in the array is presented. From equation (4.86), it can be seen that this will later enable expressing the corresponding multipole expansion of the field emitted by the full metasurface.

4.3.2 Multipole expansion of metasurface properties in spherical coordinates

We consider here an $\vec{e}_x$ polarized plane wave of magnitude E_0 propagating along the $\vec{e}_z$ direction, normally incident on the metasurface consisting in a square array of particles. We want to derive the multipole expansion of $\vec{E}_{scat}(\pm\vec{e}_z)$ the field scattered by a single particle of the array along both the forward ($\theta = 0, \varphi = 0$) and backward ($\theta = \pi, \varphi = \pi$) directions, where φ is the azimuthal angle and θ the polar angle. For these two directions, due to the polarization of the incident wave, $\vec{E}_{scat}(\pm\vec{e}_z)$ has only one non-zero component along $\vec{e}_\theta$. Our starting point is therefore the expression of the θ-component of the scattered field given in [24] expanded in terms of spherical vector wave functions that takes the following form in the far field domain:

$$E_s(\theta,\varphi) = iE_0\frac{e^{ikr}}{kr}\sum_{n=1}^{\infty}\sum_{m=-n}^{+n}\sqrt{\frac{\pi(2n+1)}{n(n+1)}}\mathcal{Q}_{nm}\left[\tau_{nm}(\cos\theta)a_{n,m}+\pi_{nm}(\cos\theta)b_{n,m}\right]e^{im\varphi} \tag{4.87}$$

where we have used the asymptotic limit of the spherical Hankel function of the first kind and their derivatives for large arguments when $kr \to +\infty$ [25]:

$$h_n^{(1)}(x) \sim (-i)^{n+1}\frac{e^{ix}}{x} \tag{4.88}$$

$$\frac{dh_n^{(1)}(x)}{dx} \sim (-i)^n\frac{e^{ix}}{x} \tag{4.89}$$

and where $\mathcal{Q}_{nm}$ is the normalization constant related to the associated Legendre functions:

$$\mathcal{Q}_{nm} = \sqrt{\frac{2n+1}{4\pi}\frac{(n-m)!}{(n+m)!}} \tag{4.90}$$

τ_{nm} and π_{nm} are the angular scattering functions defined in 2.2.6.c. Their values for $\theta = 0$ and $\theta = \pi$ can for example be found in [26] and reads:

$$\pi_{nm}(\pm1) = \begin{cases} (\pm1)^{n-1}\dfrac{n(n+1)}{2} & m = 1 \\ \dfrac{(\pm1)^{n-1}}{2} & m = -1 \\ 0 & otherwise \end{cases} \tag{4.91}$$

$$\tau_{nm}(\pm 1) = \begin{cases} (\pm 1)^n \dfrac{n(n+1)}{2} & m = 1 \\ -\dfrac{(\pm 1)^n}{2} & m = -1 \\ 0 & otherwise \end{cases} \tag{4.92}$$

The angular scattering functions cancel for all $m \notin \{1,-1\}$ for both the forward and backward directions. Using these values, the scattered electric field reads in the forward direction:

$$E_{scat}(0,0) = i\frac{E_0}{4}\frac{e^{ikr}}{kr}\sum_{n=1}^{\infty}(2n+1)\left[a_{n,1} - a_{n,-1} + b_{n,1} + b_{n,-1}\right] \tag{4.93}$$

and in the backward direction:

$$E_{scat}(\pi,\pi) = i\frac{E_0}{4}\frac{e^{ikr}}{kr}\sum_{n=1}^{\infty}(2n+1)(-1)^{n+1}\left[a_{n,1} - a_{n,-1} - (b_{n,1} + b_{n,-1})\right] \tag{4.94}$$

4.3.2.a Transmission and reflection coefficients

Combining (4.93) and (4.94) with (4.86), the field produced by the array in the two half-spaces can be accessed:

$$E_a(z+) = -\frac{\pi e^{ik|z|}}{2k^2\mathcal{S}}\sum_{n=1}^{\infty}(2n+1)\left(a_{n,1} - a_{n,-1} + b_{n,1} + b_{n,-1}\right)E_0 \tag{4.95}$$

$$E_a(z-) = -\frac{\pi e^{ik|z|}}{2k^2\mathcal{S}}\sum_{n=1}^{\infty}(-1)^{n+1}(2n+1)\left(a_{n,1} - a_{n,-1} - (b_{n,1} + b_{n,-1})\right)E_0 \tag{4.96}$$

Inserting these two expressions in $\vec{E}_t = \vec{E}_{inc} + \vec{E}_a(z+)$ and $\vec{E}_r = \vec{E}_a(z-)$ allows to finally write the reflection and transmission coefficients expressed as a function of the spherical multipole coefficients of a single resonator (or unit-cell) of the array:

$$r = -\frac{\pi}{2k^2\mathcal{S}}\sum_{n=1}^{\infty}\sum_{m=-1,+1}(-1)^{n+1}(2n+1)\left(ma_{n,m} - b_{n,m}\right) \tag{4.97}$$

$$t = 1 - \frac{\pi}{2k^2\mathcal{S}}\sum_{n=1}^{\infty}\sum_{m=-1,+1}(2n+1)\left(ma_{n,m} + b_{n,m}\right) \tag{4.98}$$

Alternatively, these coefficients can be expressed compactly in terms of symmetric or even ($\mathcal{E}_n$) and anti-symmetric or odd ($\mathcal{O}_n$) multipoles of order n:

$$r = -\frac{\pi}{2k^2\mathcal{S}}\sum_{n=1}^{\infty}\left[\mathcal{E}_n - \mathcal{O}_n\right] \tag{4.99}$$

$$t = 1 - \frac{\pi}{2k^2\mathcal{S}}\sum_{n=1}^{\infty}\left[\mathcal{E}_n + \mathcal{O}_n\right] \tag{4.100}$$

where the even and odd multipoles are given by:

$$\mathcal{E}_n = \sum_{m=-1}^{+1}\left[m(4n-1)a_{2n-1,m} + (4n+1)b_{2n,m}\right] \tag{4.101}$$

$$\mathcal{O}_n = \sum_{m=-1}^{+1}\left[m(4n+1)a_{2n,m} + (4n-1)b_{2n-1,m}\right] \tag{4.102}$$

Writing the coefficients in this way is quite convenient as a clear distinction can be made in the role of odd and even modes in the reflection and transmission.

To illustrate this formalism, we apply it to an infinite square array composed of spherical particles of radius R = 150nm made of a material with loss that has a constant index of refraction $N = 4 + 0.05i$. The surface fill fraction is taken equal to 0.4. The reflectance (R) and transmittance (T) spectra of the array calculated with eqs. (4.97) and (4.98) are represented on Fig. 4.6-A. The multipole coefficients are obtained after decomposing the current fields from finite-element numerical simulations, by mean of eqs. (2.121,2.122). These quantities reproduce perfectly over the full range of wavelength the reflectance and transmittance calculated from the input and output ports in COMSOL Multiphysics. The absorption (A) spectrum is also calculated integrating the ohmic losses in the volume of the particles and the total energy balance has been verified for the array ensuring $R + T + A = 1$. Figure 4.6-B represents the spectra of the modulus of each multipole coefficient up to the fifth order that are used to correctly reproduce R and T. The coefficients shown are the reduced coefficients that are applicable for symmetry reasons [27] ($a_n = a_{n,1} = -a_{n,-1}$ and $b_n = b_{n,1} = b_{n,-1}$).

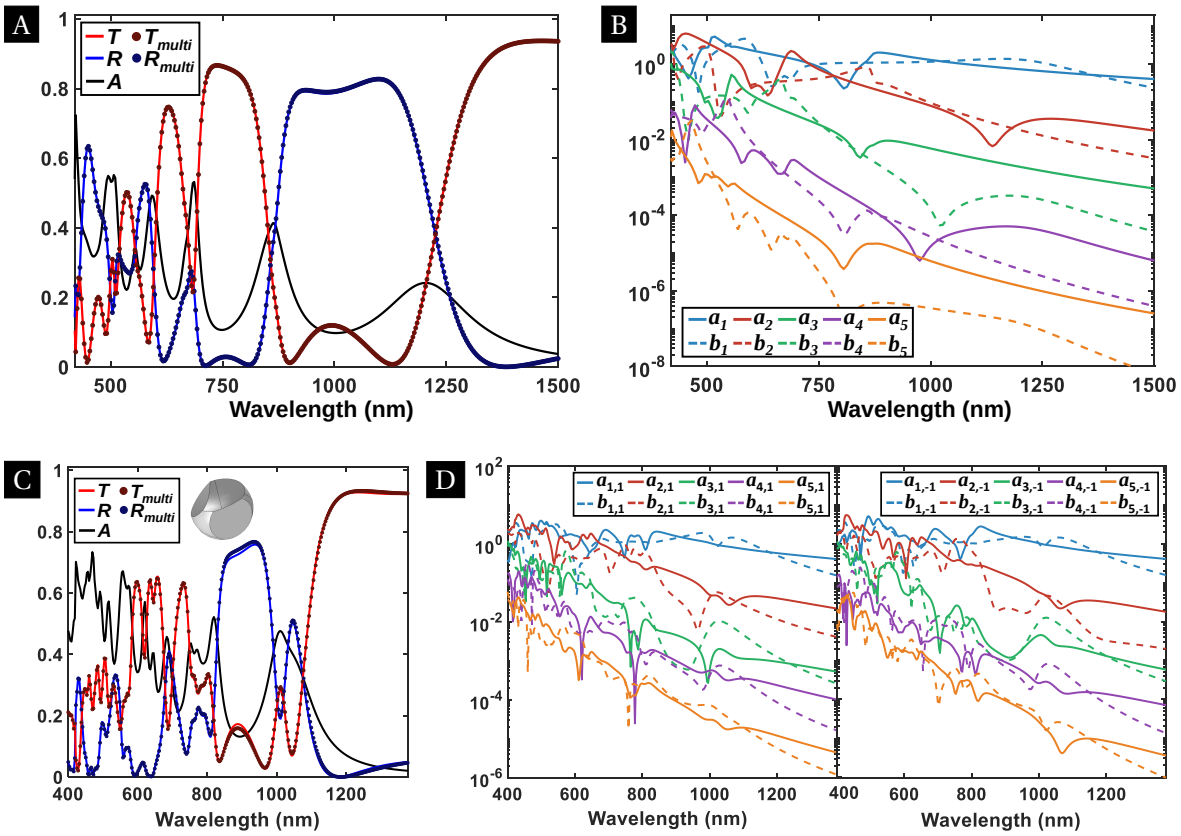

Figure 4.6 – Illustration of the metasurface multipole expansion. A) Reflectance (R), transmittance (T) and absorption (A) spectra of an infinite square periodic array of spherical particles with radius R = 150nm and refractive index $N = 4 + 0.05i$. The surface fill fraction is 0.4. The continous lines are the spectra calculated from the input and output S-parameters on the ports, while the curves with dots are computed from the current-based multipole expansion and introduced in eqs. (4.97) and (4.98). B) Spectra of the magnitude of the multipoles. Continuous (dashed) lines represent the electric (magnetic) multipoles. C) and D) are respectively the same quantities than those presented on panels A) and B) but for an array of unsymmetrical particles consisting in truncated spheres of radius R = 150nm and refractive index $N = 4+0.05i$. The surface fill fraction is 0.4.

The introduced multipole-based formalism can be used to study periodic arrays of particles with arbitrary shape. To illustrate its wide domain of validity, we also apply it to a network of truncated spherical particles as depicted in the inset of Fig. 4.6-C where truncations by 2 random planes and a curved surface are used to completely break the symmetry of the final structure. The computed multipolar coefficients presented in Fig. 4.6-D allow for a good reproduction of the

array properties as illustrated in Fig. 4.6-C.

4.3.2.b Energy balance applied to the metasurface

From equations (4.99) and (4.100), it is possible to distinguish the contribution of even and odd multipoles to both the radiation and absorption.

By definition, the fraction of energy scattered in the forward and backward directions by the array (respectively denoted as p_s^+ and p_s^-) are related to the reflection and transmission coefficients:

$$p_s^- = |r|^2 \tag{4.103}$$

$$p_s^+ = |t-1|^2 \tag{4.104}$$

Using these definitions and the expressions of the reflection and transmission coefficients (*i.e.* eqs. (4.99) and (4.100)) the fraction of energy p_s scattered by the grid is:

$$p_s = p_s^{\mathcal{E}} + p_s^{\mathcal{O}} \tag{4.105}$$

where

$$p_s^{\mathcal{E}} = 2\left|\frac{\pi}{2k^2\mathcal{S}}\sum_{n=1}^{\infty}\mathcal{E}_n\right|^2 \tag{4.106}$$

$$p_s^{\mathcal{O}} = 2\left|\frac{\pi}{2k^2\mathcal{S}}\sum_{n=1}^{\infty}\mathcal{O}_n\right|^2 \tag{4.107}$$

Cross terms between even and odd multipoles do not appear in the expression of the scattered power and the expression can be simply cast into two contributions, one originating from the symmetric multipoles $p_s^{\mathcal{E}}$ and the second one from the anti-symmetric multipoles $p_s^{\mathcal{O}}$. For later convenience, we can define the scattering cross-section of the unit-cell of the array as:

$$\sigma_{scat,a} = \frac{P_{scat,a}}{I_0} = p_s\,\mathcal{S} \tag{4.108}$$

where P_0 is the incoming power on a unit-cell, $P_{scat,a}$ is the power scattered by the unit-cell, and with $I_0 = P_0/\mathcal{S}$.

To go beyond this decomposition of the emitted power, energy balance, $A = 1-R-T$, expressed with the multipole coefficients also enables to access the proportion of absorption due respectively to the symmetric and anti-symmetric modes. Using equations (4.99) and (4.100) the energy balance reads:

$$A = -2\left(\frac{\pi}{2k^2\mathcal{S}}\right)^2\left[\left|\sum_{n=1}^{\infty}\mathcal{E}_n\right|^2 + \left|\sum_{n=1}^{\infty}\mathcal{O}_n\right|^2\right] + \frac{\pi}{k^2\mathcal{S}}\sum_{n=1}^{\infty}\Re\left(\mathcal{E}_n+\mathcal{O}_n\right) \tag{4.109}$$

or equivalently

$$\sigma_{abs} = -\sigma_{scat,a} + \sigma_{ext} \tag{4.110}$$

where σ_{ext} is the extinction cross-section of the particles in the grid, which in the case of an x-polarized incident plane wave is [27]:

$$\sigma_{ext} = \frac{\pi}{k^2}\sum_{n=1}^{\infty}\sum_{m=-1,+1}(2n+1)\Re\left(m a_{n,m} + b_{n,m}\right) \tag{4.111}$$

As for the scattering cross-section, the extinction cross-section expression can be broken down into even and odd contributions as:

$$\sigma^{\mathcal{E}}_{ext} = \frac{\pi}{k^2}\sum_{n=1}^{\infty}\Re(\mathcal{E}_n) \tag{4.112}$$

$$\sigma^{\mathcal{O}}_{ext} = \frac{\pi}{k^2}\sum_{n=1}^{\infty}\Re(\mathcal{O}_n) \tag{4.113}$$

In the same way the absorption cross-section can be decomposed into even and odd terms obtained by the differences:

$$\sigma^{\mathcal{O}}_{abs} = \sigma^{\mathcal{O}}_{ext} - \sigma^{\mathcal{O}}_{scat,a} \tag{4.114}$$

$$\sigma^{\mathcal{E}}_{abs} = \sigma^{\mathcal{E}}_{ext} - \sigma^{\mathcal{E}}_{scat,a} \tag{4.115}$$

Accessing this decomposition would usually require a configuration with double illumination from both sides of the array as described in [28] with co or anti polarization allowing for a selective excitation of either the symmetric or anti-symmetric modes of the structure. Instead, using the multipole decomposition allows for a one step procedure to retrieve both the scattering and absorption due to the even or odd excited modes.

To illustrate this approach, we present in Fig. 4.7 the decomposition of the scattering and absorption cross-sections in terms of even and odd multipoles applied to the array of spheres of index $N = 4 + 0.05i$ whose multipole expansion has been presented in the previous subsection. The absorption σ^*_{abs} and scattering $\sigma^*_{scat,a}$ cross-sections calculated with respectively the absorbed power obtained via the integration of the ohmic losses and the reflection and transmission coefficients (obtained with the S-parameters) using equations (4.103) and (4.104) are perfectly reproduced by those reconstructed from the multipole coefficients. The presented unit-cell cross-sections are quantities of interest as they carry the same information than the scattering, extinction and absorption cross-section defined for isolated particles in homogeneous space in chapter 2.2.1.b [27, 29]. Therefore they allow for a direct comparison between the optical properties of particles isolated or placed on the periodic grid.

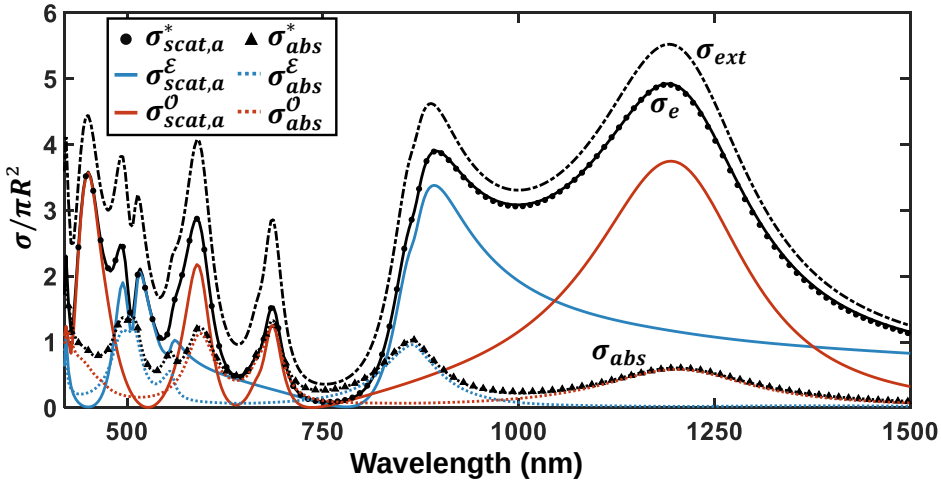

Figure 4.7 – Cross-sections decomposition in terms of even and odd contributions apply to an array of spherical particles with radius R = 150nm, refractive index $N = 4 + 0.05i$ and a surface fill fraction f = 0.4. the blue (red) lines represents the contribution of even (odd) multipoles to absorbtion and emission represented respectively with dotted and continous lines.

Using vector spherical harmonic expansion, we introduced a completely generalized multipolar description of metasurface properties. Similar approaches have already been presented in the literature in the case of arrays of cylinders using cylindrical harmonic decomposition [30, 31] but

they remain sparsely used. On the contrary, most of the works extending the well known dipole formalism to higher order resonances are based on multipolar expansions of the fields in the cartesian basis. This approach is strictly equivalent to the one we have presented, however, expressing the multipole moments in cartesian coordinates is usually quite involved as the expansions become complex for increasing multipole orders. For this reason, they are usually truncated at low orders, which potentially limits the domain of application of the multipolar description. To our knowledge, this cartesian approach has only recently been generalized to include the octupolar electrical order [32] and magnetic order [33]. Including higher order multipoles in this way does not seem very promising in comparison of the simplicity with which this can be done from the spherical harmonic based decomposition.

Since this cartesian approach is widely used in the literature, we will introduce it in the following section and show, for the first multipoles, the link existing with the coefficients obtained from the spherical basis.

4.3.3 Link with cartesian expansion

In the cartesian basis, the field scattered in a direction indicated by a unit vector $\vec{n}$ is related to the multipole moments through the following expansion [32, 34, 35] presented in chapter 2.2.6.e:

$$\vec{E}_{scat}(\vec{n}) = \frac{k^2}{4\pi\varepsilon_0}\frac{e^{ikr}}{r}\left[\vec{n}\wedge(\vec{p}\wedge\vec{n}) + \frac{1}{\eta_0}(\vec{m}\wedge\vec{n}) - \frac{ik}{6}\vec{n}\wedge(\vec{Q}_e\wedge\vec{n}) - \frac{ik}{6\eta_0}(\vec{Q_m}\wedge\vec{n}) + ...\right] \tag{4.116}$$

where the 3 components of the vectors $\vec{Q}_e$ and $\vec{Q}_m$ are defined by $Q_\alpha = \sum_\beta Q_{\alpha,\beta}\, n_\beta$ with $(\alpha,\beta) \in (x,y,z)^2$ and where $Q_{\alpha,\beta}$ are the cartesian components of the quadrupole tensor.

Considering the forward $\vec{n} = (0\,0\,1)$ and backward $\vec{n} = (0\,0\,-1)$ directions and an incident plane wave polarized along the $\vec{x}$ axis, the only excited components of the multipoles are: p_x, m_y, Q^e_{xz}, and Q^m_{yz} and the scattered electric field reads [36]:

$$E_{scat}(z+) = E_{scat}(\vec{n} = \vec{e}_z) = \frac{k^2}{4\pi\varepsilon_0}\frac{e^{ikr}}{r}\left[p_x + \frac{1}{\eta_0}m_y - \frac{ik}{6}Q^e_{xz} - \frac{ik}{6\eta_0}Q^m_{yz}\right] \tag{4.117}$$

$$E_{scat}(z-) = E_{scat}(\vec{n} = -\vec{e}_z) = \frac{k^2}{4\pi\varepsilon_0}\frac{e^{ikr}}{r}\left[p_x - \frac{1}{\eta_0}m_y + \frac{ik}{6}Q^e_{xz} - \frac{ik}{6\eta_0}Q^m_{yz}\right] \tag{4.118}$$

As only one component of the vectorial and tensorial multipoles are excited, the multipoles are linked to the field through scalar dipole and quadrupole polarizabilities. They are defined by: [14, 15]:

$$\vec{p} = \varepsilon_0\alpha^e_{eff}\vec{E}_{inc} \qquad \vec{m} = \mu_0\alpha^m_{eff}\vec{H}_{inc} \tag{4.119}$$

$$\hat{Q}^e = \varepsilon_0\alpha^{eq}_{eff}\frac{\vec{\nabla}\otimes\vec{E}_{inc} + \vec{E}_{inc}\otimes\vec{\nabla}}{2} \qquad \hat{Q}^m = \mu_0\alpha^{mq}_{eff}\frac{\vec{\nabla}\otimes\vec{H}_{inc} + \vec{H}_{inc}\otimes\vec{\nabla}}{2} \tag{4.120}$$

from these definitions, we obtain:

$$p_x = \varepsilon_0\alpha^e_{eff}E_0 \qquad m_y = \mu_0\alpha^m_{eff}H_0 \qquad Q^e_{xz} = \varepsilon_0\alpha^{eq}_{eff}\frac{ik}{2}E_0 \qquad Q^m_{yz} = \mu_0\alpha^{mq}_{eff}\frac{ik}{2}H_0 \tag{4.121}$$

Injecting (4.121) in the expressions of the scattered field leads to the following relations with the polarisabilities:

$$E_{scat}(z+) = \frac{k^2}{4\pi}\frac{e^{ikr}}{r}\left[\alpha^e_{eff} + \alpha^m_{eff} + \frac{k^2}{12}\alpha^{eq}_{eff} + \frac{k^2}{12}\alpha^{mq}_{eff}\right]E_0 \tag{4.122}$$

$$E_{scat}(z-) = \frac{k^2}{4\pi}\frac{e^{ikr}}{r}\left[\alpha^e_{eff} - \alpha^m_{eff} - \frac{k^2}{12}\alpha^{eq}_{eff} + \frac{k^2}{12}\alpha^{mq}_{eff}\right]E_0 \tag{4.123}$$

Using equation (4.86) allows to derive as previously the reflection and transmission coefficients in terms of the effective polarisabilities (here up to the quadrupolar terms) of the resonator in the unit-cell:

$$r = \frac{ik}{2\mathcal{S}}\left(\alpha^{e}_{eff} - \alpha^{m}_{eff} - \frac{k^2}{12}\alpha^{eq}_{eff} + \frac{k^2}{12}\alpha^{mq}_{eff}\right) \tag{4.124}$$

$$t = 1 + \frac{ik}{2\mathcal{S}}\left(\alpha^{e}_{eff} + \alpha^{m}_{eff} + \frac{k^2}{12}\alpha^{eq}_{eff} + \frac{k^2}{12}\alpha^{mq}_{eff}\right) \tag{4.125}$$

These expressions are similar to equations (4.97) and (4.98) generalized in terms of spherical multipole coefficients $(a_{n,m}, b_{n,m})$. The relation between the polarisabilities and the spherical multipole moments are:

$$\alpha^{e}_{eff} = \frac{i3\pi}{k^3}(a_{1,1} - a_{1,-1}) \qquad \alpha^{m}_{eff} = \frac{i3\pi}{k^3}(b_{1,1} + b_{1,-1}) \tag{4.126}$$

$$\alpha^{eq}_{eff} = \frac{i60\pi}{k^5}(a_{2,1} - a_{2,-1}) \qquad \alpha^{mq}_{eff} = \frac{i60\pi}{k^5}(b_{2,1} + b_{2,-1}) \tag{4.127}$$

These relations represent a change of basis between cartesian and spherical coordinates to express the multipole coefficients [34, 37].

4.4 Concluding remarks

In this chapter, we presented various tools and models that can be used to describe, analyze or calculate the optical properties of metasurfaces. Under the dipolar approximation, we saw that the interaction terms between particles are independent of the scattering properties of the considered particles, and can be calculated by the lattice sums of Green's function. The reflection and transmission properties are indeed related to effective polarisabilities of particles in the array. The simple dipole model assuming Lorentzian resonances will be applied to Huygens metasurfaces in the next chapter to highlight their operating principle.

Importantly, the original content of this chapter lies in the generalization of the dipolar formalism, widely used until now in the literature, to any multipolar order. We have proposed a generalized multipolar description of the reflection and transmission coefficients across a particle layer using a spherical vector harmonic expansion. This makes it possible to account for high multipolar orders without adding any particular complexity, as is the case when resorting to Cartesian multipoles, a common approach in the literature thus far. In the next chapter, we will use the generalized multipole formalism to give a physical insight into numerically calculated features of metasurfaces. Next this formalism will be used to derive conditions of complete absorption that will then be applied to provide various examples of metasurface absorbers.

4.5 References

[1] A. E. H. Love, "I. the integration of the equations of propagation of electric waves," *Philosophical Transactions of the Royal Society of London. Series A, Containing Papers of a Mathematical or Physical Character*, vol. 197, no. 287-299, pp. 1–45, 1901. 85

[2] S. Schelkunoff, "Some equivalence theorems of electromagnetics and their application to radiation problems," *The Bell System Technical Journal*, vol. 15, no. 1, pp. 92–112, 1936. 85

[3] E. F. Kuester, M. A. Mohamed, M. Piket-May, and C. L. Holloway, "Averaged transition conditions for electromagnetic fields at a metafilm," *IEEE Transactions on Antennas and Propagation*, vol. 51, no. 10, pp. 2641–2651, 2003. 87

[4] C. L. Holloway, M. A. Mohamed, E. F. Kuester, and A. Dienstfrey, "Reflection and transmission properties of a metafilm: With an application to a controllable surface composed of resonant particles," *IEEE Transactions on Electromagnetic Compatibility*, vol. 47, no. 4, pp. 853–865, 2005. 87

[5] M. Selvanayagam and G. V. Eleftheriades, "Circuit modeling of Huygens surfaces," *IEEE Antennas and Wireless Propagation Letters*, vol. 12, pp. 1642–1645, 2013. 87, 91

[6] S. Tretyakov, *Analytical modeling in applied electromagnetics*. Artech House, 2003. 88, 92, 95

[7] D. M. Pozar, *Microwave engineering*. John Wiley & Sons, 2009. 89

[8] M. Albooyeh, Y. Ra'di, M. Adil, and C. Simovski, "Revised transmission line model for electromagnetic characterization of metasurfaces," *Physical Review B*, vol. 88, no. 8, p. 085435, 2013. 91

[9] A. B. Evlyukhin, C. Reinhardt, A. Seidel, B. S. Luk'yanchuk, and B. N. Chichkov, "Optical response features of *Si*-nanoparticle arrays," *Physical Review B*, vol. 82, no. 4, p. 045404, 2010. 92, 93, 94, 97

[10] M. A. Yurkin and A. G. Hoekstra, "The discrete dipole approximation: an overview and recent developments," *Journal of Quantitative Spectroscopy and Radiative Transfer*, vol. 106, no. 1-3, pp. 558–589, 2007. 93

[11] G. W. Mulholland, C. F. Bohren, and K. A. Fuller, "Light scattering by agglomerates: coupled electric and magnetic dipole method," *Langmuir*, vol. 10, no. 8, pp. 2533–2546, 1994. 93

[12] O. Merchiers, F. Moreno, F. González, and J. Saiz, "Light scattering by an ensemble of interacting dipolar particles with both electric and magnetic polarizabilities," *Physical Review A*, vol. 76, no. 4, p. 043834, 2007. 93

[13] B. García-Cámara, F. Moreno, F. González, and O. J. Martin, "Light scattering by an array of electric and magnetic nanoparticles," *Optics express*, vol. 18, no. 10, pp. 10001–10015, 2010. 93

[14] A. B. Evlyukhin, C. Reinhardt, U. Zywietz, and B. N. Chichkov, "Collective resonances in metal nanoparticle arrays with dipole-quadrupole interactions," *Physical Review B*, vol. 85, no. 24, p. 245411, 2012. 94, 103

[15] V. E. Babicheva and A. B. Evlyukhin, "Metasurfaces with electric quadrupole and magnetic dipole resonant coupling," *ACS Photonics*, vol. 5, no. 5, pp. 2022–2033, 2018. 94, 103

[16] S. D. Swiecicki and J. Sipe, "Surface-lattice resonances in two-dimensional arrays of spheres: multipolar interactions and a mode analysis," *Physical Review B*, vol. 95, no. 19, p. 195406, 2017. 94

[17] S. D. Swiecicki and J. Sipe, "Periodic green functions for 2D magneto-electric quadrupolar arrays: explicitly satisfying the optical theorem," *Journal of Optics*, vol. 19, no. 9, p. 095006, 2017. 94

[18] V. E. Babicheva and A. B. Evlyukhin, "Analytical model of resonant electromagnetic dipole-quadrupole coupling in nanoparticle arrays," *Physical Review B*, vol. 99, no. 19, p. 195444, 2019. 94

[19] S. A. Tretyakov, A. J. Viitanen, S. I. Maslovski, and I. E. Saarela, "Impedance boundary conditions for regular dense arrays of dipole scatterers," *IEEE Transactions on Antennas and Propagation*, vol. 51, no. 8, pp. 2073–2078, 2003. 95

[20] A. Alu and N. Engheta, "Optical wave interaction with two-dimensional arrays of plasmonic nanoparticles," in *Structured Surfaces as Optical Metamaterials*, pp. 58–93, Cambridge University Press Cambridge, UK, 2011. 95

[21] M. Albooyeh, D. Morits, and S. Tretyakov, "Effective electric and magnetic properties of metasurfaces in transition from crystalline to amorphous state," *Physical Review B*, vol. 85, no. 20, p. 205110, 2012. 95, 96

[22] R. Alaee, M. Albooyeh, and C. Rockstuhl, "Theory of metasurface based perfect absorbers," *Journal of Physics D: Applied Physics*, vol. 50, p. 503002, nov 2017. 96

[23] S. Kruk, B. Hopkins, I. I. Kravchenko, A. Miroshnichenko, D. N. Neshev, and Y. S. Kivshar, "Broadband highly efficient dielectric metadevices for polarization control," *Apl Photonics*, vol. 1, no. 3, p. 030801, 2016. 97

[24] P. Grahn *et al.*, "Multipole excitations in optical meta-atoms," Master's thesis, 2012. 98

[25] C. F. Bohren and D. R. Huffman, *Absorption and scattering of light by small particles*. John Wiley & Sons, 2008. 98

[26] Y.-l. Xu, "Electromagnetic scattering by an aggregate of spheres," *Applied optics*, vol. 34, no. 21, pp. 4573–4588, 1995. 98

[27] P. Grahn, A. Shevchenko, and M. Kaivola, "Electromagnetic multipole theory for optical nanomaterials," *New Journal of Physics*, vol. 14, no. 9, p. 093033, 2012. 100, 101, 102

[28] X. Ming, X. Liu, L. Sun, and W. J. Padilla, "Degenerate critical coupling in all-dielectric metasurface absorbers," *Optics express*, vol. 25, no. 20, pp. 24658–24669, 2017. 102

[29] J. D. Jackson, *Classical electrodynamics*. AAPT, 1999. 102

[30] M. Liu, C. Zhao, and B. Wang, "Polarization management based on dipolar interferences and lattice couplings," *Optics express*, vol. 26, no. 6, pp. 7235–7252, 2018. 102

[31] W. Liu and A. E. Miroshnichenko, "Beam steering with dielectric metalattices," *ACS Photonics*, vol. 5, no. 5, pp. 1733–1741, 2017. 102

[32] P. D. Terekhov, V. E. Babicheva, K. V. Baryshnikova, A. S. Shalin, A. Karabchevsky, and A. B. Evlyukhin, "Multipole analysis of dielectric metasurfaces composed of nonspherical nanoparticles and lattice invisibility effect," *Physical Review B*, vol. 99, no. 4, p. 045424, 2019. 103

[33] V. Savinov, V. Fedotov, and N. I. Zheludev, "Toroidal dipolar excitation and macroscopic electromagnetic properties of metamaterials," *Physical Review B*, vol. 89, no. 20, p. 205112, 2014. 103

[34] R. Alaee, C. Rockstuhl, and I. Fernandez-Corbaton, "An electromagnetic multipole expansion beyond the long-wavelength approximation," *Optics Communications*, vol. 407, pp. 17–21, 2018. 103, 104

[35] P. D. Terekhov, K. V. Baryshnikova, Y. A. Artemyev, A. Karabchevsky, A. S. Shalin, and A. B. Evlyukhin, "Multipolar response of nonspherical silicon nanoparticles in the visible and near-infrared spectral ranges," *Physical Review B*, vol. 96, no. 3, p. 035443, 2017. 103

[36] A. Pors, S. K. Andersen, and S. I. Bozhevolnyi, "Unidirectional scattering by nanoparticles near substrates: generalized kerker conditions," *Optics express*, vol. 23, no. 22, pp. 28808–28828, 2015. 103

[37] S. Mühlig, C. Menzel, C. Rockstuhl, and F. Lederer, "Multipole analysis of meta-atoms," *Metamaterials*, vol. 5, no. 2-3, pp. 64–73, 2011. 104

Chapter 5

Multipolar Huygens metasurfaces

Contents

5.1 Introduction 110
5.2 Main features of Huygens metasurfaces 110
5.2.1 Understanding of their properties through the dipolar Lorentzian model . . 110
5.2.2 Generalized conditions on multipoles 115
5.2.3 Lattice coupling effects on the multipoles 116
5.3 Wavefront shaping with dielectric clusters 118
5.3.1 Phase modulation in the infrared with silicon cluster arrays 118
5.3.2 Design of beam shapping devices 124
5.3.3 Limitations of transparent Huygens metasurfaces 128
5.4 Perfect Absorbers 130
5.4.1 Absorbers based on dielectric and plasmonic spherical particles 130
5.4.2 Total absorption with core-shells 135
5.4.3 Cluster based perfect absorbers 143
5.5 Concluding remarks 149
5.6 References 150

Summary: This chapter is dedicated to the study of Huygens metasurfaces. In a first part, we investigate their properties from a theoretical point of view, based on a simple dipolar lorentzian model. We highlight how a perfect transmission accompanied by a complete coverage of the $[0\,;\,2\pi]$ interval for the phase can be obtained for lossless metasurfaces while a unit absorption can be achieved with resonators under critical coupling. We then generalize the required conditions to achieve these properties to multipolar systems. In a second part we focus on wavefront control applications. We evidence the possibility of achieving a 2π phase shift with quadrupolar resonnances of silicon clusters. A phase variation induced by the size of the clusters is then exploited to demonstrate a beam deflection and focusing abilities of cluster arrays. Finally in a last part, we exploit the generalized absorption conditions to present various designs of perfect absorbers. Spherical particle, core-shell and cluster arrays, both plasmonic and dielectric, are studied. The specificities of each design allowing for either resonant, dual band or broadband absorption are presented in details.

5.1 Introduction

One of the most important features of Huygens metasurfaces is undoubtedly their capability to arbitrarily shape the wavefront of light. The phase delay acquired by light during its interaction with a multi-resonant nanostructure can be fully controlled, by tailoring the local composition or organization of the resonators in the metasurface, in order to impose a desired spatially varying phase profile to an incident plane wave. At the same time, the zero reflection regime obtained under the Kerker condition makes it possible for the realization of devices exhibiting high transmission. These two properties combined are the reasons for the recently increasing research on advanced wavefront engineering with metasurfaces. Among the studied applications, the most popular ones are the realization of lenses, beam deflectors, spiral phase plates, holograms, etc.

The performances of such devices are directly related to the intrinsic losses of the used materials. In order to minimize the losses, most of the efforts are nowadays directed toward the use of low-loss dielectrics which constitute a promising platform for applications at optical frequencies. Although energy dissipation can be highly undesirable, certain applications take advantage of it and require on the contrary an optimization of the absorption by the device. Thus, perfect absorbers can find numerous applications as sensors, optical switches, optical modulators, energy harvesters , thermal emitters, etc. Under specific conditions, lossy Huygens metasurfaces are known to completely absorb electromagnetic radiations.

In this context, this chapter is dedicated to the study of Huygens metasurfaces for these two kind of applications: wavefront control and perfect absorption. In a first part, we will resort to the dipolar Lorentzian model in order to acquire a fundamental understanding of the properties of these two types of devices. We will evidence both the origin of the 2π-phase coverage as well as the physical mechanism behind the optimization of the absorption. The second part will be devoted to wavefront control applications with silicon cluster based metasurfaces. Finally in a last part, various designs of perfect absorbers will be presented, ranging from dipolar to highly multipolar systems.

5.2 Main features of Huygens metasurfaces

5.2.1 Understanding of their properties through the dipolar Lorentzian model

5.2.1.a Kerker condition with loss-less metasurfaces

In order to understand the response of a Huygens metasurface, we focus in this part on the Lorentzian model presented in section 4.2.5. We remind the reader that this model describes the response of an idealized metasurface under the dipolar approximation, assuming a Lorentzian spectral shape for the electric and magnetic dipole resonances of the meta-atoms. The reflection and transmission coefficients of such a metasurface take the following form:

$$r = c_e - c_m \tag{5.1}$$

$$t = 1 + c_e + c_m \tag{5.2}$$

with

$$c_j = \frac{i\omega\Gamma_j}{\omega_j'^2 - \omega^2 - i\omega\left(\Gamma_j + \gamma_j\right)} \tag{5.3}$$

where Γ_j and γ_j correspond respectively to radiation and material loss rate (expressed in rad·s^{-1}) and where ω_j' is the central frequency of the resonances.

Reviewing the work of M. Decker *et al.* [1], we first apply the model to loss-less metasurfaces with $\gamma_e = \gamma_m = 0$. Three situations, illustrated on Fig. 5.1, are investigated. In the first situation the resonances are chosen to occur at distinct wavelengths with $\lambda_e = 550$nm and $\lambda_m = 750$nm. As it can be seen on Fig. 5.1-A, two reflection peaks are obtained at the position of each resonance.

In addition, the phase of the transmitted wave, presented in Fig. 5.1-C, exhibits a discontinuity and covers a range of amplitude π at the crossing of each resonance. By bringing the electric and magnetic resonances at closer wavelengths of respectively 625nm and 675nm, a single peak of reflection is this time observed on Fig. 5.1-D, while the phase of t presents a continuous variation covering completely the interval from 0 to 2π. Finally, for an ideal Huygens metasurface as presented in Fig. 5.1-G, such that the electric and magnetic resonances are perfectly superimposed, the transmission is this time unitary over the entire spectrum while the full phase interval is still accessible.

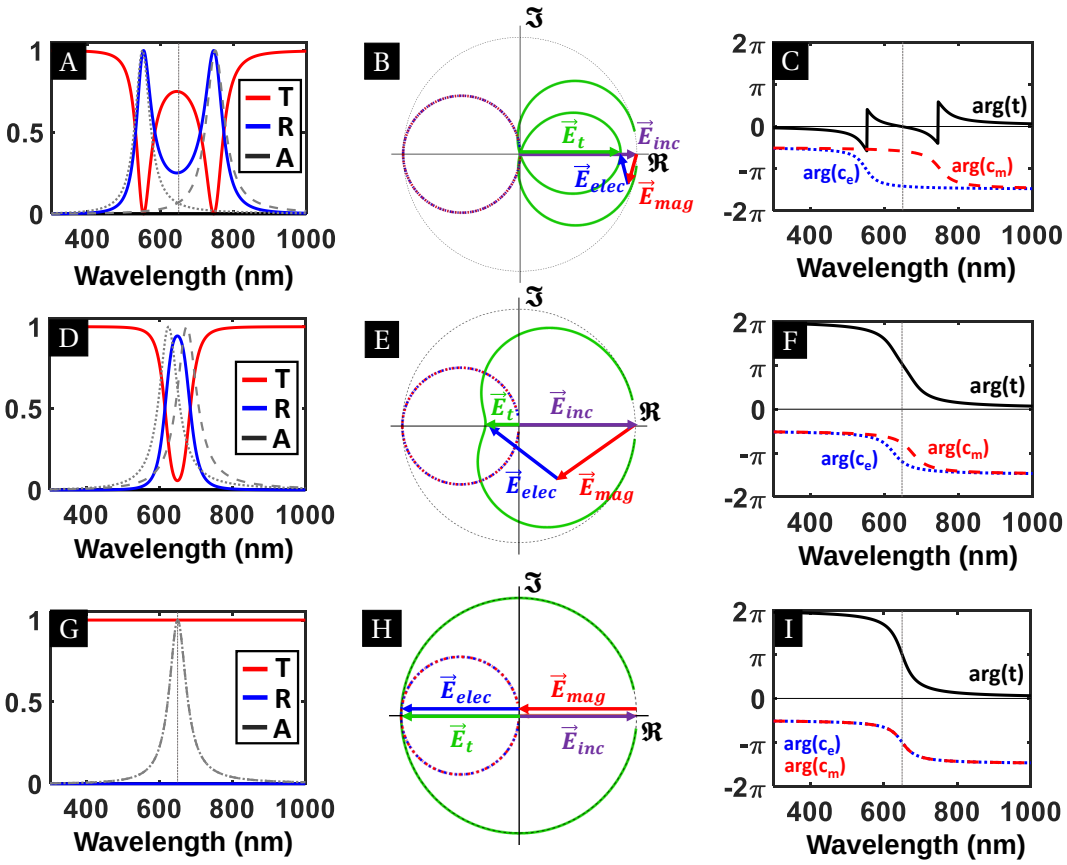

Figure 5.1 – Properties of a loss-less metasurface with spectrally separated or overlapped resonances. A) Transmission (red) and reflection (blue) spectra as a function of wavelength with λ_e = 550nm and λ_m = 750nm. Dotted and slashed grey lines are respectively the electric and magnetic resonances B) Trajectories of the t, c_e and c_m coefficients (respectively given by the continuous green, the dashed blue and the dotted red curves) in the complex plane as a function of wavelength. The vector diagram depicts the decomposition at λ = 650nm of the transmitted field $\vec{E}_t = \vec{E}_{inc} + \vec{E}_{elec} + \vec{E}_{mag}$ (green arrow) into contributions from the incident field with $|\vec{E}_{inc}| = 1$ (purple arrow), and from the electric and magnetic resonances terms (blue and red arrows respectively). C) phase spectra of the transmission and of the electric and magnetic coefficients (respectively the continuous black, the dotted blue and the dashed red curves). The triplets {D),E),F)} and {G),H),I)} correspond to the same quantities as depicted in {A),B),C)} but respectively for metasurfaces with resonances at λ_e = 625nm and λ_m = 675nm and overlapped resonances at $\lambda_e = \lambda_m$ = 650nm.

These significant changes in the response can be understood from the vector diagrams presented in Fig. 5.1-B,E,H that show the contributions of each vector $\vec{E}_{inc}$, $\vec{E}_{elec}$ and $\vec{E}_{mag}$ to the transmitted field $\vec{E}_t$ at λ = 650nm in the complex plane, as well as the trajectories of c_e, c_m and t as function of wavelength. In particular, the trajectories taken by the coefficients c_e and c_m, indicate that for any wavelength, the contributions of the electric and magnetic resonances to the transmitted field are of opposite sign regarding that of the incident field. $\vec{E}_{elec}$ and $\vec{E}_{mag}$ thus explore the phase interval $[-\pi/2\,;\,\pi/2]$ as the wavelength increases and are maximum and equal to $-\vec{E}_{inc}$

at their resonance wavelength. In the case of isolated resonances such as those presented on Figs. 5.1-A,B, this implies the cancellation of the transmission observed at λ_e and λ_m. On the other hand, when the two resonances are spectrally superimposed or in the same vicinity, they simultaneously contribute to the transmitted field. Therefore, close to their resonances, the resulting vector $\vec{E}_{elec} + \vec{E}_{mag}$ becomes bigger than $\vec{E}_{inc}$ in norm. The left part of the complex plane that was inaccessible to t in the previous case is now explored by the coefficient leading to a continuous 2π-phase variation observed in both Fig. 5.1-F and I. In addition, for the ideal metasurface, since the contribution of the electric and magnetic resonances are perfectly equal and in phase, the Kerker condition is met on the whole spectrum and it can be seen on Fig. 5.1-H that t now describes the whole unity circle $\left(\left|E_t\right| = 1\right)$ as the wavelength is increased.

As a result, we see the necessity to bring electric and magnetic resonances at the same operating wavelength to obtain a 2π-phase coverage and a unitary transmission.

5.2.1.b From high transmission devices to perfect absorbers: role of losses and critical coupling

We now analyze the impact of increasing intrinsic material losses on the properties of a Huygens metasurface. As in the previous part (Fig. 5.1-G,H and I), we consider the case of an ideal Huygens metasurface having degenerated electric and magnetic dipole resonances of equal strength and width ($\Gamma_e = \Gamma_m$) centered at 650nm, thus satisfying the Kerker condition over the full spectrum.

On Fig. 5.2, the effect of losses is investigated by varying the non-radiative decay rate γ_j of both resonances. The quantity $\gamma_j + \Gamma_j$ is kept constant and equal to 600×10^{-12} rad·s^{-1} for both resonances to ensure that the quality factors remain identical throughout the study.

Figures 5.2-A,B,C show the amplitude and phase spectral responses obtained in the case of the previously studied loss-less metasurface with $\gamma_e = \gamma_m = 0$. Figure 5.2 shows that by increasing the dissipative decay rate γ at the expense of the radiative one Γ, say as much as $\gamma_j/\Gamma_j = 0.5$, the contribution of the electric and magnetic resonances to the transmitted fields are reduced and the trajectory taken by t in the complex plane on Fig. 5.2-E does not lie on the unity circle anymore. This results in the emergence of an absorption peak centered at the resonance wavelength as observed on Fig. 5.2-D. Since the transmitted field is still out-of-phase with the incident field at the resonances, a full 2π-phase coverage is still achieve by $\arg(t)$, but the phase variation becomes much more abrupt than in the loss-less case (see Fig. 5.2-F). This regime where $\gamma < \Gamma$ is called the "overcoupled" regime.

By further increasing the dissipative damping, the amplitude of $\vec{E}_{elec}$ and $\vec{E}_{mag}$ keeps diminishing until $\vec{E}_{elec} = \vec{E}_{mag} = -\vec{E}_{inc}/2$ on resonance, obtained for $\gamma_j/\Gamma_j = 1$. In this case the electric fields $\vec{E}_{elec}$ and $\vec{E}_{mag}$ produced by the array at the resonance rigorously cancel the incident wave resulting in an absence of transmission and a perfect absorption, as observed on Fig. 5.2-G. Moreover, the phase jump becomes discontinuous at the resonance. A sudden jump between $3\pi/2$ and $\pi/2$ is observed on Fig. 5.2-I at the inflection point since half of the complex plane is no longer reached by t. Consequently the phase coverage is reduced to an amplitude of π. This condition that $\gamma_j/\Gamma_j = 1$ is called "critical coupling" indicating that the rate at which light is coupled to a resonance of the particles is equal to the dissipation rate associated to this resonance ensuring that the maximum of energy send on the metasurface is dissipated within it. On Fig. 5.3-A, we evidence the critical coupling requirements

$$\begin{cases} \gamma_e = \Gamma_e \\ \gamma_m = \Gamma_m \end{cases} \tag{5.4}$$

by mapping the absorption of a Huygens metasurface at the resonance wavelength for varying ratios γ_e/Γ_e and γ_m/Γ_m.

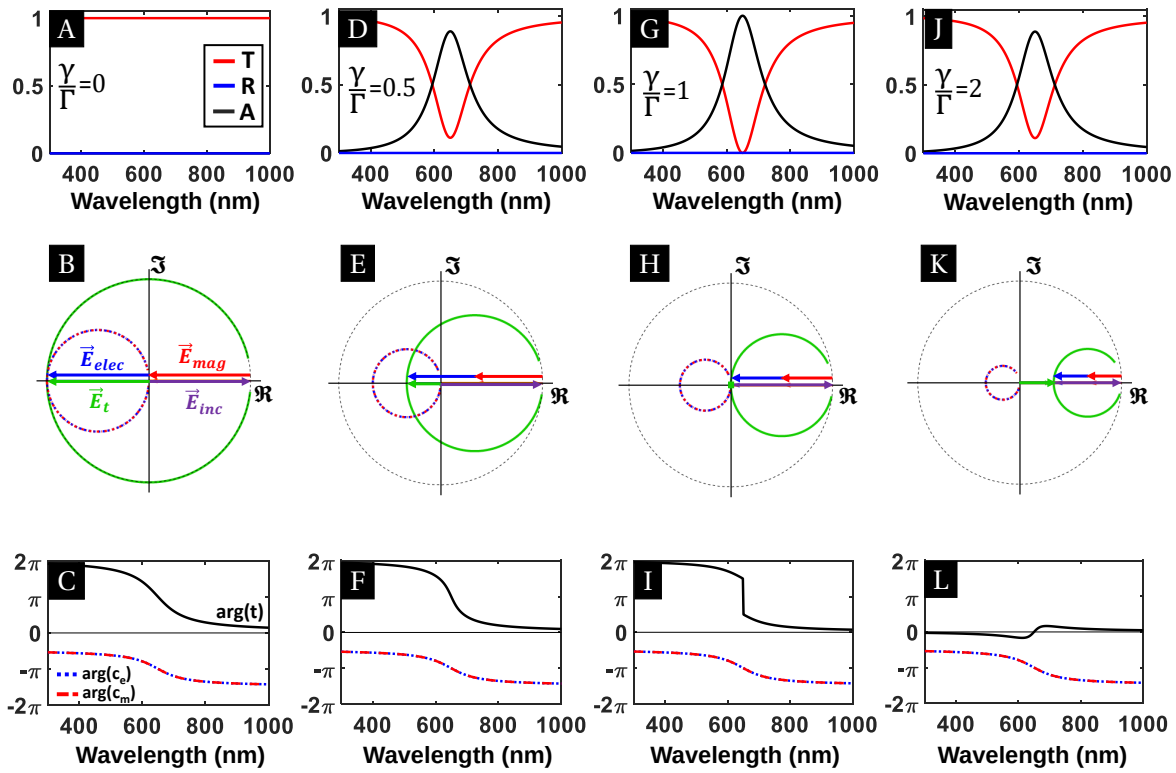

Figure 5.2 – Evolution of the spectral response of Huygens metasurfaces with degenerate electric and magnetic resonances ($\lambda_e = \lambda_m$) for increasing material losses. A) Transmission (red) and absorption (black) spectra as a function of wavelength for a loss-less metasurface with $\gamma_e = \gamma_m = 0$. B) Evolution of the t, c_e and c_m coefficients (respectively given by the continuous green, the dashed blue and the dotted red curves) in the complex plane for the loss-less metasurface as a function of wavelength. The vector diagram depicts the decomposition at $\lambda = 650$nm of the transmitted field $\vec{E}_t = \vec{E}_{inc} + \vec{E}_{elec} + \vec{E}_{mag}$. C) Total, electric and magnetic phase spectra (respectively given by the continuous black, the dotted blue and the dashed red curves). The triplets {D),E),F)}, {G),H),I)} and {J),K),L)} correspond to the same quantities as depicted in {A),B),C)} but for metasurfaces with increasing non-radiative loss rates $\gamma/\Gamma = 0.5$, $\gamma/\Gamma = 1$ and $\gamma/\Gamma = 2$. The quantity $\gamma + \Gamma$ is equal to 600×10^{-12} rad·s^{-1} and kept constant for all the plots.

It is worth noting that the critical coupling conditions do not impose γ_j (or Γ_j) to be equal for both the electric and magnetic resonances. This is illustrated on the top panel of Fig. 5.3-B, showing the absorption spectra for a metasurface under the critical coupling conditions with different values for $\gamma_e = \Gamma_e = 300 \times 10^{12}$ rad·s^{-1} and $\gamma_m = \Gamma_m = 200 \times 10^{12}$ rad·s^{-1}. The absorption is unitary at the resonance. In addition, the absorption due to each resonance is plotted on Fig. 5.3-B. They are determined by:

$$A_j = -2\left(\left|c_j\right|^2 + \Re(c_j)\right) = \frac{2\Gamma_j\gamma_j}{\left(\frac{\omega_j'^2 - \omega^2}{\omega}\right)^2 + \left(\Gamma_j + \gamma_j\right)^2} \tag{5.5}$$

with $A = A_e + A_m$. It can be seen that each resonance, being critically coupled, contributes to 50% of the absorption which corresponds to a universal maximum limit that can be obtained with a single resonance [2–5]. For critically coupled but spectrally separated resonances, the maximum of 50% of absorption would be reached at distinct wavelengths, not allowing for a total absorption by the array, hence there is also need for a metasurface with 2 spectrally overlapped resonances to optimize the absorption. The possibility to achieve 100% of absorption by a critically coupled structure has been applied to Huygens metasurfaces supporting electric and magnetic multipole moments in various recent works [6–12].

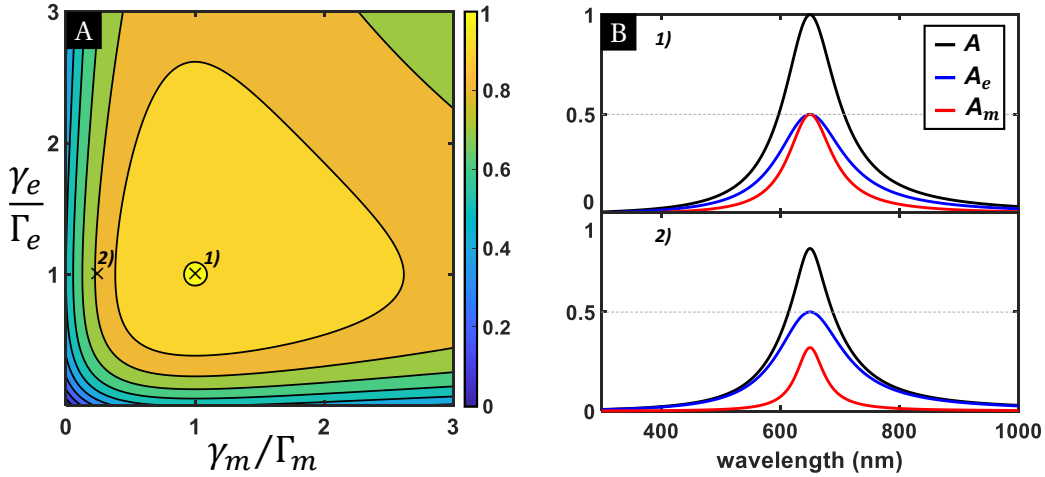

Figure 5.3 – A) Evolution of the absorption as a function of the ratios between the radiative and non-radiative decay rates of each resonance. Critical coupling and perfect absorption is obtained whenever $\gamma_j/\Gamma_j = 1$ for the electric and magnetic resonances simultaneously. B) Total absorption A and absorption per resonance (A_e and A_m) in the case of a metasurface with a critically coupled electric resonance $\gamma_e = \Gamma_e = 300\times10^{12}$ rad·s^{-1} and 1) a critically coupled magnetic resonance $\gamma_m = \Gamma_m = 200\times10^{12}$ rad·s^{-1} (top panel), and 2) an overcoupled magnetic resonance $\Gamma_m = 200\times10^{12}$ rad·s^{-1} and $\gamma_m = 50\times10^{12}$ rad·s^{-1} (bottom panel).

Finally, coming back to Fig. 5.2, the "undercoupled" regime is encountered whenever $\gamma_j > \Gamma_j$. In this case, even at the resonances, the incident field mostly contributes in the transmission response since $|\vec{E}_{inc}| > |\vec{E}_{elec} + \vec{E}_{mag}|$ for all wavelengths. The scattered plane waves are of low magnitude, therefore, the incident wave, weakly interacting with the metasurface, is almost directly transmitted. Although the transmission and absorption profiles are similar to those obtained in the overcoupling regime in Fig. 5.2-D, the phase variation is significantly different. The phase shift almost completely vanishes in this case because the contribution of the resonances to the transmission is too weak.

This study has revealed that drastically different properties are obtained, both in terms of amplitude and phase, depending on the amount of dissipative losses in the resonators. In particular, while a perfect transmission with a total phase variation can be obtained in the loss-less situation, a regime of perfect absorption can be reached by ensuring dissipative and radiative leakage rates of same magnitude. It can be noted that the transition presented here from the highly transmissive regime toward the perfectly absorbing regime has been experimentally demonstrated [13] recently. In this work, the authors employed arrays of silicon cylinders for which the dielectric losses were progressively increased by changing the concentration of dopant atoms to reach the full absorption of light by the array.

The results of this simple model can of course be generalized to situations of higher complexity, including multiple resonances and resonances of higher order, as it will be done in the next section. The underlying physics remains the same by replacing the electric (or respectively magnetic) dipole resonances of this model by any combination of symmetric (or respectively antisymmetric) resonances. However, if the analysis of the critical coupling in terms of decay rates, as used in this model, can be easily carried out for two Lorentzian resonances, it is not well suited to the study of complex multipolar systems, where the three Lorentz parameters (ω'_j, γ_j and Γ_j) might be difficult to extract for each resonance. Thus, in the following, we will instead resort to the multipolar analysis of metasurfaces presented in chapter 4.3.2.a in order to derive the Kerker condition and critical coupling equivalent criterion in terms of requirements on the multipole coefficients.

5.2.2 Generalized conditions on multipoles

Conditions for obtaining perfect transmission or absorption of light can be generalized to a multipolar system using the multipole expansion presented in section 4.3.2.a. The expression of the reflection and transmission coefficients (4.99, 4.100) are reproduced below:

$$r = -\frac{\pi}{2k^2\mathcal{S}}\sum_{n=1}^{\infty}\left[\mathcal{E}_n - \mathcal{O}_n\right] \tag{5.6}$$

$$t = 1 - \frac{\pi}{2k^2\mathcal{S}}\sum_{n=1}^{\infty}\left[\mathcal{E}_n + \mathcal{O}_n\right] \tag{5.7}$$

5.2.2.a Perfect transmission

Perfect transmission with an arbitrary phase ϕ can be obtained under the conditions that $r = 0$ and $t = e^{i\phi}$ leading to [14]:

$$\sum_{n=1}^{\infty}\mathcal{O}_n = \sum_{n=1}^{\infty}\mathcal{E}_n = \frac{\left[1 - e^{i\phi}\right]k^2\mathcal{S}}{2\pi} \tag{5.8}$$

The equality between the odd modes and even modes $\sum_{n=1}^{\infty}\mathcal{O}_n = \sum_{n=1}^{\infty}\mathcal{E}_n$ corresponds to the Kerker condition giving $r = 0$. It should be noted that this general condition only requires the sums of odd and even modes to be equal. It does not require that for every order n, the symmetric mode must be equal to the anti-symmetric odd mode, which would be a much stronger requirement. Therefore, as first emphasized in [14], using a balance between many multipoles, broadband transmission can be obtained without a need for a strict equality between two multipoles.

Furthermore, it can be seen by examining expression (5.8) that the phase taken by the sum of multipoles to ensure a unitary transmission remains completely free. For wave-shaping applications, one just needs to find the parameters of the metasurface that need to be explored in order to vary the phase ϕ on the full $[0\,;\,2\pi]$ interval.

5.2.2.b Perfect absorption

On the other hand, complete absorption occurs when both the reflection and transmission coefficients are simultaneously cancelled, that is when:

$$\sum_{n=1}^{\infty}\mathcal{O}_n = \sum_{n=1}^{\infty}\mathcal{E}_n = \frac{k^2\mathcal{S}}{\pi} \tag{5.9}$$

This last equation contains both the generalized Kerker condition and the zero transmission condition that occurs when

$$\sum_{n=1}^{\infty}\left(\mathcal{O}_n + \mathcal{E}_n\right) = 2k^2\mathcal{S}/\pi \tag{5.10}$$

Since the relation needs to be satisfied in the complex plane, it actually means that the overall sum of odd and even multipoles needs to be a purely real number and reach the exact value that enables a destructive interference with the incoming plane wave. Therefore, in eq. (5.9), the phase of the multipole sum is fixed to 0.

Equation (5.9) is a generalized critical coupling condition equivalent to the usual dipolar critical coupling condition given in terms of decay rates [4, 5] (see equation (5.4)) or polarisabilities [10, 15] (see later equation (5.13)). Indeed using eq.(5.9) in the unit-cell cross-section expressions, presented in section 4.3.2.b, evidences two of the main features of perfect absorption exhibited by symmetric metasurfaces previously discussed in the dipolar case: the power scattered by odd modes is equal to that scattered by even modes and the total scattered power is equal to the absorbed power:

$$\sigma^{\mathcal{E}}_{scat,a} = \sigma^{\mathcal{O}}_{scat,a} = \frac{\sigma_{abs}}{2} \tag{5.11}$$

Futhermore, in the dipolar case, the condition (5.9) reduces to:

$$a_1 = b_1 = \frac{k^2 \mathcal{S}}{3\pi} \tag{5.12}$$

and can be written equivalently with polarisabilities:

$$\alpha_e = \alpha_m = \frac{i\mathcal{S}}{k} \tag{5.13}$$

These conditions can only be met at the resonance wavelength for which the imaginary part (respectively real part) of the multipolar coefficients (respectively the polarisabilities) cancel. Therefore, degeneracy is necessary when considering only two resonances of opposite symmetry. On the contrary, in the multipolar case, this constraint on degeneracy no longer exists and a perfect absorption can be obtained at a wavelength different from the resonance wavelengths. In addition, while perfect absorption is limited to a single wavelength in the dipolar case, achieving broadband absorption is made possible in the multipolar case.

In section 5.4, we will see that the generalized condition (5.9) allows us to present a large variety of perfect absorbers, some of which being highly multipolar, which goes beyond what is commonly found in the literrature.

5.2.3 Lattice coupling effects on the multipoles

To complete this section, we focus in this part on the lattice coupling effect between particles. Indeed, as we saw in section 4.2.4 using the coupled dipoles model, lattice terms are part of the response of an array of particles, affecting the spectral properties of its constituents. In the following sections, we will see that lattice interactions are key parameters in obtaining Huygens surfaces and perfect absorbers. They help controlling the resonant features of the metasurfaces, hence a need to foresee their effects on particle responses.

In order to highlight the main signatures of the coupling effects, we consider an array of model particles, taken as spheres of radius R = 200nm, with a high refractive index of 4+0.05i. The particles are organized in an infinite square lattice with a variable pitch.

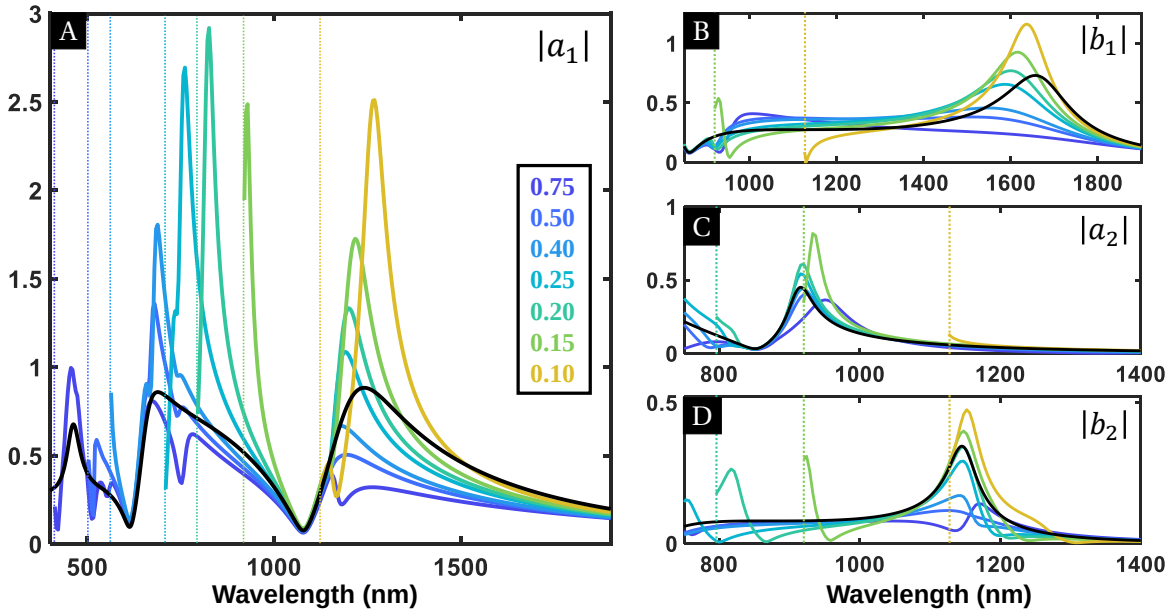

Figure 5.4 – Impact of the lattice coupling on the multipoles. A) Evolution of the modulus of the electric dipole coefficient a_1 as a function of the surface fraction of a square metasurface consisting of particles with a radius of 200nm and with constant refractive index of $4 + 0.05i$. The black line represents the Mie coefficient of a single isolated particle. Panels B),C),D) present the same study for respectively the magnetic dipole, the electric quadrupole and the magnetic quadrupole coefficients.

Figure 5.4 presents the evolution of the modulus of the first multipole coefficients of the particles for several surface fractions f_s of the array, defined as $f_s = \pi R^2/\mathcal{S}$. The multipole coefficients are obtained in COMSOL multiphysics from the knowledge of the current densities in the resonator by applying the integral projections presented in section 2.2.6.c.

In particular, panel A of Fig. 5.4 is dedicated to the electric dipole coefficient a_1. The coefficient obtained in the case of a single isolated sphere is presented in black and the fundamental resonance is around 1250nm. This resonance can also be identified for the arrays of particles, however, its spectral position and amplitude are affected by the choice of the lattice pitch. For high density arrays, we observe that the resonance maximum is attenuated compared to that which would be obtained with an isolated particle. By increasing the pitch, the resonance amplitude increases while its position is red-shifted. Similar behavior is observed for the other multipoles on Fig. 5.4. For the electric dipole, the highest value is obtained for $f_s = 0.10$. In this situation, the wavelength of the Mie dipolar resonance of the particle is located near the Rayleigh anomaly cut-off wavelength λ_R of the lattice. This wavelength delimits the transition from the specular to the diffracting domain for which diffraction lobes other than the zero-th order exist. The Rayleigh wavelength can be easily determined from the grating formula:

$$L[\sin\theta_d - \sin\theta_i] = m\lambda \tag{5.14}$$

where θ_i and θ_d are the incident and diffracted angle, $L = \sqrt{\mathcal{S}}$ is the period of the grating and m is an integer. λ_R is found at the passing-off of the first in plane diffraction order for which $\theta_d = 90°$. Under normal incidence, this leads to $\lambda_R = L$. Therefore, for $f_s = 0.1$, since the distance between the particles, indicated by the vertical dotted line, becomes comparable to the excitation wavelength of the dipole, the resonance of the particle is coupled with the lattice resonance of the Rayleigh anomaly, resulting in the strong response observed. The lattice resonance depends on the grating period rather than on the material and shape of the particles. Being in the proximity of a single particle resonance, the lattice resonances strongly enhance the initial particle response. On the other hand, far from the original particle resonance, the lattice resonances appear as additional separate features on the spectra. Thus, between 600nm and 1000nm, the displacement of the lattice resonance corresponding to the very sharp peaks can be observed as the cut-off wavelength of the diffractive domain increases.

Therefore, this study reveals that the lattice periodicity is an important parameter of control of the metasurface spectral response. A proper choice of the pitch enables a tuning in both amplitude and position of the main particle resonances and additional strong collective lattice resonances occur in the vicinity of the diffraction limit. Of course, numerous studies have been carried out that seek to engineer resonances in arrays of nanoparticles. In [16, 17], it was evidenced that by choosing lattice periods independently along each mutual-perpendicular direction of the array, $\vec{e}_x$ and $\vec{e}_y$, electric and magnetic lattice resonances can be tuned independently. Therefore, while we will mostly focus on periodic square arrays, it is important to keep in mind that a complete control over the array periodicity along the two directions enables a fine spectral tuning of the even and odd multipoles of a metasurface. In addition, it has been shown recently that the narrow lattice resonances can also be adjusted to suppress the backward scattered waves realizing a so-called resonant lattice Kerker effect [16, 18, 19]. This effect will be encountered in the next section, dedicated to the design of metasurfaces with wavefront shaping abilities. This subject has been extensively studied in the past decade [20–24].

5.3 Wavefront shaping with dielectric clusters

Wavefront engineering consists in modifying the propagation of an incident wave on a structure so that it emerges out with a desired defined pattern. The control of the emerging wavefront is directly determined by the local phase shifts induced by the device on the wave. In conventional bulk optics, phase accumulation acquired by light is modulated by varying locally the optical thickness of the device. In contrast, with metasurfaces, the phase shifts are induced by the scattering of the resonant building blocks. A control of the phase over a full 2π-range is required with the different subwavelength resonators in order to implement any desired phase profile. By properly imposing the local phase gradient, various wavefront engineering functions can be realized. In this chapter we will focus more closely on two examples: beam deflection and focusing.

Regarding beam deflection, linear gradients of phase must be implemented to achieve planar refracted wavefronts. Applying Fermat's principle [25, 26] or using the momentum conservation of wave-vectors [27, 28], the deflection angle θ_t is simply given by:

$$N_t \sin\theta_t - N_i \sin\theta_i = \frac{\lambda}{2\pi}\frac{d\phi}{dx} \tag{5.15}$$

where $d\phi/dx$ is a spatially constant phase gradient, N_t and N_i are respectively the refractive indices of the media on the transmitted and incident sides of the metasurface and θ_i is the angle of incidence. Similar to the gratting formula, equation (5.15) is also known as the generalized Snell law and indicates that a beam of light can be bent at different angles depending on the magnitude of the implemented phase gradient. In section 5.3.2.a, we will use this relation as a guideline to design a beam deflector.

Alternatively, to achieve beam focusing, a hyperboloidal phase profile must be implemented on the surface [29, 30]. In 1D, the required spatial phase profile is given by:

$$\phi(x) = \frac{2\pi}{\lambda}\left(f - \sqrt{x^2 + f^2}\right) \tag{5.16}$$

where f is the focal length of the lens.

In section 3.3.2, we presented the original idea that clusters of particles can behave as Huygens sources, making it possible to achieve the first Kerker condition. However, their possible use in metasurfaces remains to be proven. In this section we will demonstrate numerically how they may be used for wavefront shaping. We focus in particular on dielectric clusters made of silicon inclusions. This material is chosen since it exhibits negligible losses at the edge of the visible and in the near infrared, which is necessary to obtain high transmission devices. In a first part, we will evidence different control parameters of a cluster-based metasurface enabling for a complete phase variation. A local variation of the radius of the clusters or of the lattice pitch, will be shown to induce the continuous phase coverage over the $[0\ ;\ 2\pi]$ interval. In a second step, the beam-shaping capabilities of our clusters will be illustrated by designing a deflecting device as well as a flat 1D metasurface lens.

5.3.1 Phase modulation in the infrared with silicon cluster arrays

In order to demonstrate wavefront control capabilities, the starting point of our study is a cluster composed of 13 silicon particles, that is shown in Fig. 5.5-B. This cluster is chosen essentially for its low number of particles, that limits the weight of the performed finite element simulations. This configuration with 12 particles organized in a regular icosahedron around a central one is a well known configuration for forming dense homogeneous clusters, as it is also the solution to the problem of sphere packing known as the "kissing number" problem [31, 32]. In addition, we have shown in section 3.3.2 that such clusters made of 13 silicon particles are particularly interesting building blocks since they can be tuned to reach the Huygens regime with a high scattering efficiency.

Following the design procedure established in section 3.3.2, the cluster is designed to exhibit, in air, resonances in the infrared domain where silicon presents very low absorption loss. The total radius of the aggregate is taken as R = 390nm with particles of 130nm radius. The multipolar content of the spectral response of this meta-atom is presented in Fig. 5.5-A. It indicates that electric and magnetic dipole resonances are excited at close wavelengths of respectively 1370nm and 1480nm. In addition, the scattering efficiency takes values close to 4 at these wavelengths. At shorter wavelengths, the two quadrupole resonances are also jointly excited at 1125nm and 1145nm, with a scattering efficiency reaching approximately 5. As already presented in chapter 3, this two-by-two overlap of the resonances of opposite parity enables satisfying the Kerker condition over a wide frequency band. This cluster therefore constitute an interesting building block for the realization of wavefront shaping metasurfaces in the infrared.

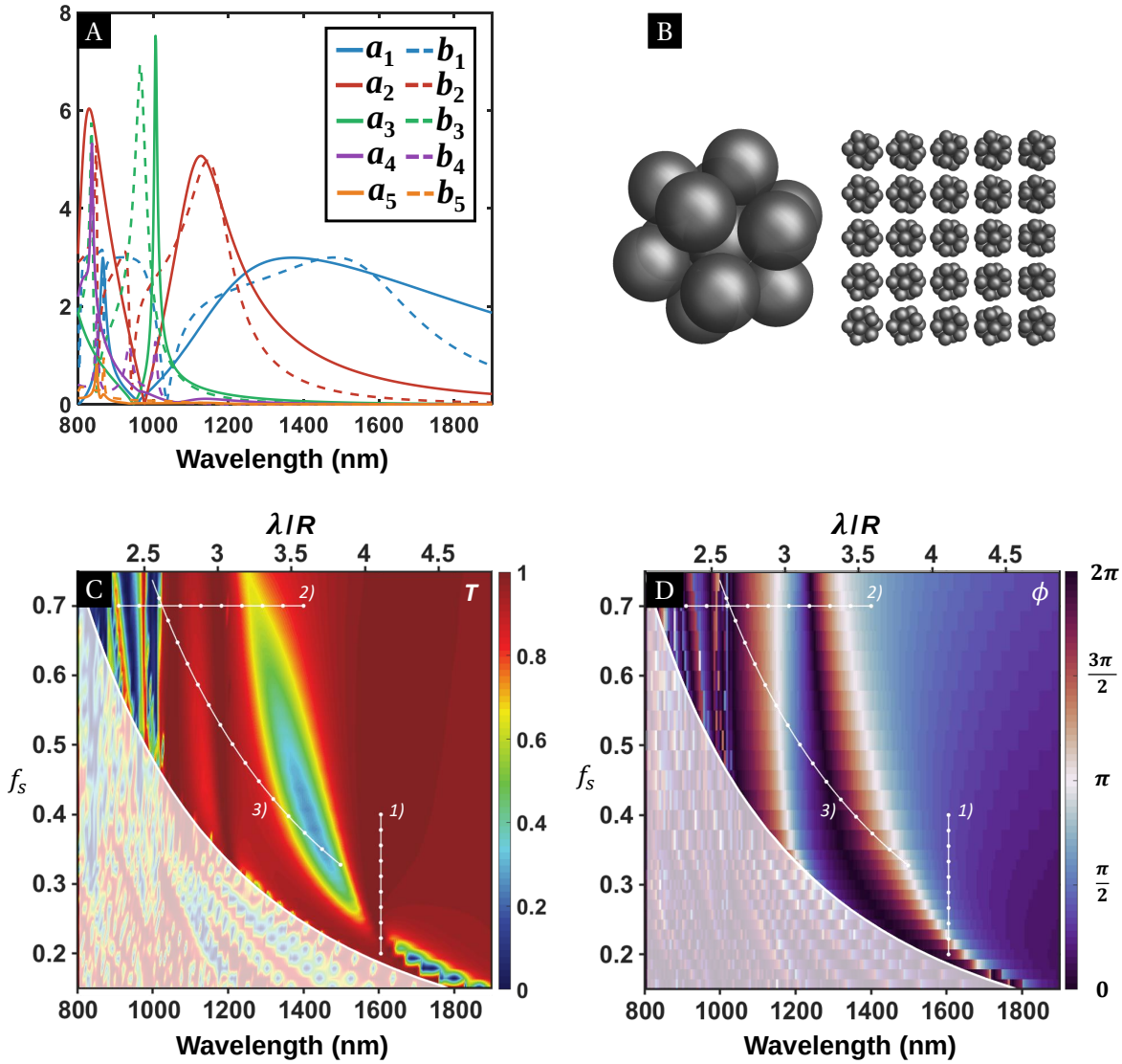

Figure 5.5 – A) spherical multipole coefficients of a cluster of radius R = 390nm made of 13 silicon particles with radius of 130nm. B) Illustration of the cluster geometry and of a square metasurface of clusters with a filling fraction f_s of 0.7. C) Transmittance and D) phase modulation of t as function of the surface fraction for an infinite periodic square array made from the cluster presented in panel B. The maps are presented both as a function of wavelength (bottom axis), for the cluster of radius R = 390nm, and as a function of size normalized wavelength (top axis) λ/R since they are identically transposable to other cluster sizes due to the constant refractive index $N \approx 3.5$ exhibited by silicon in the near-infrared domain. The whitened area corresponds to the diffraction regime found for wavelengths shorter than that of the Rayleigh anomaly $\lambda_R = L$.

Therefore, we now study the response of a metasurface consisting in an infinite square array of such a meta-atom. Figures 5.5-C,D shows respectively the transmission spectra and the phase variation of the transmitted wave obtained by varying the surface filling fraction of the metasurface. By observing Fig. 5.5-D, it can be seen that the phase essentially undergoes two continuous jumps of 2π when increasing the excitation wavelength from 1000nm to 1900nm. The first one is located on a band centered around 1200nm. This narrow phase shift band corresponds to the crossing of the two overlapped quadrupolar resonances. At the corresponding wavelengths on Fig. 5.5-C, we see that a strong transmission of about 100% is obtained on this quadrupolar band. The second phase jump is essentially observed between 1400nm and 1600nm and corresponds to the crossing of the dipole resonances of the clusters. The dipole resonances being much wider than the quadrupolar ones, the observed phase jump spreads over a significantly large interval of wavelengths. On the transmittance mapping, we see that this region of the spectrum is however accompanied by a drop in transmission, indicating that, although the dipole resonances are in the same neighbourhood, Kerker condition is not perfectly satisfied in this band. Furthermore, in this region, it is interesting to note the modulation of the transmission dip due to the interaction effects between the particles. While an important transmission higher than 70% is observed for the densest lattices, transmission drops when increasing the pitch of the array and reaches its minimum value for surface filling fractions of approximately 0.4. Therefore, for the studied design, the dilution of the metasurface degrades the fulfillment of the Kerker condition. Moreover, for surface fractions lower than 0.3, the electric and magnetic dipole resonances of the clusters are coupled to the lattice resonances. As a result, a red-shift following the displacement of the diffraction wavelength is observed for both the position of the phase jump and the position of the transmission dip. For surface fractions in the range of 0.25, the electric and magnetic dipole lattice resonances occur exactly at the same wavelength of 1600nm resulting in a resonant lattice Kerker effect providing a perfect transmission at this wavelength.

We want to emphasize here that the design of the meta-atom presented here was not further optimized to maximize the transmission of the metasurface. It would have been possible to improve the transmission, in particular in the dipole region of the particles, by working on the relative position of the dipolar resonances of our initial object. However, although it is not optimized, this system presents interesting characteristics that will be studied more in depth later on. First of all, it reveals the possibility of exploiting the quadrupolar resonances of particles to realize the phase modulation. Such devices based on higher order resonances are only sparsely studied compared to dipolar systems. We see on Fig. 5.5-C that quadrupolar resonances are less affected by coupling than their dipolar counterparts. This is evidenced by the value of the transmission, but also by the position of the quadrupolar resonances, visible on Fig. 5.5-D by looking at phase shift position, that both varies only slightly with the lattice pitch. Such metasurfaces exploiting higher order resonances could therefore exhibit a better robustness with an experimental positional uncertainty or disorder compared to dipolar system.

In the following, we will exploit two spectral regions in order to obtain the required 2π phase modulation. Firstly, the region around $\lambda = 1605$nm for which the dipolar lattice Kerker effect is obtained. Here a simple variation of the pitch, as indicated by the white line denoted as 1) on Figs. 5.5-C,D, allows to cross the region of high transmission while exploring all the available values for the phase. On the other hand, it is important to note that, since silicon takes a constant refractive index $N \approx 3.5$ over the entire studied interval of wavelengths between 800nm and 1900nm, the properties obtained for this cluster of radius 390nm, are fully tunable in wavelength by varying the size of the cluster (while keeping the 13 particles geometry and a constant ratio r/R). Thus, the transmission and phase mapping on Figs. 5.5-C,D are also presented according to the reduced wavelength λ/R (top axis) which spectrally rescales the properties of the metasurface depending on the cluster size. Therefore, we will see in a second step that, by fixing an operating wavelength and varying the cluster size R, the phase jump of the quadrupolar resonances can be exploited either by keeping a constant surface fraction, or by fixing the lattice pitch. These two situations are illustrated by the white lines denoted respectively as 2) and 3) on Figs. 5.5-C,D and will be the

object of a detailed study in section 5.3.1.b.

5.3.1.a Phase modulation by varying the surface density

In this section, we focus in particular on the excitation wavelength of 1605nm. Keeping R = 390nm, the transmittance and phase variation obtained at this wavelength as a function of the surface filling fraction of the array are presented on Fig. 5.6-A.

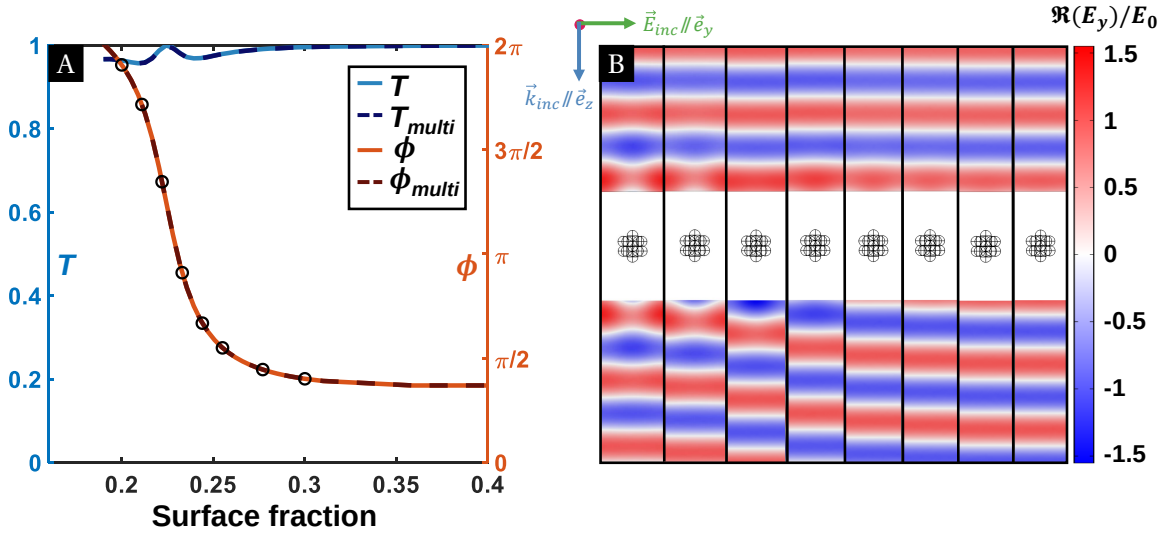

C

f_s	0.2	0.211	0.222	0.233	0.244	0.255	0.277	0.30
L (nm)	1548	1506	1468	1433	1400	1369	1313	1264

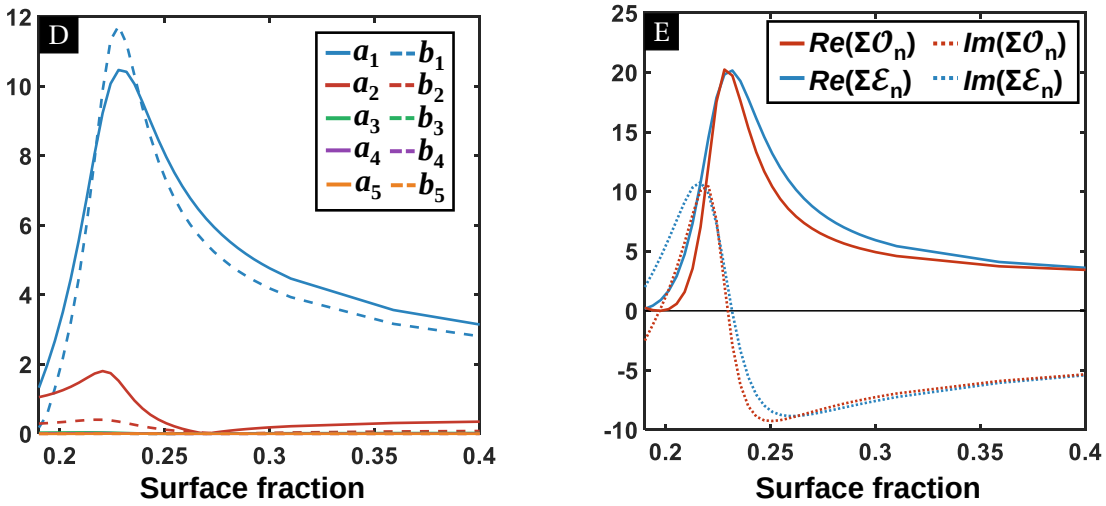

Figure 5.6 – A) Transmittance and phase modulation obtained at λ = 1605nm for increasing surface fraction. The dark blue and dark red dashed lines represent T and ϕ calculated from the multipole coefficients B) Maps of the real part of the electric field normalized by the incident electric field $E_0 = 1V/m$ calculated for eight different and independent unit-cells illustrating the phase variation of the transmitted wave. Each metasurface is shined from the top under normal incidence with an $\vec{e}_y$ polarized plane wave propagating along $\vec{e}_z$ as indicated by the trihedra. C) Surface fraction and corresponding array pitches (the corresponding phase values are indicated on panel A by the black circles). D) Modulus of the multipole coefficients. E) Wavelength dependence of the sum of the even and odd multipole coefficients verifying the Kerker condition.

As previously mentioned, a high transmission is observed at this wavelength due to the spectral

overlap of the electric and magnetic lattice resonances. The strong excitation of these two resonances is highlighted by the multipolar decomposition presented on Fig. 5.6-D, indicating only small contributions from the higher modes. It should be noted that the validity of the multipolar decomposition is verified by the excellent agreement observed on Fig. 5.6-A between the values of both the transmittance and phase calculated from the S-parameters at the ports and those retrieved from the multipole coefficients using equation (5.7). Furthermore, the Kerker condition is evidenced on Fig. 5.6-E depicting the real and imaginary parts of the sums $\sum_{n=1}^{\infty}\mathcal{O}_n$ and $\sum_{n=1}^{\infty}\mathcal{E}_n$. It can be observed that real and imaginary parts of the sums are closely overlapped whatever the considered surface fraction. Since lattice resonances are redshifted by increasing the grid pitch, the variation of the surface fraction allows the dipolar resonances to be scrolled at the wavelength of 1605nm and thus permits the exploration of a large phase interval. We see that 80% of the interval between 0 and 2π is covered by ϕ on Fig. 5.6-A.

The phase exploration is physically limited by two parameters: lower surface fractions are not accessible because of the appearance of the diffractive domain which strongly perturbs the spectral response of the metasurface. On the contrary, the high densities, limited by the maximal compacity of the array, only allows the exploration of the tail of the dipole resonances, providing solely a small variation of the phase. Therefore, most of the phase shift is obtained for surface filling fractions comprised between 0.2 and 0.3 corresponding respectively to lattice periods of 1548nm and 1264nm. The phase variation obtained by changing the grid pitch in this range of values is further illustrated in Fig. 5.6-B. The figure shows the spatial mapping of the real part of the electric field in a unit-cell, for 8 different periodic arrays of constant pitch, whose values are summarized in the table in Fig. 5.6-C. Each of the meta-lattice is illuminated from the top under normal incidence by a $\vec{e}_y$ polarized plane wave propagating in the $\vec{e}_z$ direction. Due to the low reflection exhibited by the metasurfaces, the electric field corresponding to that of the incident plane wave of wavelength 1605nm is essentially visible above the arrays. The juxtaposition of the maps allows to visualize the phase variation of Fig. 5.6-A obtained in transmission after the interraction of the incident beam with the particles. A shift in the position of the wavefront of almost a wavelength can be observed between the leftmost panel corresponding to the array of pitch L = 1548nm and the rightmost panel where the periodicity is L = 1264nm.

To conclude this part, we can note that the control of the phase by the grid pitch at the position of the lattice Kerker effect, as presented here for our system, has already been efficiently applied to silica disk arrays in different works [18, 33, 34]. In particular in [33] a vortex-beam shaping metasurface composed of four quadrants of varying lattice spacing was reported.

5.3.1.b Phase modulation induced by a variation in the size of the clusters

On Fig. 5.5-C we observe that, at a surface filling fraction of 0.7, a transmission greater than 60% is obtained over the entire spectrum between 1000nm and 1800nm covering the dipolar and quadrupolar resonances of the clusters of radius R=390nm. Since the metasurface features are preserved and only spectrally shifted when changing the clusters sizes, it is possible to scroll through this broadband transmission and to explore the important phase variation that is simultaneously observed on Fig. 5.5-D, by simply varying R at a given operating wavelength (top axis used).

Therefore, in the following, we arbitrarily consider an operating wavelength of 1400nm, and we vary the size of the clusters from R = 390nm to R = 600nm, making a homothety of all the geometric parameters which maintain the ratio r/R and the density of inclusions constant. At the same time, the pitch of the metasurface is also adjusted in order to guarantee a constant surface fraction of 0.7. This results in the exploration of the metasurface properties along the white line 2) on Figs. 5.5-C,D.

Figure 5.7-A shows both the transmission and phase obtain following this strategy. As expected, a transmission higher than 60% is obtained for cluster sizes comprised between 390nm and 540nm. Figures 5.7-C and D, present the results of the multipole expansions performed for the clusters in metasurfaces. They show respectively the modulus of the excited multipoles at

λ = 1400nm and the corresponding sums of the even and odd multipoles which make it possible to analyze the physical origin of the transmission evolution by resorting to the generalized Kerker criteria. From Fig. 5.7-C, it can be seen that clusters of radius between 400nm and 450nm sustain mostly dipolar resonances at 1400nm while quadrupole resonance are mainly excited at this wavelength for bigger clusters with 450nm< R <550nm. As already mentioned, the transmission dip obtained with the dipole resonances is explained by the slightly shifted excitation of the even and odd modes of the structure that can be observed on Fig. 5.7-D and explained by the Lorentzian model (Fig. 5.1-D). Increasing the cluster size above 450nm, a better balance between multipole of opposite parity is observed and a strong transmission is recovered over the entire range of the quadrupolar resonances, reaching as much as 100% on two points. Finally, the strong drop in transmission obtained for larger clusters is explained by the excitation of the structures' octupolar modes. It is interesting to stress here a benefit from using a multipolar structure: due to the successive excitation of the dipolar and quadrupolar orders, a continuous variation of the phase covering almost 4π is induced by the size variation (see Fig. 5.7-A). This double coverage of the 2π interval provides more flexibility in the choice of unit-cells to be selected for implementing the wavefront control functions. This wide phase variation is further evidenced by the mapping of the electric field presented on Fig. 5.7-B for several unit-cells. The large modulation in the position of the wavefront of the transmitted wave is clearly identifiable. The unit-cells used for this figure and their respective phases are indicated by the black circles on Fig. 5.7-A.

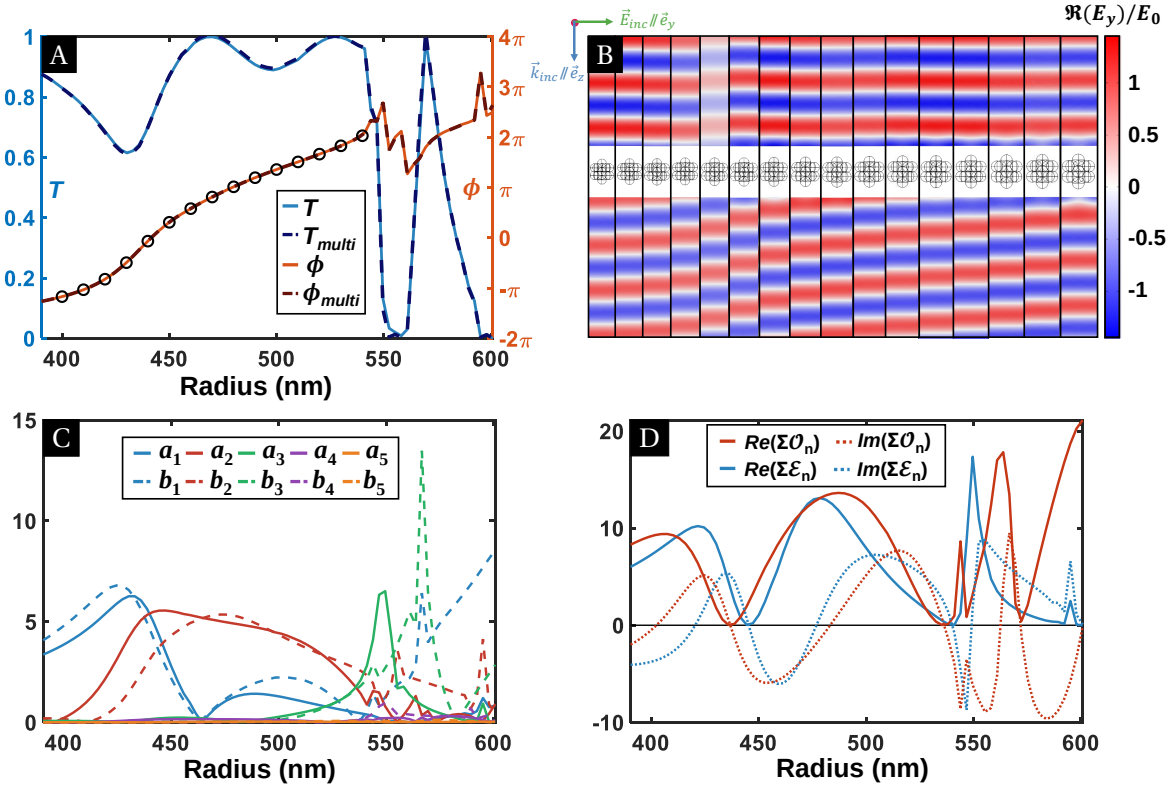

Figure 5.7 – A) Transmittance and phase modulation at λ = 1400nm for metasurfaces with clusters of increasing radius R. The particle size is varied by homothety and the filling surface fraction of the metasurface is kept constant at 0.7. The dark blue and dark red dashed lines represent T and ϕ calculated from the multipole coefficients. B) Maps of the real part of the electric field normalized by the incident electric field $E_0 = 1V/m$ calculated for sixteen different array unit-cells. Metasurfaces are illuminated under normal incidence by a $\vec{e}_y$ polarized plane wave propagating along $\vec{e}_z$. The selected unit-cells are those indicated by the black circles on panel A. C) Modulus of the multipole coefficients of the clusters in array. D) wavelength dependence of the sum of even and odd multipole coefficients.

In the previous study, in order to guarantee a constant surface fraction, the size variation of the

clusters was accompanied by an adjustment of the lattice pitch. In practice however, it might be easier to vary these two parameters independently, *i.e.* to fix the pitch and induce only a cluster size variation at different locations on the metasurface. Figure 5.8 presents the results of such an approach. Here, the operating wavelength is set at 1000nm and the cluster size is reduced from 390nm to 260nm. At the same time, the lattice periodicity is kept constant at a value of 806nm. A behaviour very similar to that of the previous case is observed, a difference being that the decrease of the surface fraction, from 0.74 to 0.33, induced by the diminishing cluster sizes, leads to a lower transmission in the region of the dipole resonances reaching only 30% at its minimum. Nevertheless, a transmission greater than 90% accompanied by a phase variation covering an amplitude of 2π remains observable in the region of the quadrupolar resonances for clusters of size comprised between 300nm and 380nm. The evolution of the surface filling fraction f_s of the arrays explored in this study as a function of the normalized size parameter λ/R of the clusters of varying size is indicated by the white curve denoted 3) on Figs. 5.5-C,D.

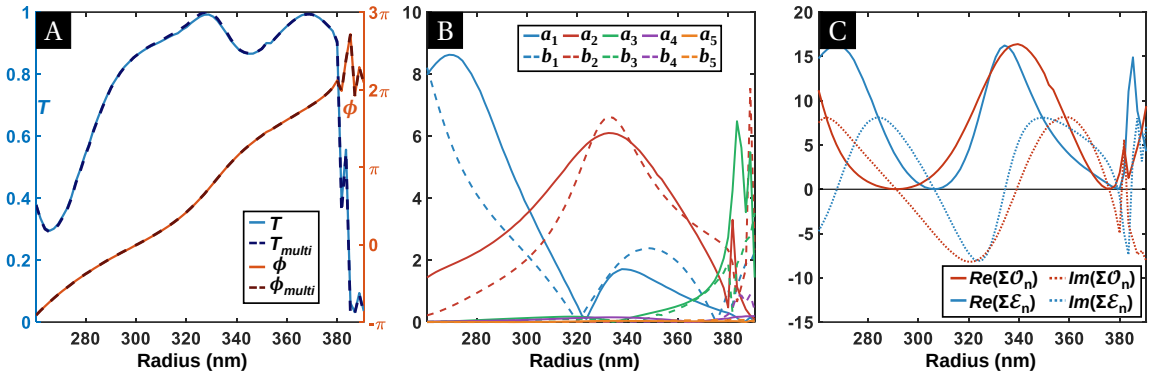

Figure 5.8 – A) Transmittance and phase modulation at $\lambda = 1000$nm for increasing cluster radius. The particle size is increased by homothety and the lattice pitch of the metasurface is kept constant and equal to 806nm. The dark blue and dark red dashed lines represent T and ϕ calculated from the multipole coefficients. B) Modulus of the multipole coefficients. C) Wavelength dependence of the sum of even and odd multipole coefficients.

The results obtained in this study with the clusters of radius comprised between 300nm and 380nm will serve as a reference for the next section, where designs of a beam deflector and a lens will be presented.

5.3.2 Design of beam shapping devices

In this part, to illustrate the phase control capability of *Si* cluster based transparent metasurfaces, we use the modulation of the phase induced by the size of the cluster to implement two wavefront control applications: beam deflection and focussing. As in the last part, the size variation is realized for a constant pitch of 806nm.

5.3.2.a Beam deflector

We start by designing a beam deflector at $\lambda = 1000$nm. The super-cell, on which the 2π-phase gradient is implemented, is composed of 8 elements each separated by 806 nm, allowing to obtain a deflection angle of 8.9° according to the generalized Snell's law. This choice of 8 elements is justified by the need to obtain both a phase gradient sampling with enough elements for a correct reconstruction of the wavefront and a small enough super-cell to guarantee deflection at a large enough angle. The diffraction efficiency, defined as the power emitted in the desired diffraction order divided by the incident power, is directly limited by the number of elements chosen to sample the phase. While a continuous phase profile would permit 100% efficiency in the first order, a sampling of the phase performed with 4 elements leads on the other hand to a maximum

achievable efficiency of only 81%, while 16 values are required to reach a 99% [35, 36]. 8 elements represent therefore a good compromise allowing theoretically a maximum of 95% of energy to be directed at an angle of 8.9°. In Fig. 5.9-A, we show the selected size of clusters allowing the sampling of the phase in 8 equal intervals of amplitude $\pi/4$. The sampling is performed on a range of sizes presenting a transmission above 90%.

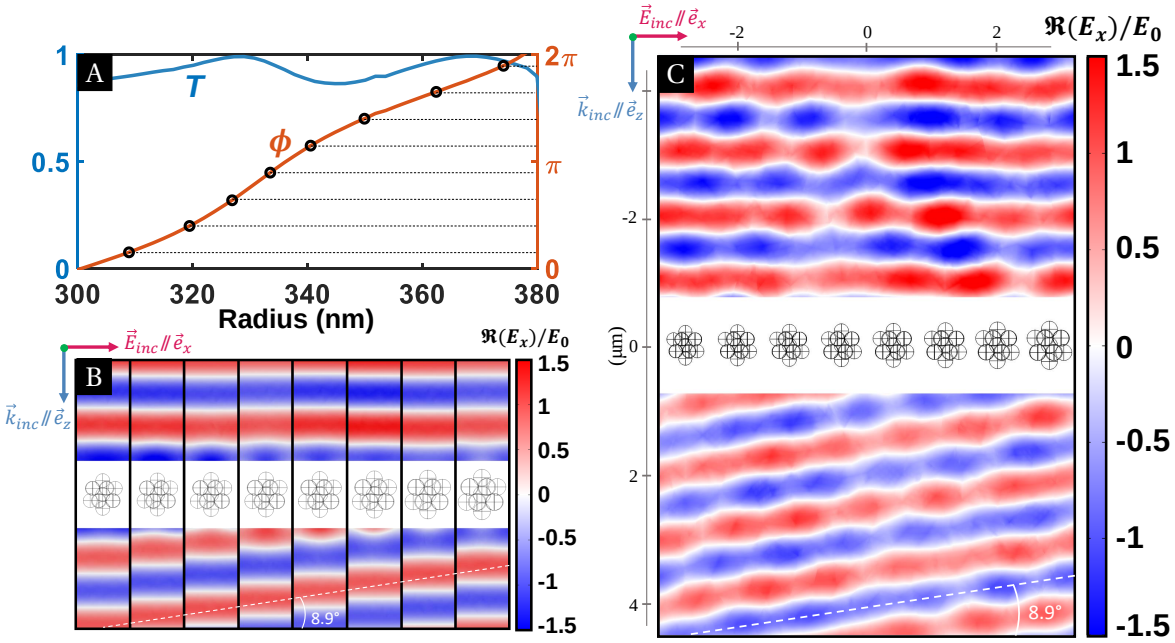

Figure 5.9 – A) Phase sampling over 8 constant width intervals. B) Visualization of the beam deflection at $\lambda = 1000$nm by comparing the individual response of the 8 selected unit-cells (indicated by the black circles on panel A). The maps present the real part of the electric field normalized by $E_0 = 1V/m$. Each independent unit-cell is illuminated from the top under normal incidence by an $\vec{e}_x$ polarized plane wave propagating along $\vec{e}_z$. C) Map of the real part of the normalized electric field for a super-cell comprising the 8 clusters illuminated from the top under normal incidence.

The desired wavefront profile is illustrated on Fig. 5.9-B. The figure is obtained by simply juxtaposing the mapping of the real part of the electric field of the selected periodic surfaces. It illustrates how the accumulated phase difference of $\pi/4$ from one unit-cell to the next one allows for the deflection at the theoretical angle of 8.9° by the ensemble. The entire super-cell comprising the 8 resonators was finally investigated trough full wave simulation and the results are presented on Fig. 5.9-C. The beam deflector is illuminated from the top under normal incidence by an $\vec{e}_x$ polarized plane wave propagating along $\vec{e}_z$. Periodic boundary conditions were applied along the $\vec{e}_x$ and $\vec{e}_y$ directions of the domain, thus replicating the super-cell in an infinite periodic array. As predicted, a diffraction angle of about 9° can be observed on the figure. The device presents a total transmission of 75% with 87% of the transmitted energy being emitted in the desired first diffraction order. The transmission of the structure is therefore lower than the minimum value of 90% of transmission suggested by the choice of elements from Fig. 5.9-A. Such a difference originates from the couplings between the neighbouring particles that make the selected elements behave differently in the gradient array compared with the homogeneous arrays studied in Fig. 5.9-A. The creation of a gradient metasurfaces with maximal performances in transmission would therefore require additional optimization steps of the entire super-cell as performed in [37, 38].

5.3.2.b Lens

The second Huygens metasurface device consists in a 1D focusing lens made from 13 clusters. The 2π variation of phase is realized symmetrically over 7 unit-cells providing a theoretical focal distance of $f = 11.2\mu$m and a numerical aperture $N.A. = 0.42$. The total size of the lens is 10.48μm.

The phase profile sampling, following equation (5.16), is indicated on Fig. 5.10-A by the black circles. The targeted phase profile is additionally evidenced on Fig. 5.10-B presenting the real part of the electric field obtained from the different unit-cells taken separately.

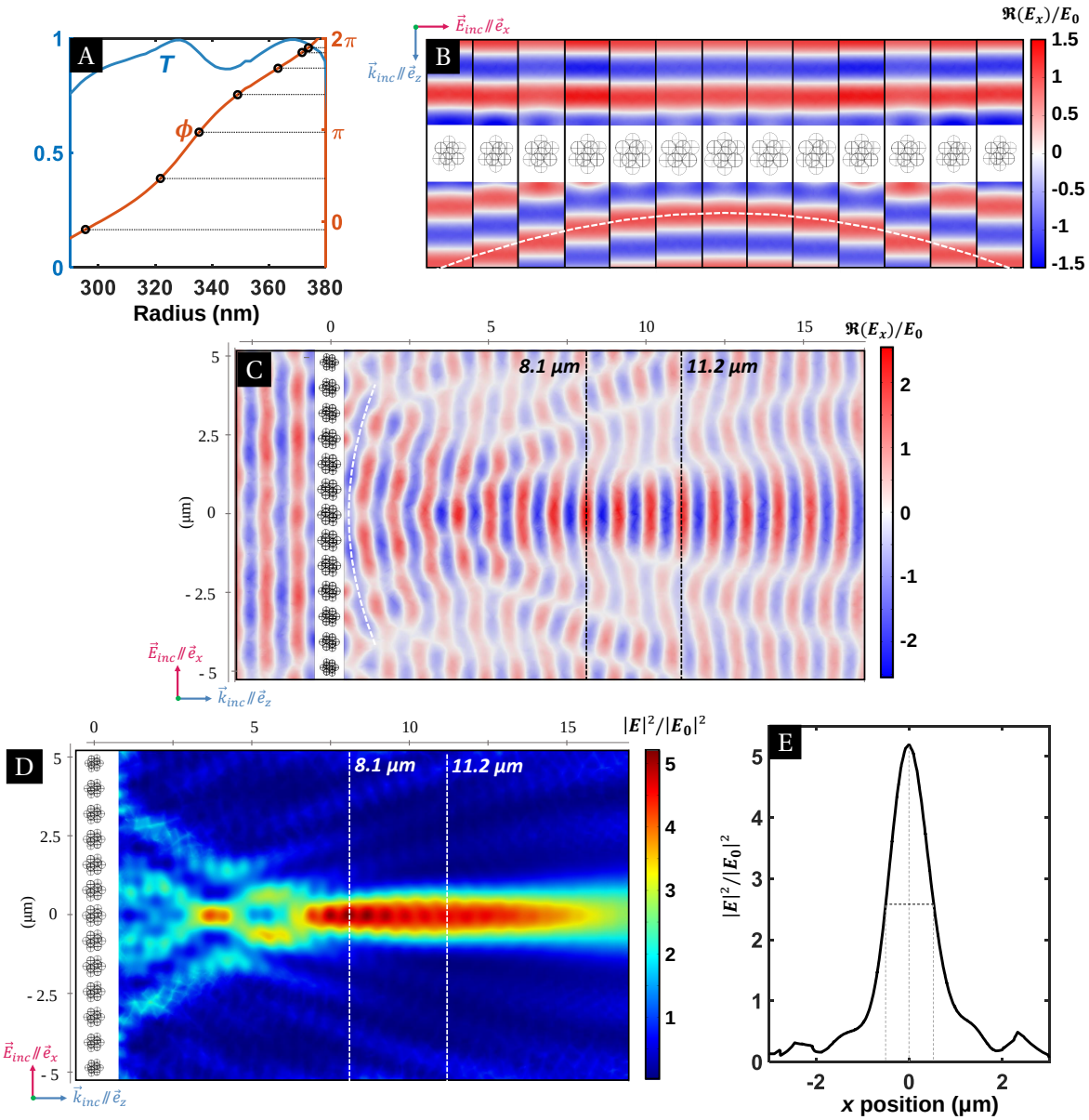

Figure 5.10 – A) Discretization of the phase according to a 1D hyperboloidal profile. B) Visualization of the phase profile at $\lambda = 1000$nm by juxtaposing symmetrically the 7 selected unit-cells (indicated by the black circles on panel A). The maps present the real part of the electric field normalized by $E_0 = 1V/m$. Each meta-lattice is illuminated from the top under normal incidence by an $\vec{e}_x$ polarized plane wave propagating along $\vec{e}_z$. The white dotted line represent the theoretical phase profile satisfying eq. (5.16) with $f = 11.2\mu$m and is also reproduced in black on panel C. C) and D) are respectively the map of the real part and squared modulus of the normalized electric field for a lens comprising the 13 clusters that is illuminated under normal incidence by a plane wave. The position of the focal plane and the targeted focal distance are indicated by the two vertical dashed lines. E) Electric field intensity distribution along the $\vec{e}_x$ axis in the focal plane at $z = 8.1\mu$m.

On Figs. 5.10-C,D, the entire metalens integrating the thirteen clusters in the same cell is investigated. The lens is illuminated by a $\vec{e}_x$ polarized plane wave propagating along the $\vec{e}_z$ direction. The Figs. 5.10-C and D show respectively the real part and the squared modulus of the electric field. For this simulation, perfectly matched layers were used at the edges situated along the $\vec{e}_x$

direction in order to truncate the simulation domain, while periodic boundary conditions were used along $\vec{e}_y$. Figure 5.10-C reveals the converging wavefront obtained with the lens. The wavefront profile of the wave emerging from the meta-lens is in excellent agreement with the desired theoretical profile plotted in black on the figure. This indicates that the coupling between the different elements of the lens only weakly perturbs the cluster responses obtained in the case of the homogeneous arrays. The focusing of the incident beam is further revealed by the spatial mapping of the electric field intensity shown on Fig. 5.10-D. A narrow concentration of the energy is achieved along the $\vec{e}_x$ direction while the focal spot extends more widely along the $\vec{e}_z$ direction. This shape for the focal spot is inherent to the implemented phase profile and therefore, similar focusing patterns are observed in the literature for a wide variety of meta-lens [30, 39–44]. Although our numerical simulation has a limited resolution, due to the large size of the numerical domain, the focal length can be estimated from Fig. 5.10-D at a value close to 8.1μm. This is well below the targeted value of 11.2μm. This shift in the focal distance is a well known phenomenon in traditional optics and can be explained by the diffraction effect of the incident wave occurring at the edge of the lens of finite size that induce a significant perturbation in the device response [45–47]. In particular, the influence of lens size on the focusing position shift has been the object of a detailed study in [47]. It turns out that the 12% decrease in focal length observed in our case, is in excellent agreement with the theoretical prediction made in this work. On the other hand, the intensity distribution in the estimated focal plane is presented on Fig. 5.10-E. The full width at half maximum of the intensity peak at the distance of 8.1μm is 1μm, thus a concentration of energy over a distance of size similar to the wavelength, close to the diffraction-limited spot size. In addition, the transmission efficiency of the lens is approximately 80%. A precise value, cannot be given, mostly due to the presence of the PMLs that absorb on the edges of the simulation domain.

Despite the phase sampling, and the limited size of the lens which is accompanied by the important perturbations due to diffraction effect at the edge of the device, we have clearly demonstrated in this part the lensing effect enabled by a properly designed cluster based metasurface. Of course this design is not intended to compete with state-of-the-art lenses, and presents poor characteristics in comparison. It is rather proposed here as an illustration of the beam shaping capabilities of the clusters. For this reason, we do not push further the characterization or optimization of performances of the devices which remains at this point a perspective of this work.

5.3.2.c Comments and perspectives

The system we studied presents some limitations. First of all, we note the large sizes of the structures used in comparison to the operating wavelength of the devices. While most of the recent works are based on high refractive index nanocylinders and nanodisks for which the Kerker regime can be obtained by tuning the aspect ratio, the use of spherical objects as in this study requires a low effective refractive index for the Kerker conditions to be met. However, the decrease in the refractive index is accompanied by resonances occurring at shorter wavelengths. At the same operating wavelength, spherical meta-atoms with a low index are therefore larger than their non-spherical counterparts with high refractive index. Therefore, they may not be the best choice of elements for implementing large phase variation over very short distances, which is a requirement for obtaining lenses with large numerical aperture (or equivalently small focal spot sizes) and beam-deflectors with high diffraction efficiency.

Moreover, using clusters for an application requiring fine control over the position and size of the objects represents an important challenge. Our designs require the ordered juxtaposition of different clusters whose sizes vary by only a dozen nm. Such a degree of control is beyond what is achievable today with simple self assembly processes. One possibility to obtain such ordered metasurfaces would be to resort to template-directed colloidal self-assembly method. These methods permit to directly inked colloidal solution onto patterned substrates, whose engineered chemistry, wetting properties, or topographical structuring ensure well organized nanoparticles with a high placement accuracy [48–52]. As an illustration, transfer printing has been successfully

applied in [53] to obtain two-dimensional square arrays of gold nanoparticle clusters.

Finally, we can mention that this study was conducted on clusters with a low number of particles in order to lighten the weight of the simulations. We also implemented the variation in the cluster size by increasing the particle size. Experimentally however, it might be more realistic to induce a variation in size of big clusters by adding or removing particles while keeping a constant volume fraction. Although this has not been studied here, one can expect fairly similar results and limitations. To confirm this, it would be necessary to verify the conservation of the Kerker regime for a set of arrays with clusters with variable numbers of particles. This would be a possible extension to the study conducted here.

5.3.3 Limitations of transparent Huygens metasurfaces

An important limitation for the applicability of resonant metasurfaces for beam shaping was recently underlined by P. Lalanne *et al.* in [36]. In this study, the authors showed that the high transmission of Huygens metasurfaces observed under normal incidence was strongly degraded at oblique incidences of only a few degrees. Studying a model system proposed by M. Decker *et al.* [1], consisting in a square array of silicon nanodisks, they indeed revealed that the efficiency of such a Huygens metasurface was considerably reduced by the emergence of several dips, strongly polarization dependent, in the transmission spectra under oblique incidence. The dips, as explained by the authors, are due to the excitation of anti-symmetric localized Bloch modes [54] not excited under normal incidences but inherently present in Huygens metasurfaces.

Also in this part, we study the angular dependence of the transmission spectra of our silicon cluster based metasurfaces. Complementarily to the study conducted in [36, 54], we apply here a multipolar decomposition, highlighting the excitations of vertical components of different multipoles, to explain each of the observed dips.

Our investigation is conducted on the same cluster based square metasurface as studied in section 5.3.1. In particular we focus on the dense metasurface with a surface filling fraction of 0.7, for which the transmission obtained over the whole spectrum is larger than 60% as reproduced on Fig. 5.11-A. Although we have used the spherical coordinates to express multipoles so far, cartesian coordinates are more relevant in this problem as they enable to easily distinguish components excited in and out of the plane of the array. For this reason, we adopt in this part the equivalent description of multipoles in terms of scalar and tensor polarisabilities rather than spherical coefficients. We recall that the metasurface is illuminated by a plane wave propagating along the $\vec{e}_z$ axis (under normal incidence) and polarized in this case along $\vec{e}_x$. Under normal incidence, the excited multipoles are presented on Figs. 5.11-B,C showing the components of the dipole polarisabilities and of the quadrupolar polarisability tensor of the clusters. The polarisabilities are obtained by applying the decomposition presented in section 2.2.6.e.

Logically, the multipolar decomposition reveals electric and magnetic dipoles excited along to the $\vec{e}_x$ and $\vec{e}_y$ directions of the array respectively. In addition, at shorter wavelengths, the excitation of the xz and yz components of the electric and magnetic polarisabilities quadrupolar tensor are evidenced respectively.

Figures 5.11-D and G show the evolution of the transmittance spectra obtained for incident angles of 3° and 5° in the case of TM and TE polarizations respectively. As observed in [36], the figures reveal the apparition of four sharp dips in transmission for an angle of incidence as small as 3°. For an angle of 5°, the peaks drop to even lower values, close to a zero transmission in each case. In addition, the spectral position and amplitude of the peaks differ according to the polarization of the incident wave. The multipolar content obtained in these two configurations for a 3° angle is presented in Figs. 5.11-E,H,F,I. For the TM polarization, we can see that the component of the electric field outside of the plane of the metasurface excites an electric dipole oriented along the $\vec{e}_z$ axis at the wavelength of 1332nm. The excitation of this multipole leads to a very sharp resonance which perfectly coincides with the position of the dip in transmission observed at the longest wavelength. Similarly, the dip obtained at the high wavelength in the TE config-

uration is due to the excitation of a vertical magnetic dipole by the component of $\vec{H}$ out of the metasurface plane. The other three peaks can be associated with the quadrupolar resonances of the resonator. Also, the two peaks observed at wavelengths close to 1100nm involve the xx, yy and zz components of the polarisability tensor. On the other hand, resonance observed near 1200nm can be explained by the sole component yx of the magnetic and electric quadrupole polarisabilty in respectively the TM and TE configurations.

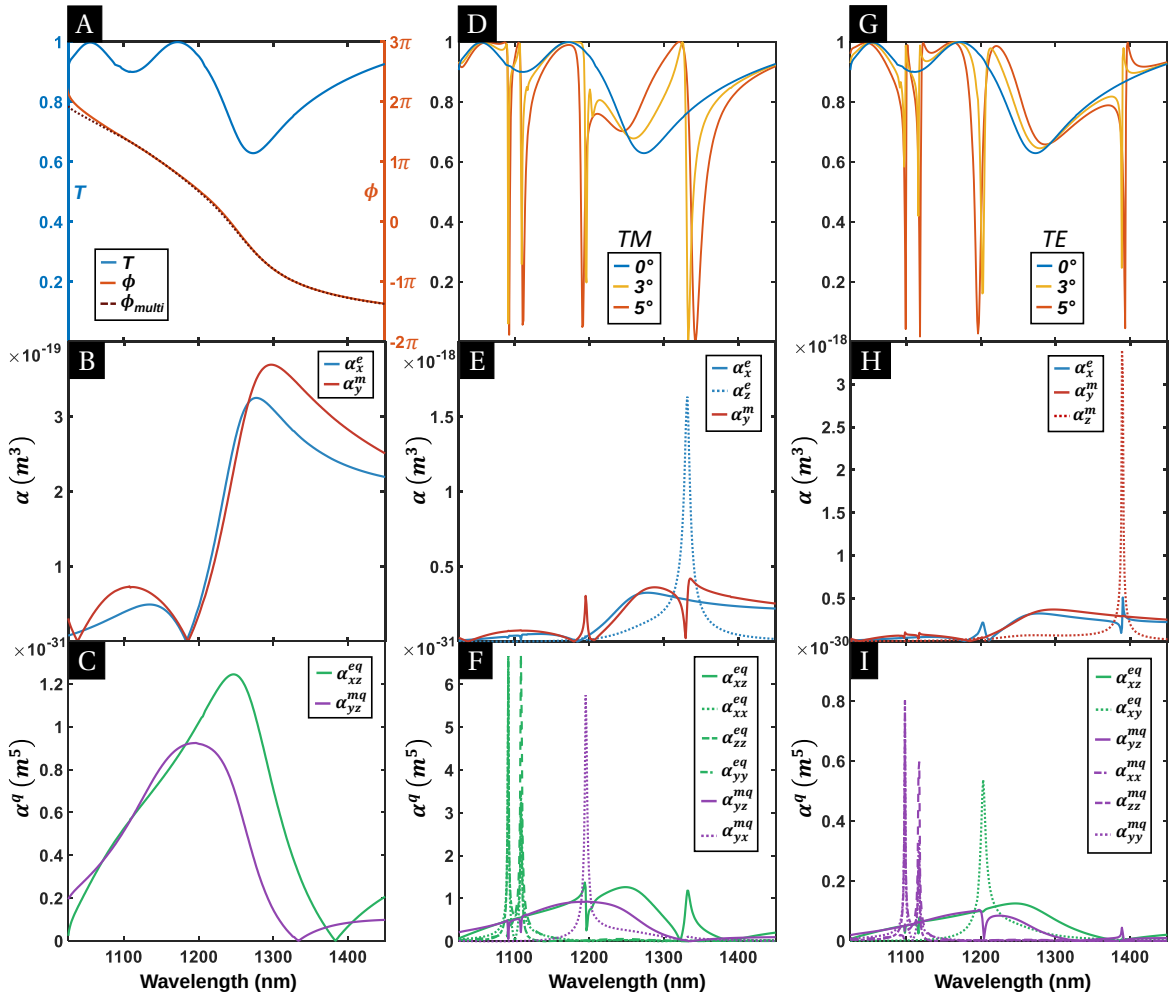

Figure 5.11 – A) Transmission (blue) and phase modulation (orange) dependence with wavelength for a metasurface made of *Si* clusters of radius 390nm with a surface fill fraction of 0.7. B) Excited components in the cartesian basis of the dipolar polarisabilities C) Excited components in the cartesian basis of the quadrupolar tensor polarisabilities. D) and G) present respectively the evolution of the transmission with the angle of incidence for TM and TE illumination. The couples {(E),F)} and {(H),I)} present the same quantities as {(B),C)} for a metasurface illuminated under an angle of incidence of 3° for respectively the TM and TE configurations.

To conclude, the study performed here, reveals the multipolar content of additional resonances attributed to anti-symmetric localized Bloch modes in [36]. The drop in transmission accompanied by the excitation of these additional resonances can significantly lower the efficiency of the devices designed for normal incidence. This would be the case in a situation where the impinging beam is poorly collimated or under a slightly tilted incidence. Also, we believe that regions of high transmission exploited in practice by the Huygens metasurface devices should be truncated as much as possible from the areas of appearance of those peaks at the early stages of the design procedure, in order to guarantee a good efficiency and a better angular robustness to the devices despite experimental difficulties.

5.4 Perfect Absorbers

Under the assumption that the multipoles of a single particle are only weakly perturbed by the array, the multipolar description presented in section 4.3.2.a becomes a powerful tool for designing perfect absorbers. Indeed, in a first step, the perfect absorption condition given by eq. (5.9)

$$\frac{\pi}{k^2}\sum_{n=1}^{\infty}\mathcal{O}_n = \frac{\pi}{k^2}\sum_{n=1}^{\infty}\mathcal{E}_n = \mathcal{S} \tag{5.17}$$

can be tested on single isolated particle multipoles before resorting to periodic calculation much heavier numerically. This preliminary step is performed in our case with the $\mathcal{T}$-matrix method or Mie theory since we focus on objects of spherical geometry. This allows us to identify and design meta-atoms that are good candidates for achieving total absorption in a metasurface. Relevant meta-atoms are those that closely satisfy the Kerker condition and for which the sum of multipoles normalized by π/k^2 are real and are greater than $\mathcal{S}^*$, the unit-cell area corresponding to the limiting case of an array of maximum compacity. Neglecting the lattice effects, these criteria ensure the existence of a metasurface of unit-cell area $\mathcal{S}$ satisfying eq. (5.17). We want to emphasize that since the formalism employed here is generalized to multipoles of any order, it makes it possible to design dipolar or strongly multipolar systems without added difficulty.

Obviously, since the coupling between particles is omitted, this approach is not infallible. Due to the lattice interactions, adjustments of the initial design of the meta-atoms are usually necessary when verifying the properties of the periodic arrays. In some cases even, an optimization of the absorption might be impossible to reach. Even though we may not be able to systematically identify all possible absorber designs, this simplified approach provides a guideline for designing absorbers by restricting the range of parameters to be explored.

Thus, in the rest of this chapter we will present a wide selection of absorbers that we have been designing using the approach described above, and which are all based on particles achievable through bottom-up fabrication routes.

5.4.1 Absorbers based on dielectric and plasmonic spherical particles

5.4.1.a Dielectric particles

Dielectric materials exploiting phonon resonances and for which $\Im(N)$ is high enough to generate non-radiative losses, has recently been pointed out as a promising platform for obtaining perfect absorber with the Huygens-Kerker regime. However, most of the proposed structures so far consist in dipolar nanodisks [11–13, 55–57]. In this part, we reveal, through two examples, that dense arrays of spherical particles behaving in a highly multipolar regime constitute an interesting alternative that would suit colloidal self-assembly fabrication process.

First we consider a homogeneous micro-sphere made of silica (SiO_2) with a radius $R = 4.12\mu$m. The sphere is initially examined individually through Mie theory and R is tuned in the mid-infrared region to exploit the phonon resonance that occurs near 10 μm. As mentioned in the introduction of this part, the particle size is chosen to satisfy the generalized Kerker condition $\sum_{n=1}^{\infty}\mathcal{O}'_n = \sum_{n=1}^{\infty}\mathcal{E}'_n$, where the priming denotes the coefficients of the isolated particle. In addition, the sums $(\pi/k^2)\sum\mathcal{O}'_n$ and $(\pi/k^2)\sum_{n=1}^{\infty}\mathcal{E}'_n$, plotted on Fig. 5.12-A, must be real and larger than $\mathcal{S}^* = (2R)^2$, considered as the threshold value for possibly reaching the zero transmission condition (5.10). Figure 5.12-A evidences that these conditions are met for this design at wavelengths near 10.1 μm indicated by the red shaded area. Moreover, on the basis of the values taken by the real part of the sums of multipoles, it is possible to assess that a metasurface with a surface density slightly below that of the array of maximum compactness should enable the absorption conditions to be achieved.

Therefore, we next simulate an array of these particles with a fill fraction $f_s = 0.7$, as illustrated by Fig. 5.12-E, corresponding to a unit-cell area $\mathcal{S}$ reported on Fig. 5.12-A. The multipole sums of

the particles in the array are plotted on Fig. 5.12-B and compared to $\mathcal{S}$. The perfect absorption conditions (5.17) is closely satisfied by the metasurface. Compared to the isolated case, the coupling induce only a slight change on the amplitude of the scattering coefficients as well as on the wavelength at which the conditions (5.17) are satisfied. In this case our design strategy is efficient. Figure 5.12-C shows the spectra of R, T, and A of the array. The quantities calculated directly from COMSOL Multiphysics through the knowledge of the S-parameters at the ports of the domain, are compared to those retrieved using the multipoles. An excellent agreement is found. As expected, perfect absorption is reached at a wavelength close to 10.2 μm. As revealed by Fig. 5.12-D, the system operates in a heavily multipolar regime (see gray region), where at least 8 multipoles are required to account for the perfect absorption behavior. To our knowledge, it is the first time such a multipolar perfect absorber is evidenced up to now.

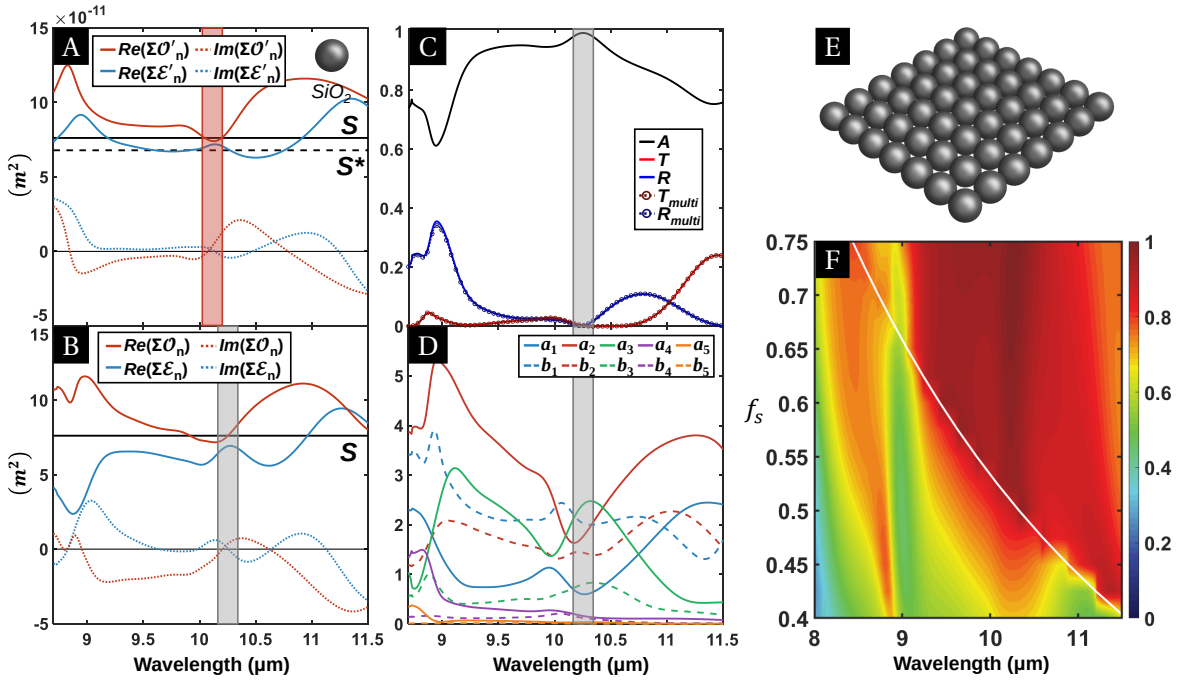

Figure 5.12 – Perfect absorption with SiO_2 particles. A) Wavelength dependence of the sum of even (blue) and odd (red) multipole coefficients, normalized by k^2/π, of an individual SiO_2 microsphere in vacuum that is 4.12μm in radius. The black dotted line represents S^*, the area of the smallest unit-cell achievable for a compact lattice. B) Sum of even and odd multipole coefficients of SiO_2 microspheres in an infinite square array with a surface fill fraction of 0.7. The black continuous line is the area of the lattice unit-cell. C) Spectra of R, T and A calculated for the SiO_2 metasurface and reproduced using the multipole coefficients (circle points). D) Spectra of the modulus of the retrieved multipole coefficients of the particles in the array. E) Geometry of the considered SiO_2 metasurface. F) Evolution of the absorption spectrum with the surface density of the array. The white line corresponds to the diffraction limit.

In addition, we see that the absorption band of this array is quite broad, reaching values of at least 0.9 in the 9.3μm-10.3μm range. This is explained by the presence of many multipoles on this spectral band. In contrast to dipolar absorbers requiring degenerate resonances with a narrow operating band at the resonance wavelength, by combining many multipoles, the appropriate conditions are less stringent and can be achieved over a wider spectral band as observed in Figs. 5.12-A and B.

Figure 5.12-F shows the dependence of the absorption with the grating pitch. It can be seen that the filling surface fraction has a minor influence on the absorption which is maintained at very high values above the diffraction limit. In the same way, Fig. 5.13 shows the angular dependence of the design. For both TE and TM polarisations the absorption is maintained up to the diffraction limit (indicated by the withe line on the figures) and remains at high values beyond.

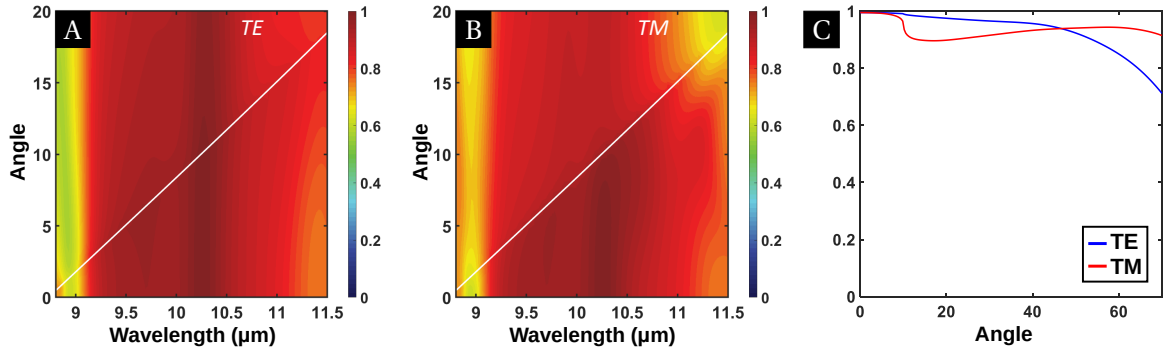

Figure 5.13 – Dependency of the SiO_2 metasurface absorption with the angle of incidence under A) TE and B) TM illumination. White lines correspond to the diffraction limit. The filling fraction of the array is 0.7. C) Angle dependence of the absorption at $\lambda = 10.25\mu$m.

Let consider a second system consisting of a aluminium oxide (Al_2O_3) particle with a radius of 9.3μm. As before, the study of the multipoles of the isolated scatterer, carried out using Mie theory and presented on Fig. 5.14, reveals that it is a good candidate for absorption applications. Indeed, the sums of the multipole coefficients strongly approximate the required conditions on a band around 20.5μm shown in red in Fig. 5.14-A.

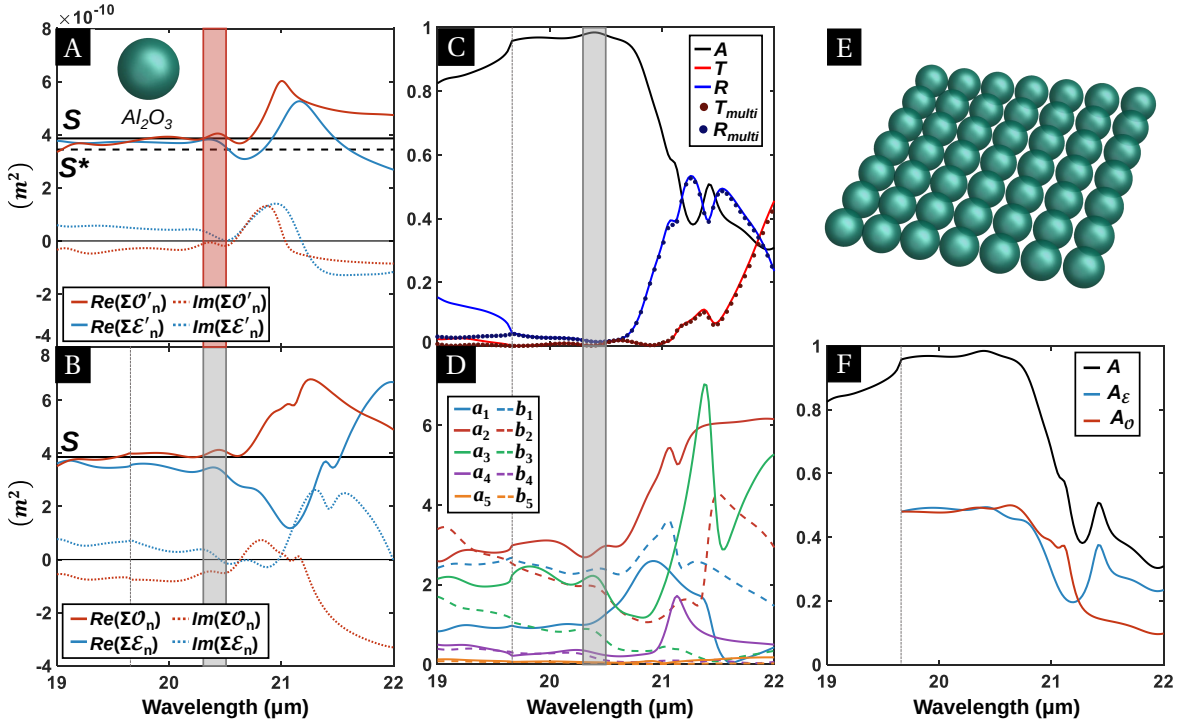

Figure 5.14 – Perfect absorption with Al_2O_3 particles. A) Wavelength dependence of the sum of even (blue) and odd (red) multipole coefficients of an individual Al_2O_3 microsphere in vacuum that is 9.3μm in radius. The black dotted line is S^*, the area of the smallest unit-cell achievable for a compact lattice. B) Sum of even and odd multipole coefficients of Al_2O_3 microspheres in an infinite square array with a surface fill fraction of 0.7. The black continuous line corresponds to the area of the lattice unit-cell. C) Corresponding spectra of R, T and A, and reproduced using the multipole coefficients (circle points). D) Spectra of the modulus of the retrieved multipole coefficients of the particles in the array. E) Geometry of the considered Al_2O_3 metasurface. F) Contributions of even (blue) and odd (red) modes to the absorption. On panels B,C,D and F, the diffraction limit is indicated by the gray dotted vertical line.

The particles are then organized to form a lattice of surface filling fraction $f_s = 0.7$ as illustrated on Fig. 5.14-E. The multipolar decomposition of the array is presented on Fig. 5.14-B. This time, for

wavelengths between 21μm and 22μm, the multipoles are strongly affected by lattice interactions, especially the even multipoles, whose sums undergo a significant red-shift. However, in the band around 20.5μm identified before, the perfect absorption conditions are still fairly satisfied by the array. On Fig. 5.14-C, it can be seen that 98.4% of absorption is therefore reached by the array at $\lambda = 20.41$ μm with only 1.3% of reflection resulting from the small mismatch in amplitude, visible on 5.14-B, between the even and odd multipoles in this region of the spectra.

As in the previous example, the near total absorption at this wavelength results from the excitation of numerous electric and magnetic multipoles up to the 4^{th} order, as highlighted in Fig. 5.14-D. A broadband absorption greater than 90% is also observed between 20.5μm and the diffraction limit represented by the gray dotted vertical line. Additionally, Fig. 5.14-F evidences that even and odd multipoles contribute to approximately half the absorption each in this large band of wavelength, which is characteristic of symmetric perfect absorbers as mentioned in section 5.2.1.b.

We have shown with this part the possibility of using dense arrays of dielectric particles in a multipolar regime to obtain a unitary absorption. Although the phonon resonances of SiO_2 and Al_2O_3 in the far infrared have been exploited for this purpose, the results remain transposable to other wavelengths. The design is totally scalable, for example to the near infrared and visible, provided that dielectrics with similar index values can be used. For the considered examples, the refractive index of SiO_2 is $2.35 + 0.26i$ at $\lambda = 10.25\mu$m while that of Al_2O_3 at $\lambda = 20.41\mu$m is $1.94 + 0.57i$.

5.4.1.b Plasmonic particles

Small plasmonic nanoparticles are known to behave as perfect electric dipoles. However, an increase in the particle size lead to the excitation of higher order plasmonic resonances. In particular, the first excited higher order mode corresponds to an electric quadrupole whose radiation pattern has an opposite symmetry to that of the electric dipole. In this part we show that dipolar and quadrupolar electric resonances of plasmonic particles occurring in the same range of wavelength can be tuned in arrays to reach the Kerker regime and enable perfect absorpting metasurfaces.

We consider in the following a silver nanoparticle of radius 78nm. The silver data are taken from Palik's handbook [58]. As evidenced by Fig. 5.15-A, such a particle presents a broad electric dipole resonance extending in the visible domain, as well as a narrower electric quadrupole resonance excited at 365nm. Although the degeneracy conditions are not perfectly fulfilled for this isolated scatterer, the simultaneous excitation of these two resonances of opposite symmetry with similar amplitudes and at overlapping wavelengths suggest it may nonetheless be exploited to reach the total absorption regime in a metasurface.

Also, we simulated metasurfaces consisting of square arrays of these particles. Figure 5.15-F shows the evolution of the absorption of this plasmonic array as a function of its surface fraction. A rather high absorption is obtained in the excitation region of the quadrupolar resonance, taking values around 80% towards 365nm for surface fractions between 0.2 and 0.6. At higher densities, a strong red-shift of the absorption peak is observed. The plasmonic metasurface response is more strongly impacted in high-density regimes than with previously studied dielectric analogues. This is explained by the large field enhancement obtained between neighbouring plasmonic particles resulting in strong near-field interaction. Moreover, for surface fractions above 0.7, a quasi unitary absorption is reached. In Figs. 5.15-B,C,D, we study in more detail the array illustrated in Fig. 5.15-E obtained for a surface fraction of 0.75 close to maximum compactness. The multipolar decomposition applied to this array reveals a quadrupolar resonance around 435nm which has therefore undergone a significant red-shift compared with the isolated case. The red-shift of plasmonic resonances is a well-known result for particle dimers. By decreasing the gap between two neighbouring particles, their resonances start to hybridize, and the position of their resonances peak red-shift. The red-shift gets more important as the gap is narrowed. This same phenomenon is found here for high density arrays for which inter-particle distances are smaller.

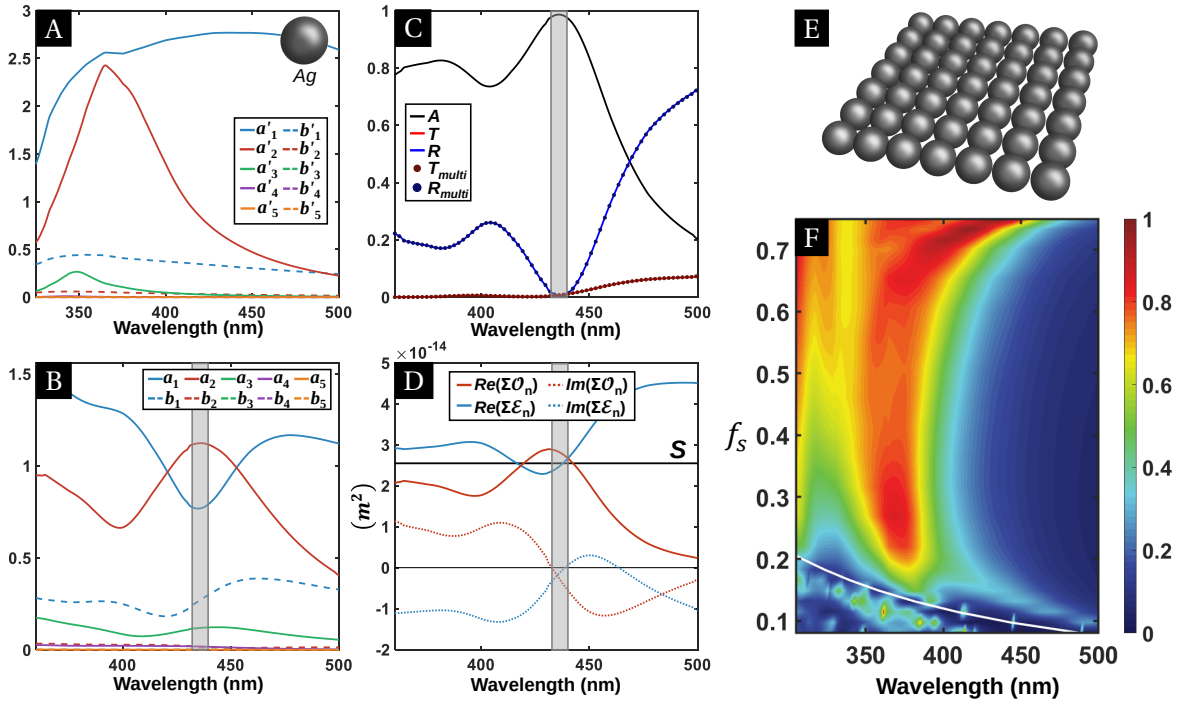

Figure 5.15 – Perfect absorption with *Ag* particles. A) Wavelength dependence of the modulus of the multipole coefficients of an individual *Ag* particle in vacuum that is 78nm in radius. B) Spectra of the modulus of the multipole coefficients for a square infinite array of silver particles with a surface fill fraction of 0.75. C) Spectra of R, T and A calculated for the metasurface and reproduced using the multipole coefficients (circle points). D) Sum of even (blue) and odd (red) multipole coefficients of the *Ag* particles in the metasurface. The black continuous line is the area of the lattice unit-cell. E) Geometry of the considered dense *Ag* metasurface. F) Evolution of the absorption spectrum with the surface density of the array.

Figures 5.15-D and B show that due to the spectral tuning of the electric quadrupolar resonance, the conditions of perfect absorption are met in the grey region around 435nm. There, the balance between even and odd modes produces the cancellation of both the transmitted and reflected waves through destructive interferences, resulting in the perfect absorption observed on panel 5.15-C. A maximum of 98.6% of absorption is achieved at 435nm.

Although small plasmonic particles have been used for a long time for absorber applications, traditional designs require however the use of a reflecting substrate [59–61]. Indeed, we recall the absorption by a mono-layer of small dipolar particles faces the fundamental limitation that 50% of the incident energy can be absorbed at maximum. Here we revealed instead that by exploiting the two first plasmonic resonances of the particles, the absorption can be realized within a single layer metasurface without the need of a backing metallic layer. A similar idea was previously advanced in [10]. The authors proposed to use dense arrays of large silver spheres of radius 148nm. A unitary absorption was obtained in their case on a large band of wavelengths between 250nm and 285nm. However the contribution of the electric quadrupole and higher order modes was disregarded in that work and the origin of the absorption was therefore not evidenced. Since their broadband absorption was obtained at shorter wavelengths than the operating wavelength of our design, it is likely it originated from the balance of numerous multipoles of higher order. We can notice in addition that their proposed design is thicker than the wavelength and presents an absorption in the diffractive region of the array, while we achieve in our case an absorption in the visible and using a subwalength layer.

Alternatively, in the same paper, the authors also proposed to use dense monolayers of silver particles encapsulated in an homogeneous dielectric layer to reach absorption in the visible. In this case, they revealed an artificial magnetic response originating from circulating electric currents taking place in the dielectric media, at the close vicinity of the particles. In addition, most

of the energy was dissipated in their n-doped silicon dielectric slab. Altough it is an interesting alternative, the physics of this design is rather different to the one we propose here where all the absorption is realized within the particles.

Therefore, the idea of exploiting the electric dipole and quadrupole plasmonic resonances of spherical particles is presented here as an original idea. We have to acknowledge that these 2 multipoles giving radiation of opposite parity were already exploited to reach total absorption in a more complex structure [62]. The authors employed in this case metallic nanodisks filled with dielectric placed on a dielectric substrate. However the substrate was shown to play an important role in this case, breaking the symmetry of the proposed device, and as a result total absorption was reached for illumination from one side of the array only.

5.4.2 Total absorption with core-shells

5.4.2.a Dipolar core-shells

Infinite grating of perfectly conducting rods coated by lossy dielectrics were among the first proposed designs of symmetric single-layer perfect absorber [9]. The authors showed that the electric and magnetic dipole moments of the structure could be balanced by adjusting the cladding layer to form Huygens pairs while the right amount of dissipative loss can additionally ensure full absorption by the array. The 3D equivalent of this structure, *i.e.* spherical core-shell particles, was presented a year later as an alternative structure to realize symmetric absorbers in the infrared [10]. More recently, optimization of the absorption with both coated nanowire or spherical core-shell was investigated [63, 64] showing the possibility to achieve high absorption at different wavelengths in the visible using a large combination of plasmonic and dielectric media. However, it should be mentioned that these last studies were performed on isolated particles, not on metasurfaces.

In this part we revisit the spherical metallo-dielectric core-shell based metasurface absorber to evidence that our design strategy can be efficiently applied to this dipolar system. The absorption peak of the array can be easily tuned at different wavelengths in the near infrared domain by adjusting a few design parameters.

As an example, we consider a model core-shell made of a silver core of radius 50nm covered by a 145nm thick dielectric layer of refractive index 2.5+0.08i. The design geometry is tuned to ensure electric and magnetic resonances at the same wavelength while the index of the dielectric layer is chosen to guarantee both electric and magnetic responses of similar amplitudes as well as sufficient losses for the absorption to occur. As it can be seen on Fig. 5.16-A, the normalized sums of multipoles, obtained with the extended Mie theory for multi-layered spherical particles, meet the perfect absorption requirement in the spectral region evidenced by the red shaded area around 990nm. The imaginary part of both sums of coefficients rigorously cancel at close wavelengths while the real parts take similar values indicating that the Kerker condition is closely met. Moreover, since the real parts take large values compared to $\mathcal{S}^*$, an optimization of the absorption can be expected for arrays of low surface fraction (in contrast to the very dense metasurfaces studied previously).

We then turn to a metasurface composed of these core-shells. The evolution of the absorption with the surface fraction is presented in Fig. 5.16-G. As expected, a strong absorption is observed at the wavelengths of the dipole resonances for relatively low surface fractions, of the order of $f_s = 0.2$. At low density, the absorption peak also undergoes an important red-shift due to the coupling of the particle resonances to the lattice resonances at the onset of the diffraction limit. In particular, perfect absorption is observed for a surface fill fraction of 0.187, corresponding to a lattice periodicity of 800nm, as shown in Fig. 5.16-C. For this metasurface, the absorption conditions are presented in Fig. 5.16-B. It is interesting to note that the conditions are met at wavelengths of 1001nm very close to that determined when studying the isolated meta-atom. The overlap of the even and odd modes is nearly perfect in this range and Fig. 5.16-D shows an almost exclusive contribution from the dipoles. The excellent spectral overlap of the two resonances results in

the extremely low reflection, below 2%, observed over the entire spectrum covered by them. The response of the array is therefore close to that of the ideal dipolar Huygens absorber investigated with the Lorentzian model in section 5.2.1.b, with a suppression of the transmission observed at the resonance of the dipole. Additionally on Figs. 5.16-A,B, it can be noticed that the multipole coefficients are enhanced by the lattice coupling in the dilute regime. The balance between the unit-cell area and the real part of the sums is optimized for a surface area $\mathcal{S}$ finally higher than that expected at first when studying the isolated particle. Therefore, although obtaining the Kerker condition can be approached in a robust way by engineering the isolated core-shell, the optimum lattice pitch is still needed to be found step by step by fully taking into account the coupling between the particles in arrays in this case.

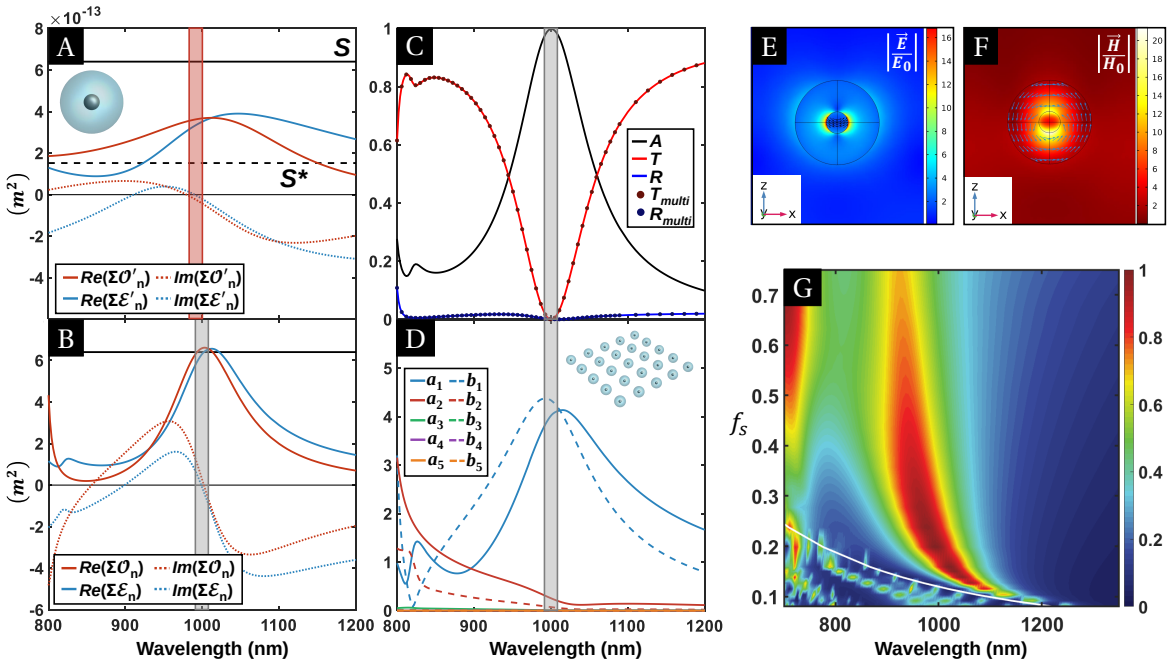

Figure 5.16 – Perfect absorption with metallo-dielectric core-shells. A) Wavelength dependence of the sum of even (blue) and odd (red) multipole coefficients of an individual core-shell in vacuum. The particle consists in a silver core of 50nm radius surrounded by a dielectric shell of constant refractive index of $2.5+0.08i$. The outer radius is 195nm. B) Sum of even and odd multipole coefficients of the core-shell particles assembled in an infinite square array with a surface fill fraction of 0.187. The black continuous line corresponds to the area of the lattice unit-cell. C) corresponding spectra of R, T and A also reproduced using the multipole coefficients (circle points). D) Spectra of the modulus of the retrieved multipole coefficients of the particles in the array. Maps of the normalized electric E) and magnetic F) field at the maximum of absorption for $\lambda = 1001$nm. The arrows indicate the direction of the electric field in the dielectric and metallic layers. G) Evolution of the absorption spectrum with the surface density of the array.

It is interesting to note that at the absorption maximum of Fig. 5.16-C, 91% of the energy is dissipated within the dielectric layer while 9% only within the plasmonic core. The mapping of the normalized electric and magnetic field in the unit-cell, obtained at the wavelength of 1001nm, are presented in Figs. 5.16-E and F. Figure 5.16-E clearly evidence the electric dipole behaviour of the localized plasmon resonance taking place at the interface between the metallic core and the dielectric layer while the magnetic field on Fig. 5.16-F is mainly localised inside the dielectric layer characteristic of a magnetic dipole resonance of dielectric particles. The strong field enhancement mostly observed in the dielectric coating is consistent with the high dissipation of energy occurring in the shell.

In Fig. 5.17, we further investigate the angular dependence of the absorption peak of the metasurface whose lattice periodicity is 800nm. As can be seen, for both polarization, the absorption peak is conserved for angle up to 15° corresponding to the diffraction limit. At higher values in

the diffractive regime (white lines on the color-maps) the absorption is significantly reduced for certain angles, different for the TE and TM polarization, due to the crossing of additional angle dependant modes. No further investigations have been carried out to analyse this behaviour.

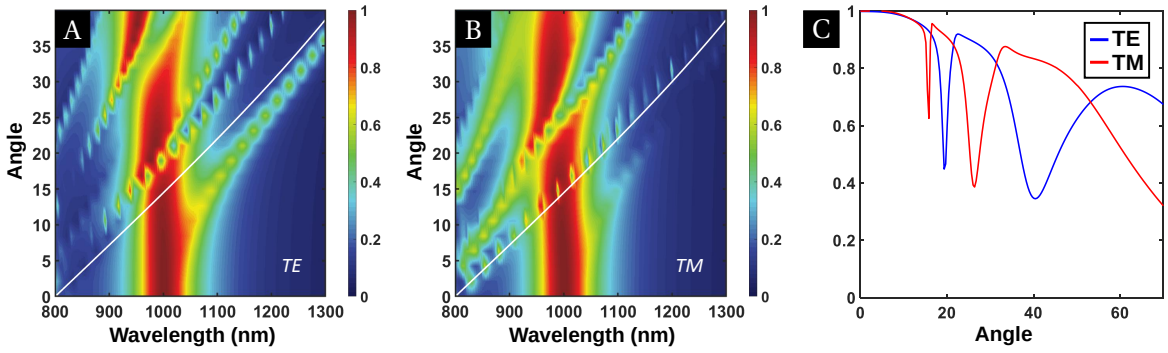

Figure 5.17 – Angular dependency of the absorption of the metasurface made from the metallo-dielectric core-shell particles of radius 195nm under A) TE and B) TM illumination. White lines correspond to the diffraction regime limit. The filling fraction of the array is 0.187. C) Angle dependence of the absorption at $\lambda = 1001$nm.

5.4.2.b Tunable absorption peaks in the infrared domain

The perfect absorption obtained in the previous section at 1000nm can be tuned by realizing slight changes in the design. Figure 5.18 indeed reveals that near perfect absorption can be achieved at any wavelength in most of the near infrared domain, from 800nm to 1700nm.

To illustrate the main trend in required size and material index, seven examples are presented on Fig. 5.18-A and their corresponding parameters are reported in the table of Fig. 5.18-B. The metasurface studied in the previous part corresponds to design 3). By decreasing the over all size of the core-shell particles while keeping the index of the shell unchanged, a blue shift is observed in the resonances, resulting in an absorption peak at the edge of the visible domain for design 1). Nevertheless, absorption at lower wavelengths in the visible are hard to get due to the fact that by further decreasing the core size, the electric dipole resonance associated with the localized surface plasmon becomes much less pronounced and the core-shell response begins to closely resemble that of a simple dielectric particle without the silver core. On the other hand coming back to design 3) as a starting point, increasing the index of the shell from 2.5 to 3 and 3.5, resonances at higher wavelengths are achieved for design 4) and 6) leading to absorption peaks at respectively 1144nm and 1304nm. The size of the plasmonic core in this case is kept while that of the shell undergoes a small adjustment only to ensure that the Kerker condition is fulfilled. Finally, reaching higher wavelengths requires both a bigger meta-atom and a higher index dielectric shell. To illustrate this, an absorption of 94% is reached at 1715nm for design 7) consisting in a $R = 215$nm big core-shell particle in radius with a metal core of $r = 65$nm and a shell of index 4+0.05i. Optimizing the absorption at higher wavelengths might be possible by further increasing the size and refractive index of the structure but has not been studied in any more detail here.

On the other hand, we studied for two examples the impact of the core plasmonic material. Taking as a starting point the arrays 1) and 4) and replacing the *Ag* core with *Au* ones of the same size, arrays 2) and 5) can respectively be obtained. Interestingly, it appears that the designs are not strongly impacted by the core material. Indeed a slight increase of only a few nm in the size of the dielectric layer allows in either case to reach a near perfect absorption for surface density values very close to that of the original *Ag* designs. Therefore, both *Ag* and *Au* core-shell particles might be promising building blocks for perfect absorber applications in the near infrared domain.

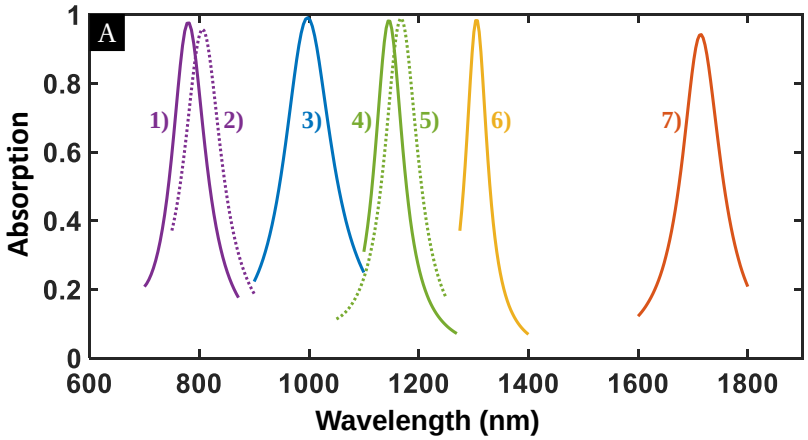

B

Design	r (nm)	R (nm)	N_{core}	N_{shell}	f_s	λ_{abs} (nm)
1)	32	150	Ag	2.5+0.08i	0.167	781
2)	32	155	Au	2.5+0.08i	0.179	806
3)	50	195	Ag	2.5+0.08i	0.187	998
4)	50	182	Ag	3+0.05i	0.106	1144
5)	50	186	Au	3+0.05i	0.111	1169
6)	50	177	Ag	3.5+0.05i	0.068	1304
7)	65	215	Ag	4+0.05i	0.101	1715

Figure 5.18 – A) Near-perfect absorption obtained at various frequencies within a wide frequency band in the near infrared by changing the core-shell geometry and composition. The corresponding parameters for each design are presented in B).

5.4.2.c Broadband absorption with multipolar core-shells

While in the previous section dipolar core-shells were studied to realize resonant absorption, core-shell designs were also proposed by Ra'di *et al.* [10] to obtain a high broadband absorption in the visible. However, since the origin of the large absorption band was not clearly revealed in their work, as we will show later, we find pertinent in this part to apply our multipole decomposition method to their system to evidence the multipolar nature of their absorbers and properly differentiate the origin of the broadband absorption from that of the resonant one obtained in the last section.

The design studied in [10] is reproduced in Fig. 5.19-A, Figs. 5.19-A,B,C being directly extracted from their work. It consists in a silver core of $r = 104$nm in radius covered by a thin layer of n-doped silicon of thickness 16nm. The particles are arranged in a square array with a 250nm periodicity. The absorption graph obtained in their case for the layer is reproduced on Fig. 5.19-B and reveals a broad absorption band from 1200THz to 500Thz, corresponding respectively to wavelengths of 250nm and 600nm. The absorption is maintained at a value higher than 80% in this range.

The absorption conditions are reproduced here:

$$\eta_0 \hat{\alpha}_{ee} = \frac{\hat{\alpha}_{mm}}{\eta_0} = \frac{i\mathcal{S}}{\omega} \tag{5.18}$$

corresponding to the dipolar case (see equation (5.13)) with polarisabilities defined as $\hat{\alpha}_{ee} = \alpha_e/\epsilon_0$ and $\hat{\alpha}_{mm} = \alpha_m/\mu_0$. This system was investigated by the author on the graph reproduced on Fig. 5.19-C. This plot shows the electric and magnetic dipolar polarisabilities, for which the real parts oscillate around zero and the imaginary parts around the appropriate value of $1/\omega$. This condition was used by the authors as evidence that the broadband absorption was originating from the large spectral balancing of two properly tuned electric and magnetic dipoles. However due to the large

size of the meta-atoms considered and from the aspect of the absorption band in Fig. 5.19-B, we know that the sole consideration of the dipole moments is insufficient to explain the absorption exhibited here, and that multipolar resonances of higher order must necessarily be involved.

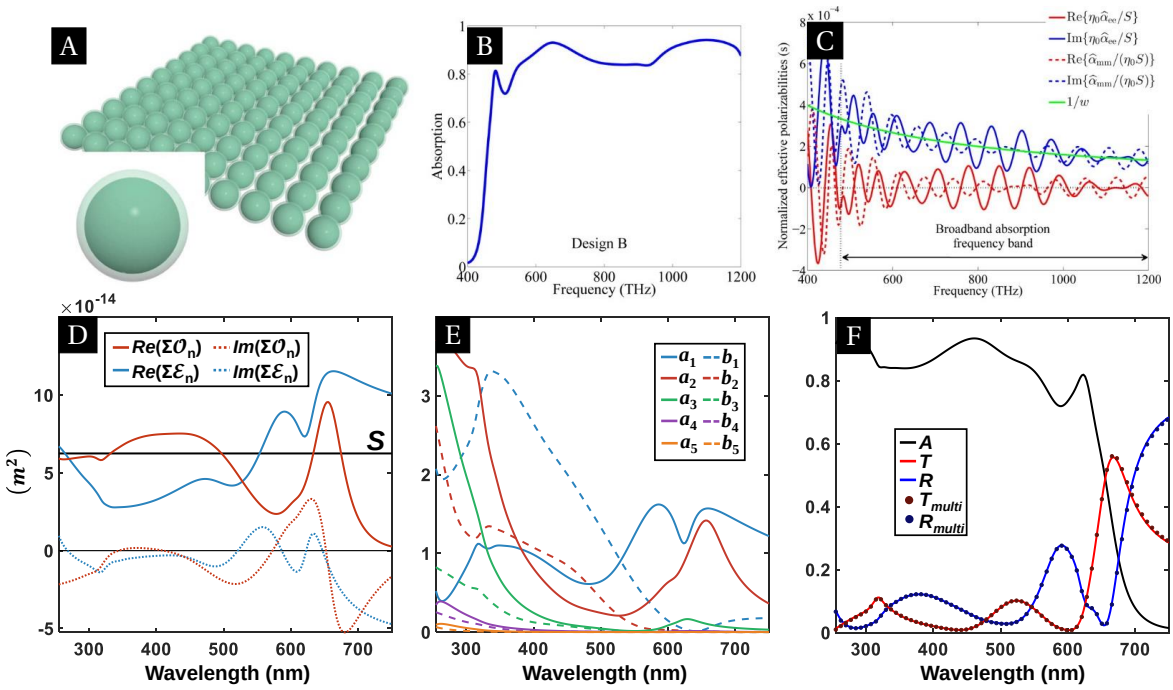

Figure 5.19 – A) Geometry of the design proposed in [10]. The resonator consists in a silver core of 104nm in radius surrounded by a 16nm thick layer of n-doped silicon. B) Absorption as a function of the frequency. C) Normalized effective electric and magnetic polarisabilities retrieved from the reflection and transmission coefficient assuming a dipole approximation. D) Wavelength dependence of the sum of even (blue) and odd (red) multipole coefficients of the core-shells in a metasurface with a lattice periodicity of 250nm. E) Spectra of the modulus of the retrieved multipole coefficients of the particles in the array. F) Spectra of R, T and A calculated from the S-parameters and reproduced using the multipole coefficients (circle points). Panels A,B and C are directly taken from [10].

To evidence this statement and reveal the origin of the broadband absorption, we applied our multipolar decomposition technic to the core-shell mono-layer. Figure 5.19-E indeed reveals that the broadband absorption, well reproduced on Fig. 5.19-F, involves a combined excitation of the dipole, quadrupole and octupole resonances of the particles. The fulfillment of the generalized absorption condition is investigated on Fig. 5.19-D presenting the normalized sums of the symmetric and anti-symmetric multipoles. Because the absorption does not rise above 90% it is not possible to identify a region of the spectrum where perfect absorption conditions are rigorously met. Therefore, the absorption condition is only loosely satisfied as the cancellation of R and T arise at separated wavelengths in the spectra. One can, for example, identify that the Kerker condition is closely satisfied at wavelengths close to 290nm and 500nm where the sums of odd and even multipoles are nearly the same, near the crossing points of their imaginary or real parts. These regions coincide with the reflection minima observed on Fig. 5.19-F. Similarly, the low transmission observed around 450nm and 600nm comes from a small imaginary part of coefficient sums at these wavelengths with a real part higher than $\mathcal{S}$ for one and lower than $\mathcal{S}$ for the other, leading to a resulting sum of multipoles of about $2\mathcal{S}$ as required for the cancellation of t (see eq. (5.10)). Moreover, in the range between 250nm and 550nm, the imaginary (real) part of the coefficient sums oscillate relatively close to zero (to $\mathcal{S}$). The overall reflection and transmission remain therefore low and broadband absorption occurs.

In fact, the authors failed to properly explain the origin of the absorption in their system as their whole study relied on the dipolar approximation. The polaribalities they presented on Fig.

5.19-C were not calculated through a multipole expansion, but from the knowledge of r and t, by inverting the equations (4.52) and (4.53) linking the transmission and reflection coefficient to polarisabilities in the dipole approximation. This inverse retrieval procedure cannot be successfully applied to this system due to the excited higher order multipoles we revealed.

To conclude, we believe the generalized multipolar formalism is ideal to understand and optimize devices that exhibit broadband absorption. We have illustrated it here by applying the formalism to the case of metallo-dielectric core-shell particles which were presented by Ra'di *et al.* [10] as a promising system for realizing broadband absorption in the visible.

5.4.2.d All-dielectric core-shells

In this section we adress the possibility to reach the perfect absorption regime with all dielectric core-shells.

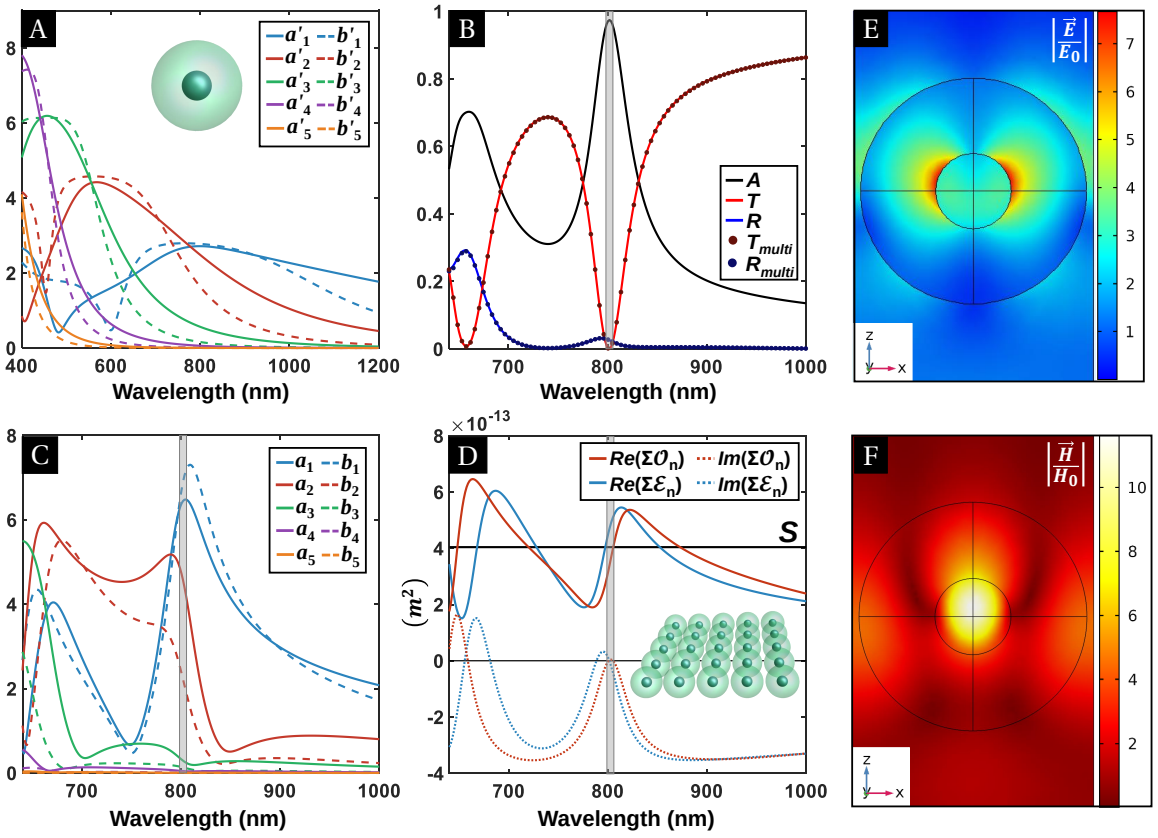

Figure 5.20 – Perfect absorption with all dielectric core-shell particles. A) Wavelength dependence of the multipole coefficients of a single core-shell consisting in a dielectric core of 100nm radius and a constant refractive index of $3+0.03i$ surrounded by a dielectric shell of refractive index equal to $1.5+0.03i$. The radius of the entire particle is 300nm. B) Spectra of R, T and A calculated for the metasurface and reproduced using the multipole coefficients. C) Spectra of the modulus of the retrieved multipole coefficients of the meta-atoms in the array. D) Sum of even and odd multipole coefficients of the core-shell in a square array with a surface fill fraction of 0.7. E) Maps of the norm of the normalized electric field and F) normalized magnetic field at the maximum of absorption for $\lambda = 802$nm.

We consider first an individual model core-shell with a radius of 300nm, composed of a dielectric core of 100nm radius with an index of 3+0.03i and surrounded by a dielectric shell of index 1.5+0.03i. The multipole coefficients of this meta-atom are shown on Fig. 5.20-A. The figure reveals an overlap two by two of the multipoles of same degree. As mentioned in section 3.4.2, this characteristic originates from the encapsulation of the core of high index by the dielectric layer of lower index that render the core-shell particle well impedance matched with the exterior environ-

ment. Since this meta-atom exhibits the features of a broadband Huygens source, the introduction of the losses in the dielectric layers should make it possible for the total absorption regime to take place.

As evidence on Fig. 5.20-B, a near perfect absorption of 97.5% is indeed achieved at the wavelength of 802nm for an array assembled with a surface fill fraction of 0.7. The multipolar decomposition presented on Fig. 5.20-C indicates that both dipolar and quadrupolar resonances are excited in the grey shaded area in which the total absorption is achieved. Although the multipolar content of the particles in the array is essentially the same as that of the isolated core-shell between 650nm and 1000nm, the excited multipoles are however significantly affected by the coupling effects between particles. In particular, the strong modification observed at the lowest wavelengths which results in the additional resonance peaks around 660nm, are a signature of the lattice resonances, the Rayleigh cut-off wavelength being at 635nm for this array. Although the above mentioned changes indicate that the hypothesis of weak coupling is not applicable, the overlapping two by two of the multipoles is substantially preserved, which shows our design strategy is sound. Indeed, the sums of symmetric and anti-symmetric multipoles are ploted on Fig. 5.20-D which reveals an excellent superposition of multipoles of opposite parity, resulting in a near zero reflection (Kerker condition) observed between 700nm and 1000nm.

In addition, at the position of the maximum of absorption, 88% of the energy is dissipated in the shell. This result may come as a surprise, since the refractive index of both the core and the shell have equal imaginary parts (0.03). However, the mapping of the electric field presented at λ =802nm on Fig. 5.20-E, reveals a field distribution very similar to the one observed for the metallo-dielectric core-shell, with a strong field enhancement in the dielectric surrounding the core. It is therefore not surprising that the absorption is distributed in a similar manner. In contrast with the other metallic core-shell systems however, the mapping of the magnetic field on Fig. 5.20-F, reveals its strong localization in the central particle of higher index, indicating this time the important contribution of the core to the magnetic response. Electric and magnetic dipoles dominating the response of the particles at 802nm, the dipolar field distributions remain identifiable on the maps of Figs. 5.20-E,F.

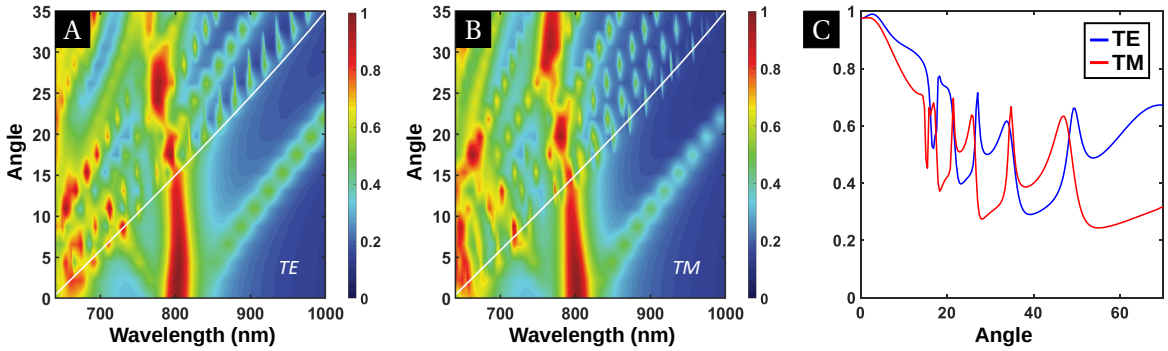

Figure 5.21 – Angular dependency of the absorption of the metasurface made from the all dielectric core-shell particles of radius 300nm under A) TE and B) TM illumination. White lines correspond to the diffraction limit. The filling fraction of the array is 0.7. C) Angle dependence of the absorption at λ = 802nm.

The angular dependency has also been studied for this design and is presented on Fig. 5.21. The angular robustness of the absorption is weak. A somewhat large absorption is maintained up to the diffraction limit, however, it is then strongly degraded in the diffractive domain.

As can be seen on Fig. 5.20-B, the resonances occurring at about 660nm leads to a second peak of absorption. Due to a slight detuning between the even and odd multipoles, the absorption is however not optimized, resulting in an absorption of 70% only, with 30% reflection obtained. Also, looking at a second design that we will present in the following, we investigated the possibility of optimizing the absorption at the position of this second peak.

We consider a meta-atom similar to the previous one, now consisting of a core of index 3.5+0.1i (no longer 3.0+0.03i) with a radius of 110nm (100nm before), surounded by a shell of index 1.5+0.05i (1.5+0.03i before), the total radius of the particle being 350nm (300nm before). The multipole coefficients of the isolated core-shell are plotted on Fig. 5.22-A. The figure shows that, for this design also, an overlap two by two of multipoles of same degree is obtained over the entire spectrum leaving once again the possibility of obtaining a very low reflection.

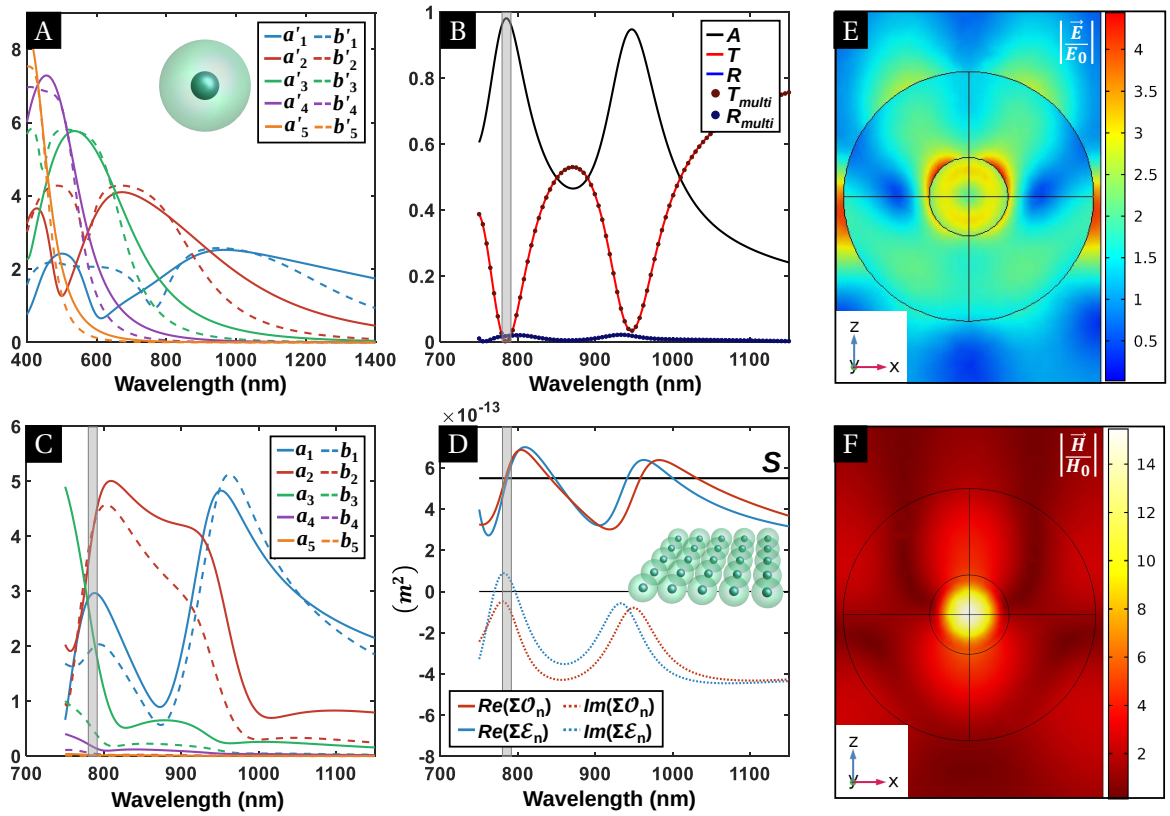

Figure 5.22 – Perfect absorption with all dielectric core-shells. A) Wavelength dependence of multipole coefficients of an individual core-shell in vacuum. The particle consist in a dielectric core of 110nm radius and a constant refractive index of $3.5+0.1i$ surrounded by a dielectric shell of refractive index equal to $1.5+0.05i$. The radius of the entire particle is 350nm. The multipoles coefficients are calculated using the extended Mie theory for core-shell particles. B) corresponding spectra of R, T and A and reproduced using the multipole coefficients (circle points). C) Spectra of the modulus of the retrieved multipole coefficients of the meta-atoms in the array. D) Sums of even and odd multipole coefficients of the core-shell particles placed in an infinite square array with a surface fill fraction of 0.7. The black continuous line is the area of the lattice unit-cell. E) Maps of the norm of the normalized electric field and F) normalized magnetic field at the maximum of absorption for $\lambda = 785$nm.

Figure 5.22-B shows the properties obtained for an array with a surface fill fraction of 0.7. Two peaks of high absorption are obtained, reaching 98 % at 785nm and 95% for the second peak at 947nm. The excellent overlap of the sums of symmetric and antisymmetric multipoles, resulting in the very low reflection obtained over the wide spectrum, is clearly visible on Fig. 5.22-D. Figure 5.22-C shows that, at the position of the strongest absorption peak, the quadrupolar resonances dominate the response of the particles, but that the contributions of the dipoles and octupoles must also be taken into account to fully describe the metasurface response. Additionally, the maps on Fig. 5.22-E reveal the complex electric field distribution inside the unit-cell at $\lambda = 785$nm, consistent with a strongly multipolar response of the particle at this wavelength. Compared to the core-shells previously studied, an important electric field is this time also observed in the central particle. Nevertheless, at 785nm, 68.5% of the absorption is still dissipated in the surrounding shell.

To conclude this section, we have shown the possibility of using all dielectric core-shells, acting as excellent broadband Huygens sources, for absorption applications. Due to the relatively low effective index of the structure, large meta-atoms organised in dense arrays are required. We found that two peaks of absorption can be obtained, one located close at the wavelengths where the dipole resonances are maximum and the other one in a region where the quadrupoles dominate, located close to the diffractive regime. The studies were realised on systems consisting in only two layers, similar behaviours are neverthless expected with multilayered core-shells or even particles with continuous gradient index, with decreasing refractive index from center to exterior. The introduction of extra layers could in fact provide additional control parameters in the tuning of the structure resonances. Moreover, our second design has revealed the possibility of obtaining a dual band absorption, although the absorption peak located at the highest wavelength can still be optimized. Finally, it should be noted that these designs have been optimized by considering constant indices freely chosen. The adjustment of the real and imaginary parts of the indices in both layers has therefore served as an additional control parameter allowing the fine adjustment of the resonances. Considering instead realistic material dispersions, this additional degree of adjustment becomes very tough to achieve, even with doped or composite materials, and might render the optimization of the absorption by the structure more delicate or even impossible for certain combinations of materials.

5.4.3 Cluster based perfect absorbers

In this section, we demonstrate the possibility of using clusters of particles for perfect absorber applications. Both plasmonic and dielectric clusters are investigated.

5.4.3.a Dielectric clusters

In section 5.3.1, we found that silicon clusters can theoretically be used for wavefront control in the infrared, where the negligible absorption loss of silicon allows to reach high values transmission. On the contrary, in this part, we show that exploiting the significant absorption loss of silicon around 400nm, perfect absorption with *Si* clusters can be achieved at the edge of the visible domain.

The cluster we investigate consists in 13 *Si* particles of radius $r = 41$nm and corresponding to a total radius $R = 141$nm. The properties of this cluster, studied using the $\mathcal{T}$-matrix method, are presented on Figs. 5.23-A,B. The cluster was designed to exhibit Huygens source features close to 450nm. We see that the perfect absorption conditions are closely met for wavelengths around 440nm indicated by the red shaded area. Figure 5.23-B shows that this region corresponds to the excitation wavelength of the quadrupolar resonances of the cluster. The dipolar resonances excited at very close wavelengths also contribute to the perfect absorption. Moreover, the overlapping of the dipoles and quadrupoles two by two is at the origin of the superposition of the sums of symmetric and anti-symmetric modes observed on Fig. 5.23-B around $\lambda = 450$nm. It suggests that very low reflection may be obtained with cluster arrays.

Metasurfaces made of such particles are now considered. The complete dependency of the array absorption with the grid pitch is presented further, on Fig. 5.27-B in section 5.4.3.c. It can be seen that two peaks of high absorption are obtained around 430nm and 440nm. Interestingly, the first band seems to be only slightly affected by the choice of the grid pitch and a high absorption at the same wavelength remains when varying the surface fraction between the maximum compactness and the diffraction limit obtained for $f_s \approx 0.35$ (represented by the white line in the figure). The evolution of the second absorption band is quite different. A unitary absorption is observed at densities in the range of $f_s \approx 0.6$. By diluting the array however, the absorption is weakened and the peak position red-shifts, indicating it is much more sensitive to lattice interactions.

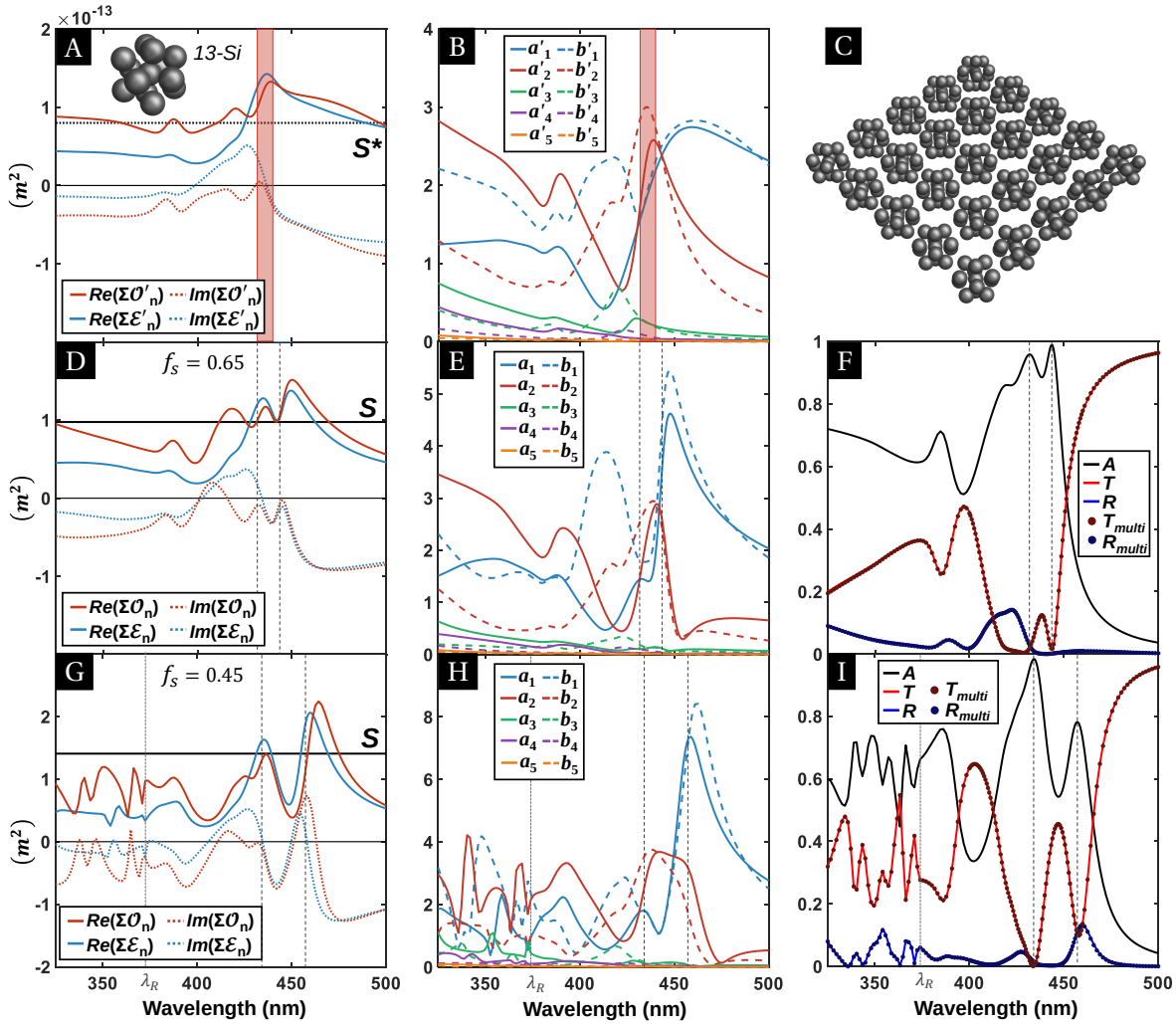

Figure 5.23 – Perfect absorption with *Si* clusters. A) Wavelength dependence of the sum of even (blue) and odd (red) multipole coefficients of an individual *Si* cluster in vacuum. The cluster is 141nm in radius and made from 13 homogeneously distributed *Si* particles with 41nm radius. The black dotted line represents S^*, the area of the smallest unit-cell achievable for a close-packing of such particles. B) Spectra of the modulus of the multipole coefficients of a single isolated cluster. The individual cluster properties are investigated using the $\mathcal{T}$-matrix method. C) Geometry of a square metasurface with a surface fill fraction of 0.65. D) Sum of even and odd multipole coefficients of *Si* clusters organized in an infinite square array with a surface fill fraction of 0.65. The black continuous line is the area of the lattice unit-cell. E) Spectra of the modulus of the retrieved multipole coefficients of the clusters in the array. F) Spectra of R, T and A calculated for the metasurface and retrieved using the multipole coefficients (circle points). Panels G),H) and I) represent respectively the same quantities as D),E) and F) for a metasurface with a surface fraction of 0.45. The diffraction limit λ_R is indicated by the dotted black vertical line.

In order to understand more in depth the origin of the two peaks observed, two metasurfaces are studied in more detail. The first one, presented in Figs. 5.23-D,E,F, consists of a cluster array with a surface fraction of 0.65 for which two absorption peaks of high values are obtained (see Fig. 5.23-F). The second one, presented in Figs. 5.23-G,H,I, consists in an array with $f_s = 0.45$, for which a total absorption is obtained for the peaks at shorter wavelengths while the absorption of the second peak is close to 80% (the positions of the peaks are pointed by vertical dotted lines on the figures).

The multipole expansion of Figs. 5.23-E,H show that the two absorption peaks are obtained in a region where dipoles and quadrupoles coexist. We notice, however, that the first absorption peak observed at shorter wavelengths appears on the tail of the quadrupole resonances, slightly before reaching its maximum. On the contrary, the second peak is observed on the tail of the dipole reso-

nance just before their maximum. As already noticed for the clusters studied in section 5.3.1, Figs. 5.23-E,H also shows that, although the quadrupole resonances are broadened when increasing the lattice pitch, their positions are practically unaffected by the interactions between particles. For both metasurfaces, the resonances are observed at wavelengths close to 440nm, which also corresponds to the wavelengths obtained for the isolated scaterrer. On the contrary, that of the dipole resonances vary considerably. For increasing lattice pitches, approaching the diffraction limit, the dipole resonances undergo a significant red-shift. Thus we understand that the displacement of the absorption peak found at high wavelengths is directly related to the red-shift of the dipole resonances. In addition, Fig. 5.23-I shows that the drop in absorption occurs in favour of transmission and reflection in equal proportions. The increase in the reflection originates from the increased detuning between even and odd modes that can be seen on Fig. 5.23-G, that could be due to the tail of the quadrupole resonances excited with slightly different amplitudes in this region. On the other hand, the multipolar coefficients being strongly reinforced at low densities, the peaks of the real parts of the sums of multipoles in Fig. 5.23-G take large values compared to $\mathcal{S}$, not allowing for a perfect destructive interference of the transmitted wave, hence also an increase of the transmission. On the contrary, the first absorption peak ($\lambda = 432$nm) independent of the lattice pitch results directly from the low impact of the interactions between particles on the quadrupole resonance positions. This low dependence of the absorption with f_s suggests that such a metasurface could be well suited for self-assembly manufacturing where the inter-particle distance is less controlled than in top-down approaches. It might also indicate a relative insensitivity of the properties of the metasurface with a certain positional disorder of the meta-atom.

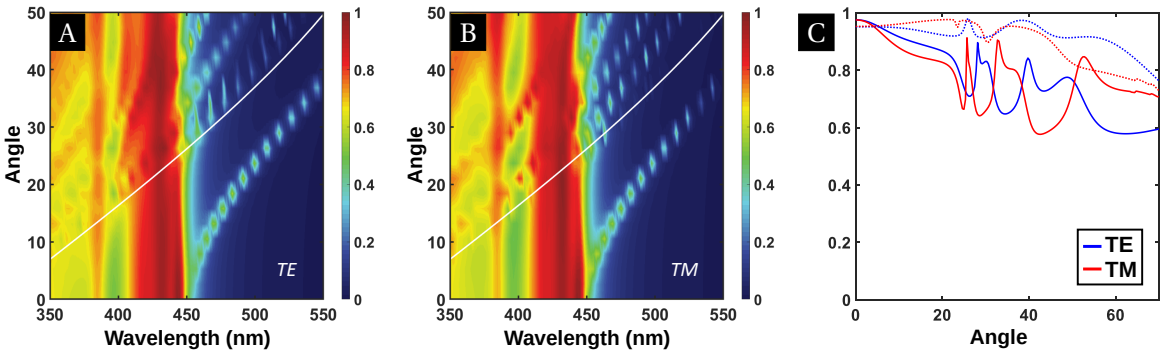

Figure 5.24 – Angular dependency of the absorption of the metasurface made from *Si* clusters under A) TE and B) TM illumination. The fill fraction of the array is 0.65. C) Solid and dotted lines are the angle dependence of the absorption at $\lambda = 443$nm and $\lambda = 432$nm respectively, corresponding to the wavelength of the two absorption peaks obtained at normal incidence.

To complete this study, we investigate the angular stability of the two absorption peaks obtained for the metasurface of fill fraction equals to 0.65. The results presented in Figs. 5.24-A,B show the great angular robustness of the absorption at $\lambda = 432$nm whatever the transverse polarisations. On the contrary, as evidenced on Fig. 5.24-C, the strong absorption obtained at $\lambda = 443$nm is found less robust and is decaying to values below 90% for angles of incidence above 10°.

We should point out the contrast between the evolution with the angle of the transmission of the loss-less silicon cluster arrays, studied in section 5.3.3, and that of the absorption of the arrays presented in Fig. 5.24. While the transmission in section 5.3.3 was found as strongly degraded at small angles by the excitation of the components of the multipoles outside the metasurface plane, here, the absorption of the silicon cluster arrays does not seem to undergo any dramatic changes at higher angles. We have not been able to interpret the origin of this difference in behavior so far.

In addition, we would like to take the opportunity to point out that the angular performances of the different designs have just been presented as complementary information in this chapter. The origin of the observed properties however, whether it is a high or low stability, as well as the presence or not of the pronounced dips in the diffractive region has not been studied in more de-

tail from a fundamental point of view. One of the reasons for this is that the multipolar formalism we have used is not at all suited for such a study, since it only applies under normal incidence, and outside the diffractive domain. Its generalization for oblique incidence and for wavelengths below λ_R, although theoretically possible, is beyond the scope of this work, and may not be the most adequate tool for this kind of study because of the enormous amount of multipolar components that might be excited in these cases. Nonetheless, given the very different behaviors observed from one design to another, properly understanding the properties of the Huygens absorbers illuminated at oblique incidence constitutes an interesting perspective of work, still lacking focus in the literature.

5.4.3.b Plasmonic clusters

In this section we show that it is also possible to achieve perfect absorption with plasmonic clusters.

We are interested in a cluster of 118nm in radius composed of 23 silver particles that are 25nm in radius each. Figure 5.25-B shows the multipolar decomposition obtained for this isolated cluster.

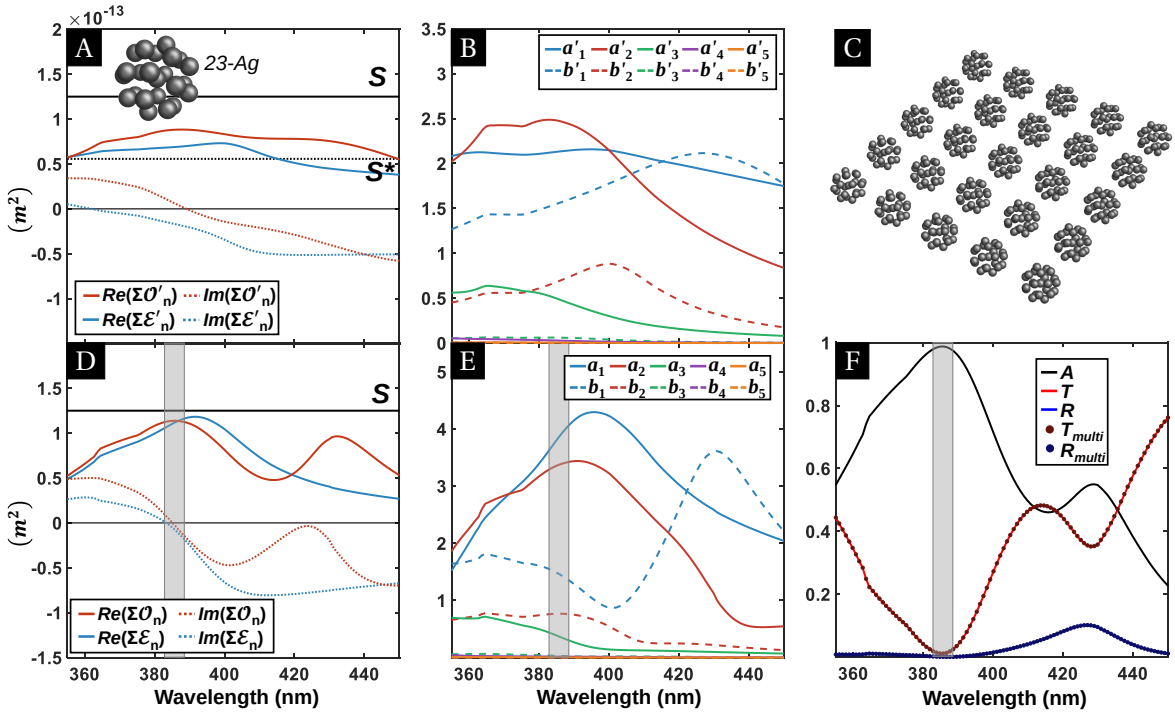

Figure 5.25 – Perfect absorption with *Ag* clusters. A) Wavelength dependence of the sum of even (blue) and odd (red) multipole coefficients of an individual plasmonic cluster in vacuum. The cluster is 118nm in radius and made from 23 pseudo-homogeneously distributed *Ag* particles with a 25nm radius. B) Spectra of the modulus of the multipole coefficients of a single isolated cluster. The individual cluster properties are investigated using the $\mathcal{T}$-matrix method. C) Geometry of a cluster-based square metasurface with a surface fill fraction of 0.35. D) Sum of even and odd multipole coefficients of *Si* clusters organized in an infinite square array with a surface fill fraction of 0.35. The black continuous line is the area of the lattice unit-cell. E) Spectra of the modulus of the retrieved multipole coefficients of the clusters in the array. F) Spectra of R, T and A calculated for the metasurface and retrieved using the multipole coefficients (circle points).

It can be seen that the electric dipole has a very wide resonance, while a magnetic dipole is excited near 430nm and preceded by a quadrupolar electric resonance near 390nm. The successive excitation of the magnetic dipole and the electric quadrupole, provide the sum of odd multipoles a behaviour close to that of the even multipoles dominated by the electric dipole. Although the absorption condition is not reached the fact that both sums evolve in a similar way with an imag-

inary part intercepting the x-axis, still suggests the possibility of reaching the Kerker regime and perfect absorption.

Indeed, the absorption obtained for arrays of these clusters is presented in the following, in Fig. 5.27-A of section 5.4.3.c. A large absorption band is obtained between 350nm and 400nm. For low density arrays, close to $f_s = 0.35$, a full absorption is achieved. Such an array is studied in more detail in Figs. 5.25-D,E,F. The important modifications of the multipoles visible close to the diffraction limit, due to the interactions between the particles and the coupling to the lattice resonances of the array can be seen on Fig. 5.25-E. In particular, the two dipole resonances are noticeably sharper than in the isolated case, resulting in an electric dipole matching relatively well the electric quadrupolar resonance of the particles. As a result, the overlap of these two resonances provide the absorption conditions that are met at a wavelength close to 385nm resulting in 98% of the incident energy being absorbed on Fig. 5.25-F.

Therefore we evidence with this study the possibility of obtaining a unitary absorption from the electric dipole and quadrupole moments of plasmonic clusters. However, since in this case the perfect absorption condition is poorly reached at the level of the single meta-atom, the necessity of relying on lattice interactions to properly tune the resonances makes the design research more complex compared to systems studied so far. The design of the meta-atom and that of the lattice can hardly be carried out independently.

5.4.3.c Tunable absorption

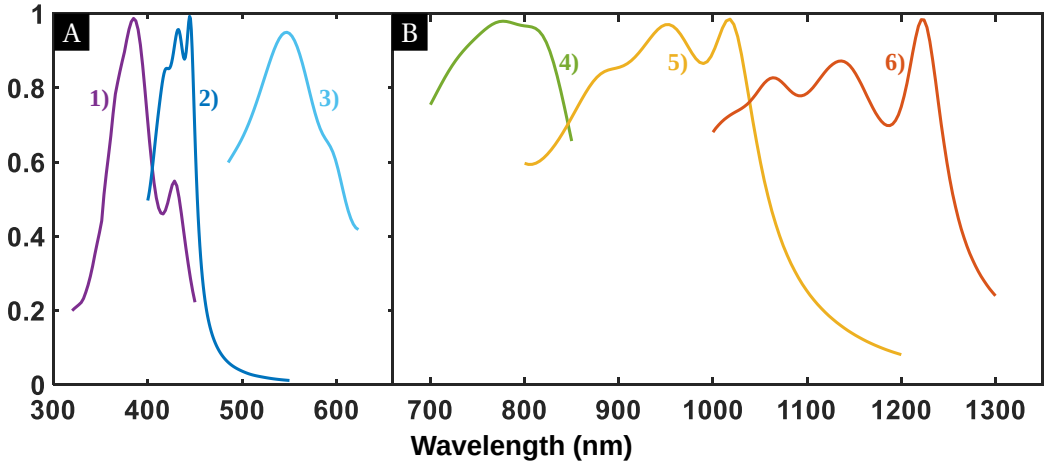

C

Design	Material	R (nm)	r (nm)	f_v	n_h	f_s	λ_{abs} (nm)
1)	Ag	118	25	0.22	1	0.35	385
2)	Si	141	41	0,32	1	0.65	444
3)	Au	120	25	0.33	1.33	0.35	547
4)	Ge	250	75	0.35	1	0.6	776
5)	Ge	324	97	0.35	1	0.6	1018
6)	Ge	400	120	0.35	1	0.7	1221

Figure 5.26 – Near-perfect absorption obtained at various frequencies A) in the visible domain by changing the chemistry and geometry of clusters B) in the near infrared by varying the geometry of *Ge* particle based clusters. The corresponding parameters for each design are listed in C).

In this part, we provide additional examples of cluster based plasmonic and dielectric absorbers to illustrate the versatility of our design procedure.

To begin, exploiting the surface plasmon absorption band of gold particles close to 550nm, a near perfect absorption in the visible domain with gold cluster arrays can be achieved as presented on Fig. 5.26-A. The design, denoted as 3) on Fig. 5.26-A consists in a cluster of radius 120nm made from 36 *Au* particles. The surface fraction (f_s) dependency of the absorption of the metasurface is shown on Fig. 5.27-C. It reveals a behaviour close to that of the silver arrays, revealing that the underlying physics behind the high absorption is similar. A maximum of absorption of 96% at 558nm is achieved for a surface fraction of 0.33 similar to that of the silver cluster metasurfaces. We can mention that due to the difficulty in obtaining the Huygens regime with this design, a modification of the surrounding medium is introduced in this case as an additional parameter to approaching the perfect absorption condition. Therefore the host medium was taken as water for this specific array.

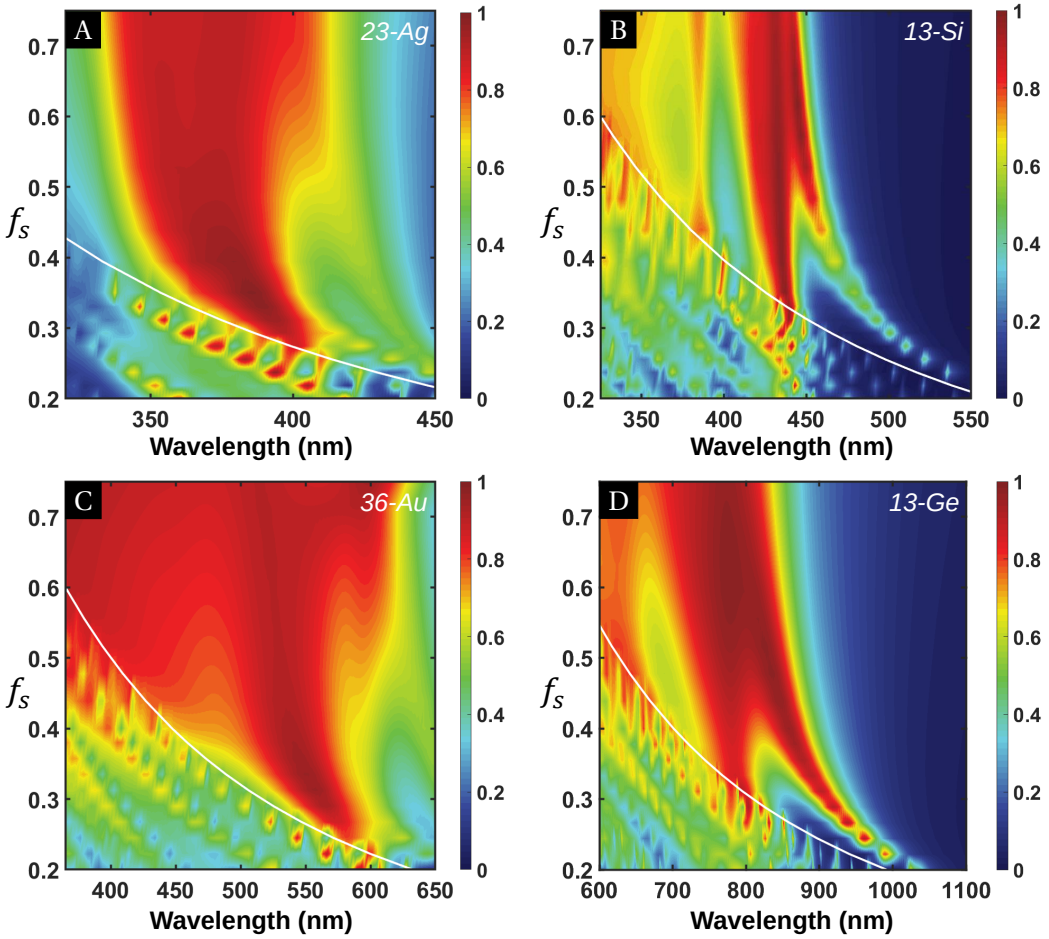

Figure 5.27 – Evolution of the absorption spectra with the surface fill fraction for metasurfaces made of A) clusters of 118nm in radius made from 23 *Ag* particles with 25nm radius, B) clusters of 141nm in radius made from 13 *Si* particles with 41nm radius, C) clusters of 120nm in radius made from 36 *Au* particles with 25nm radius and D) clusters of 250nm in radius made from 13 *Ge* particles with 75nm radius

We also investigated germanium (*Ge*) clusters for the infrared domain. Germanium exhibits both important absorption losses in the visible and at the onset of the near infrared domain as well as a high refractive index, taking near constant values close to 4 on this range. Due to these two properties, total absorption by a *Ge* cluster lattice is possible and, compared to silicon, the design is easily scalable to achieve absorption at different wavelengths. The tunability of the absorption peak between 800nm and 1250nm is evidenced for three designs on Fig. 5.26-B. In each case, the clusters consist of 13 particles of germanium homogeneously packed with a volume density of 0.35. As can be seen on table 5.26-C, the modulation of the position of the absorption peak is

obtained by a simple variation in the particle size, the optimal surface fractions being very close in the range of 0.6 to 0.7. In addition, the evolution of the absorption with the lattice density is presented for one of the designs on Fig. 5.27-D. We see an evolution very similar to that of the silicon metasurface on panel 5.27-B, revealing that the underlying physics and the multipolar origin of the absorption band are identical. This explains why the designs presented in this section have not been the object of a detailed presentation.

In conclusion, we have revealed clusters of particles as an ideal platform for perfect absorber applications. It is applicable to various lossy materials, both plasmonic and dielectric, the one studied here constituting a non-comprehensive list. With Figs. 5.26-A,B we have also shown the possibility of reaching perfect absorption in a wide spectral range in the visible and near infrared domain depending on the material used, with potentially tunable absorption peaks and scalable designs when allowed by the material refractive index dispersion. The results presented here remain entirely transferable to other regions of the electromagnetic spectrum.

5.5 Concluding remarks

In this chapter we explored Huygens metasurfaces for achieving wavefront manipulation and perfect absorption. We considered building-blocks of the same types as those studied in chapter 3. The original contributions are listed below:

- First of all, we have successfully demonstrated that beam shaping was possible with arrays of silicon clusters in the near infrared domain. Phase modulation combined with high transmittance is obtained by varying cluster size or/and lattice pitch. Following these results, we have exploited the phase variation to design both a beam deflector and a lens.
- The originality of this work also resides in the exploitation of overlapping quadrupolar resonances, compared to common realizations relying on dipolar resonances. The benefits of this approach can be found in the low sensitivity of quadrupole resonances to variation of lattice pitch.
- Also, the generalized multipolar formalism presented in section 4.3.2.a has been applied here in an original way to the problem of perfect absorption. The complete absorption conditions, first tested on single meta-atoms, allowed an identification of a large number of building-blocks suitable for absorber applications.
- Among the presented designs, we have demonstrated in particular the possibility to obtain perfect absorption with dense arrays of large silver spheres exploiting interferences between their electric dipole and quadrupole resonances. Clusters of lossy dielectrics also turn out to be excellent candidates for perfect absorption. They exhibit strong absorption peaks weakly affected by lattice filling fractions, as well as an interesting scalability demonstrated for the *Ge*-based absorber.

5.6 References

[1] M. Decker, I. Staude, M. Falkner, J. Dominguez, D. N. Neshev, I. Brener, T. Pertsch, and Y. S. Kivshar, "High-efficiency dielectric Huygens' surfaces," *Advanced Optical Materials*, vol. 3, no. 6, pp. 813–820, 2015. 110, 128

[2] W. Woltersdorff, "Über die optischen konstanten dünner metallschichten im langwelligen ultrarot," *Zeitschrift für Physik A Hadrons and Nuclei*, vol. 91, no. 3, pp. 230–252, 1934. 113

[3] S. Tretyakov, "Maximizing absorption and scattering by dipole particles," *Plasmonics*, vol. 9, no. 4, pp. 935–944, 2014. 113

[4] J. R. Piper, V. Liu, and S. Fan, "Total absorption by degenerate critical coupling," *Applied Physics Letters*, vol. 104, no. 25, p. 251110, 2014. 113, 115

[5] R. Alaee, M. Albooyeh, and C. Rockstuhl, "Theory of metasurface based perfect absorbers," *Journal of Physics D Applied Physics*, vol. 50, 2017. 113, 115

[6] Y. Ra'di, V. S. Asadchy, and S. A. Tretyakov, "Total absorption of electromagnetic waves in ultimately thin layers," *IEEE Transactions on Antennas and Propagation*, vol. 61, no. 9, pp. 4606–4614, 2013. 113

[7] V. S. Asadchy, I. A. Faniayeu, Y. Ra'Di, S. Khakhomov, I. Semchenko, and S. Tretyakov, "Broadband reflectionless metasheets: frequency-selective transmission and perfect absorption," *Physical Review X*, vol. 5, no. 3, p. 031005, 2015. 113

[8] A. Balmakou, M. Podalov, S. Khakhomov, D. Stavenga, and I. Semchenko, "Ground-plane-less bidirectional terahertz absorber based on omega resonators," *Optics letters*, vol. 40, no. 9, pp. 2084–2087, 2015. 113

[9] C. A. Valagiannopoulos and S. A. Tretyakov, "Symmetric absorbers realized as gratings of PEC cylinders covered by ordinary dielectrics," *IEEE Transactions on Antennas and Propagation*, vol. 62, no. 10, pp. 5089–5098, 2014. 113, 135

[10] Y. Ra'di, V. S. Asadchy, S. U. Kosulnikov, M. M. Omelyanovich, D. Morits, A. V. Osipov, C. R. Simovski, and S. A. Tretyakov, "Full light absorption in single arrays of spherical nanoparticles," *ACS Photonics*, vol. 2, no. 5, pp. 653–660, 2015. 113, 115, 134, 135, 138, 139, 140

[11] X. Ming, X. Liu, L. Sun, and W. J. Padilla, "Degenerate critical coupling in all-dielectric metasurface absorbers," *Optics express*, vol. 25, no. 20, pp. 24658–24669, 2017. 113, 130

[12] X. Liu, K. Fan, I. V. Shadrivov, and W. J. Padilla, "Experimental realization of a terahertz all-dielectric metasurface absorber," *Optics express*, vol. 25, no. 1, pp. 191–201, 2017. 113, 130

[13] A. Cardin, K. Fan, and W. Padilla, "Role of loss in all-dielectric metasurfaces," *Optics express*, vol. 26, no. 13, pp. 17669–17679, 2018. 114, 130

[14] S. Kruk, B. Hopkins, I. I. Kravchenko, A. Miroshnichenko, D. N. Neshev, and Y. S. Kivshar, "Broadband highly efficient dielectric metadevices for polarization control," *Apl Photonics*, vol. 1, no. 3, p. 030801, 2016. 115

[15] Y. Ra'Di, C. Simovski, and S. Tretyakov, "Thin perfect absorbers for electromagnetic waves: theory, design, and realizations," *Physical Review Applied*, vol. 3, no. 3, p. 037001, 2015. 115

[16] V. E. Babicheva and A. B. Evlyukhin, "Resonant lattice Kerker effect in metasurfaces with electric and magnetic optical responses," *Laser & Photonics Reviews*, vol. 11, no. 6, p. 1700132, 2017. 117

[17] A. B. Evlyukhin, C. Reinhardt, A. Seidel, B. S. Luk'yanchuk, and B. N. Chichkov, "Optical response features of *Si*-nanoparticle arrays," *Physical Review B*, vol. 82, no. 4, p. 045404, 2010. 117

[18] J. Li, N. Verellen, and P. Van Dorpe, "Engineering electric and magnetic dipole coupling in arrays of dielectric nanoparticles," *Journal of Applied Physics*, vol. 123, no. 8, p. 083101, 2018. 117, 122

[19] V. E. Babicheva and A. B. Evlyukhin, "Resonant suppression of light transmission in high-refractive-index nanoparticle metasurfaces," *Optics letters*, vol. 43, no. 21, pp. 5186–5189, 2018. 117

[20] N. Yu and F. Capasso, "Flat optics with designer metasurfaces," *Nature materials*, vol. 13, no. 2, p. 139, 2014. 117

[21] F. Ding, A. Pors, and S. I. Bozhevolnyi, "Gradient metasurfaces: a review of fundamentals and applications," *Reports on Progress in Physics*, vol. 81, no. 2, p. 026401, 2017. 117

[22] J. Scheuer, "Metasurfaces-based holography and beam shaping: engineering the phase profile of light," *Nanophotonics*, vol. 6, no. 1, p. 137, 2017. 117

[23] S. M. Kamali, E. Arbabi, A. Arbabi, and A. Faraon, "A review of dielectric optical metasurfaces for wavefront control," *Nanophotonics*, vol. 7, no. 6, pp. 1041–1068, 2018. 117

[24] P. Genevet, F. Capasso, F. Aieta, M. Khorasaninejad, and R. Devlin, "Recent advances in planar optics: from plasmonic to dielectric metasurfaces," *Optica*, vol. 4, no. 1, pp. 139–152, 2017. 117

[25] N. Yu, P. Genevet, M. A. Kats, F. Aieta, J.-P. Tetienne, F. Capasso, and Z. Gaburro, "Light propagation with phase discontinuities: generalized laws of reflection and refraction," *science*, vol. 334, no. 6054, pp. 333–337, 2011. 118

[26] F. Aieta, P. Genevet, N. Yu, M. A. Kats, Z. Gaburro, and F. Capasso, "Out-of-plane reflection and refraction of light by anisotropic optical antenna metasurfaces with phase discontinuities," *Nano letters*, vol. 12, no. 3, pp. 1702–1706, 2012. 118

[27] A. M. Shaltout, A. V. Kildishev, and V. M. Shalaev, "Evolution of photonic metasurfaces: from static to dynamic," *JOSA B*, vol. 33, no. 3, pp. 501–510, 2016. 118

[28] Z. Wang, Y. Sun, L. Han, and D. Liu, "General laws of reflection and refraction for subwavelength phase grating," *arXiv preprint arXiv:1312.3855*, 2013. 118

[29] M. Khorasaninejad, W. T. Chen, R. C. Devlin, J. Oh, A. Y. Zhu, and F. Capasso, "Metalenses at visible wavelengths: Diffraction-limited focusing and subwavelength resolution imaging," *Science*, vol. 352, no. 6290, pp. 1190–1194, 2016. 118

[30] F. Aieta, P. Genevet, M. A. Kats, N. Yu, R. Blanchard, Z. Gaburro, and F. Capasso, "Aberration-free ultrathin flat lenses and axicons at telecom wavelengths based on plasmonic metasurfaces," *Nano letters*, vol. 12, no. 9, pp. 4932–4936, 2012. 118, 127

[31] F. Pfender and G. M. Ziegler, "Kissing numbers, sphere packings, and some unexpected proofs," *Notices-American Mathematical Society*, vol. 51, pp. 873–883, 2004. 118

[32] J. H. Conway and N. J. A. Sloane, *Sphere packings, lattices and groups*, vol. 290. Springer Science & Business Media, 2013. 118

[33] K. E. Chong, I. Staude, A. James, J. Dominguez, S. Liu, S. Campione, G. S. Subramania, T. S. Luk, M. Decker, D. N. Neshev, *et al.*, "Polarization-independent silicon metadevices for efficient optical wavefront control," *Nano letters*, vol. 15, no. 8, pp. 5369–5374, 2015. 122

[34] I. Staude, A. E. Miroshnichenko, M. Decker, N. T. Fofang, S. Liu, E. Gonzales, J. Dominguez, T. S. Luk, D. N. Neshev, I. Brener, *et al.*, "Tailoring directional scattering through magnetic and electric resonances in subwavelength silicon nanodisks," *ACS nano*, vol. 7, no. 9, pp. 7824–7832, 2013. 122

[35] G. Swanson, "Binary optics technology: the theory and design of multilevel diffractive optical elements MIT Lincoln Laboratory Technical Report 854," 1989. 125

[36] P. Lalanne and P. Chavel, "Metalenses at visible wavelengths: past, present, perspectives," *Laser & Photonics Reviews*, vol. 11, no. 3, p. 1600295, 2017. 125, 128, 129

[37] Z. Zhou, J. Li, R. Su, B. Yao, H. Fang, K. Li, L. Zhou, J. Liu, D. Stellinga, C. P. Reardon, *et al.*, "Efficient silicon metasurfaces for visible light," *ACS Photonics*, vol. 4, no. 3, pp. 544–551, 2017. 125

[38] A. J. Ollanik, J. A. Smith, M. J. Belue, and M. D. Escarra, "High-efficiency all-dielectric Huygens metasurfaces from the ultraviolet to the infrared," *ACS Photonics*, vol. 5, no. 4, pp. 1351–1358, 2018. 125

[39] M. Kang, T. Feng, H.-T. Wang, and J. Li, "Wave front engineering from an array of thin aperture antennas," *Optics express*, vol. 20, no. 14, pp. 15882–15890, 2012. 127

[40] S. Zhang, M.-H. Kim, F. Aieta, A. She, T. Mansuripur, I. Gabay, M. Khorasaninejad, D. Rousso, X. Wang, M. Troccoli, *et al.*, "High efficiency near diffraction-limited mid-infrared flat lenses based on metasurface reflectarrays," *Optics express*, vol. 24, no. 16, pp. 18024–18034, 2016. 127

[41] E. Arbabi, A. Arbabi, S. M. Kamali, Y. Horie, and A. Faraon, "High efficiency double-wavelength dielectric metasurface lenses with dichroic birefringent meta-atoms," *Optics Express*, vol. 24, no. 16, pp. 18468–18477, 2016. 127

[42] S. Wang, P. C. Wu, V.-C. Su, Y.-C. Lai, C. H. Chu, J.-W. Chen, S.-H. Lu, J. Chen, B. Xu, C.-H. Kuan, *et al.*, "Broadband achromatic optical metasurface devices," *Nature communications*, vol. 8, no. 1, p. 187, 2017. 127

[43] A. Zhan, S. Colburn, R. Trivedi, T. K. Fryett, C. M. Dodson, and A. Majumdar, "Low-contrast dielectric metasurface optics," *ACS Photonics*, vol. 3, no. 2, pp. 209–214, 2016. 127

[44] A. Özdemir, Z. Hayran, Y. Takashima, and H. Kurt, "Polarization independent high transmission large numerical aperture laser beam focusing and deflection by dielectric Huygens' metasurfaces," *Optics Communications*, vol. 401, pp. 46–53, 2017. 127

[45] Y. Li and E. Wolf, "Focal shifts in diffracted converging spherical waves," *Optics Communications*, vol. 39, no. 4, pp. 211–215, 1981. 127

[46] W. Wang, A. T. Friberg, and E. Wolf, "Structure of focused fields in systems with large Fresnel numbers," *JOSA A*, vol. 12, no. 9, pp. 1947–1953, 1995. 127

[47] Y. Gao, J. Liu, X. Zhang, Y. Wang, Y. Song, S. Liu, and Y. Zhang, "Analysis of focal-shift effect in planar metallic nanoslit lenses," *Optics express*, vol. 20, no. 2, pp. 1320–1329, 2012. 127

[48] T. Kraus, L. Malaquin, H. Schmid, W. Riess, N. D. Spencer, and H. Wolf, "Nanoparticle printing with single-particle resolution," *Nature nanotechnology*, vol. 2, no. 9, p. 570, 2007. 127

[49] Y. Yin, Y. Lu, B. Gates, and Y. Xia, "Template-assisted self-assembly: a practical route to complex aggregates of monodispersed colloids with well-defined sizes, shapes, and structures," *Journal of the American Chemical Society*, vol. 123, no. 36, pp. 8718–8729, 2001. 127

[50] N. Vogel, M. Retsch, C.-A. Fustin, A. del Campo, and U. Jonas, "Advances in colloidal assembly: the design of structure and hierarchy in two and three dimensions," *Chemical reviews*, vol. 115, no. 13, pp. 6265–6311, 2015. 127

[51] Y. Xia, Y. Yin, Y. Lu, and J. McLellan, "Template-assisted self-assembly of spherical colloids into complex and controllable structures," *Advanced Functional Materials*, vol. 13, no. 12, pp. 907–918, 2003. 127

[52] I. Lee, H. Zheng, M. F. Rubner, and P. T. Hammond, "Controlled cluster size in patterned particle arrays via directed adsorption on confined surfaces," *Advanced Materials*, vol. 14, no. 8, pp. 572–577, 2002. 127

[53] J. H. Lee, Q. Wu, and W. Park, "Metal nanocluster metamaterial fabricated by the colloidal self-assembly," *Optics letters*, vol. 34, no. 4, pp. 443–445, 2009. 128

[54] P. Lalanne, J. P. Hugonin, and P. Chavel, "Optical properties of deep lamellar gratings: a coupled Bloch-mode insight," *Journal of Lightwave Technology*, vol. 24, no. 6, pp. 2442–2449, 2006. 128

[55] J. Tian, H. Luo, Q. Li, X. Pei, K. Du, and M. Qiu, "Near-infrared super-absorbing all-dielectric metasurface based on single-layer germanium nanostructures," *Laser & Photonics Reviews*, vol. 12, no. 9, p. 1800076, 2018. 130

[56] M. A. Cole, D. A. Powell, and I. V. Shadrivov, "Strong terahertz absorption in all-dielectric Huygens' metasurfaces," *Nanotechnology*, vol. 27, no. 42, p. 424003, 2016. 130

[57] K. Fan, J. Y. Suen, X. Liu, and W. J. Padilla, "All-dielectric metasurface absorbers for uncooled terahertz imaging," *Optica*, vol. 4, no. 6, pp. 601–604, 2017. 130

[58] E. D. Palik, *Handbook of optical constants of solids*, vol. 3. Academic press, 1998. 133

[59] S. Ogawa and M. Kimata, "Metal-insulator-metal-based plasmonic metamaterial absorbers at visible and infrared wavelengths: A review," *Materials*, vol. 11, no. 3, p. 458, 2018. 134

[60] N. Liu, M. Mesch, T. Weiss, M. Hentschel, and H. Giessen, "Infrared perfect absorber and its application as plasmonic sensor," *Nano letters*, vol. 10, no. 7, pp. 2342–2348, 2010. 134

[61] A. Moreau, C. Ciracì, J. J. Mock, R. T. Hill, Q. Wang, B. J. Wiley, A. Chilkoti, and D. R. Smith, "Controlled-reflectance surfaces with film-coupled colloidal nanoantennas," *Nature*, vol. 492, no. 7427, p. 86, 2012. 134

[62] R. Alaee, *Optical nanoantennas and their use as perfect absorbers*. PhD thesis, 2015. 135

[63] A. Abrashuly and C. Valagiannopoulos, "Limits for absorption and scattering by core-shell nanowires in the visible spectrum," *Physical Review Applied*, vol. 11, no. 1, p. 014051, 2019. 135

[64] A. Sheverdin and C. Valagiannopoulos, "Core-shell nanospheres under visible light: Optimal absorption, scattering, and cloaking," *Physical Review B*, vol. 99, no. 7, p. 075305, 2019. 135

Chapter 6

Conclusions and Outlook

The field of Huygens metasurfaces is recent and has experienced a rapid development. The main objective of this thesis work was to study the feasibility of Huygens sources and metasurfaces compatible with self-assembly methods by focusing on colloidal particles, with the at its heart central question: is it possible to propose realistically achievable metasurface designs. We have produced several original and promising results contributing to the development of functional Huygens metasurfaces, that are summarized below:

Demonstrations of resonant and extremely broadband Huygens sources

- We have shown that spherical particles placed in a homogeneous medium with an index contrast $\gamma \approx 2$ satisfies the Kerker condition with two closely overlapped dipole resonances. For decreasing values of γ , tending towards 1.5, it is possible to reach an extremely broadband forward-scattering that can cover the entire visible domain relying on the successive spectral overlapping two by two of the electric and magnetic dipole, quadrupole and octupole resonances.
- In addition, we have demonstrated that clusters of particles are an excellent alternative geometry to realize resonant and broadband Huygens sources. Resonance tuning is achieved via the geometric parameters that are the inclusion's size and their density. This constitutes an advantageous path compared to the simple spheres for which a limited number of materials with the required dispersion at optical frequencies are available.

A comprehensive theoretical tool for metasurface analysis and design

- We presented a formalism, that relates reflection and transmission coefficients, that are essential observables of metasurfaces, to the scattering coefficients of its elements. Based on a vector spherical harmonic expansion, this formalism is generalized to any order and indeed constitutes a powerful extension to the dipolar description (and its extended version in the Cartesian basis) that are routinely used in the literature. This formalism fills the gap for a simple, powerful, totally general analysis of complex metasurfaces that may consist of highly multipolar units.

Demonstrations of metasurface functionalities with several original features

- Considering lossless dielectric clusters in the infrared (*Si*), we have numerically demonstrated that wavefront shaping is possible by exploiting quadrupolar resonances of clusters. We have shown that it is possible to adjust both the size of the clusters and the pitch between elements to obtain the full phase variation in the 2π-range with high transmission. This result was used to demonstrate, based on tailored cluster arrays, a 9° beam deflector and a focusing meta-lens.
- We have shown that a perfect absorber consisting in an array of large dielectric particles can operate in a heavily multipolar regime, where at least eight multipoles are required to account for the total absorption behavior. To our knowledge, it is the first time such a multipolar perfect absorber has been proposed or evidenced up to now.

Synthesis guidelines and design procedures

- Metallo-dielectric core-shells are promising building blocks due to their ideal dipole behavior and high scattering efficiency in the infrared. We have provided a comprehensive list of designs that may serve as guidelines for the nanochemistry community in the synthesis of Huygens sources and their production for perfect absorber applications.
- We have presented a cluster design procedure to reach Huygens sources that is based on their homogenization by means of the extended Maxwell-Garnett theory and the proper tailoring of their effective refractive index. We have demonstrated the great versatility of this approach as well as some of its limitations.
- We have shown the generalized multipolar description of metasurface properties can be applied effectively to design perfect absorbers. In particular, an initial parameter exploration is carried out on individual particles before resorting to periodic calculation. This design

procedure is powerful as it has enabled a large variety of systems, with different multipolar content, as perfect absorbers.

The study carried out in this thesis is pioneering for the fields of nanochemistry and self-assembly as it is probably the first to address the possibility of designing nanoresonators that can be chemically synthetized with interesting directional scattering properties and that may be subsequently used in functional metasurfaces. We are confident that experimental realizations are indeed possible and will follow-up to this work. Nonetheless, there are limitations to our findings. In particular, only theoretical ideal structures and surfaces have been considered. This means in particular, that the inherent limitations and imperfections of experimental systems have not been taken into account rigorously, hence the need for further complementary studies. Several questions that remain to be answered and may hamper the designs in the bottom-up logic are listed below.

Experimental plausibility of the studied designs

- Self-assembly techniques introduce disorder and polydispersity. One important avenue to explore for the clusters before concluding on their experimental plausibility as Huygens sources would be to deepen the draft study initiated in section 3.3.4, and to carry out a complete statistical investigation on the impact of voids, disorder and polydispersity on their response. It should be noted however that the work initiated at the CRPP in the frame of Rajam Elancheliyan's thesis on the synthesis of nanoclusters is quite promising as she has shown that strong magnetic responses could be obtained with plasmonic clusters using the emulsion route.
- In addition, it would be interesting to investigate in more detail the all-dielectric core-shell particles, whose multipole content appears to be very similar to that of dielectric clusters. Indeed, it is not uncommon to obtain structures of this type during colloidal synthesis of dielectric particles. Oxidation of the surface, porosity and amorphous growth can typically lead to particles with effectively lower indices near the surface compared to the core of the particle. Also, it would be interesting to conduct studies considering realistic dispersions and performing a more systematic investigation on the dependency of the properties with the number of layers and refractive index.
- The metal-dielectric core-shells investigated thus far are very promising. However, the required geometry to reach the Kerker regime is still quite far from what is experimentally achievable to our knowledge. Indeed, at the moment, it seems quite hard to make coatings that are so large (over a 100 nm).

Disorder and positional uncertainties for metasurfaces

- In section 5.4 dedicated to absorbers, we have shown that some designs consist of very dense particle arrays. These results are very encouraging from the manufacturing point of view, since these arrays could be obtained by means of conventional self-assembly methods. In addition, some designs, such as the Si clusters based metasurface, have absorption peaks that vary only slightly with the grid pitch, which could indicate a low sensitivity to disorder. Indeed, the robustness of the absorption properties to disorder is a particularly interesting question that would deserve to be explored in the future. We believe that disordered designs will work in the perfect absorber regime, but this still needs to be demonstrated.
- On the other hand, wavefront-manipulation applications as presented in section 5.3.2 appears as particularly challenging since they require a high degree of control in the spatial arrangement of particles that are different one from one another, thus requiring their sizes to be well controlled as well. Clearly this type of application is very unlikely without resorting to patterned templates. The use of pre-patterned templates probably means that the structures that will be fabricated will require hybrid top-down/bottom-up approaches. Furthermore, the disorder inherent to self-assembly techniques needs to be looked at to see its impact on metasurfaces as for the perfect absorber design.

Impact of a substrate

- In this thesis, the metasurfaces are considered as free standing arrays. This is still realistic in the sense that metasurfaces can be built on glass substrates and then covered with a polymer superstrate so as to ensure that both materials have the same index of refraction below and above the metasurface. However, it will be practical experimentally to simply have monolayers on a substrate, without the use of a superstrate. This requires an extensive study of the interaction of the particles with the substrate in the metasurface.

Analysis of Huygens metasurfaces at oblique incidence

- It should be noted that the formalism used in this work that analyzes the multipolar content of nanoaresonators in the metasurface is only valid under normal incidence and is not adapted to oblique incidence. New tools are required to study these situations.

Appendix A

A.1 Spherical functions

We develop here in a compact form the expressions of the vector spherical harmonics $\vec{M}^{(l)}_{n,m}$ (2.75) and $\vec{N}^{(l)}_{n,m}$ (2.76)

$$\vec{M}^{(l)}_{n,m}(\vec{r},\omega) = \frac{-i}{\sqrt{l(l+1)}}\left[\frac{-im}{\sin\theta} z^{(l)}_n(kr) Y_{n,m}(\theta,\varphi)\vec{e}_\theta + z^{(l)}_n(kr)\frac{\partial}{\partial\theta} Y_{n,m}(\theta,\varphi)\vec{e}_\varphi\right] \tag{A.1}$$

$$= iO_{n,m}\left[i z^{(l)}_n(kr)\pi_{n,m}(\theta)\vec{e}_\theta - z^{(l)}_n(kr)\tau_{n,m}(\theta)\vec{e}_\varphi\right] e^{im\varphi} \tag{A.2}$$

$$\vec{N}^{(l)}_{n,m}(\vec{r},\omega) = iO_{n,m}\left[\frac{z^{(l)}_n(kr)}{kr} n(n+1) P^m_n(\cos\theta)\vec{e}_r\right. \tag{A.3}$$

$$\left. + \frac{1}{kr}\frac{\partial}{\partial(kr)}[(kr) z^{(l)}_n(kr)]\tau_{n,m}(\theta)\vec{e}_\theta + \frac{i}{kr}\frac{\partial}{\partial(kr)}[(kr) z^{(l)}_n(kr)]\pi_{n,m}(\theta)\vec{e}_\varphi\right] e^{im\varphi} \tag{A.4}$$

Where $\pi_{n,m}$ and $\tau_{n,m}$ are the so-called scalar tesseral functions defined by

$$\tau_{n,m} = \frac{d}{d\theta} P^m_n(\cos\theta) \tag{A.5}$$

$$\pi_{n,m} = \frac{m}{\sin\theta} P^m_n(\cos\theta) \tag{A.6}$$

and where

$$O_{n,m} = \frac{1}{\sqrt{n(n+1)}}\sqrt{\frac{2n+1}{4\pi}\frac{(n-m)!}{(n+m)!}} \tag{A.7}$$

A.2 Field quantities generated from magnetic currents

Electromagnetic fields produced by magnetic current sources $\vec{J}_{s,m}$ can be directly derived from expression (2.116) and (2.117) by exploiting duality relations between electric and magnetic fields in Maxwell equations. Using the inversions ($\vec{E} \to \vec{H}$), ($\vec{H} \to -\vec{E}$), ($\epsilon \to \mu$), ($\mu \to \epsilon$), and ($\vec{J}_{s,e} \to \vec{J}_{s,m}$) equations (2.116) and (2.117) become for magnetic sources:

$$\vec{E}_{scat}(\vec{r},\omega) = -\iiint_{V'}\left[\vec{\nabla}\wedge\overleftrightarrow{G}(\vec{r},\vec{r}')\right]\vec{J}_{s,m}(\vec{r}',\omega)dV' \tag{A.8}$$

$$\vec{H}_{scat}(\vec{r},\omega) = i\omega\epsilon\iiint_{V'}\overleftrightarrow{G}(\vec{r},\vec{r}')\vec{J}_{s,m}(\vec{r}',\omega)dV' \tag{A.9}$$

Where the integrals are performed over the whole source volume and where $\overleftrightarrow{G}(\vec{r},\vec{r}')$ is the dyadic Green's function. These expressions can be found in various textbooks such as in [1].

A.3 Far field scattering patterns

The relation between incident and scattered field in the far-field zone can be written in a matrix form [2]:

$$\begin{pmatrix} E_{scat,\parallel} \\ E_{scat,\perp} \end{pmatrix} = \frac{e^{ikr}}{-ikr} \begin{bmatrix} S_2 & S_3 \\ S_4 & S_1 \end{bmatrix} \begin{pmatrix} E_{inc,\parallel} \\ E_{inc,\perp} \end{pmatrix} \tag{A.10}$$

The subscripts $\parallel$ and $\perp$ indicate components parallel and perpendicular to the scattering plane containing the incident and scattered directions respectively. The matrix S is known as the amplitude scattering matrix and provides a complete description of the far-field scattering pattern. Each of the four scattering matrix elements S_1, S_2, S_3 and S_4 are in general functions of θ and φ.

In the case of an $\vec{e}_x$ polarized incident plane wave propagating along the $\vec{e}_z$ direction, the scattered electric field reads:

$$\vec{E}_{scat}(\theta,\varphi) = \frac{e^{ikr}}{-ikr}\vec{V}(\theta,\varphi)E_0 \tag{A.11}$$

with $\vec{V}$, the scattering amplitude vector given by:

$$\vec{V}(\theta,\varphi) = \left[S_2(\theta,\varphi)\cos\varphi + S_3(\theta,\varphi)\sin\varphi\right]\vec{e}_\theta - \left[S_4(\theta,\varphi)\cos\varphi + S_1(\theta,\varphi)\sin\varphi\right]\vec{e}_\varphi \tag{A.12}$$

The quantity

$$\sigma_d(\theta,\varphi) = \frac{dP_{scat}}{d\Omega} = \frac{\left|\vec{V}\right|^2}{k^2} \tag{A.13}$$

corresponds to the differential scattering cross section. It provides the angular distribution of the scattered energy, *i.e.* the normalized intensity scattered in a direction into a unit solid angle.

A.3.1 Isotropic scaterrers [2, 3]

For isotropic scatterers, the amplitude scattering matrix is diagonal:

$$\begin{bmatrix} S_2 & 0 \\ 0 & S_1 \end{bmatrix} \tag{A.14}$$

According to Mie theory, the elements S_1 and S_2 are expressed as:

$$S_1(\cos\theta) = \sum_{n=1}^{\infty} \frac{2n+1}{n(n+1)}\left(a_n\pi_n(\cos\theta) + b_n\tau_n(\cos\theta)\right) \tag{A.15}$$

$$S_2(\cos\theta) = \sum_{n=1}^{\infty} \frac{2n+1}{n(n+1)}\left(a_n\tau_n(\cos\theta) + b_n\pi_n(\cos\theta)\right) \tag{A.16}$$

The far field scattering intensity is in this case simply given by:

$$\sigma_d(\theta,\varphi) = \frac{1}{k^2}\left(\left|S_2\right|^2\cos^2\varphi + \left|S_1\right|^2\sin^2\varphi\right) \tag{A.17}$$

The expression (A.17) was used to produce the scattering pattern of different combinations of multipoles in section 3.1.

In addition, for $\theta = 0°$,

$$\tau_n(1) = \pi_n(1) = \frac{n(n+1)}{2} \tag{A.18}$$

hence the forward scattering cross-section:

$$\sigma_{for} = \sigma_d(0°, \varphi) = \frac{\pi}{k^2}\left|\sum_{n=1}^{\infty}(2n+1)(a_n + b_n)\right|^2 \tag{A.19}$$

On the other hand, at $\theta = 180°$,

$$\tau_n(-1) = -\pi_n(-1) = (-1)^n \frac{n(n+1)}{2} \tag{A.20}$$

leading to the backward scattering cross-section

$$\sigma_{back} = \sigma_d(180°, \varphi) = \frac{\pi}{k^2}\left|\sum_{n=1}^{\infty}(-1)^n(2n+1)(a_n - b_n)\right|^2 \tag{A.21}$$

For non spherical particles, the forward and backward scattering cross-section expressions can be generalized into equations (2.127,2.128).

A.4 References

[1] A. Lahiri, *Basic Optics: Principles and Concepts*. Elsevier, 2016. I

[2] C. F. Bohren and D. R. Huffman, *Absorption and scattering of light by small particles*. John Wiley & Sons, 2008. x, II

[3] W. Liu, J. Zhang, B. Lei, H. Ma, W. Xie, and H. Hu, "Ultra-directional forward scattering by individual core-shell nanoparticles," *Optics express*, vol. 22, no. 13, pp. 16178–16187, 2014. x, II

Résumé

Sommaire

1 Introduction V
1.1 Nanophotonique, métamatériaux et métasurfaces V
1.2 Concept et applications des métasurfaces de Huygens VI
1.3 L'auto-assemblage comme plateforme prometteuse pour la réalisation de métasurfaces optiques VII
1.4 Problématiques et motivations de la thèse VII
2 Conception de sources de Huygens isotropes à partir de particules colloïdales . . VIII
2.1 Développement multipolaire et condition de Kerker VIII
2.2 Sources de Huygens basées sur des particules sphériques de faible indice . IX
2.3 Des clusters de particules comme sources de Huygens résonnantes ou large bande X
2.4 Diffusion unidirectionnelle par des particules multicouches XI
3 Métasurfaces de Huygens multipolaires XI
3.1 Formalisme multipolaire et propriétés de métasurfaces XI
3.2 Métasurfaces à forte transmission pour des applications de contrôle de front d'ondes XII
3.3 Absorbeurs parfaits XIII
4 Conclusion XV

1 Introduction

1.1 Nanophotonique, métamatériaux et métasurfaces

La nanophotonique est un domaine très actif de la recherche moderne qui combine nanotechnologies et optique. Elle peut être définie comme la discipline dédiée à la compréhension et au contrôle des interactions lumière-matière à l'échelle nanométrique. La génération, la manipulation et la détection de la lumière par des dispositifs nanostructurés sont d'une importance significative pour de nombreux domaines et promettent de nombreuses applications pour les télécommunications, l'imagerie, les systèmes de visualisation, le biomédical, ou le secteur de l'énergie par exemple.

En particulier, les vingt dernières années ont vu le développement intense et rapide d'une nouvelle branche de la nanophotonique dédiée aux *métamatériaux*. Ce terme, construit autour du préfixe grec "meta" qui signifie "aller au-delà", désigne des matériaux composites artificiels, dont les sous-unités consistent généralement en des résonateurs sub-longueurs d'onde organisés périodiquement et appelés *meta-atomes*. Les métamatériaux sont spécifiquement conçus pour présenter des propriétés électromagnétiques non conventionnelles telles que des indices de réfraction doublement négatifs, des permittivités proches de zéro, du magnétisme artificiel, ou une chiralité artificielle géante, et ont été largement étudiés avec l'idée de développer des lentilles pour imager au-delà de la limite diffractive ou pour la réalisation de capes d'invisibilités suivant les lois de l'optique de transformation.

Largement exploré aux fréquences micro-ondes, le concept de métamatériaux a également été développé avec succès aux fréquences optiques en réduisant la taille des structures. Malgré de nombreuses démonstrations élégantes, le domaine des métamatériaux optiques est encore aujourd'hui confronté à deux problèmes majeurs limitant leur utilisation. Tout d'abord, leur complexité structurelle, qui nécessite une fabrication 3D, les rend difficiles à produire à grande échelle, et requiert des procédés souvent longs et onéreux. De plus, les métamatériaux présentent généralement des pertes par dissipation élevées, peu propices à la propagation de la lumière sur des épaisseurs importantes.

Aussi, les *métasurfaces*, équivalents bidimensionnels des métamatériaux pour lesquels les limites mentionnées précédemment sont assouplies en raison de leur faible épaisseur, ont suscité un intérêt croissant au cours de la dernière décennie. Les métasurfaces sont des interfaces structurées ultra-minces capables d'affecter un faisceau de lumière sur une échelle sub-longueur d'onde. Leur principe de fonctionnement repose en général sur la diffusion collective de leurs sous-unités organisées en des réseaux périodiques. Une manipulation arbitraire de l'amplitude, de la phase et/ou de la polarisation est possible en choisissant de manière adaptée la forme, la nature, l'orientation et l'organisation de leurs différents constituants. Au cours de ces dernières années, les métasurfaces ont été largement explorées pour réaliser des fonctionnalités de composants optiques conventionnels tels que des lentilles, des lames à retard, des polarimètres, des déflecteurs de faisceau, des lames de phase en spirale, des hologrammes, ainsi que pour des applications d'absorption de lumière, de filtrage optique, ou des dispositifs non linéaires. En raison de leurs capacités exceptionnelles de manipulation de la lumière, les métasurfaces devraient constituer la prochaine génération d'éléments optiques et conduire à de nouvelles fonctionnalités innovantes. À long terme, elles pourraient permettre de substituer des composants optiques conventionnels encombrants ou des éléments diffractifs par des équivalents beaucoup plus compacts.

1.2 Concept et applications des métasurfaces de Huygens

Parmi les différents types de métasurfaces, émerge en 2013 le concept de *métasurface de Huygens*. Ces métasurfaces tirent leur nom du principe théorique de Huygens-Fresnel et peuvent être considérées comme son implémentation pratique. Ce principe fondateur de l'optique ondulatoire énoncé au XVII$^{\text{ème}}$ siècle décrit la propagation des ondes électromagnétiques dans un milieu comme le résultat d'interférences entre des ondes hémisphériques émises dans la direction de la propagation par un ensemble de sources secondaires appelées *sources de Huygens*. Les métasurfaces de Huygens sont constituées de méta-atomes présentant des propriétés analogues à ces sources de Huygens théoriques, c'est-à-dire se comportant comme des diffuseurs unidirectionnels, diffusant la lumière uniquement vers l'avant. Ces métasurfaces sont ainsi caractérisées par une absence de réflexion. Par ailleurs, en introduisant des variations spatiales dans le retard de phase des diffuseurs, une modulation arbitraire du front d'onde du faisceau transmis au travers de l'interface est rendue possible. Ces métasurfaces ont ainsi conduit à la démonstration d'une large variété de méta-dispositifs dédiés à la mise en forme de faisceaux présentant de fortes valeurs de transmission, qui plus est indépendantes de l'état de polarisation du faisceau incident.

Les réalisations récentes de métasurfaces de Huygens optiques sont pour l'essentiel basées sur des particules diélectriques polarisables et sublongueur d'onde. Ces résonateurs de Mie supportent de fortes réponses multipolaires de types électriques et magnétiques dans le visible et le proche infrarouge, susceptibles d'être excitées simultanément sur une même gamme spectrale. De l'interférence entre ces différents multipôles peut résulter un diagramme de rayonnement fortement asymétrique. En particulier, la suppression de la rétrodiffusion est atteinte dans la condition où les contributions des multipôles de parités spatiales opposées sont équilibrées. Cette configuration conduit à des interférences destructives entre les ondes électromagnétiques émises par chaque famille de multipôles dans la direction arrière ainsi qu'à des interférences constructives dans la direction avant. Cette condition est également connue sous le nom de *condition de Kerker* en référence aux travaux pionniers de Milton Kerker.

Au-delà des dispositifs à forte transmission, il convient de mentionner que les métasurfaces de Huygens pourraient bénéficier à de nombreuses applications nécessitant de minimiser voire annuler la réflexion d'une surface. C'est par exemple le cas des absorbeurs électromagnétiques qui sont d'importance notable pour de nombreuses applications telles que le filtrage, la collecte d'énergie, les systèmes de détection, le contrôle des émissions thermiques, etc. Les métasurfaces de Huygens apportent une nouveauté importante à ce domaine des absorbeurs puisqu'elles offrent la possibilité de réaliser des absorbeurs parfaits symétriques et transparents en dehors de leur gamme d'opération, avec une simple monocouche de particules, sans la nécessité de recourir à des substrats réfléchissants comme dans les configurations traditionnellement rencontrées.

1.3 L'auto-assemblage comme plateforme prometteuse pour la réalisation de métasurfaces optiques

Aujourd'hui, l'essentiel des métasurfaces sont produites par des technologies de nano-fabrication de type "top-down", c'est-à-dire par voie descendante, regroupant notamment les diverses techniques lithographiques. Cette approche permet un contrôle très précis des géométries et une résolution spatiale inégalée pour organiser des éléments sur une surface. Toutefois, ces méthodes sont généralement longues et onéreuses. Ainsi le développement de techniques de fabrication à faible coût permettant de couvrir rapidement de large surface est également un sujet d'étude actif. Les techniques par voie ascendante dites "bottom-up" offrent à ce regard une alternative prometteuse.

L'approche par voie ascendante est basée sur la combinaison de la nanochimie colloïdale, permettant la synthèse d'un grand nombre de méta-atomes optiques (généralement de l'ordre de 10^{13} par synthèse en laboratoire), et de méthodes d'auto-assemblage permettant leur organisation spontanée en matériaux ou leur dépôt sur des surfaces avec une production grande échelle.

Une large variété de méta-atomes de complexité plus ou moins importante peut être synthétisée par la nano-chimie. Certains d'entre eux constituent des éléments intéressants pour les métasurfaces de Huygens. Il est possible de synthétiser diverses nanoparticules diélectriques telles que *Si*, TiO_2, Cu_2O, etc. Des réponses magnétiques, non naturelles aux fréquences optiques mais nécessaires pour obtenir des sources Huygens dipolaires, peuvent également être obtenues en considérant des particules cœurs-écorces métalo-diélectriques ou des structures plus complexes présentant des réponses magnétiques dites artificielles. Celles-ci consistent généralement en un ensemble compacte de nano-objets métalliques pour lesquelles des boucles de courants plasmoniques sont excitées, générant à leur tour un moment magnétique oscillant à la fréquence de l'onde incidente.

Concernant les méthodes d'assemblages, des films minces couvrant des superficies conséquentes peuvent par exemple être produits par les méthodes de Langmuir-Blodgett, par immersion, par centrifugation, ou par des méthodes d'évaporation de ménisque. Des alternatives répandues consistent à utiliser des substrats pré-structurés comme supports à la déposition, afin de guider l'agencement des nanoparticules sur les surfaces et obtenir des motifs aux périodes contrôlables.

1.4 Problématiques et motivations de la thèse

Si les métasurfaces de Huygens ont démontré leur fort intérêt et potentiel, les principales démonstrations reposent néanmoins sur des structures obtenues par lithographie et s'appuient sur des résonateurs anisotropes, tels que des disques et des nano-piliers. Des sources de Huygens isotropes obtenues en solution seraient particulièrement bien adaptées à la réalisation de métasurfaces de Huygens suivant une approche bottom-up, et présenteraient l'intérêt de limiter la complexité du processus d'auto-assemblage en s'affranchissant du besoin d'aligner les particules sur le substrat. Néanmoins, les métasurfaces de Huygens basées sur des éléments isotropes ont reçu une attention extrêmement limitée dans la littérature par rapport aux géométries anisotropes.

Le but de ce travail de thèse était donc d'évaluer le potentiel de particules colloïdales isotropes pour la réalisation de métasurfaces optiques de Huygens. Les objectifs sous-jacents étaient de proposer des outils théoriques et des procédures de conception de sources de Huygens pouvant conduire à des métasurfaces de Huygens fonctionnelles réalisables par des techniques de fabrication par voie ascendante. Dans cette thèse, nous étudions plusieurs types de sources de Huygens isotropes et leurs applications potentielles en tant que métasurfaces, tant pour des applications de mise en forme de front d'onde que pour des applications d'absorption parfaite. Nous nous concentrons sur des structures pouvant être obtenues par la nanochimie colloïdale. Celles-ci consistent en des particules sphériques diélectriques et métalliques, des clusters d'inclusions plasmoniques ou diélectriques ainsi qu'en des particules multicouches.

La thèse est divisée en deux parties distinctes. Dans un premier temps, nous étudions les propriétés de diffusion de méta-atomes considérés individuellement et présentons des directives pour adapter leurs différents moments multipolaires afin de remplir la condition de Kerker et obtenir des sources Huygens résonantes ou large bande. Une deuxième partie est consacrée à l'étude des propriétés de métasurfaces de Huygens formées de ces particules agencées en réseaux périodiques carrés.

2 Conception de sources de Huygens isotropes à partir de particules colloïdales

2.1 Développement multipolaire et condition de Kerker

Un développement multipolaire constitue un outil particulièrement intéressant pour la conception de sources de Huygens et plus généralement encore, pour la compréhension des propriétés de diffusion de systèmes rayonnant complexes. Avec cet outil, le champ produit par une structure est exprimé dans la base des harmoniques sphériques vectorielles comme une somme de multipôles pondérés par leur coefficient (ou moment) multipolaire complexe associé donnant phase et amplitude d'excitation. Ces multipôles électromagnétiques correspondent aux champs produits par des distributions simples de charges et de courants ponctuellement localisés. Chaque multipôle rayonne dans des proportions parfaitement identiques dans les deux demi-espaces situés vers l'avant et vers l'arrière de la particule. Par ailleurs, la dépendance spatiale du champs électrique produit par chaque multipôle est une fonction de l'espace soit paire, soit impaire. Ainsi, dipôles électriques, quadrupôles magnétiques, etc. rayonnent des champs électriques en phase dans les deux directions opposées de l'espace (avant et arrière) tandis que dipôles magnétiques et quadrupôles électriques rayonnent des champs électriques en opposition de phase selon ces deux mêmes directions. Du fait d'interférences, l'excitation combinée de multipôles de parité spatiale opposée affecte fortement la directionalité du rayonnement diffusé par une particule et peut conduire à une diffusion fortement asymétrique. La suppression du rayonnement dans la direction opposée au vecteur d'onde incident est obtenue en équilibrant les contributions de l'ensemble des multipôles présentant une symétrie spatiale paire avec celle des multipôles de symétrie spatiale impaire. Cela se traduit par la condition suivante sur les coefficients multipolaires :

$$\sum_{n=1}^{\infty} \mathcal{O}_n = \sum_{n=1}^{\infty} \mathcal{E}_n \tag{R.1}$$

avec

$$\sum_{n=1}^{\infty} \mathcal{E}_n = \sum_{n=1}^{\infty} \sum_{m=-1,+1} m(4n-1)\, a_{2n-1,m} + \sum_{n=1}^{\infty} \sum_{m=-1,+1} (4n+1)\, b_{2n,m} \tag{R.2}$$

$$\sum_{n=1}^{\infty} \mathcal{O}_n = \sum_{n=1}^{\infty} \sum_{m=-1,+1} (4n-1)\, b_{2n-1,m} + \sum_{n=1}^{\infty} \sum_{m=-1,+1} m(4n+1)\, a_{2n,m} \tag{R.3}$$

les sommes pondérées des moments des multipoles paires ($\mathcal{E}_n$) et impaires ($\mathcal{O}_n$), n et m étant des entiers quantifiant respectivement le degré et l'ordre des multipôles. Cette condition connue sous

le nom de condition de Kerker permet l'obtention de particules se comportant comme des sources de Huygens.

Avec cette thèse nous avons cherché à approcher cette condition de Kerker pour différents systèmes consistant en des sphères homogènes, des particules sphériques multicouches et des clusters sphériques de particules. Contrairement aux structures anisotropes telles que les nanodisques communément étudiés dans la littérature, l'ajustement des multipôles pour des particules isotropes telles que considérées ici nécessite l'identification de leviers de contrôle autre que le rapport d'aspect géométrique des particules.

2.2 Sources de Huygens basées sur des particules sphériques de faible indice

Dans un premier temps nous avons cherché à identifier, d'un point de vue théorique, les performances, en terme d'efficacité de diffusion et de directionalité du rayonnement, pouvant être obtenues avec de simples particules colloïdales sphériques d'indice constant placées dans un milieu hôte homogène sans perte. Une permittivité unitaire est choisie pour l'ensemble des matériaux traduisant l'absence de réponse magnétique des matériaux naturels aux fréquences optiques. Cette étude met en lumière la possibilité d'ajuster le contraste d'indice entre une particule et son milieu hôte de manière à obtenir une annulation de la rétrodiffusion, sur une bande spectrale qui est d'autant plus grande que le contraste d'indice est faible. Ce résultat découle de la convergence deux à deux et de la fusion spectrales progressives des paires de multipoles de même ordre, présentant des parités opposées, lors de la diminution du contraste d'indice. La conséquence directe de ce phénomène est la possibilité d'approcher la condition de Kerker particulière $a_n = b_n$ pour successivement chacune des paires de multipôles à mesure que le contraste d'indice diminue. Néanmoins, si cette condition de Kerker peut être approchée, la diminution du contraste d'indice s'accompagne également d'une baisse des efficacités maximales de diffusion. Il est important de noter que par conséquent, un compromis est à trouver entre les efficacités des sources de Huygens et leur largeur de bande. Aussi, nous nous sommes intéressés aux performances optimales pouvant être obtenues pour ce type de système présentant de faible contraste d'indice.

L'efficacité maximale pouvant être obtenue pour une paire de multipôles de même ordre remplissant rigoureusement les conditions de Kerker est de 3.7. Elle est obtenue par l'excitation de deux dipôles pour une particule présentant un contraste d'indice (noté γ) de 2.5. Néanmoins il est à noter qu'une telle source de Huygens, maximisant l'efficacité de diffusion, n'est pas résonnante, du fait que les deux dipôles sont excités à des longueurs d'ondes distinctes. Cette source "optimale" en terme d'efficacité présente ainsi une largeur de bande très limitée. Une situation plus favorable, du point de vue de la largeur spectrale pour une source de Huygens dipolaire, est obtenue pour des particules présentant un contraste d'indice plus faible de 1.9. Cette valeur est celle permettant de maximiser l'efficacité de diffusion à la résonance de deux dipôles. Les pics d'intensités de diffusion des deux dipôles coïncident alors spectralement. Dans cette situation, une diffusion dirigée au moins à 90% vers l'avant est obtenue sur toute la plage d'excitation des résonances dipolaires. Néanmoins, les conditions de Kerker sont relaxées par rapport au cas précédent et ne sont pas rigoureusement remplies à la résonance. L'efficacité de diffusion maximale obtenue dans cette situation est de 3.6, soit une valeur très proche de la valeur optimale. En diminuant d'autant plus le contraste d'indice, la superposition progressive des paires de multipôles d'ordres plus élevés élargit progressivement la bande spectrale sur laquelle le comportement de sources de Huygens est observé. Dans la limite $\gamma = 1.5$ (en deçà de laquelle les résonateurs ne sont plus sub-longueur d'onde) une efficacité importante de 3.5 est encore atteinte par les sources de Huygens multipolaires. Aussi, des efficacités de diffusion significative restent accessibles pour des particules présentant des faibles valeurs de contrastes d'indices jusqu'à 1.5.

Cette étude préliminaire révèle donc que l'ajustement de l'indice de réfraction de particules ou de leur milieu hôtes est une alternative intéressante aux paramètres géométriques permettant d'affecter leurs multipôles et d'atteindre le régime de Huygens. Elle fournit par ailleurs une ligne

directrice pour la conception de sources Huygens dipolaires résonantes ou multipolaires large-bande. Ces caractéristiques, étudiées pour des particules d'indice constant, ont par ailleurs été vérifiées numériquement sur des particules de TiO_2 placées dans l'eau et d'Al_2O_3 placées dans l'air, présentant des contrastes d'indices respectifs de 1.9 et 1.7. Les résultats obtenus mettent effectivement en évidence une diffusion unidirectionnelle vers l'avant, très large bande, couvrant dans le cas des particules d'Al_2O_3 toute la gamme du visible entre 400nm et 800nm et résultant de l'excitation des résonances dipolaires, quadrupolaires et octupolaires des particules. Ces résultats sont particulièrement intéressants pour la communauté de la nanochimie, puisque la synthèse colloïdale de particules d'indice élevé est plutôt difficile (matériau amorphe, porosité, oxydation, etc...) tandis que des particules d'indice modéré ou faible sont en général plus simples à obtenir. De telles particules diélectriques sont par exemple disponibles à la commande dans le commerce.

Néanmoins, pour certaines applications, il peut s'avérer compliqué de jouer sur le milieu hôte ou de trouver un matériau dont la dispersion conduit à un indice de réfraction prenant la valeur appropriée sur une gamme de longueurs d'onde désirée.

2.3 Des clusters de particules comme sources de Huygens résonnantes ou large bande

Comme alternative à ces sphères homogènes, nous avons proposé de manière originale de recourir à des particules composites, constituées d'inclusions assemblées de manière homogène. Celles-ci permettent de gagner en flexibilité dans la conception de sources de Huygens, et présentent dans certains cas de meilleures performances par rapport aux simples sphères. Nous nous sommes donc intéressés à des clusters de petites particules, dont les densités et tailles déterminent les propriétés optiques de l'agrégat formé et permettent d'ajuster à souhait l'indice de réfraction effectif des clusters. Notre procédure de conception repose sur la théorie étendue de Maxwell-Garnett, une méthode d'homogénéisation des propriétés d'un milieu composite. Bien que présentant certaines limitations et un aspect plus qualitatif que quantitatif, cette approche se révèle suffisamment polyvalente et efficace pour nous permettre de concevoir une large variété de clusters se comportant comme des sources de Huygens résonantes ou large bande pour le domaine du visible.

Nous présentons à ce titre deux exemple de clusters, simulés par la méthode de la $\mathcal{T}$-matrice, un cluster plasmonique et un diélectrique, se comportant comme des sources de Huygens dipolaires résonantes à la longueur d'onde de 500nm. Le premier est un cluster de 60 particules d'argent placées dans l'eau présentant une efficacité de diffusion à la résonnance de 2.5. Un résultat particulièrement notable est obtenu pour le second cluster consistant en 13 particules de silicium qui, lui, présente une efficacité de diffusion de 5 à la résonance, dépassant ainsi le maximum théorique pouvant être obtenu pour une simple sphère homogène de perméabilité unitaire. Une hypothèse avancée pour expliquer cette valeur de diffusion surprenante est la modulation additionnelle de la perméabilité effective de l'objet composite, apportée par la réponse magnétique de ses constituants, que l'on ne retrouve pas pour de simples particules homogènes naturelles. Par ailleurs un cluster de 80 particules de silicium dispersées dans l'eau est également présenté pour réaliser une source de Huygens extrêmement large bande avec une proportion de diffusion vers l'avant supérieure à 95% sur toute la plage de longueur d'onde entre 500nm et 1500nm. Ce comportement est obtenu par l'excitation successive de paires de multipôles jusqu'à l'ordre 5.

Aussi une structure de type "cluster" est riche, car facilement modulable pour cibler différentes longueurs d'onde de travail, et est adaptée à de nombreux matériaux tant plasmoniques que diélectriques. Au vu des progrès significatifs réalisés ces dernières années dans le domaine de l'auto-assemblage de particules colloïdales, nous espérons que le comportement de sources de Huygens de clusters, tel que révélé ici, pourra être vérifié expérimentalement dans un avenir proche. Par ailleurs, des simulations préliminaires ont été conduites prenant en compte l'impact d'imperfections expérimentales telles que peuvent l'être la présence de vides localisés, un désordre positionnel des particules ou une dispersion dans la taille des inclusions. Nous avons étudié l'impact de ces défauts sur les réponses dipolaires d'un cluster plasmonique. Il ressort de cette première

étude que le paramètre le plus susceptible de compromettre l'obtention de deux résonances dipolaires superposées satisfaisant à la condition de Kerker est le désordre positionnel des particules dans l'agrégat qui tend à atténuer drastiquement la réponse magnétique des clusters. Ce résultat est néanmoins encourageant d'un point de vue expérimental puisque de simples revêtements de faible indice autour des inclusions plasmoniques devraient empêcher des degrés élevés de désordre dans les clusters, en garantissant une distance inter-particule minimale pendant le processus d'auto-assemblage.

2.4 Diffusion unidirectionnelle par des particules multicouches

Finalement, dans une dernière partie, nous nous sommes intéressés aux particules multicouches. Notre intérêt s'est tout d'abord porté sur des particules de type cœur-écorce composées d'un cœur plasmonique et d'une écorce diélectrique. De tels méta-atomes, déjà partiellement explorés dans la littérature, sont extrêmement prometteurs pour obtenir des sources de Huygens résonantes purement dipolaires. Ils ont l'avantage de présenter des efficacités de diffusion très élevées dans le domaine du proche infrarouge, dont les valeurs rivalisent avec celles des objets anisotropes de fort indice de réfraction considérés dans la majorité des réalisations de métasurfaces. Contrairement aux sphères et clusters précédemment étudiées, le recouvrement spectral des résonances n'est pas réalisé au détriment d'un indice de réfraction élevé. La particule supporte à fois une forte résonance dipolaire magnétique de Mie, provenant de l'enveloppe diélectrique d'indice élevé, et une résonance dipolaire électrique provenant de la résonance du plasmon de surface localisé du cœur métallique.

Nous présentons notamment dans cette thèse un abaque pouvant servir de référence à la conception de particules cœur-écorce présentant des résonances dipolaires superposées dans l'infrarouge. Le recouvrement spectral des résonances est obtenu en ajustant correctement l'épaisseur relative des deux couches, déterminée lors d'une exploration systématique des paramètres géométriques. Il résulte de cette étude que l'épaisseur de la couche diélectrique nécessaire pour obtenir une source de Huygens est d'autant plus grande que l'épaisseur du cœur augmente et que l'indice de réfraction de la couche diélectrique diminue. Pour donner un ordre de grandeur, l'épaisseur du diélectrique peut varier entre 2 à plus de 4 fois l'épaisseur du cœur plasmonique. Un résultat par ailleurs intéressant est la faible dépendance des paramètres géométriques requis pour atteindre le régime de Kerker, avec la nature du cœur plasmonique qu'il soit d'or ou d'argent.

Pour finir, nous illustrons avec plusieurs exemples la possibilité de recourir à des particules multicouches entièrement diélectriques pour la conception de sources de Huygens. Nous montrons notamment que des particules de type cœur-écorce sont capables de surpasser les performances de simples sphères en terme d'efficacité de diffusion dans la condition résonante dipolaire de Kerker. Avec un deuxième exemple, nous révélons par ailleurs l'excellente superposition entre multipôles de même ordre obtenue pour une particule constituée de 3 couches. La superposition deux à deux des multipôles est bien meilleure que celle obtenue dans le cas de simples sphères. L'ajout de couches résulte en fait en une adaptation graduelle de l'impédance de la particule avec son milieu hôte, due au gradient décroissant de l'indice de réfraction de la particule de son cœur à sa surface.

Ayant révélé le potentiel de plusieurs types de structures isotropes pour des applications de sources de Huygens et ayant identifiés différentes procédures et tendances permettant de les concevoir efficacement, la seconde partie de la thèse est dédiée à l'étude des métasurfaces.

3 Métasurfaces de Huygens multipolaires

3.1 Formalisme multipolaire et propriétés de métasurfaces

Relier les coefficients de réflexion et de transmission d'un réseau de particules aux propriétés de diffusion et d'absorption de ces constituants est un concept crucial pour la conception de

métasurfaces et la compréhension de leurs propriétés. En utilisant la décomposition en harmoniques sphériques vectorielles, nous proposons une description multipolaire très générale des coefficients de réflexion et de transmission d'une monocouche de particules, venant étendre et généraliser à tout ordre multipolaire le formalisme dipolaire (parfois étendu aux quadrupôles) communément rencontré dans la littérature.

Le point de départ pour établir ce formalisme est d'exprimer le champ produit par un réseau de particules comme la superposition du champ diffusé par chacune de ces particules. En faisant ensuite intervenir les fonctions périodiques de Green et en écrivant le développement multipolaire du champ lointain diffusé par une des cellules élémentaires dans les directions avant et arrière, il est alors possible d'établir le lien entre réflexion/transmission de la métasurface et moments multipolaires. L'expression compacte de ces coefficients de réflexion et de transmission en terme des multipôles symétriques ou pairs ($\mathcal{E}_n$) et antisymétriques ou impairs ($\mathcal{O}_n$), d'ordre n, est la suivante :

$$r = -\frac{\pi}{2k^2\mathcal{S}} \sum_{n=1}^{\infty} \left[\mathcal{E}_n - \mathcal{O}_n\right] \tag{R.4}$$

$$t = 1 - \frac{\pi}{2k^2\mathcal{S}} \sum_{n=1}^{\infty} \left[\mathcal{E}_n + \mathcal{O}_n\right] \tag{R.5}$$

$\mathcal{S}$ étant l'aire de la maille élémentaire de la métasurface. Cette formulation est pratique puisqu'une distinction claire peut être faite dans le rôle des multipoles pairs et impairs. Ainsi, à partir de ces expressions, les conditions d'obtention d'une transmission ou d'une absorption parfaite de la lumière par un système multipolaire quelconque peuvent être dérivées.

3.2 Métasurfaces à forte transmission pour des applications de contrôle de front d'ondes

Pour des systèmes sans perte, une transmission parfaite avec une phase arbitraire peut être obtenue sous la simple condition que r s'annule, c'est à dire lorsque $\sum_{n=1}^{\infty}\mathcal{O}_n = \sum_{n=1}^{\infty}\mathcal{E}_n$. Cette égalité entre contribution des multipôles pairs et impairs correspond à la condition de Kerker.

Dans cette thèse nous démontrons que des clusters de particules peuvent être théoriquement exploités pour réaliser des métasurfaces à forte transmission destinées à des applications de manipulation de front d'onde. Nous nous intéressons pour cela à des clusters diélectriques de particules de silicium, ce matériau présentant des pertes négligeables dans le proche infrarouge. Nous mettons en évidence qu'une variation locale du rayon des clusters ou du pas du réseau permettent d'induire un déphasage continu compris entre 0 et 2π à l'onde transmise par la surface, et ce tout en conservant une transmission élevée supérieure à 80%.

À partir de ces résultats, des applications de mise en forme de faisceaux par des clusters sont illustrées par la conception et la caractérisation numérique de deux dispositifs exploitant la modulation de la phase induite par une variation de la taille des clusters pour un pas constant entre les particules. Une des originalités notables de ce travail réside dans le fait que nous exploitons les résonances quadrupolaires des clusters pour obtenir le régime de Kerker.

Le premier dispositif proposé est un déflecteur de faisceaux permettant la déflection d'un faisceau incident selon un angle de 9°. Le gradient linéaire de phase de 2π est implémenté à partir de 8 clusters de *Si*, de rayons croissants, séparés par 806nm chacun. Le dispositif présente une transmission totale de 75%, où 87% de l'énergie transmise est émise dans le premier ordre de diffraction souhaité.

Le second dispositif que nous étudions est une métasurface de Huygens se comportant comme une lentille plate semi-infinie permettant de focaliser une onde incidente grâce à un motif symétrique constitué de 13 clusters. Une variation de phase de 2π selon un profil spatial hyperboloïdal est ainsi implémentée par des clusters dont les rayons décroissent en se rapprochant des extrémités de la lentille. Le dispositif étudié numériquement présente une distance focale de 8.1μm environ et une ouverture numérique N.A. de 0.42. Par ailleurs, la transmission obtenue au travers de la lentille est d'environ 80%.

Les études mentionnées ici sont menées sur des métasurfaces illuminées en incidence normale, néanmoins plusieurs travaux récents rapportent des performances fortement dégradées en terme de transmission pour une illumination oblique. À partir d'une décomposition multipolaire, nous mettons en évidence l'excitation de composantes verticales de certains multipôles à de faibles angles d'incidence, permettant d'expliquer la diminution de la transmission observée à certaines longueurs d'onde. Ces observations confirment que des résonances supplémentaires sont susceptibles de réduire considérablement l'efficacité de métasurfaces de Huygens dès lors qu'une incidence normale n'est plus garantie.

3.3 Absorbeurs parfaits

3.3.a Conditions d'absorption généralisées

Pour des systèmes capables de dissiper l'énergie, l'absorption par une monocouche de particules peut être optimisée et une absorption totale de l'énergie incidente est obtenue dans la condition:

$$\sum_{n=1}^{\infty} \mathcal{O}_n = \sum_{n=1}^{\infty} \mathcal{E}_n = \frac{k^2 \mathcal{S}}{\pi} \tag{R.6}$$

Cette relation contient à la fois la condition de Kerker généralisée permettant d'annuler la réflexion et la condition de transmission nulle. Cette relation devant être remplie dans le plan complexe, cela implique que la phase de chacune des sommes multipolaires est fixée à 0 de sorte que chaque somme soit purement réelle et de valeur $k^2\mathcal{S}/\pi$. Cette condition permet une interférence destructive parfaite entre l'onde diffusée vers l'avant par le réseau et l'onde plane incidente.

En supposant que les multipôles d'une particule ne sont que faiblement perturbés par le réseau, c'est-à-dire en négligeant les effets de couplages entre particules dans une métasurface, le formalisme multipolaire devient un outil puissant pour concevoir des absorbeurs parfaits. En effet, la condition d'absorption parfaite peut dans un premier temps être testée sur des particules isolées, avant de recourir dans un second temps à des calculs pour des réseaux périodiques beaucoup plus lourds numériquement. Tout l'intérêt de cette procédure en deux étapes, scindant conception des particules et de la métasurface, est qu'elle permet d'identifier au préalable les méta-atomes qui seront à priori de bons candidats pour atteindre le régime d'absorption totale une fois organisés en métasurface. Par ailleurs, il est important de souligner que le formalisme étant généralisé à des multipôles de tout ordre, il permet de concevoir, sans ajouter de difficultés supplémentaires, des absorbeurs dipolaires ou fortement multipolaires. Ainsi, en exploitant cette approche, nous avons présenté et étudié une large variété d'absorbeurs, constitués de différentes particules isotropes, pouvant être obtenue par des voies de fabrication ascendante.

3.3.b Absorbeurs basés sur des particules sphériques

Nous avons par exemple révélé la possibilité d'utiliser des réseaux de particules sphériques diélectriques pour obtenir une absorption unitaire. Nous donnons deux exemples en exploitant les résonances phononiques de la silice et de l'alumine dans l'infrarouge lointain, présentant des pertes non radiatives suffisamment élevées. Nos résultats restent cependant transposables à d'autres longueurs d'onde pour des matériaux présentant des indices similaires. Nous démontrons ainsi deux absorbeurs constitués de réseaux denses de microsphères homogènes de SiO_2 de 4,12μm de rayon et de particules d'Al_2O_3 de 9,3μm de rayon, opérant toutes deux dans des régimes fortement multipolaires où au moins 8 multipôles sont nécessaires pour expliquer les fortes absorptions observées. À notre connaissance, c'est la première fois que des absorbeurs fonctionnant dans un régime aussi multipolaire sont mis en évidence. Combiner un nombre important de multipôles offre la possibilité conceptuelle d'atteindre des régimes d'absorption large bande par opposition aux absorptions nécessairement résonantes obtenues avec des structures supportant uniquement 2 résonances multipolaires. À ce titre, les deux absorbeurs étudiés présentent des bandes spectrales relativement larges sur lesquelles l'absorption reste supérieure à 90%. Par

ailleurs, l'absorption maximale de ces métasurfaces ne varie que faiblement avec la densité des réseaux et l'angle d'incidence.

Dans un second temps nous nous intéressons à des particules plasmoniques et révélons une absorption de presque 99% obtenue avec un réseau dense de nanoparticules d'argent de 78nm de rayon présentant une fraction surfacique en particule de 0.75, très proche de la compacité maximale. Ce résultat est important en ce qu'il souligne qu'une réponse magnétique n'est pas nécessaire pour atteindre le régime de Kerker ou celui d'absorption totale. Ici l'absorption presque unitaire s'explique par l'excitation conjointe de deux multipôles électriques, à savoir un dipôle et un quadrupôle, excités en bordure du visible à une longueur d'onde proche de 450nm. Contrairement aux réseaux diélectriques, l'absorption de la métasurface plasmonique est beaucoup plus sensible aux effets de couplage et se dégrade rapidement pour des réseaux plus dilués.

Nous montrons ainsi que de simples particules sphériques diélectriques ou plasmoniques peuvent être envisagées pour réaliser des absorbeurs. Néanmoins, il convient de souligner qu'avec ce type de méta-atome simple, dès lors que le matériau est choisi, le choix des structures sera limité, et par ailleurs difficilement accordable en longueur d'onde du fait que l'unique paramètre pouvant être ajusté est le rayon des particules. Aussi, d'une manière générale, considérer des structures plus complexes va permettre un gain notable en flexibilité, mais au détriment sans doute d'une fabrication plus difficile.

3.3.c Absorbeurs basés sur des particules de type cœur-écorce

Nous montrons qu'avec des particules de type cœur-écorce métalo-diélectriques, une absorption résonante presque parfaite peut être obtenue à des longueurs d'onde arbitraires dans le domaine du proche infrarouge. Pour de faibles tailles de particules cœur-écorce de l'ordre de 150nm, et pour des diélectriques aux indices de réfraction proche de 2.5, les pics d'absorption se situent en bordure du domaine visible, proche de 800nm. En augmentant progressivement l'indice des coquilles de 2.5 à 3 et 3.5, et pour des particules de taille allant jusqu'à 215nm, les pics d'absorption sont obtenus à des longueurs d'onde plus élevées allant jusqu'à presque 1800nm. Il est à noter que les très fortes absorptions présentées par les réseaux de particules cœur-écorce sont obtenues pour des métasurfaces diluées, présentant typiquement des fractions surfaciques en particules de l'ordre de 0.1. Nous étudions également au cours de cette thèse des particules cœur-écorce entièrement diélectriques et mettons en lumière la possibilité d'obtenir deux pics d'absorption résonant en bordure du visible avec des monocouches de tels objets. Ceci s'explique par l'excitation successive d'une paire de dipôles et d'une paire de quadrupôles.

3.3.d Absorbeurs parfaits exploitant des clusters de particules

Finalement, nous démontrons la possibilité d'utiliser des clusters de particules, tant diélectriques que plasmoniques, pour des applications d'absorption parfaite. Nous montrons que des réseaux de clusters de silicium présentent de fort pics d'absorption proches des positions des résonances quadrupolaires excitées vers 450nm. Par ailleurs, les pics d'absorption varient peu avec la densité des réseaux et présentent une grande robustesse angulaire. Nous révélons également la souplesse intéressante amenée par ce type de structure avec l'exemple de clusters de germanium. Ce matériau, à faible dispersion dans le proche infrarouge, permet un ajustement simple des dimensions des objets pour cibler différentes longueurs d'onde de travail, typiquement entre 800nm et 1300nm. Finalement en exploitant les bandes d'absorption plasmoniques de particules d'or et de particules d'argent, une absorption quasi-parfaite peut-être obtenue avec des réseaux de clusters d'argent et d'or organisés périodiquement avec un pas proche de la limite diffractive. Ces métasurfaces présentent des pics d'absorption atteignant 98% et 96% respectivement à 385nm et 558nm pour les cluster d'Ag et d'Au.

Le formalisme multipolaire fournit ainsi une ligne directrice pour la conception d'absorbeurs parfaits pouvant s'appliquer à des méta-atomes au contenu multipolaire varié. Il en résulte égale-

ment des comportements très divers avec des métasurfaces présentant des absorption résonantes, double-bandes ou large bandes.

4 Conclusion

Le domaine des métasurfaces de Huygens est récent et a connu un développement rapide. L'objectif principal de ce travail de thèse était d'étudier la faisabilité de sources et de métasurfaces de Huygens qui seraient compatibles avec des méthodes d'auto-assemblage, en se concentrant sur des particules colloïdales. Nous avons produit plusieurs résultats originaux et prometteurs qui devraient contribuer au développement de métasurfaces de Huygens fonctionnelles. Ceux-ci sont résumés ci-dessous :

Démonstrations de sources de Huygens sphériques résonantes ou large bandes

- Nous avons montré que des particules diélectriques sphériques placées dans un milieu homogène avec un contraste d'indice $\gamma \approx 2$ satisfont à la condition de Kerker et présentent deux résonances dipolaires électrique et magnétique étroitement superposées. Pour des valeurs décroissantes de γ , tendant vers 1.5, il est possible d'atteindre une diffusion unidirectionnelle vers l'avant, très large bande, pouvant couvrir tout le domaine visible. Celle-ci résulte de la superposition spectrale deux à deux des deux résonances dipolaires, quadrupolaires et octupolaires électriques et magnétiques des objets. Ces résultats montrent que l'ingénierie du contraste d'indice peut être une alternative intéressante ou complémentaire au levier que constitue le contrôle du rapport d'aspect de particules.
- Par ailleurs, nous avons démontré que des clusters de particules constituent une excellente alternative pour réaliser des sources de Huygens résonantes ou large bandes. L'ajustement des résonances pour ces structures est obtenu par les paramètres géométriques que sont la taille des inclusions et leur densité dans l'agrégat. La présence de plusieurs paramètres ajustables présente un avantage certain par rapport au recours à de simples sphères homogènes, pour lesquelles le nombre restreint de matériaux ayant la dispersion adaptée aux fréquences optiques est limitant.

Un outil théorique rigoureux pour l'analyse et la conception de métasurfaces

- Nous avons présenté un formalisme multipolaire reliant les coefficients de réflexion et de transmission, observables essentielles des métasurfaces, aux coefficients de diffusion de ses constituants. Basé sur un développement en harmoniques sphériques vectorielles, ce formalisme est généralisé à tout ordre et constitue ainsi une extension rigoureuse à la description dipolaire couramment utilisée dans la littérature. Ce formalisme permet une analyse simple et totalement générale des propriétés de métasurfaces complexes pouvant être constituées d'unités fortement multipolaires.

Démonstrations numériques de métasurfaces avec plusieurs propriétés originales

- En considérant des clusters diélectriques sans perte dans l'infrarouge (*Si*), nous avons démontré numériquement que la mise en forme de fronts d'onde est possible en exploitant les résonances quadrupolaires de ces objets. Nous avons montré que deux paramètres permettent une variation de phase complète couvrant l'intervalle de 0 à 2π avec une transmission élevée : la taille des clusters et le pas entre les éléments dans la métasurface. Ce résultat a été utilisé pour démontrer un déflecteur de faisceau à un angle de 9° avec une barrette de 8 clusters et une méta-lentille de 13 clusters permettant la focalisation d'une onde plane incidente.
- D'autre part, nous avons montré que des absorbeurs parfaits, consistant en des réseaux de particules diélectriques, peuvent fonctionner dans un régime fortement multipolaire, pour lequel au moins huit multipôles sont nécessaires pour rendre compte de l'absorption unitaire. À notre connaissance, c'est la première fois que de tels absorbeurs parfaits multipolaires sont proposés ou mis en évidence.

Ligne directrice pour l'identification et la conception de structures

- Les particules de type cœur-écorce métallo-diélectriques sont des éléments prometteurs en raison de leur comportement dipolaire idéal et de leur forte efficacité de diffusion dans l'infrarouge. Nous avons fourni une liste détaillée de structures se comportant comme des sources de Huygens, sous la forme d'un abaque, pouvant servir de guide à la communauté de la nanochimie pour la synthèse de ces particules.
- Nous avons présenté une démarche permettant d'identifier des clusters de particules qui présenterons un comportement de source de Huygens. Notre approche est fondée sur l'homogénéisation des agrégats au moyen de la théorie étendue de Maxwell-Garnett et sur l'ajustement de leur indice de réfraction effectif. Nous avons démontré la grande versatilité de cette approche ainsi que certaines de ses limitations.
- Nous avons montré que le formalisme multipolaire généralisé décrivant les propriétés de métasurfaces peut être exploité efficacement pour concevoir des absorbeurs parfaits. En particulier, une exploration préliminaire des paramètres est effectuée sur des méta-atomes considérés individuellement et permet d'identifier de bons candidats aux applications d'absorbeurs parfaits avant de recourir à un calcul périodique rigoureux. Cette procédure de conception est puissante puisque nous avons montré qu'elle est applicable avec succès à une large variété de systèmes présentant des contenus multipolaires distincts.

L'étude menée dans le cadre de cette thèse est pionnière dans les domaines de la nanochimie et de l'auto-assemblage. Elle est probablement la première à aborder la possibilité de concevoir des nano-résonateurs, pouvant être synthétisés chimiquement avec des propriétés de diffusion directionnelle intéressantes, et être exploités ultérieurement pour la fabrication de métasurfaces. Nous sommes optimistes quant au fait que des réalisations expérimentales exploitant de telles particules pourraient voir le jour dans les années à venir. Néanmoins, nos travaux présentent certaines limites. En particulier, nous nous sommes essentiellement intéressés à des structures et surfaces idéalisées. Cela signifie notamment que les imperfections inhérentes aux systèmes expérimentaux n'ont pas été abordées, d'où le besoin à l'avenir de compléter ces travaux par un certains nombres d'études supplémentaires. Plusieurs points méritant une analyse approfondie, car susceptibles d'impacter de manière significative les propriétés de structures obtenues dans la logique d'une fabrication par voie ascendante, sont énumérés ci-dessous.

Viabilité expérimentale des structures étudiées théoriquement

- Les techniques d'auto-assemblage introduisent à la fois désordre et polydispersité. Une piste importante à explorer pour les clusters de particules, avant de conclure sur leur faisabilité expérimentale comme sources de Huygens, serait de mener une enquête statistique complète sur l'impact de vides localisés, de désordre et de polydispersité sur leurs réponses optiques, complétant ainsi les travaux présentés dans cette thèse. Il est à noter que des travaux initiés au CRPP dans le cadre de la thèse de Rajam Elancheliyan concernant la synthèse de nanoclusters sont prometteurs et montrent que de fortes réponses magnétiques peuvent être obtenues avec des clusters plasmoniques élaborés à partir d'émulsions.
- Par ailleurs, il serait intéressant d'étudier plus en détail les particules de types cœur-écorce entièrement diélectriques, dont le contenu multipolaire semble très similaire à celui des clusters diélectriques. En effet, il n'est pas rare d'obtenir des structures de ce type lors de la synthèse de particules colloïdales diélectriques. Oxydation en surface, porosité et croissance amorphe peuvent typiquement conduire à des particules présentant des indices effectivement plus faibles en surface qu'au cœur de la particule. Il serait également intéressant de mener des études complémentaires tenant compte de dispersions d'indice réalistes et d'effectuer une investigation plus systématique de la dépendance des propriétés optiques avec le nombre de couches et leur indice de réfraction.
- Les particules cœur-écorce métalo-diélectriques étudiées dans la littérature et dans ce travail semblent particulièrement prometteuses. Néanmoins, les paramètres géométriques

requis pour atteindre le régime de Kerker restent à notre connaissance au-delà de ce qui est aujourd'hui réalisable expérimentalement. Notamment, un des défis majeurs du point de vue expérimental réside en la réalisation de revêtements à fort indice et d'épaisseur conséquente autour des cœurs des particules (supérieure à 100 nm).

Désordre positionnel dans les métasurfaces

- Dans la section consacrée aux absorbeurs, nous avons présenté certaines structures consistant en des réseaux très denses de particules. Ces résultats sont encourageants du point de vue de la fabrication, car ces réseaux peuvent a priori être obtenus par des méthodes d'auto-assemblages classiques. Qui plus est, certaines propositions de métasurfaces, comme par exemple celles constituées de clusters de silicium, présentent des pics d'absorption ne variant que très légèrement avec le pas du réseau. Ceci pourrait indiquer une faible dépendance à un désordre positionnel des particules sur la surface. La conservation des propriétés d'absorption avec le désordre est une question particulièrement importante qui mériterait d'être explorée à l'avenir pour l'ensemble des structures que nous avons proposé. Si nous sommes optimistes quant au fait que des surfaces désordonnées puissent fonctionner dans le régime d'absorption parfaite, ce point mérite cependant une démonstration.
- D'autre part, les applications de manipulation du front d'onde, telles que celles que nous avons démontrées numériquement, posent un véritable défi pour une fabrication de type bottom-up. En effet, celles-ci nécessitent de contrôler très finement l'agencement spatial des particules sur la surface, ainsi que leur taille afin d'implémenter les gradients spatiaux désirés. Ce type d'applications semble peu probable sans le recours à des substrats pré-structurés qui serviraient de guides pour positionner les particules. L'utilisation de tels substrats signifie une approche hybride combinant voies descendante et ascendante. En outre, le désordre inhérent aux techniques d'auto-assemblage mériterait d'être examiné de manière systématique, afin de se rendre compte de son impact sur les propriétés des métasurfaces, que ce soit pour la modulation de front d'onde ou pour les applications comme absorbeurs.

Impact d'un substrat

- Dans cette thèse, les métasurfaces considérées sont des réseaux placés en espace libre. Cette considération reste pertinente dans le sens où des métasurfaces peuvent être élaborées sur des substrats en verre puis recouvertes d'un superstrat de polymère garantissant que les deux matériaux hôtes entourant la métasurface soient de même indice de réfraction. Toutefois, il est pratique, à titre expérimental, de simplement disposer les monocouches de particules sur un substrat, sans recourir à un superstrat. Aussi, une étude approfondie prenant en compte l'interaction des particules d'une métasurface avec un substrat constituerait une extension particulièrement intéressante à ce travail.

Analyse des propriétés de métasurfaces de Huygens en incidence oblique

- Finalement, il est à noter que le formalisme utilisé dans ce travail pour analyser le contenu multipolaire des nano-résonateurs constituant une métasurface périodique n'est valable qu'en incidence normale et ne permet pas de rendre compte de l'évolution des propriétés en incidence oblique. Aussi, de nouveaux outils seront nécessaires pour étudier ces situations et interpréter ou prévoir les évolutions des propriétés de réseaux de particules avec l'angle d'incidence.

Résumé

Les avancées récentes en optique à l'échelle nanométrique ont donné naissance à une nouvelle branche de la nano-photonique visant à manipuler la diffusion de nanoparticules, avec de nombreuses applications potentielles en communication optique, en photovoltaïque, pour le développement de nano-antennes, de capteurs, etc. La réponse de nano-diffuseurs est souvent caractérisée en termes de multipoles électromagnétiques dont les ajustements constituent un moyen efficace pour façonner à souhait les diagrammes de rayonnement de particules. En particulier, des interférences destructives entre multipoles de parité spatiale opposée peuvent être exploitées pour annuler la rétro-diffusion d'objets de petites tailles. Cet effet, théoriquement prédit il y a 30 ans par Milton Kerker, permet aujourd'hui de concevoir des particules sub-longueur d'onde diffusant la lumière uniquement vers l'avant, partageant ainsi les principales caractéristiques des sources théoriques fictives utilisées dans le principe de Huygens-Fresnel. Une fois assemblées en réseau périodique bidimensionnel, ces particules, appelées "sources de Huygens", offrent des opportunités uniques dans le développement de composants optiques plats et ultrafins, appelés "métasurfaces", permettant un contrôle arbitraire de la phase, de l'amplitude et/ou de la polarisation de faisceaux lumineux. Ainsi, au cours des dernières années, les métasurfaces de Huygens ont été très largement explorées comme alternative à l'optique traditionnelle pour la conception de surfaces remplissant les fonctions de lentilles, de déflecteurs de faisceau, de vortex optique, d'hologrammes ou d'absorbeurs parfaits. Ces travaux se sont notamment appuyés sur des sources de Huygens anisotropes pouvant être obtenues par les technologies dites "top-down". Contrairement aux approches étudiées jusqu'à présent, cette thèse porte sur l'étude de sources de Huygens isotropes. Nous étudions en particulier des particules homogènes, composites ou de types coeur-coquille pour atteindre le régime de Kerker. Nous démontrons la possibilité de façonner le front d'onde de faisceaux optiques en utilisant des systèmes sphériques constitués d'amas de particules diélectriques. Nous présentons également un formalisme multipolaire pouvant être exploité pour optimiser l'absorption de surface de Huygens. Comme fil conducteur de notre projet, les objets que nous étudions sont adaptés aux technologies ascendantes (dite "bottom-up") et pourraient de manière réaliste être obtenue par synthèse colloïdale et procédés d'auto-assemblage, offrant ainsi une alternative aux métasurfaces classiquement obtenues par lithographie.

Mots clés : *photonique, résonateurs optique, nanoparticules, diffusion, sources de Huygens, métasurfaces*

Abstract

Recent developments in optics at the nanoscale have given rise to a new branch of nano-photonics aimed at manipulating the scattering of nanoparticles, with numerous potential applications in optical communication, nano-antennas, photovoltaics, sensing, etc. The response of nano-scatterers is often characterized in terms of electromagnetic multipoles. Tailoring these multipoles represents an efficient scheme to engineer three-dimensional radiation diagrams. For instance, destructive interferences between multipoles of opposite spatial parity can be exploited to cancel backscattering. This effect, theoretically predicted 30 years ago by Milton Kerker, makes it possible to produce subwavelength particles that scatter light in the forward direction, thus sharing the main features of the fictitious sources used in the Huygens-Fresnel principle. Once assembled in a periodic two-dimensional network, such particles, named "Huygens sources", offer unique opportunities for the development of flat and ultrathin optical components called "metasurfaces" that enable the arbitrary control of the phase, amplitude and/or polarization of a beam of light. Over the past few years, Huygens metasurfaces have been widely explored to engineer highly efficient lenses, beam deflectors, vortex beams, holograms or perfect absorbers, that have relied on two-dimensional anisotropic Huygens sources. In contrast to approaches investigated thus far, this thesis focuses on the study of isotropic Huygens sources. We investigate homogeneous, composite and core-shell particles as a solution to reach the Kerker regime. Subsequently, we demonstrate that wave-front shaping is indeed possible by using spherical systems composed of clusters of dielectric inclusions and we present a multipolar formalism that can be used as a guideline to optimize the absorption of Huygens arrays. The structures we study are realistically achievable by bottom-up fabrication and self-assembly, offering an alternative to the classical lithographically fabricated metasurfaces.

Keywords : *photonic, optical resonators, nanoparticles, scattering, Huygens sources, metasurfaces*